

Estimation of evaporative fractions by the use of vegetation and soil component temperatures determined by means of dual-looking remote sensing

Estimation of evaporative fractions by the use of vegetation and soil component temperatures determined by means of dual-looking remote sensing

**J. Rauwerda
G.J. Roerink
Z. Su**

Alterra-report 580

Alterra, Green World Research, Wageningen, 2002

ABSTRACT

J. Rauwerda, G.J. Roerink, Z. Su, 2002. Estimation of evaporative fractions by the use of vegetation and soil component temperatures determined by means of dual-looking remote sensing. Wageningen, Alterra, Green World Research.. Alterra-report 580. 148 pp. 9 figs.; 6 tables; 69 refs.

Knowledge of evaporation on local scale is a prerequisite for the prediction of drought. The *Surface Energy Balance System (SEBS)* provides the means to do this. Input data of SEBS is satellite data, and a limited set of ground measurements. By making use of the dual-looking viewing capabilities of the ATSR sensor on board of the ERS-II, it is possible to determine vegetation and soil temperature separately. These two temperatures can be used in SEBS – *the dual source SEBS* – in order to gain more insight in the evaporation process and to improve the physical basis of the algorithm.

Testing and validation of single and dual source SEBS has been carried out with the use of existing data sets of the Netherlands and Spain. The algorithm sensitivity towards input variables is established. Air and surface temperature and wind speed have a large impact on the results. Two input variables prove to be very hard or impossible to measure, i.e. the roughness length for momentum and the roughness length for heat transfer. The existing methods and models don't give satisfactory results. Validation is carried out with ground fluxes, measured by eddy devices and scintillometers.

Keywords: remote sensing, component temperatures, ATSR, roughness, energy balance, flux

ISSN 1566-7197

This report can be ordered by paying €24,25 into bank account number 36 70 54 612 in the name of Alterra, Wageningen, the Netherlands, with reference to report 580. This amount is inclusive of VAT and postage.

© 2002 Alterra, Green World Research,
P.O. Box 47, NL-6700 AA Wageningen (The Netherlands).
Phone: +31 317 474700; fax: +31 317 419000; e-mail: postkamer@alterra.wag-ur.nl

No part of this publication may be reproduced or published in any form or by any means, or stored in a data base or retrieval system, without the written permission of Alterra.

Alterra assumes no liability for any losses resulting from the use of this document.

Contents

Acknowledgement	9
Executive summary	11
1 Introduction	13
1.1 The China Drought Project	13
1.2 Estimation of Evaporation by Means of Remote Sensing	14
1.3 Research Objectives	15
1.4 Outline of this Paper	16
2 Relevance of this Project to Environmental Sciences	17
3 A Turbulent Atmosphere	19
3.1 The Planetary Boundary Layer	19
3.2 The Energy Balance at the Earth's Surface	19
3.3 Turbulence	20
3.4 Atmospheric Similarity Methods	23
3.5 Estimation of Evaporation: the Penman-Monteith equation	25
4 The Surface Energy Balance System (SEBS) for the Estimation of Evaporative Fractions	29
4.1 The Atmospheric Correction and the Preprocessing of Satellite Data.	29
4.1.1 Cloud and Water Surface Screening	30
4.1.2 Water Vapor Determination	31
4.1.3 Retrieval of Aerosol Optical Depth	31
4.1.4 Atmospheric Correction for VIS/NIR Channels	32
4.1.5 Fractional Vegetation Cover	32
4.1.6 Atmospheric Correction Thermal Infrared Channels	32
4.1.7 Separation of Soil and Foliage Temperatures	33
4.1.8 Geometric Correction	35
4.2 Models for the Determination of the Roughness Length for Heat Transfer	35
4.2.1 Massman's kB^{-1} Model	36
4.2.2 Blümel's kB^{-1} Model	38
4.3 The Bulk Atmospheric Similarity Model (BAS)	41
4.4 The Surface Energy Balance Index (SEBI)	43
4.5 Emissivity and Soil Heat Flux	46
4.6 Roughness Length for Momentum	47
4.7 The Parallel Source Model	49
4.8 Modifications to the Original Code	50
4.9 Flux measurements	51
4.9.1 Eddy devices	51
4.9.2 Scintillometers	51
5 Estimation of heat fluxes in Spain and the Netherlands	53
5.1 Measurement Sites in Spain and the Netherlands	53

5.1.1 Sensitivity Analysis: Sensitivity towards Input Parameters	55
5.1.2 Sensitivity Analysis: Sensitivity towards Variability of Meteorological Data	60
5.2 Time Series	62
5.2.1 Time Series: Loobos	63
5.2.2 Time Series: Tomelloso	65
5.3 ATSR Data: Single Source	66
5.3.1 ATSR Data: Single Source – the Netherlands	66
5.3.2 ATSR Data: Single Source – Badajoz	68
5.3.3 ATSR Data: Single Source – Lleida	68
5.3.4 ATSR Data: Single Source – El Saler	69
5.3.5 ATSR Data: Single Source – Tomelloso	70
5.3.6 ATSR Data: Single Source – Discussion	71
5.4 ATSR Data: Parallel Source	73
5.4.1 ATSR Data: Parallel Source – Badajoz	74
5.4.2 ATSR Data: Parallel Source - Lleida	74
5.4.3 ATSR Data: Parallel Source – Tomelloso	74
5.4.4 ATSR Data: Parallel Source – Discussion	75
6 Conclusion	77
References	81

Appendices

1 Program code	87
a ALB.PRO code	87
b FC_NDVI.F code	87
c TOBY.PRO code	88
d CORINEZ.PRO code	88
e LOGAGG.PRO code	90
f LOGRECAGG.PRO code	91
g LOGRECQUADAGG.PRO code	92
h HASAG.PRO code	93
i Modifications to the original SEBS code	96
j REKEN.PRO code	97
2a Corine Land cover database - roughness length for momentum transfer	99
2b Radio Sonde Data - de Bilt, September 8, 1997	101
3 Sensitivity Analysis - Loobos - May 7, 1997 Tower Measurements	103
Sensitivity Analysis - Loobos - May 7, 1997 Radio Sounding De Bilt	107
Sensitivity Analysis - Tomelloso - June 2, 1999 Tower Measurements	111

	Sensitivity Analysis - Tomelloso - June 2, 1999 Radio Sounding Madrid	115
3b	Sensitivity Analysis - Loobos, May 7, 1997	119
	Sensitivity Analysis - Tomelloso, June 2, 1999	120
3c	Sensitivity Analysis - Fractional Cover and kB^{-1} factor	121
3d	Sensitivity Analysis - Tower measurements and radio soundings - Loobos, May 1997	123
3e	Sensitivity Analysis - sensitivity towards meteorological variables	125
4a	Time series - Loobos, May, July, September 1997 - Tower measurements – Massman heat transfer	129
4b	Time series - Loobos, May, July, September 1997 - Radio Soundings – Blümel heat transfer	131
5a	ATSR Data - Loobos, Fleditebos 1997	137
5b	ATSR Data – Single Source – Tomelloso, Lleida 1999	139
6	ATSR Data – Single Source - Statistics Spain 1999	141
7	ATSR Data – Single Source – South North Profile Badajoz July 30, 1999	143
8	ATSR Data – Parallel Source – Lleida, Badajoz	145
9	ATSR Data – Parallel Source - Statistics Spain 1999	147

Acknowledgement

This report presents the highlights of the MSc thesis of Drs. J. Rauwerda. The research has been carried out at Alterra as graduation project in Environmental Sciences at the Open University of the Netherlands during the period January – October 2001. It has been carried out within the framework of (I) the China_Drought project (contract number 2000WEME13002HL), financed by the Chinese Ministry of Water Resources and (ii) the “ENVISAT Land Surface Processes Phase 2” project, financed by the Netherlands Remote Sensing Board (BCRS, contract number 4.2/AP-14).

This report describes a wealth of data sets and results obtained through their analysis. These data sets have been provided by several organizations, which have supported us in many ways. The authors would like to thank:

- Ir. A.F. Moene and Dr. H.A.R. de Bruin of the Dept. of Meteorology of the Wageningen University for the provision of the scintillometer flux measurements of the three Spanish sites (Lleida, Badajoz, Tomelloso).
- Mr. P. Camara and Ms. S. Cosin of the Mediterranean Center for Environmental Studies (CEAM) for the provision of the eddy correlation flux measurements of the fourth Spanish site (El Saler).
- Ir. E.J. Moors of the Dept. of Water & Environment of Alterra for the provision of the eddy correlation flux measurements of the two Dutch sites (Loobos, Fleditebos)
- British Atmospheric Data Center (BADC) for the provision of radio soundings of the Netherlands and Spain.
- Eurimage for the provision of ATSR imagery.

The authors wish to acknowledge the following persons for their valuable contributions to the project:

- Ms.MSc. Li Jia of Alterra.
- Prof.Dr. M. Menenti of the University of Strasbourg.
- Dr. B.J.J.M. van den Hurk of the Royal Netherlands Meteorological Institute (KNMI).
- Dr. W. Verhoef of the National Aerospace Laboratory (NLR).

Executive summary

This research project has been carried out within the framework of the *China Drought Project*. Aim of the *China Drought Project* is to monitor and predict drought in continental China, by means of a combination of remote sensing, drought statistics, atmospheric models and hydrological models. Knowledge of evaporation on local scale is a prerequisite for the prediction of drought. The *Surface Energy Balance System (SEBS)*, developed at Alterra, provides the means to do this. SEBS recognizes the turbulent nature of the atmosphere, input data of SEBS is satellite data, and a limited set of ground measurements.

By making use of the dual-looking viewing capabilities of the *Along Track Scanning Radiometer (ATSR)* on board of the *European Remote Sensing Satellite (ERS-II)*, it is possible to determine vegetation and soil temperature separately. These two temperatures can be used in SEBS – the *dual source SEBS*, in this project *the parallel source SEBS* – in order to gain more insight in the evaporation process and to improve the physical basis of the algorithm.

Validation of single and dual source SEBS has been carried out with the use of existing data sets of the Netherlands (mid-latitude) and of Spain (semi-arid). Sensitivities of the algorithm towards input variables are established and the influence of variability of meteorological data is assessed. The possibility to use measurements in the Atmospheric Boundary Layer by radio soundings in order to calculate evaporative fractions over a larger area, has been looked into. By comparing time series and ATSR data an impression of the validity of atmospheric correction methods could be acquired. Furthermore the elaboration of time series – by using only ground measurements – removes some of the statistical uncertainties which are associated with a limited number of ATSR images. Throughout this project the influence of two variables which are very hard or impossible to measure, i.e. the roughness length for momentum and the roughness length for heat transfer, are assessed. Roughness length for momentum is determined either from NDVI or by making use of a land cover database.

On the ground fluxes are measured by eddy devices (the Netherlands and one site in Spain) or by scintillometers. Roughness length for heat transfer is studied by means of models by Blümel, which focuses on aggregation, and by Massman, which emphasizes within canopy processes.

SEBS proved to be sensitive to all input variables but specific humidity. Especially errors in measurement of air temperature, soil temperature and wind speed can cause large errors in the calculation of evaporation. Also determination of roughness length for momentum and albedo has a major impact on calculated evaporation. Within certain limits, these sensitivities however could well reflect a physical reality. Measurements from radio soundings seem to be less suited as input for SEBS, probably because these measurements have too coarse a resolution in the atmospheric boundary layer. Generally calculated values showed a correlation with measured values less than hoped for. Results from time series appeared to have a better fit with measurements than results from ATSR images. This error can be attributed to atmospheric correction. For Spain there seems to be a tendency to

underestimate evaporation, for the Netherlands often an overestimation of evaporation is seen. Here parameterization of atmospheric correction functions could play a role. Determination of roughness length for momentum remains an issue. Determination of roughness length from NDVI does not work properly for high vegetation. Also in a number of cases NDVI-determined roughness length definitely seems too small. With the determination of roughness length from a land cover database, the limited number of land cover classes, seasonal effects and differences in plant size due to environmental conditions form a serious drawback. The two models for roughness length for heat transfer also have a significant result on calculated evaporation, although this effect is smaller than the effect of the roughness length for momentum. Both in the Netherlands and in Spain the ratio of roughness for momentum and roughness for heat transfer always appeared to be higher than 10, a value often used in literature.

With the parallel source model it has been possible to calculate evaporative fractions, even in semi arid areas. In a number of cases but not always the parallel source model gave a better fit of calculated and measured values. Development of a fully dual source model, i.e. by coupling aerodynamic resistances for vegetated areas and for bare soil into an aerodynamic resistance for the area under study, could be a further improvement.

1 Introduction

1.1 The China Drought Project

Availability of water resources poses a serious problem to development and food security in China. Average available water resources per capita are about a quarter of the world average. Available water resource per mu (i.e. approximately 1/15 hectare) is 1900 m³, which is three quarters of the world average. Furthermore both spatial and temporal distribution of water resources is very heterogeneous. For instance 46.5% of the Chinese population lives north of the Yangtze river, an area which for 43 % is farmland, whereas figures from the Chinese Ministry of Water and Hydropower report available water supplies less than 10 % of the whole of China. In the mid north of China (13.7 % farmland) for 11.8 % of the Chinese population only 1.8% of the total Chinese water supplies is available. These water shortages and inhomogeneous distribution of water resources make the country vulnerable to droughts, which indeed frequently occur. Once each two years in China a drought of catastrophic extent takes place. These droughts are attended with human suffering through hunger and social instability. Also drought is a major constraint on the development of rural areas of China. Since Chinese government has shifted its focus for economic development from the coastal zone to the poor inland provinces – in which conservation of ecological system is one of the priorities (Li, 2001) – drought relief is a prerequisite for the success of this policy. Drought research should yield a timely recognition of developing droughts. Since evaporation is an important component in the water balance, reliable and spatially and temporally well distributed measurements of evaporation are of major importance. Up till now evaporation mainly has been measured at meteorological stations through pan evaporation. Although in China a well equipped network of meteorological stations exists, more regionalized data is needed. Due to vastness of the country and the sometimes inaccessibility of the terrain, newly developed methods to estimate evaporation from remote sensing could provide an alternative to measurements on the ground.

The aim of the *China Drought Project* is to monitor and predict drought in continental China, by means of a combination of remote sensing, drought statistics, atmospheric models and hydrological models. In 2006 these efforts should result in a drought early warning system, which will be made available through the internet. Subsequently this early warning system can be used in order to formulate a policy within the framework of water management to prevent the consequences of occurring droughts.

The project is a joint Chinese Dutch co-operation. The Chinese participants are the China Institute of Water Conservancy and Hydroelectric Power Research (IWHR), the Ministry of Water Resources - Meteorological division/Water Resource Information Center (MWR), the Water Resources Development and Utilization Laboratory (Hohai University), the Lanzhou Institute of Plateau Atmospheric Physics (LIPAP) and the Chinese Academy of Meteorological Science - Research Center for Agrometeorology and Remote Sensing application. On the Dutch side Alterra and the KNMI - Royal Dutch Meteorological Institute are participating.

1.2 Estimation of Evaporation by Means of Remote Sensing

The surface energy balance is given by converting the net radiation at the earth's surface into three different energy fluxes: the soil heat flux, the latent heat flux and the sensible heat flux. The soil heat flux is the amount of energy absorbed per unit time by the soil profile. The latent heat flux consists of the product of the actual evaporation and the evaporation warmth of water. The sensible heat flux is the amount of energy consumed by the rising of warm air from the surface. This surface energy balance must equal the radiation balance which is given by converting the net radiation at the earth's surface into the up welling and down welling short wave and long wave radiation. Since radiation can be measured with a satellite, this could offer a+ means to estimate heat fluxes near the earth's surface.

In recent years a number of advanced algorithms are developed by the Alterra Green World Research (for instance SEBI, Surface Energy Balance Index, Menenti & Choudhury, 1993), in order to estimate heat fluxes. This development resulted in the computational scheme SEBS (Surface Energy Balance System, Su, 2000) for estimation of turbulent heat fluxes from point to continental scale. Input data of SEBS are remotely sensed surface parameters, a data set obtained by measurements at reference height and the downward long wave and short wave radiation. The remotely sensed data are albedo, surface temperature, vegetation coverage etc. estimated by measurement of spectral reflectance and radiance. The data obtained near the earth's surface include pressure, air temperature, humidity and wind speed. The downward radiation can either be measured or be parameterized as model output. The evaporative fraction (Λ) can be estimated as the quotient of latent heat flux and the sum of the net radiation minus the soil heat flux. Since air flow only near to the ground is laminar, SEBS recognizes the turbulent nature of air movements.

Evaporative fraction appears to be constant during the day (Shuttleworth, 1989, Brutsaert en Sugita, 1992) and is, given a certain atmospheric forcing, mainly controlled by the availability of soil water. Therefore a momentary recording of the surface energy balance can give a good indication of the availability of water near the root zone. If it is possible to establish a physical relation between the availability of soil water and EF, i.e. to formulate a drought index, then this drought index can be used within the hydrological model in order to establish a quantitative and continuous estimation of drought by means of remote sensing.

If soil temperature is determined by radiometric measurements from a satellite platform, this will be an average temperature of the pixel. Vegetated patches within this pixel normally will have a lower temperature than bare soil patches. Because of the non-linearity of the process, for this pixel, average soil temperature will obviously be not a proper input variable in order to determine heat fluxes. Ideally surface temperature observations would account for the heterogeneity of terrestrial landscapes. A step forward would be to be able to determine a soil temperature and a vegetation temperature within each pixel.

Recent advances in space observations offer a way to do this by using simultaneous measurements at two viewing angles. The Along-Track Scanning Radiometer (ATSR) aboard the European Remote Sensing satellite (ERS) has been designed for this purpose. Quasi-simultaneously (i.e. two minutes after one another) two images are

made. The first view is taken at a forward viewing angle of 53° to the earth's surface, the second record is taken at nadir. Li et al. have developed a method to estimate soil and vegetation temperature from these ATSR-images. The resolution of the ATSR images is 1 km x 1 km, so no separate vegetation elements can be recognized.

1.3 Research Objectives

In recent years a number of campaigns have been carried out to measure fluxes of energy and matter (e.g. water vapor and carbon dioxide). Since these campaigns are both time-consuming and very expensive it has been obvious that within this project no field work could be carried out. On grounds of availability of satellite images together with flux measurements two different environments could be chosen as research area. For a semi arid environment in Spain data sets from the *MEDEFU project (Carbon and Water fluxes of Mediterranean forests)* and the *EWBMS project (Energy and Water Balance Monitoring System)* are used. In the Netherlands two forested areas are studied and validated with flux measurements from the Alterra project '*Hydrologie en waterhuishouding van bosgebieden in Nederland*'.

Meteorological data are obtained from the flux measurement towers themselves or from meteorological stations in the vicinity of the measurement sites. Additionally meteorological data at a higher level in the atmosphere are obtained from standard radio soundings which are operated by the national meteorological institutes in Spain and the Netherlands.

In order to assess the results from the dual source model, first the single source model is extensively studied. A sensitivity analysis is carried out for each input parameter of the algorithm.

Next an analysis is performed to assess the sensitivity of the algorithm towards variability of meteorological data. This variability is established by using meteorological data from measurement towers and radio soundings. A time series of one month is calculated by increasing and decreasing the input of the algorithm with one standard deviation of this variability.

For one site in Spain and one site in the Netherlands and without using satellite images, available data of three months are processed in a time series. To enable a comparison with the results from the satellite data these time series are calculated for each day at 11.00 a.m., i.e. the approximate time of the satellite overpass. A time series can remove some of the statistical uncertainty which accompanies the processing of a limited number of satellite images.

In the third part of this project the single source model is assessed. Heat fluxes at 4 sites in Spain are calculated from 19 satellite images for 13 days from April to September 1999. In the Netherlands heat fluxes at two sites are estimated for 4 days in May and August 1997 and 1998 using four satellite images. Calculations are performed using meteorological data at different heights and using different ways to establish the roughness of the terrain.

After separating soil and vegetation temperatures finally a dual source model is invoked using the same data set.

Initially it has been planned to study relationship between evaporative fraction and the soil water content, in order to establish a quantitative measure for drought (i.e.

the drought index), which can be acquired by remote sensing. Here two problems emerged. First of all only with the available data sets of forested areas soil water content has been measured. Since trees obtain water at larger depth than lower vegetation, it is to be expected that the relation between soil water and evaporative fraction is rather weak and will show a delayed response. Therefore a study of the relationship between evaporative fraction and soil water content should start with vegetation which has its root zone at a depth where a direct relation between with evaporation can be expected. Secondly, the validation of SEBS appeared to be much more time consuming than initially has been thought. Therefore, in agreement with Alterra, this part of the project has been omitted.

1.4 Outline of this Paper

After this introduction in chapter 2 some attention is paid to the relevance of this research project within the framework of Environmental Sciences. In chapter 3 some basic concepts of turbulence and vertical fluxes in the lower atmosphere are briefly discussed. K-theory and a combined theory using the Penman Monteith equation are given some attention. The Surface Energy Balance System SEBS is dealt with in chapter 4. Atmospheric and geometrical corrections are discussed. Parameterization of the algorithm is given some attention, especially where concepts of roughness are involved. Next the dual source model used in this project – which more truthfully should be called *parallel source model* – is introduced. In the last sections of chapter four modifications to the original SEBS code and flux measurement devices are discussed. Chapter five deals with the estimation of heat fluxes in Spain and the Netherlands, which were carried out within the framework of this project. In the first section a description of the measurement sites is given, in the next sections results from the sensitivity analysis, the time series and the single source measurements are represented and discussed. Finally the parallel source results are given and discussed. In chapter six the conclusions which can be drawn from this project are represented.

2 Relevance of this Project to Environmental Sciences

A study of evaporation into the atmosphere essentially involves the study of exchange of mass and energy between the earth's surface and the lower part of the atmosphere. It is this part of the atmosphere where many living creatures spend most of their life time. In the next chapter it will be made clear that the very nature of the exchange processes make life on land possible. A better understanding of processes in the lower atmosphere therefore will also help to increase the understanding of threats to the environment. A few examples will be given below.

Many arid areas of the world are affected by soil salinity. Canopy temperature and vegetation temperature seems to be good indicators of salinity (Myers et al., 1968). By making use of this property, desertification could be studied. Areas prone to desertification could be identified in an early stage.

Most pollutant sources are near the earth's surface and are transported by eddies. Therefore transport models of pollutants must use descriptions of the turbulent atmosphere. Analogous to moisture flux equations, pollutant or tracer flux equations can be formulated. From the nature of turbulent transport, it can be understood why pollution normally does not penetrate the higher layers of the atmosphere. It also can predict the trapping of pollutants in '*inversion layers*' when atmospheric pressure is high (Stull, 1999).

Among atmospheric boundary conditions, soil wetness is second only to sea surface temperature in its impact on climate (U.S. National Research Council, 1994). Over warm continental areas, including mid-latitude continents during spring and summer, it often is the most important boundary condition. Soil wetness affects the status of overlying vegetation, and determines transpiration. Therefore and foremost in the study of semi arid areas, soil wetness must be known in climate studies. Soil wetness measurement on the ground is expensive and cumbersome. But even if resources are unlimited remote sensing will be able to provide soil wetness data with a spatial resolution much larger than ever possible with ground measurements. Parallel and dual source models provide a way to establish this data set through a method which is physically based.

Transpiration of vegetation and carbon dioxide assimilation are related. As a result of photosynthesis carbon dioxide is taken up through the stomata of the plants and water vapor is given off. On the other hand soil respiration increases the carbon dioxide concentration in the air. Zhang et al. (2001) have formulated a model of CO_2 -flux for wheat for the NOAA-AVHRR platform. With the dual source capabilities of the ATSR satellite, fractional cover, vegetation and soil temperature can be retrieved. Hence the model of Zhang et al. could be extended with these two temperatures. Then the parameterization of both temperatures with two experimental coefficients (C_1^* and C_2^*) can be discarded and the physical basis of the model will be improved. Again the nature of remote sensing makes it possible to calculate carbon dioxide budgets for large and inaccessible areas.

Although the type of this research is fundamental, SEBS is a tool that can be used in a number of applications in the field of environmental sciences. In this project elements from remote sensing (e.g. the atmospheric corrections), boundary layer meteorology

(e.g. the description of the lower atmosphere and roughness) and computer science (the programming of algorithms) have been integrated.

3 A Turbulent Atmosphere

3.1 The Planetary Boundary Layer

The troposphere can be divided into a number of layers. The upper part of the troposphere has been called the *free atmosphere* and lies on top of a *boundary layer* near the earth's surface. The *Atmospheric or Planetary Boundary Layer* (PBL) is defined as the part of the atmosphere that is directly influenced by the underlying surface and responds to surface forcings with a timescale of about an hour or less (Stull, 1999). The depth of this layer evolves during the day. During the day the earth's surface is heated by the sun. This causes warm air bubbles to rise causing a growth of the PBL by entraining air from above into the PBL. Depending on meteorological conditions the depth of the PBL will lie between a few hundred meters and a few kilometers (de Bruin, 1998). After sunset this mechanism stops and the PBL can be divided into a *Residual Layer* and a *Stable Boundary Layer* with a depth of a few hundred meters. The bottom 10% of the PBL is called the *Atmospheric Surface Layer* (ASL). In this layer differences in wind speed, temperature and humidity with height are much larger than in the remaining part of the PBL, called the *Mixed Layer*.

3.2 The Energy Balance at the Earth's Surface

Exchange processes between land surface and atmosphere are driven by solar irradiation. The net radiative flux at the earth's surface (for convenience but not entirely correct also called the net radiation) is given by:

$$Q^* = (1 - r_0) K^\downarrow + e \cdot L^\downarrow - e s T_{0s}^4 \quad (3.1)$$

where r_0 is the *albedo*, K^\downarrow is the short wave clear sky radiation at the earth's surface (Wm^{-2}), L^\downarrow is the downward longwave radiation (Wm^{-2}), e is the emissivity of the soil, s is the Stefan Boltzmann's constant and T_{0s} is the soil temperature.

At the earth's surface these radiation energies are transformed into other forms of energy. The air above the soil is heated up, representing a certain amount of energy per unit time per unit surface. This entity is defined as the *Sensible Heat Flux* (H). The soil beneath the surface is heated up, causing a *Soil Heat Flux* (G_0). Water will evaporate into the atmosphere. The corresponding flux is given by the product of the latent heat of evaporation and the amount of water evaporating and is called the *Latent Heat Flux* IE . Some energy is used for the formation of biomatter: ΔS . Neglecting this last term, which in comparison to the other three terms usually is very small, the *Energy Balance* is given by:

$$Q^* = H + IE + G_0 \quad (3.2)$$

In a steady state eq. 3.1 must equal eq. 3.2.

3.3 Turbulence

Except for the micro layer just above the soil where molecular diffusion is the main transport mechanism, air flow or wind governs the transport of matter in the atmosphere. Examination of near-surface wind speed measurements shows an irregular variation on a timescale of about ten minutes or less from a clearly discernable mean value. Each variation seems to be built up of smaller variations superimposed on each other and can be associated with irregular swirls of motion or *eddies*. The largest variations of wind speed occurring at a frequency of about 6 cycles per hour are thought to represent eddy sizes of a few km whereas the smallest detectable variations at 360 cycles per hour represent eddies of about 50 m (van der Hoven, 1957). Thus the larger eddies with the highest energies generate smaller ones with lesser energy, while at the smallest eddy sizes the energy is dissipated into heat by molecular viscosity. This phenomenon of gustiness superimposed on the mean wind speed is called *turbulence* and the associated eddy frequencies can be described by the *turbulence spectrum*. The mean wind too varies with time but this variation takes place at a scale of a few hours or more (for instance diurnal variations). There appears to be a distinct lack of wind speed variation in time periods of about one hour, the *spectral gap*. Thus wind speed variations in time periods higher than the spectral gap must be associated with variations in the mean wind speed, whereas variations in time periods smaller than the spectral gap can be attributed to turbulence. From the definition of the atmospheric boundary layer this implies that the responses to surface forcings under study are mainly of turbulent nature.

The existence of the spectral gap allows the wind speed U on a certain point in time to be written as:

$$U = \overline{U} + u' \quad (3.3)$$

with the mean wind speed \overline{U} and the turbulent part u' . Let γ_m represent a generic unit vector (a vector of length unity and direction in one of the three Cartesian directions), then $\gamma_1 = \mathbf{i}$, $\gamma_2 = \mathbf{j}$ and $\gamma_3 = \mathbf{k}$. Using Einstein's summation notation as a shorthand notation for up to nine fluxes, with the *Kronecker Delta* δ_{mn} (a scalar, $\delta_{mn} = +1$ for $m = n$ and $\delta_{mn} = 0$ for $m \neq n$) and the *Alternating Unit Tensor* ϵ_{mnq} (a scalar, $\epsilon_{mnq} = +1$ for $mnq = 123, 231, \text{ or } 312$, $\epsilon_{mnq} = -1$ for $mnq = 321, 213, \text{ or } 132$ and $\epsilon_{mnq} = 0$ for any two or more indices alike), the equation for Conservation of Momentum can be written as:

$$\frac{\partial U_i}{\partial t} + U_j \frac{\partial U_i}{\partial x_j} = -\delta_{i3}g + f_c \epsilon_{ij3} U_j - \frac{1}{\rho} \frac{\partial p}{\partial x_i} + \nu \frac{\partial^2 U_i}{\partial x_j^2} \quad (3.4)$$

The first term describes the storage of momentum, the second term represents advection, the third term is the gravity term with g being the gravitational constant, the fourth term represents the influence of the earth's rotation with the Coriolis parameter f_c , the fifth term describes pressure gradient forces, ρ being the density of moist air and the last term represents the influence of viscous stress with kinematic viscosity ν . Combining equations 3.3 and 3.4 and applying some approximations (assuming

shallow convection conditions, neglecting subsidence) gives the equation for Conservation of Momentum using mean wind speeds:

$$\frac{\partial \overline{U}_i}{\partial t} + \overline{U}_j \frac{\partial \overline{U}_i}{\partial x_j} = -\delta_{i3} g + f_{ci} \overline{U}_j - \frac{1}{\rho} \frac{\partial \overline{P}}{\partial x_i} + \nu \frac{\partial^2 \overline{U}_i}{\partial x_j^2} - \frac{\partial (\overline{u_i' u_j'})}{\partial x_j} \quad (3.5)$$

Here the last term represents the influence of Reynolds' stress on the mean motions. Reynolds stress is a property of turbulent flow which originates from the mixing of a parcel of air by different wind speeds. The important implication of this last term is that turbulence must be considered in making forecasts in the boundary layer, even if we are trying to forecast only mean quantities (Stull, 1999).

The following example may illustrate this idea. Let θ_v be the virtual potential air temperature (i.e. the temperature for which variation due to changes in pressure and humidity has been removed) and let the vertical wind component u_3 be given by w . C_p represents the specific heat of air and ρ the density of moist air. Then the mean value of the vertical sensible heat flux is (the second term being the definition of the sensible heat flux):

$$\overline{H_{vert}} = \overline{r w C_p (q_v - q_0)} \approx \overline{r C_p w' q'_v} \quad (3.6)$$

In the last term of eq. 3.6 the quantities $\langle w' \rho' \theta'_v \rangle$ and $\langle w \rangle \langle \rho' \theta'_v \rangle$, which are relatively small are neglected. Now let us consider a small eddy which mixes some air up and some air down. Keeping in mind that the temperature in an unstable environment (during the day) decreases in the direction of w (the air lower to the surface being warmer than the air higher in the ASL), the upward moving air will be warmer than its surroundings (positive θ'_v) whereas the downward moving air will be cooler than its surroundings (negative θ'_v). In both cases the product $\langle w' \theta'_v \rangle$ will be positive and will contribute to a positive sensible heat flux. The average motion caused by the turbulence however is null.

Analogous with eq. 3.6 the mean latent heat flux in the vertical direction can be described by:

$$\overline{E_{vert}} = \overline{r w q} \approx \overline{r w' q'} \quad (3.7)$$

Where q is the specific humidity and q' is the specific humidity perturbation. Thus fluxes in the turbulent ASL can be described by the statistical concept of correlation.

Using the summation notation the *Turbulent Kinetic Energy* TKE can be written as TKE/m = \overline{e} , where m is mass:

$$\overline{e} = 0.5 \overline{u_i'^2} \quad (3.8)$$

By inserting eq. 3.3 into eq. 3.4 and subsequently subtracting the mean part represented by eq. 3.5 it is possible to formulate a prognostic equation for just the turbulent gust u_i' . The Turbulent Kinetic Energy then is represented by:

$$\frac{\partial \overline{e}}{\partial t} + \overline{U}_j \frac{\partial \overline{e}}{\partial x_j} = +\delta_{i3} \frac{g}{\theta_v} (\overline{u_i' \theta'_v}) - \overline{u_i' u_j'} \frac{\partial \overline{U}_i}{\partial x_j} - \frac{\partial (\overline{u_j' e})}{\partial x_i} - \frac{1}{\rho} \frac{\partial (\overline{u_i' p'})}{\partial x_i} - \epsilon \quad (3.9)$$

Here the first term describes the local storage of TKE, the second term represents the advection of TKE by the mean wind. The third term is related to buoyancy. It

describes how vertically moving parcels of air can produce or consume TKE. During the day the heat flux $u\theta_v$ will be positive and will contribute to TKE (i.e. creating turbulence), during nighttime a negative heat flux will consume TKE. The fourth term represents production (or loss) of TKE due to shear. Generally the wind speed decreases towards the earth's surface. Although through the summation notation nine terms are represented, this decrease originating from shear in the direction of w will exert the most significant contribution to momentum change. Thus, air moving upward (positive w) will have a lower momentum and air mixing downward (negative w) will have a larger momentum than the surrounding air. Due to the negative sign generally the fourth term will increase the amount of turbulence. Because wind speeds at the earth's surface are zero, higher wind speeds will show a greater decrease of wind speed towards the surface and thus will cause more turbulence.

The fifth term describes how TKE is moved around by the turbulent eddies. Term six describes the redistribution of TKE by pressure perturbations. The seventh term finally represents the viscous dissipation of TKE into heat.

Equation 3.9 illustrates that the two mechanisms in the atmosphere that are able to create turbulence are buoyancy and wind shear. A useful approximation to determine whether flow becomes laminar or stays turbulent is formulated by the Flux Richardson Number, i.e. the ratio of the third and the fourth term from eq. 3.9 (omitting the negative signs). If the Flux Richardson number is greater than +1, flow becomes laminar. This only is possible when the buoyancy term is negative (the wind shear term generally is negative) and exceeds the wind shear term. In other words the buoyancy must consume more turbulence than the wind shear produces. This only is possible in a stable atmosphere.

In eq. 3.5, which is a prognostic equation for the mean wind speed, we must solve the turbulence term with the quantity $\langle u_i' u_j' \rangle$, which is called a double correlation. It turns out that the prognostic equation for the mean value of this double correlation $\langle u_i' u_j' \rangle$ contains a triple correlation, which implies that the number of unknowns in the set of equations for turbulent flow is larger than the number of equations. This closure problem still remains one of the unsolved problems of classical physics. Several closure approximations have been developed. In first order closure the double correlation is approximated, in second order closure the triple correlation is approximated. Widely used are similarity methods which can be classified as a zero closure approximation. In similarity methods a dimensional-analysis is carried out in which from identified or guessed relevant variables dimensionless groups are formed. Numerical values of these dimensionless groups are determined by series of experiments.

Subsequently the relationship between these groups is determined by curve fitting or regression analysis. Now in comparable conditions the curve of a relation between each two dimensionless groups should show a *similar* form. Thus similarity methods are semi-empirical.

3.4 Atmospheric Similarity Methods

A first example of dimensional analysis will show that under circumstances without buoyancy, the wind profile shows a logarithmic form. Dimensional analysis starts with the determination of the relevant variables. In a neutral atmosphere, which occurs in situations with strong winds and overcast skies the contribution of buoyancy to turbulence is null. In that case one can guess the relevant variables to describe the state of the atmosphere to be shear stress, air density, wind speed and height above the earth's surface. If shear stress and air density are joined together in the *friction velocity* u_* .

$$u_* = (\tau/\rho)^{1/2} \quad (3.10)$$

with these variables one and only one dimensionless group can be formed, which then must be constant. In experiments this relationship has been confirmed and the constant is called the *von Karman constant* k :

$$\frac{u_*}{z} \bigg/ \frac{\partial \bar{u}}{\partial z} = k \quad (3.11)$$

After integration of equation 3.11 for the ASL the logarithmic wind profile is obtained: Equation 3.12 states that wind speed decreases logarithmically with height. If wind

$$\bar{u}(z) = \frac{u_*}{k} \ln \left[\frac{z}{z_0} \right] \quad (3.12)$$

speed measurements in a neutral atmosphere are extrapolated, a height z_0 is found at which the wind speed becomes zero. This height is called the *roughness length for momentum transfer*. It should be noted that at this roughness length the logarithmic wind profile certainly does not apply anymore: the validity of eq. 3.12 has been assessed by Wieringa (1993) as to be ranging from a few meters above the ground up to 50-100 m. The physical meaning of the roughness length for momentum is that it describes the extent at which a surface can generate turbulence. Because the vegetation has a certain height and only the upper part of it is contributing to roughness, an imaginary surface of the earth should be elevated to comply with equation 3.12. Generally this is done by subtracting a displacement height d from the height above the surface z .

As a starting point for the description of vertical fluxes by similarity methods, we take the K-theory. This theory assumes that by using turbulent exchange coefficients instead of the (laminar) diffusivities turbulent flows can be described in the same way as laminar flows. Vertical heat fluxes and shear stress (i.e. momentum flux) then are described by:

$$H = -r C_p K_h \frac{\partial \bar{q}}{\partial z} \quad (3.13)$$

$$E = -\rho K_e \frac{\partial \bar{q}}{\partial z} \quad (3.14)$$

$$\tau = \rho K_m \frac{\partial \bar{u}}{\partial z} \quad (3.15)$$

Here ρ is the density of air, C_p is the specific heat of air and θ represents the potential air temperature (i.e. the temperature for which variation due to changes in pressure has been removed). q is the specific humidity of air and u is the wind speed. K_h , K_e and K_m are the turbulent counterparts of the laminar diffusivities (i.e. thermal diffusivity, the molecular diffusion coefficient for water vapor and the kinematic viscosity of air).

These turbulent diffusion coefficients are called Eddy diffusivities.

One can consider the friction velocity (eq. 3.10) as a scale which facilitates the description of the neutral ASL. Other scales used to describe processes in the ASL are *specific temperature* q_*

$$\theta_* = -H / \rho C_p u_* \quad (3.16)$$

and the *Obukhov Length* L :

$$L = -\rho C_p \bar{\theta}_v u_*^3 / k g H \quad (3.17)$$

in which $\langle \theta_v \rangle$ is the mean virtual potential temperature. In the ASL the relevant variables to describe vertical Sensible Heat Flux and wind shear appear to be the height above the earth's surface (z), mean air density (ρ), gravitational constant (g), shear stress (τ), sensible heat flux (H) and evaporation (E). According to the theory of dimensional analysis each dimensionless group of variables then must be a function of other dimensionless groups. One possible way of arranging the relevant variables into such groups is:

$$\frac{\partial \bar{\theta}}{\partial z} \frac{kz}{\theta_*} = \phi_h \left(\frac{z}{L} \right) \quad (3.18)$$

$$\frac{\partial \bar{u}}{\partial z} \frac{kz}{u_*} = \phi_m \left(\frac{z}{L} \right) \quad (3.19)$$

The functions ϕ_h and ϕ_m have been called *stability correction functions*. These stability correction functions have to be determined experimentally. After inserting eq. 3.16 and eq. 3.17 into 3.18 and eq. 3.19 and combining them with eq. 3.13 and 3.14 a general expression ($x = h, m$) for the Eddy diffusivities is obtained:

$$K_x = \frac{k u_* z}{\phi_x} \quad (3.20)$$

Thus rather than on molecular composition Eddy diffusivities are properties of the state of flow in the atmosphere. This property is a prerequisite to life on earth as we

know it. Without it exchange processes between vegetation and atmosphere and between soil and atmosphere would unfold at a rate too slow to safeguard normal metabolic processes.

Now it is possible to derive an expression for the sensible heat flux in terms of buoyancy and wind shear. After inserting eq. 3.19 into eq. 3.13 and 3.14 the two resulting expressions are joined:

$$H = -\rho C_p k^2 z^2 \frac{\partial \bar{u}}{\partial z} \frac{\partial \bar{\theta}}{\partial z} \frac{1}{\phi_m \phi_h} \quad (3.21)$$

For practical purposes expressions containing derivatives are not very convenient to work with. Therefore usually eq. 3.17 and 3.18 are used in an integrated form, using integrated stability correction functions. This integration has to be carried out between two heights. In the description of the logarithmic wind profile it was shown that the flux profile relationship is not valid anymore just above the earth's surface. On integrating the wind profile this led to the introduction of the roughness length for momentum transfer as the lower integration limit. In eq. 3.17 and 3.18 we are faced with the integration of the temperature profile. In the same way as with the wind profile (i.e. by extrapolating it to a height where the temperature would be equal to the surface temperature) a lower integration limit for the potential temperature profile has been defined: *the roughness height for heat transfer*. One could interpret it as a measure for the capacity of a surface to heat up the ASL due to the surface's radiometric temperature (i.e. the temperature which can be attributed to a body from Stefan-Boltzmann's law).

$$H = (\theta_0 - \theta_a) k u_* \rho C_p \left[\ln \left(\frac{z-d}{z_{0h}} \right) - \Psi_h \left(\frac{z-d}{L} \right) + \Psi_h \left(\frac{z_{0h}}{L} \right) \right]^{-1} \quad (3.22)$$

$$u = \frac{u_*}{k} \left[\ln \left(\frac{z-d}{z_{0m}} \right) - \Psi_m \left(\frac{z-d}{L} \right) + \Psi_m \left(\frac{z_{0m}}{L} \right) \right] \quad (3.23)$$

Thus the result of the integration of eq. 3.17 and eq. 3.18 is where θ_0 is the potential temperature at the surface, θ_a is the potential air temperature, d is the displacement height, z_{0m} is the roughness for momentum transfer, z_{0h} is the roughness for heat transfer and Ψ_h and Ψ_m are the integrated stability correction functions which are given by

$$\Psi_x \left(\frac{z}{L} \right) = \int_0^{z/L} \frac{(1 - \phi_x(z'/L)) dz'}{z'/L} \quad (3.24)$$

where x equals m or h . As with the stability correction functions the integrated stability correction functions have to be determined by experiment. The set of equations 3.17, 3.22 and 3.23 enables the estimation of sensible heat flux in the ASL and generally is referred to as the *Monin Obukhov Similarity Theory*.

3.5 Estimation of Evaporation: the Penman-Monteith equation

Problems related to water resource and irrigation management require a reliable estimate of evaporation by vegetation. These estimates should be acquired by as little input variables as possible, preferably no more than standard meteorological data.

Furthermore it should be founded on physical principals. The Penman-Monteith equation largely satisfies these demands. Nowadays, apart from the mentioned research topics, it is used in the prediction of thermal pollution in rivers and in air pollution control (de Bruin, 1998). In a way the Penman-Monteith equations is a solution to eq. 3.14 by making use of the energy balance equation (eq. 3.2) and some boundary conditions.

By definition the *aerodynamic resistance for transport of heat, water vapor and impulse* r_x is

$$r_x = \int_{z_1}^{z_2} \frac{dz}{K_x} \quad (3.25)$$

where K_x is the Eddy diffusivity and $x = h, e, m$.

Relative humidity can be expressed in terms of vapor pressure e , evaporation warmth of water λ , specific heat of air C_p and the psychrometric constant γ .

$$q = \frac{C_p e}{\lambda \gamma} \quad (3.26)$$

Now equations 3.13 and 3.14 can be rewritten as

$$\lambda E = \frac{\rho C_p}{\gamma} \frac{e_0 - e}{r_e} \quad (3.27)$$

$$H = \rho C_p \frac{T_0 - T}{r_h} \quad (3.28)$$

At a water surface the water vapor pressure equals the saturated water vapor pressure, the latter only being a function of surface temperature. This function is non linear and can be linearized by a Taylor series. If higher polynomials are neglected, the function can be approximated by

$$e_w(T_0) \approx e_w(T) + \frac{de_w}{dT}(T_0 - T) \quad (3.29)$$

where T is the air temperature, T_0 is the surface temperature and e_w is the saturated water vapor pressure. After inserting eq. 3.28 into eq. 3.27 and by representing the first derivative as s , an expression for the latent heat flux is obtained:

$$\lambda E = \frac{\rho C_p}{\gamma} \left[\frac{e_w(T) - e}{r_w} + s \frac{T_0 - T}{r_w} \right] \quad (3.30)$$

Now eq. 3.30 can be joined with the energy balance equation 3.2 and, if aerodynamic resistances for transport of heat and for transport of water vapor can be assumed equal, with eq. 3.28

$$\lambda E = \frac{s(Q^* - G) + \frac{\rho C_p}{r_a} [e_w(T) - e]}{s + \gamma} \quad (3.31)$$

where r_a is the aerodynamic resistance. Equation 3.31 is called the *Penman equation*. Because the soil heat flux G is considered as an independent entity, it is valid only for

water surfaces of shallow waters or for completely wet and completely vegetated land surfaces.

Plants are, within certain limits and depending on environmental conditions, able to regulate the amount of evaporation by opening or closing their stomata. When these conditions favor stomata to be partially closed, aerodynamic resistance for water vapor transport can be seen to be built up by the aerodynamic resistance as described in the Penman formula increased with a surplus resistance caused by the stomata. This surplus resistance has been called the *Aerodynamic Surface Resistance* (r_s). In other words the denominator in eq. 3.27 becomes $\gamma(r_a + r_s)$ whereas eq. 3.28 stays unchanged. Now after a derivation analogous the one that led to the Penman equation, the Penman-Monteith equation is obtained:

$$\lambda E = \frac{s(Q^* - G) + \frac{\rho C_p}{r_a} [e_w(T) - e]}{s + \gamma \left(1 + \frac{r_s}{r_a} \right)} \quad (3.32)$$

If the vegetation is covered with a layer of water then the aerodynamic surface resistance will be zero and eq. 3.32 will become equal to eq. 3.31. On the other hand, if the stomata are fully closed, the aerodynamic surface resistance will go to infinity and the latent heat flux will be zero.

4 The Surface Energy Balance System (SEBS) for the Estimation of Evaporative Fractions

In recent years a number of advanced algorithms for the estimation of heat fluxes have been developed at Alterra Green World Research, for instance *SEBI*, *Surface Energy Balance Index* (Menenti & Choudhury, 1993). This development has led to the computational scheme *SEBS* (*Surface Energy Balance System*, Su, 2000). Input data of SEBS are satellite data in the visible, near infra-red and thermal infra-red frequency range, a data set of several meteo data at reference height and the downward long wave and short wave radiation. SEBS consists of four components:

- The preprocessing of satellite data to estimate albedo, soil temperature, NDVI and fractional vegetation coverage.
- Models for the determination of the roughness length for heat transfer.
- The *Bulk Atmospheric Similarity Model* (BAS) for determination of friction velocity, sensible heat flux and the Obukhov length.
- The *Surface Energy Balance Index SEBI* for the determination of evaporative fractions.

Depending on the satellite being used appropriate atmospheric correction models can be chosen.

In this project two different models for the determination of the roughness length for heat transfer have been used and the SEBI model has been modified to meet the demand of processing separate vegetation and soil temperatures.

In each component of SEBS for *each* pixel a complete calculation is carried out.

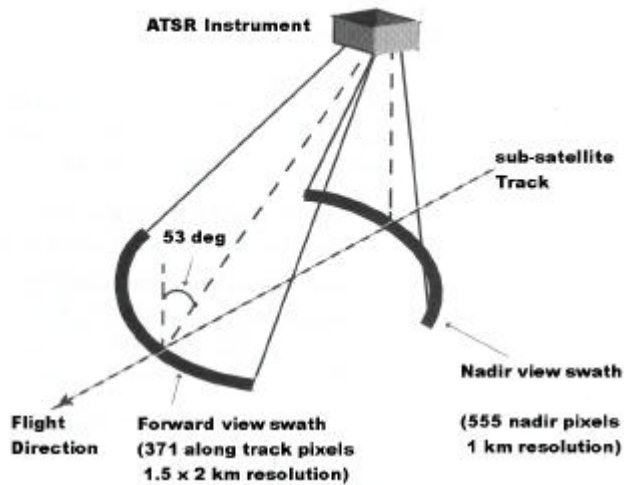
All image processing has been carried out on a Windows NT-2000 platform using ENVI version 3.4 (Environment for Visualizing Images, Research Systems Inc.) as the tool for image manipulation, Microsoft Developer Studio for the compiling of the FORTRAN-code of the first component and IDL version 5.4 Win32 (Interactive Development Language, Research Systems Inc.) as programming language for the other components.

In this chapter first the four components of SEBS will be discussed and the estimation of emissivity, soil heat flux and roughness length for momentum will be looked at. Next a method will be outlined to estimate heat fluxes using separate vegetation and soil temperatures. Modifications to the original code are discussed and finally some attention will be paid to the instruments used for validation.

4.1 The Atmospheric Correction and the Preprocessing of Satellite Data.

On board of the *European Remote Sensing Satellite ERS-2* is the *Along Track Scanning Radiometer II (ATSR-2)*. The ATSR instrument is capable of making two observations of the same point on the earth's surface through differing amounts of atmosphere by tilting its viewing angle (*figure 1*). First the ATSR views the surface along the direction of the orbit track at an incidence angle of 53° as it flies towards the scene. Then, some 150 seconds later, ATSR records a second observation of the scene at an angle close to nadir (Mutlow et al. 1999). This viewing geometry enables the separation of soil and vegetation temperatures. Because of this feature in this project images from the ATSR instrument are used.

Figure 1 - ATSR-2 Viewing Geometry



A second advantage of this viewing geometry is that by combining the data from these two views a direct measurement of the effect of the atmosphere is obtained, thus enabling an improvement of the atmospheric correction as compared with single view data.

The ATSR-2 instrument carries seven spectral bands: three thermal infrared (TIR) channels centered at 3.7 μm (bandwidth 0.3 μm), 10.8 μm (bandwidth 1.0 μm), and 12 μm (bandwidth 1.0 μm), one short wave infrared (SWIR) channel at 1.6 μm (bandwidth 0.3 μm) and three visible/near infra red (VIS/NIR) channels at 0.55 μm , 0.67 μm and 0.87 μm (all with bandwidth 20 nm).

For the atmospheric correction and for the retrieval of separate soil and vegetation temperatures the model of Li et al. (Li et al., 2001/1) has been used. This model consists of seven steps, which briefly will be elucidated in the following. The FORTRAN-code for this model has been made available by Jia (personal communication). After atmospheric corrections and surface temperature retrieval the resulting image data is geometrically corrected.

4.1.1 Cloud and Water Surface Screening

Clouds and water surfaces have to be masked in order to guarantee a proper estimation of the atmospheric water vapor content (i.e. the second step in this model). The screening algorithm is based on the method of Saunderson and Kriebel (1988) in which two thresholds subjectively are determined in order to identify clouds and water surfaces. The first threshold is set at the minimum value in the 12 μm spectrum which could be attributed to cloud free land pixels. The second threshold is set at the maximum reflectance in the 0.67 μm band which can be attributed to cloud free land pixels. Thus clouds which have a temperature much lower than the land surface and a reflectance much higher than the land surface are masked. The same applies for sea pixels, be it that here the distinction between land and sea pixels especially in late summer primarily will be based on the second threshold. In the screening program CLOUDAY.F it is possible to set a third threshold at the saturation temperature of the ATSR-sensors ($> 319 \text{ K}$). The program requires a set of calibration parameters which can be retrieved from the ATSR website (<http://www.atsr.rl.ac.uk>).

4.1.2 Water Vapor Determination

In the atmosphere water vapor acts as a greenhouse gas and plays an important role in the absorption and emission of radiative energy. Hence it is plausible that knowledge of water vapor content in the atmosphere allows remote sensing scientists to improve the accuracy of the remotely sensed surface parameters (Sobrino et al. 1994, Francois and Ottle , 1996). The column of water vapor is determined by a split-window technique using the thermal channels at 11 μm and 12 μm (Li , Z.L. et al. 2001 /2). It is shown that in good approximation water vapor content is a linear function W of the transmittance ratio of these two channels. The transmittance can be estimated from the covariance and the variance of the brightness temperature, directly measured by the ATSR instrument. Furthermore this function W can be expressed in terms of the angle of observation, the channel average absorption coefficients for water vapor and other absorption gases and the content in the air column of other gases. Its numerical form has been derived from a linear regression analysis of a number of results obtained through a simulation model. The algorithm has been implemented (program WV.F) by introducing a box of 10 by 10 pixels, within which the variances and covariances are calculated. In this way a value for the water vapor content for each 10 km by 10 km grid is obtained.

4.1.3 Retrieval of Aerosol Optical Depth

The main atmospheric effects that have to be estimated to be able to determine the surface reflectance from the (measured) top of atmosphere (TOA) reflectance are molecular absorption and molecular and aerosol scattering. Radiative transfer models (Vermote et al., 1997, Beck et al., 1999) provide a means to calculate these from vertically integrated gaseous contents, aerosol optical properties and geometric conditions. In the model of Li (Li et al., 2001 /3) this radiative transfer model is used in combination with the dual view capabilities of the ATSR instrument. In a first estimate using an initial guess for atmospheric aerosol content and optical depth eight surface reflectances (at 0.55 μm , 0.67 μm , 0.87 μm and 1.6 μm for nadir and forward views) are calculated. In this calculation the peak value in the water vapor estimation from the preceding step and a climatological ozone content are used. North et al. (1999) developed a model which describes $\rho_i(\theta_s, \theta_v, \Delta\phi)$ as a function of seven independent variables where ρ_i is the surface reflectance in channel i , θ_s and θ_v are the solar and viewing zenith angles respectively and $\Delta\phi$ is the relative azimuth between sun and satellite direction. In this model the specular (i.e. non-Lambertian) properties of land surfaces are accounted for. Because eight surface reflectances are being calculated this leaves one degree of freedom to the description of the aerosol optical depth. Thereupon the bi-directional (i.e. through atmosphere to surface and back to sensor) land surface reflectance is fitted into the transfer model by minimizing the error metric function

$$E = \sum_{\theta_v=1}^2 \sum_{i=1}^4 \left[\rho_i(\theta_s, \theta_v, \Delta\phi) - \rho_i^m(\theta_s, \theta_v, \Delta\phi) \right]^2 \quad (4.1)$$

where ρ_i^m is the surface reflectance in channel i . To minimize noise and misregistration between nadir and forward views, again a 10 pixel by 10 pixel box is used (program: AERO_M2.F). Solar zenith and azimuth angles are retrieved from the header in the ATSR file. In this project the header retrieval has been executed by a simple Visual Basic routine.

4.1.4 Atmospheric Correction for VIS/NIR Channels

Now for all visible and near infrared channels the surface reflectances can be calculated at pixel resolution by inserting the peak optical depth from the preceding step and the water vapor content together with the solar zenith and azimuth angles of the ATSR instrument into the radiative transfer model (program AERO_M1.F).

The albedo is obtained by taking the mean of the surface reflectances of the four channels (Jia, personal communication). The calculation of the albedo is performed by an IDL function ALB.PRO (appendix 1 a). To prevent the occurrence of artefacts resulting from different cloud screening results in the separate VIS/NIR channels this function has been designed to mask any pixel with a corresponding masked pixel in any of the channels. The function ALB.PRO is operated through Band Math functionality in ENVI.

4.1.5 Fractional Vegetation Cover

The *Normalized Difference Vegetation Index (NDVI)* is calculated using the atmospherically corrected channels at 0.67 μm (visible) and 0.87 μm (near infra red): $NDVI = (\rho_{0.87} - \rho_{0.65}) / (\rho_{0.87} + \rho_{0.65})$. Using a pixel by pixel calculation the program FC_NDVI.F produces a nadir view NDVI image and a forward view NDVI image. Next the minimum and maximum values in these images are determined by using ENVI's 'Statistics' tool. Baret et al. (1995) established a semi-empirical relationship between fractional vegetation cover and NDVI

$$F(\theta) = 1 - \left(\frac{NDVI(\theta) - NDVI_{\max}(\theta)}{NDVI_{\min}(\theta) - NDVI_{\max}(\theta)} \right)^K \quad (4.2)$$

where $K = 0.4631$. With the maximum and minimum NDVI values the program FC_NDVI.F is invoked again, after which for both view directions a fractional cover image is produced.

The original code has been extended to avoid dividing by zero reflectances and to avoid signed byte files, which ENVI does not accommodate for (Appendix 1 b).

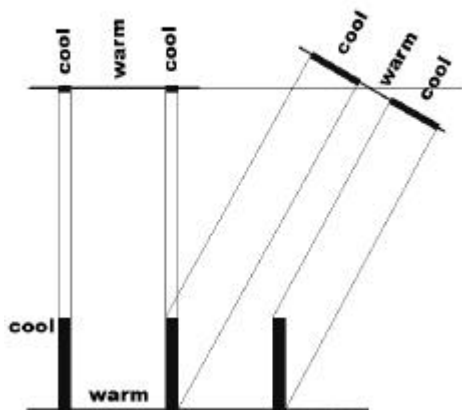
4.1.6 Atmospheric Correction Thermal Infrared Channels

If between 10.3 μm and 12.5 μm channels emissivity can be assumed constant, ground brightness temperature will be independent of the channels used to measure it. Then the two channels at 11 μm and 12 μm can be used to derive the ground brightness temperature in a split window approach. Becker and Li (1995) have derived a split window algorithm for the ATSR instrument using the total column water vapor in the atmosphere and a separate parameterization for nadir and forward views. Using the 10 by 10 pixel water vapor grid from section 4.1.2 the program ATMCOR_SW.F produces on a pixel by pixel basis two atmospherically corrected ground brightness temperature images (nadir and forward view).

4.1.7 Separation of Soil and Foliage Temperatures

As can be seen from figure 1 nadir and forward view have a different spatial resolution (1km x 1 km and 1.5 km x 2 km respectively). In this project the ATSR gridded products are being used. Nadir- and forward-view pixels are collocated, and have been regridded (mapped) onto a 1 km grid (Mutlow et al., 1999). This means that an uncertainty is introduced because the forward pixels have to be redistributed over a grid that does not have the same aspect ratio (length x width) as the forward scan. To minimize this effect of co-registration error as well as noise before invoking the separation algorithm a low pass filter is applied to both temperature and fractional coverage images. Kernel sizes are 5x5 for the nadir image and 3x3 for the forward image. Low pass convolution filters are standard functionality in ENVI. Output files after convolution are of integer type (16 bits/pixel). The function TOBY.PRO (Appendix 1 c) can be used to convert convoluted fractional coverage integer files to byte (8bits/pixel) files which are needed for the temperature separation (inversion) program INV_TV_TS.F. This can be done without any risk because the highest value in the output file will never be higher than the default for a masked pixel (120).

Figure 2 - effect of oblique viewing angle



The principle of separating soil and vegetation temperatures is illustrated by figure 2. If the upright bars represent vegetation figure 2 depicts a partly vegetated area. Because vegetation has a certain height the nadir view looking straight downward records a larger area of bare soil than the oblique view. A model for separation of vegetation and soil temperatures from directional TIR measurements (the temperature inversion model) has to comprise a number of key parameters describing the geometry, structure, composition of the vegetation, the radiative parameters of both vegetation and soil, as well as meteorological data (Kimes, 1983, Francois and Ottle, 1997). Since not all of these parameters are available and because the coarse resolution of the ATSR instrument allows for some generalization, here a more simple approach has been used. Vegetation is thought to be of uniform structure covering the surface. This vegetation layer is described by one single property i.e. the vegetation fractional coverage which has been determined with the fifth step in this scheme. Within this structure vegetation temperature is taken to be constant and vegetation and soil surfaces are assumed to be Lambertian. The model used (Li et al., 2000; Menenti et al., 2000) describes the emitted radiance B at a viewing angle θ as a linear composition of the contributions of radiance from vegetation and soil where $P(\theta)$ is the ground fractional cover viewed at angle θ with

$P(\theta) = 1 - F(\theta)$, ϵ_s and T_s are the soil emissivity and temperature, ϵ_v is the emissivity of leaf, P_h is the hemispheric gap frequency defined as the ratio of the radiation traveling the canopy and reaching the soil to the incident radiation into the canopy over the hemisphere, α and β are the probability of the radiation emitted by a leaf and reflected by other leaves in the canopy and the probability of the radiation emitted by soil and reflected by leaves respectively, ϵ_c is the canopy emissivity and $R_{atm\downarrow}$ is the downward hemispheric atmospheric radiance divided by π .

$$B(T_g(\theta)) = P(\theta)\epsilon_s B(T_s) + [1 - P(\theta)]\epsilon_v B(T_v) + (1 - P_h)\epsilon_v B(T_v)P(\theta)(1 - \epsilon_s) + \alpha(1 - \epsilon_v)B(T_v)[1 - P(\theta)] + \beta(1 - \epsilon_v)\epsilon_s B(T_s)[1 - P(\theta)] + (1 - \epsilon_c)R_{atm\downarrow} \quad (4.3)$$

The first and the second term represent the radiation of respectively soil and leaves that reaches the top of the vegetation layer directly. The last term describes the reflection of the downward hemispheric atmospheric radiance by the canopy. The other terms represent radiation that reaches the top of the canopy after interactive processes between vegetation and soil. The third term describes the radiation emitted by the vegetation towards the soil and reflected by the soil (vegetation-soil interaction). The fourth term represents the radiation emitted by leaves and reflected by leaves (vegetation-vegetation interaction). The fifth term describes radiation emitted by the soil and reflected by leaves (soil-vegetation interaction).

For soil and vegetation effective emissivities are defined as

$$E_s = \epsilon_s + \frac{(1 - P_h)\epsilon_v(1 - \epsilon_s)B(T_v)}{B(T_s)} \quad (4.4)$$

$$E_v = \epsilon_v + \alpha(1 - \epsilon_v)\epsilon_v + \frac{\beta(1 - \epsilon_v)\epsilon_s B(T_s)}{B(T_v)} \quad (4.5)$$

which allows equation 4.3 to be written as

$$B(T_g(\theta)) = [1 - F(\theta)]E_s B(T_s) + F(\theta)E_v B(T_v) + (1 - \epsilon_c)R_{atm\downarrow} \quad (4.6)$$

The effective emissivities are considered to be equal for the two viewing angles and are set to $E_s = 0.97$ and $E_v = 0.99$ (Li et al. 2001, /1). Downward hemispheric atmospheric radiance usually is small and is neglected (Jia, personal communication). Hence the two radiance components from vegetation $B(T_v)$ and soil $B(T_s)$ can be determined.

Because the relationship between radiation and temperature is non linear and due to measurement errors a statistical method (the Levenberg-Marquardt algorithm) is invoked to fit the effective temperatures.

From figure 2 it will be clear that generally the difference between nadir and forward view temperatures are of positive sign: $T_{nadir} - T_{forward} > 0$. In the temperature inversion algorithm three cases are distinguished in which the derived temperatures are masked. In the first case $T_{nadir} - T_{forward} < 0$. This situation can occur when cloud screening did not work properly: if in the nadir path of view clouds occur and the forward view is clear then the nadir temperature will be lower than the forward temperature. Also it is conceivable that in the nadir view a larger vegetation fraction is observed than in the forward view: in very heterogeneous terrain at pixel edges vegetation may not be 'seen' in the forward view. The second class of pixels to be masked are those in homogeneous terrain. In this situation the nadir temperature will only be slightly higher than the forward temperature. The threshold is put at 0.5 K: $T_{nadir} - T_{forward} < 0.5$ K. The last case comprises pixel pairs with nadir view temperatures much larger than forward view temperatures. The difference between nadir and forward view temperatures will rise from early morning towards solar noon because the fraction of shaded soil will decrease during the morning. For agricultural

areas with dominant crops being corns and beans and for areas with sparse short grass, temperature differences should not exceed 10 K (Menenti et al., 2000). Higher temperature differences could be attributed to clouds occurring in the forward path of view while the nadir path of view is clear. In the program INV_TV_TS.F this temperature threshold has been set to 7.5 K.

4.1.8 Geometric Correction

In this project satellite images from the Netherlands and Spain have been processed. In contrast to for instance a *Latitude- Longitude projection* a *Universal Transverse Mercator (UTM) projection* offers a way to relate the satellite image to coordinates on the geode, without too much stretching or condensing the original image for either country.

The ATSR gridded products are supplied with latitude and longitude files, i.e. for each pixel latitude and longitude are available as attribute. ENVI offers functionality to combine these latitude and longitude files together with a chosen projection method into a *Geometric Lookup Table (GLT)*. Each band of the ATSR product or image produced from it (e.g. evaporation files from SEBS) now easily can be geometrically corrected using this GLT.

The *Corine Land cover Database* (resolution 100 m), which is used to determine roughness lengths for momentum has been made available from Arc Info to Erdas Imagine with an Albers Conical Equal Area projection. First two files have been cropped from this database to cover the research area in the Netherlands and Spain. Since the land cover files had to be aggregated to a 1 km resolution, in this re-dimensioning process file sizes were kept at a multiplicity of ten pixels. The two files have been resampled to UTM and the header information has been filed. After aggregation the resulting 1 km resolution files were supplied with this header information.

For each measurement site a comparison between ATSR image and Corine land cover file has been carried out. This has been done by identifying four points in the vicinity of the measurement site with known coordinates (Casado, 2001, Termaat, 2001). In one instance (the El Saler site) the difference between land cover file and ATSR image appeared to be more than 1 pixel. In this case, instead of a reprojection procedure, a translation has been carried out. In all other cases observed geometrical inconsistencies were well below 1000 m.

4.2 Models for the Determination of the Roughness Length for Heat Transfer

The relationship between the roughness height for momentum transfer and the roughness height for heat transfer is given by

$$z_{0h} = z_{0m} / \exp(kB^{-1}) \quad (4.7)$$

where k is the von Karman constant and B^{-1} is the inverse Stanton number, a dimensionless heat transfer coefficient. Stanton number nor roughness height for heat transfer can be measured but can be calculated from measured heat fluxes, using eq. 3.22 and eq. 3.23. The potential temperature in eq. 3.22 has to be derived from radiometric temperatures using Stefan-Boltzmann's law. Thus the potential temperature will show a great sensitivity towards uncertainties in the determination of the emissivity. Furthermore the footprint of the measured flux generally will differ from the footprint of the measurement of the radiometric temperature (Blümel,

1999). Both uncertainties will contribute to the uncertainty in the determination of kB^{-1} (Su et al., 2001). This approach has yielded numerous empirical formulas for roughness height for heat transfer. An evaluation of a number of these by Verhoef et al. (1997) has shown that none of them are able to describe both bare soil (bluff-rough surface), vegetation (permeable-rough surface) and surfaces with intermediate roughness properties. Furthermore none of these formulas are capable of describing the observed diurnal variation of the roughness length for heat transfer. Two recent models by Massman (1999) and Blümel (1999) consider both bare soil and vegetation. The Massman model primarily is dealing with an advanced description of within-canopy processes. The Blümel model focuses on formulating a function to aggregate contributions from bare soil and vegetation patches into one entity to describe roughness for heat transfer for partly vegetated surfaces. In a study by Su et al. (2001) both models seemed to provide reliable estimates of the roughness heights for heat transfer.

4.2.1 Massman's kB^{-1} Model

Heat transfer from soil to atmosphere occurs in the lower part of the ASL near to the earth's surface and within the plant canopy. Here K-theory will fail. Transport processes can be described by adopting a Lagrangian viewpoint in which particles are advected by a given Eulerian velocity field $\mathbf{u}(\mathbf{x},t)$ according to the differential equation $d\mathbf{x}/dt = \mathbf{u}(\mathbf{x},t) = \mathbf{v}(t)$. Despite its apparent simplicity the problem of connecting the Eulerian property of \mathbf{v} to the Lagrangian properties of the trajectories $\mathbf{x}(t)$ is a difficult task, even more by the recognition of the ubiquity of Lagrangian chaos i.e. chaotic advection (Bohr et al. 1998). Exchange processes of energy and water at the soil-plant-atmosphere interface occur over a wide range of spatial scales. Eddy correlation methods provide a way to measure these fluxes at the scale of the ASL, whereas exchange rates on the scale of an individual plant are measured by chamber methods. A way to link these scales is by describing these processes in a Lagrangian framework. Raupach (1989) has developed a method to model transport within plant canopies using Lagrangian Dispersion Analysis. Massman (1999) used this approach to construct a kB^{-1} model by combining a canopy momentum transfer model, a canopy turbulence model (Massman and Weil, 1999), the soil boundary layer resistance (Sauer and Norman, 1995) and Raupach's model with a canopy source function and leaf boundary layer resistance. This model requires quite a lot of input variables, which makes the use of it in Remote Sensing applications less feasible. A simplified model (Massman, 1999) removes this limitation by invoking the canopy only model of Choudhury and Monteith (1998) and a soil only term to describe the contributions from fully vegetated patches and bare soil to the combined aerodynamic resistance. In SEBS (Su et al., 2001) two modifications were brought upon this concept: the weighting factors of the simplified Massman model are replaced with a weighting based on fractional vegetation coverage and the kB^{-1} for soil only is calculated according to Brutsaert (1982). The model reads

$$kB^{-1} = \frac{kC_d}{4C_t \frac{u_*}{u(h)} (1 - e^{-n/2})} F^2 + \frac{k \frac{u_*}{u(h)} \frac{z_{0m}}{h}}{C_t^*} \cdot 2 \cdot F \cdot (1 - F) + kB_s^{-1} (1 - F)^2 \quad (4.8)$$

where F is the fractional vegetation coverage, C_d is the foliage drag coefficient which has been set to 0.2. C_t is the heat transfer coefficient of the leaf. kB_s^{-1} is given by:

$$kB_s^{-1} = 2.46(Re)^{0.25} - \ln(7.4) \quad (4.9)$$

In this project C_t has been set to 0.01. According to Massman (1999, eq. 14) friction velocity divided by wind speed at canopy height h can be modeled as

$$\frac{u_*}{u(h)} = 0.32 - 0.264 e^{(-15.1 \cdot C_d \cdot LAI)} \quad (4.10)$$

where the *Leaf Area Index* is given as a function of NDVI (Su, 1996):

$$LAI = \left(NDVI \cdot \frac{(1 + NDVI)}{(1 - NDVI)} \right)^{1/2} \quad (4.11)$$

Equation 4.11 should be applied to low vegetation only. The within-canopy wind speed profile extinction coefficient n is given by Massman (1999, eq. 13) as:

$$n = \frac{C_d \cdot LAI}{2 (u_* / u(h))^2} \quad (4.12)$$

The heat transfer coefficient of the soil C_t is represented as a function of the Prandtl number ($Pr=0.7$) and the roughness Reynolds number (Re_*). The Reynolds number is defined as $Re \equiv \mathbf{V} \mathbf{L} / \nu$ where \mathbf{V} and \mathbf{L} are velocity and length scales in the boundary layer (Stull, 1999). In the roughness Reynolds number these scales are friction velocity and roughness height of the soil (h_s):

$$C_t = Pr^{-2/3} Re_*^{-1/2} = 0.7 \cdot \frac{h_s u_*}{\nu} \quad (4.13)$$

In SEBS in the second term of eq. 4.8 (i.e. in the expression for the heat transfer coefficient of the soil) Re_* the canopy height is taken as the length scale:

$$Re_* = \frac{u_*}{u(h)} \cdot u(h) \cdot \frac{h}{\nu} \quad (4.14)$$

where the first term is calculated using eq. 4.10 and the second term is calculated by surface layer similarity theory (Brutsaert, 1982)

$$u(h) = u_{ref} \frac{\ln(h - d/z_0)}{\ln(z_{ref} - d/z_0)} \quad (4.15)$$

assuming neutral conditions and by taking roughness height $z_0 = 0.136 \cdot h$ and displacement height $d = 0.667 \cdot h$. The canopy height is calculated using (Brutsaert, 1982):

$$h = z_{0m} / 0.136 \quad (4.16)$$

Wind speed at reference height and reference height are given by u_{ref} and z_{ref} . The kinematic viscosity of air is taken from Massman (1999, /2):

$$\nu = 1.327 \cdot 10^{-5} \left(\frac{p_0}{p} \right) \left(\frac{T}{T_0} \right)^{1.81} \quad (4.17)$$

with p and T the ambient pressure and temperature and $p_0 = 101325$ Pa and $T_0 = 273.15$ K.

In the third term Re_* is calculated according to 4.13 with (the superscript s indicating that this formulation is only applicable to bare soil)

$$u_*^s = \frac{u_{ref} k}{\ln(z_{ref}/h_s)} \quad (4.18)$$

The roughness height for bare soil h_s can be set to 0.009 m (Su et al. 1997).

With this parameterization it is possible to calculate the kB^{-1} factor from the roughness height for momentum transfer, the reference height, the wind speed at reference height, the fractional canopy coverage and the ambient pressure and temperature. All this input can be retrieved from either remote sensing or meteorological observations.

4.2.2 Blümel's kB^{-1} Model

Blümel (1999) has developed a method for estimation of the *effective roughness length* for heat transfer for partly vegetated surfaces. This effective roughness length allows the use of formulas for the calculation of fluxes which originally were developed for homogeneous surfaces (e.g. eq. 3.22). In this sense equation 4.8 can be seen as an expression for an effective kB^{-1} value. Blümel however does not apply a fixed weighting but establishes a weighting function. The derivation of Blümel's method consists of three steps. First a multi source transfer model is developed, i.e. a model that comprises bare soil and vegetation elements (with known or empirically established roughness lengths). Next effective roughness lengths are defined and the kB^{-1} factor is expressed in terms of this model by defining a function $C(F)$ of fractional vegetation coverage. Finally a procedure is carried out that fits simulated transfer model results into this $C(F)$ function. Thus the weighting function is obtained which allows us to calculate the effective roughness lengths for heat transfer for surfaces ranging from bare soil to full canopy coverage. In this formula only wind speed at reference height, fractional vegetation coverage, effective roughness length for momentum, *Leaf Size* (D_f) and *Leaf Stem Area Index* ($LSAI$) is prescribed as input.

If measurements of wind speed and air temperature at two different heights are available heat and momentum fluxes (eq. 3.13 and 3.15) can be calculated from K theory without any additional information by assuming a quasi stationary state and horizontal homogeneity. In his multi source transfer model Blümel expresses fluxes according to K theory in terms of conductivities (i.e. the reciprocal values of resistances in eq. 3.26 and 3.27), temperatures of soil T_s , of vegetation T_v , and of air T_a at reference height z_a . Four different sensible heat fluxes can be distinguished: the flux H_{gc} from the vegetation covered soil into the air between the leaves, the flux H_{ga} from the bare soil to the reference height, the flux H_{fc} from the surfaces of the leaves into the canopy air, and the flux H_{ca} from the canopy air to the reference height, each flux with its own conductance:

$$H_{xy} = \rho_a C_{p,xy,H} (T_x - T_y) \quad (4.19)$$

with $xy \in \{gc, ga, fc, ca\}$.

Similarly four different momentum fluxes can be distinguished (compare eq. 3.15 and 3.24). The momentum flux τ_{gc} from the vegetation covered soil into the canopy air is represented by

$$\tau_{gc} = -\rho_a C_{gc,M} u_c \quad (4.20)$$

with u_c the effective wind speed inside the vegetation.

For the description of the momentum flux absorbed inside the vegetation $\tau_{fc,M}$ and the momentum flux at the vegetation covered soil $\tau_{gc,M}$ not the Lagrangian approach by Raupach has been used but a model by Taconet et al. (1986).

$$\tau_{fc} = -\sigma_a \rho_a c_{ca,M} u_a = -\sigma_a \rho_a u_{*ca}^2 \quad (4.21)$$

$$\tau_{gc} = -(1 - \sigma_a) \rho_a c_{ca,M} u_a = -(1 - \sigma_a) \rho_a u_{*ca}^2 \quad (4.22)$$

An expression for the momentum partition factor σ_a has been derived by Taconet et al. by fitting data from a second order closure model (see section 3.3) of momentum transfer within vegetation.

$$\sigma_a = 1 - \frac{0.5}{0.5 + LSAI} \exp\left(-\frac{LSAI^2}{8}\right) \quad (4.23)$$

In equation 4.23 the *Leaf Stem Area Index* $LSAI$ is defined as sum of single sided *Leaf Area Index* (LAI) and *Stem Area Index*. In SEBS LAI is calculated according to eq. 4.11, the $LSAI$ over fully vegetated area is estimated as $1.1 \cdot LAI$ (i.e. an approximation in which the stem area is thought to consist of 10% of the LAI).

Two model variations to investigate the influence of various stand geometries are considered. If the typical length scale of bare soil patches is equal or less than ten times the mean vegetation height the total momentum flux is

$$\tau_{total} = -\rho_a c_{total,M} u_a \quad (4.24)$$

This model is suitable for vegetation units which stand tightly packed. The total conductivity is composed of a vegetation and a bare soil part by a weighting function of fractional cover. This function uses two geometry parameters and reaches a maximum at a fractional vegetation coverage of 0.78 which can be explained by the fact that dense closed canopies can show a smaller roughness for momentum than vegetation with a fractional cover less than 1 (see Blyth and Dolman, 1995).

On the other hand if the typical length scale of bare soil patches is equal or greater than hundred times the mean vegetation height, one considers dense vegetation clusters which are separated by quite large patches of bare soil. If the effect of transient areas is neglected (i.e. if it is assumed that the momentum fluxes are completely adapted to the relevant surface type) the total momentum flux is (with F the fractional cover)

$$\tau_{total} = F \tau_{ca} + (1 - F) \tau_{ga} \quad (4.25)$$

Of the eight conductivities to be solved the expressions which relate to reference height (i.e. $c_{ga,H}$, $c_{ga,M}$, $c_{ca,H}$, $c_{ca,M}$) clearly will be sensitive to atmospheric stability, which can be expressed by means of the stability correction functions (section 3.3). Here Blümel's transfer model uses a stability factor which basically is another way of writing eq. 3.22 and 3.23 to express conductivities in terms of the integrated stability correction functions. Since the stability correction functions depend on the Obukhov Length, which is a function of friction velocity (and so by definition a function of momentum flux) and sensible heat flux, Blümel proposes the calculation of the fluxes in an iterative procedure, starting at neutral stability. Displacement height and roughness lengths (for bare soil, for vegetated areas) are calculated analogous to the Massman model. Estimation of the conductivities is adapted to the two model variations.

The conductivity from the leaf and stem surfaces into the canopy air for heat fluxes is estimated after Gates (1980). Gates established a semi empirical formula by means of experiments in a wind tunnel which used rectangular strips of dry and wet blotting paper of various sizes under conditions of forced convection. In this formula

conductivity from the leaf surfaces into canopy air is expressed as a function of *Characteristic Leaf Dimension* or *Leaf Size* (D_f) and *Effective LSAI* ($LSAI_{eff}$). The latter can be seen as the LSAI corrected for the fact that only the upper layers of the canopy take part at the momentum transfer because the lower layers are already sheltered considerably by the leaves and stems above them.

The conductivity for vegetation covered soil into the canopy air ($c_{gc,M}$) and for leaf and stem surface into the canopy air, $c_{fc,M}$ (both expressions for momentum fluxes) is estimated by respectively combining eq. 4.22 and eq. 4.21 with eq. 4.20. Here Blümel follows the model by Taconet et al. adapting it to the two proposed model variations. Finally the conductivity c_{gc} for heat fluxes for the two model variations is calculated in a similar way. Here in the model for patched surfaces for small LSAI an alternative formula has been proposed.

Now *total* heat and momentum fluxes can be calculated in an iterative procedure, using eight flux components depending on the model variation chosen. Next the expressions for the total momentum and heat flux in this model are used to define the corresponding effective roughness lengths and an effective kB^{-1} value. Eq. 4.24 and eq. 4.25 show that for the different geometries different expressions for effective roughness length for momentum transfer will have to be derived. In the definition of the effective roughness length for sensible heat an effective surface temperature has been defined as arithmetic areal mean of the temperatures of vegetation and bare soil.

Let $z_{a,eff}$ be the effective reference height. Then if a function $C(F)$ is defined as

$$C(F) = \ln\left(\frac{z_{a,eff}}{z_{0M,eff}}\right) \ln\left(\frac{z_{a,eff}}{z_{0H,eff}}\right) \quad (4.26)$$

equation 4.7 can be rewritten as:

$$kB^{-1} = \frac{C(F)}{\ln\left(\frac{z_{a,eff}}{z_{0M,eff}}\right)} - \ln\left(\frac{z_{a,eff}}{z_{0M,eff}}\right) \quad (4.27)$$

From the previously formulated multi source transfer model Blümel has derived the two limiting expressions for C for bare soil and for totally vegetated area:

$$C(0) = \ln\left(\frac{z_a}{z_{0M,g}}\right) \left[\ln\left(\frac{z_a}{z_{0M,g}}\right) + kB_s^{-1} \right] \quad (4.28)$$

$$C(1) = \ln\left(\frac{z_a - d}{z_{0M,c}}\right) \left[\ln\left(\frac{z_a}{z_{0M,c}}\right) + kB_c^{-1} \right] \quad (4.29)$$

where kB_s^{-1} is given by equation 4.9 and kB_c^{-1} is

$$kB_c^{-1} = 16.4 \left(\sigma_a \cdot LSAI_{eff}^3 \right)^{-1/4} \left[D_f u / \ln\left(\frac{z_a - d}{z_{0M,c}}\right) \right] \quad (4.30)$$

and the momentum partition function σ_a is given by eq. 4.23. In SEBS the characteristic leaf dimension size is set to 0.05 m.

The last step in the derivation of the model is to run a number of simulations, using different geometry parameters to solve eq. 4.24 and different stability conditions.

Blümel has fitted these results into a single expression which gives C at a certain fractional vegetation coverage as a function of this vegetation coverage:

$$C(F) = \frac{C(0) - C(1)}{1 - \exp(-a_1)} \exp(-a_1 F) + C(0) - \frac{C(0) - C(1)}{1 - \exp(-a_1)} \quad (4.31)$$

where a_1 is fitted as

$$a_1 = 2.6 \left(\frac{10 h}{z_a} \right)^{0.355} \quad (4.32)$$

and h is the vegetation height. Hence kB^{-1} and the roughness height for heat transfer is easily calculated from equation 4.27.

In SEBS calculation of the Blümel kB^{-1} value sets out with the calculation of an effective roughness length for momentum according to the model variation with tightly packed vegetation units. Next the C functions for bare soil and fully vegetated patches are calculated which subsequently are inserted into eq. 4.31. Finally kB^{-1} is calculated by equation 4.27.

4.3 The Bulk Atmospheric Similarity Model (BAS)

As pointed out in chapter 3 Monin Obukhov Similarity enables the calculation of surface heat fluxes in the ASL from mean wind and temperature profiles together with air pressure and humidity.

Although still no unanimity is reached about the exact form of the stability correction functions (De Bruin, 1998), the ϕ_i functions proposed by Brutsaert (1999) are based on a physical approach. Brutsaert's formulation is based on a model by Kader and Yaglom (1990) which divides the ASL into three sub layers, in each of which the turbulence moments can be described by simple power laws. In order to extend the availability of the model throughout the ASL Brutsaert has developed a set of interpolation equations that exhibit the same behavior as the model by Kader and Yaglom.

With $y = -(z-d)/L$ these functions are given by

$$\phi_m(y) = \left(\frac{a + b \cdot y^{m+1/3}}{a + y^m} \right) \quad (4.33)$$

$$\phi_h(y) = \left(\frac{c + d \cdot y^n}{c + y^n} \right) \quad (4.34)$$

After considering the data of Kader and Yaglom (1990) as well as data collections prior to 1988 (for a review, see Högström, 1988) it was decided to assign the following values to the constants: $a = 0.33$, $b = 0.41$, $m = 1.0$, $c = 0.33$, $d = 0.057$ and $n = 0.78$. A graphical representation eq. 4.33 shows that ϕ_m exceeds unity for $y > b^{-3}$. Since this is not in agreement with experimental data, eq. 4.33 has been constrained to values below this threshold and ϕ_m has been set to unity for values above it. Hence with the use of eq. 3.24 it is possible to write down the integrated MOS correction functions (eq. 4.34a for $y \leq b^{-3}$ and eq. 4.34b for $y > b^{-3}$):

$$\Psi_m(y) = \ln(a + y) - 3by^{1/3} + \frac{ba^{1/3}}{2} \ln \left[\frac{(1+x)^2}{1-x+x^2} \right] + \sqrt{3} \cdot ba^{1/3} \tan^{-1} \left[\frac{(2x-1)}{\sqrt{3}} \right] + \Psi_0 \quad (4.34a)$$

$$\Psi_m(y) = \Psi_m(b^{-3}) \quad (4.34b)$$

$$\Psi_h(y) = \left[\frac{(1-d)}{n} \right] \ln \left[\left(\frac{c+y^n}{c} \right) \right] \quad (4.35)$$

where $x = (y/a)^2$ and $\Psi_0 = (-\ln a + 3^{1/2} \cdot ba^2 \cdot \pi/6)$ is an integration constant. In SEBS the integrated stability correction functions are coded as IDL functions which are called from the main program.

With Monin Obukhov Similarity all data should be measured in the ASL. For this purpose measurement towers will be appropriate facilities. Thus with a set of measurements at one height and with sufficient information about the surface (roughness length, displacement height, surface temperature) the influence of atmospheric stability on the form of the profiles can be established.

Under convective conditions the part of the PBL above the ASL is well mixed (section 3.1). In the mixed layer wind speed and potential temperature are nearly constant. Brutsaert (1999) therefore assumes that the unstable ABL consists of an inner region, where MOS is valid, and an outer region, which is essentially a slab layer where the profiles are constant. Brutsaert has formulated a *Bulk Atmospheric Boundary Layer Transport Formulation* in which measurement from this outer region can be used to describe the stability correction functions. With standard meteorological soundings, which are readily available it should be possible to establish the mixed layer temperatures, wind speed and humidity. This offers a possibility to calculate heat fluxes without the use of meteorological data from the ASL. Furthermore data from *Numerical Weather Prediction Models* could serve as input.

From experimental evidence the top of the ASL h_{st} , where inner and outer region meet, should be scaled with the thickness of the ABL h_i over moderately rough surfaces and with the surface roughness over very rough terrain (Brutsaert, 1999). From eq. 4.36 and eq. 4.37 either h_{st} should be chosen, which ever is larger:

$$h_{st} = \alpha_b \cdot h_i \quad (4.36)$$

$$h_{st} = \beta_b \cdot z_0 \quad (4.37)$$

In SEBS α_b is set to 0.12 and β_b is set to 125 which implies the separation between moderately rough and very rough terrain to lie at about 0.96 m assuming an ASL height of 1 km. This is in agreement with Brutsaert's model where a cutoff value of 1 m is given.

Next a dimensional analysis is carried out (section 3.3) and the inner region is joined with the outer region of the ABL. With u_m and θ_m as respectively the wind speed and the potential temperature in the mixed layer two similarity relationships are obtained:

$$\frac{u_*}{u_m} = k \left[\ln \left(\frac{h_i}{z_0} \right) - B_w \left(-\frac{h_i}{L} \right) \right]^{-1} \quad (4.38)$$

$$\frac{H}{u_*(\theta_s - \theta_m)} = k \left[\ln \left(\frac{h_i}{z_{0h}} \right) - C \left(-\frac{h_i}{L} \right) \right]^{-1} \quad (4.39)$$

At the top of the ASL Monin Obukhov Similarity is still valid. Hence the inner and outer region of the ABL can be joined such that $u = u_m$ and $\theta = \theta_m$ at $z = h_{st}$. Subsequently expressions can be derived for u^*/u_m and $H/u^* \Delta\theta$ by inserting eq. 4.36 (for moderately rough surfaces) or eq. 4.37 (for very rough surfaces) into eq. 3.22 and eq. 3.23. Thus expression for the bulk stability functions B_w and C are obtained. For moderately rough terrain they read

$$B_w = -\ln(\alpha) + \Psi_m \left(\frac{\alpha h_i}{L} \right) - \Psi_m \left(\frac{z_{0m}}{L} \right) \quad (4.40)$$

$$C = -\ln(\alpha) + \Psi_h \left(\frac{\alpha h_i}{L} \right) - \Psi_h \left(\frac{z_{0h}}{L} \right) \quad (4.41)$$

whereas for very rough terrain the bulk stability functions are written as:

$$B_w = -\ln \left(\frac{h_i}{\beta z_{0m}} \right) + \Psi_m \left(\frac{\beta z_{0m}}{L} \right) - \Psi_m \left(\frac{z_{0m}}{L} \right) \quad (4.42)$$

$$C = -\ln \left(\frac{h_i}{\beta z_{0m}} \right) + \Psi_h \left(\frac{\beta z_{0m}}{L} \right) - \Psi_h \left(\frac{z_{0h}}{L} \right) \quad (4.43)$$

If the reference height (i.e. the measurement height) is below the top of the ASL in SEBS MOS similarity (the IDL function '*ASLfunc*') is invoked. Otherwise BAS similarity (the IDL function '*BASfunc*') is used. In section 4.2 it already has been noted that the stability correction functions depend on Obukhov Length which again is a function of friction velocity and heat flux. Therefore an iterative procedure is used to calculate the set of three equations (eq. 3.17, eq. 3.22 and eq. 3.23). In SEBS this system of nonlinear equations is estimated by invoking Broyden's Method, which is available as a standard iterative routine in IDL. The convergence criterion has been set to 0.01 and the maximum number of iterations is put to 400. Integrated stability correction functions and bulk stability functions are coded as separate IDL functions which are made available in the program file *stability.pro*.

4.4 The Surface Energy Balance Index (SEBI)

The *Surface Energy Balance Index SEBI* (Menenti and Choudhury, 1993) uses the Penman Monteith equation (eq. 3.32) to establish a relation between surface temperature and the relative evaporation (i.e. the ratio of actual and maximum evaporation). As already noted in section 3.5, the Penman Monteith equation assumes the aerodynamic resistance for transport of heat to be equal to the resistance for transport of water vapor. Furthermore in the Penman Monteith model the Aerodynamic Surface Resistance only has been defined for vegetated areas. In SEBI this definition is stretched to comprise soil also.

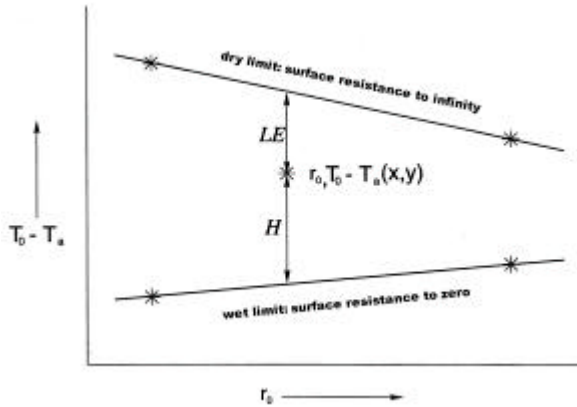


Figure 3 - SEBI: temperature vs. albedo

If the difference between surface and air temperature is plotted against albedo, respectively for a surface resistance approximating zero (i.e. a totally wet vegetation) and for a surface resistance approximating infinity (i.e. a vegetation with closed stomata), a diagram is obtained in which for every point within the two limits the relative contribution of the heat fluxes can be determined (figure 3). In SEBS (Su, 2001) for each pixel for both wet and dry limit, the temperature difference and the external resistance is calculated. These calculations are based on energy balance considerations and stability effects are taken into account. Next the actual temperature difference and actual external resistance are used to calculate the relative evaporation, from which evaporative fraction easily can be retrieved.

From eq. 3.13, eq. 3.22 and eq. 3.25 it follows that the external aerodynamic resistance can be written as:

$$r_a = \frac{1}{ku_*} \left[\ln \left(\frac{z-d}{z_{0h}} \right) - \Psi_h \left(\frac{z-d}{L} \right) + \Psi_h \left(\frac{z_{0h}}{L} \right) \right] \quad (4.44)$$

By combining the energy balance equation (3.2) and the expressions for sensible and latent heat flux (eq. 3.27 and eq. 3.28) with the Penman Monteith equation an expression for the difference between surface temperature and temperature at reference height is obtained:

$$(T_0 - T_a) = \frac{[(r_a + r_s)(Q^* - G_0)/(\rho C_p)] - (e - e_w(T_a))/\gamma}{1 + \Delta/\gamma + r_s/r_a} \quad (4.45)$$

Since no water is available at the dry limit the latent heat flux will be zero. Thus the energy balance equation can be rewritten as

$$H_d = Q^* - G_0 \quad (4.46)$$

After inserting equation 4.46 into eq. 3.17, eq. 4.44 and eq. 4.45 and with $r_i \rightarrow \infty$ respectively a dry limit Obukhov Length L_d , a dry limit external aerodynamic resistance r_{ad} and a dry limit temperature difference are obtained:

$$L_d = -\frac{\rho C_p u_*^3 \bar{\theta}}{k g (Q^* - G_0)} \quad (4.47)$$

$$r_{ad} = \frac{1}{k u_*} \left[\ln \left(\frac{z-d}{z_{0h}} \right) - \Psi_h \left(\frac{z-d}{L_d} \right) + \Psi_h \left(\frac{z_{0h}}{L_d} \right) \right] \quad (4.48)$$

$$(T_0 - T_a)_d = r_{ad} \frac{Q^* - G_0}{\rho C_p} \quad (4.49)$$

where $\langle \theta \rangle$ is the average of the potential surface temperature and the potential temperature at reference height.

For the wet limit the energy balance equation can be rewritten as

$$H_w = Q^* - G_0 - \lambda E_w \quad (4.50)$$

At a totally wet surface almost all energy will be used for evaporation and H_w will be approximately zero. The Obukhov Length at the wet limit can be determined using a formula by Brutsaert (1982) in which this stability length is expressed in terms of potential instead of virtual potential temperature:

$$L = -\frac{\rho u_*^3}{k g \cdot \frac{H}{\theta \cdot C_p} + 0.61 \cdot E} \quad (4.51)$$

With $H_w = 0$ the Obukhov Length for the wet limit then is expressed by

$$L_w = -\frac{\rho C_p u_*^3 \bar{\theta}}{k g \cdot 0.61 (Q^* - G_0) / \lambda} \quad (4.52)$$

Analogous to the dry limit the external aerodynamic resistance for the wet limit is given by

$$r_{aw} = \frac{1}{k u_*} \left[\ln \left(\frac{z-d}{z_{0h}} \right) - \Psi_h \left(\frac{z-d}{L_w} \right) + \Psi_h \left(\frac{z_{0h}}{L_w} \right) \right] \quad (4.53)$$

The temperature difference for the wet limit can be written as

$$(T_0 - T_a)_w = \frac{r_{aw} \cdot \frac{Q^* - G_0}{\rho C_p} - \frac{e_s - e}{\gamma}}{1 + \Delta / \gamma} \quad (4.54)$$

Menenti and Choudhury (1993) have demonstrated that the relative evaporation can be expressed by the normalized actual temperature gradient with reference to the theoretical limits (i.e. the wet and the dry limits, see figure 3):

$$\Lambda_r = \frac{\lambda E}{\lambda E_w} = 1 - \frac{\frac{(T_0 - T_a)_d}{r_{ad}} - \frac{(T_0 - T_a)_w}{r_{aw}}}{\frac{(T_0 - T_a)_d}{r_{ad}} - \frac{(T_0 - T_a)_w}{r_{aw}}} \quad (4.55)$$

The evaporative fraction is defined as the ratio of the latent to the total heat flux and after inserting eq. 4.55 into this definition can be expressed by

$$\Lambda = \frac{\lambda E}{\lambda E + H} = \frac{\Lambda_r \cdot \lambda E_w}{Q^* - G_0} \quad (4.55a)$$

From the approximation made for H_w in eq. 4.50 it will be clear that the relative evaporation approximately equals the evaporative fraction.

Su (2001) has shown that if relative evaporation is retrieved from the actual sensible heat flux and the sensible heat fluxes at wet and dry limits, an expression equivalent to eq. 4.55 is obtained. In other words an approach based on energy balance considerations leads to the same results as the SEBI formulation.

Compared to the original SEBI model in the model by Su (2001) three major improvements are brought about:

- radiation balance, temperature limits and evaporative fraction are calculated for each pixel;
- roughness length for heat transfer is calculated for each pixel (see section 4.2);
- in the calculation of wet and dry limits atmospheric stability is taken into account. The estimation of the extremes for Obukhov length and aerodynamic resistance is physically based by invoking MOS or BAS scaling (see section 4.3).

4.5 Emissivity and Soil Heat Flux

In section 4.1 a method to retrieve albedo and surface temperature from ATSR images has been outlined. If longwave and short wave radiation data are available and if emissivity is known, this enables us to estimate the net radiation at the earth's surface (eq. 3.1).

Emissivity of vegetated soil can be approximated by a relationship proposed by Van de Griend and Owe (1993), provided the NDVI are greater than 0.16 but smaller than 0.74:

$$\varepsilon = 1.009 + 0.047 \ln(NDVI) \quad (4.56)$$

The BAS model (section 4.3) enables the estimation of the sensible heat flux. The SEBI model (section 4.4) enables the estimation of the latent heat flux. Furthermore in this project the latent heat flux also is estimated from the BAS model by treating it as a rest term in the energy balance equation (eq. 3.2). In the same way the sensible heat flux also is estimated from the SEBI model. This implies that the soil heat flux has to be either measured or parameterized. Out of many models (e.g. Stull, 1999, De Bruin, 1998, Bastiaanssen et al., 1998) in SEBS an empirical approach is used partitioning the soil heat flux according to fractional canopy coverage:

$$G_0 = Q^* [\Gamma_c + (1 - F) \cdot (\Gamma_s - \Gamma_c)] \quad (4.57)$$

where Γ_x is the ratio of soil heat flux to net radiation with $x = c, s$ respectively for full canopy and bare soil and F is fractional vegetation coverage. Γ_c is set to 0.05 (Monteith, 1973) and Γ_s is set to 0.3 (Fuchs and Hadas, 1972).

4.6 Roughness Length for Momentum

Roughness of the earth's surface is to a considerable extent determined by vegetation. Since NDVI is a measure for vegetation, NDVI could enable the determination of roughness length for momentum from the satellite image itself. Moran (1990) represents the roughness length of a pixel in row x and column y as

$$z_{0M} = \exp(c_2 + c_3 \cdot NDVI(x, y)) \quad (4.58)$$

with c_2 and c_3 as coefficients depending on the study area. Roerink et al.(2001) use a relationship depending on the maximum NDVI in the image and which, provided $NDVI \leq 0.7$, appeared to be in good agreement with a parameterization of eq. 4.58 by Bastiaanssen (1995) in which $c_2 = -5.2$ and $c_3 = 5.3$:

$$z_{0M} = 0.005 + 0.5 \cdot \left(\frac{NDVI}{NDVI_{\max}} \right)^{2.5} \quad (4.59)$$

Throughout this project eq. 4.59 has been used to estimate the roughness length for momentum transfer.

Using NDVI as only measure for roughness confronts us with a number of problems. For conditions of natural vegetation with dispersed shrubs and trees, z_{0M} depends on the spacing, shape, size, distribution and density of these obstacles (Lettau, 1969). Here NDVI will not adequately describe surface roughness. If a surface covered by coniferous forest is compared to a patch with pastures, it is possible that the pastures will show a larger NDVI whereas the forest will have an appreciable higher surface roughness. Furthermore, roughness length will also depend on obstacles other than vegetation (e.g. buildings, rocks) and will be a function of landscape structure and orography. Stull (1999) reports roughness lengths in very hilly to mountainous areas ranging from 1.1 m to 80 m.

These problems could be overcome by using a suitable land cover database, preferably one in which landscape structure is available as attribute. If a land cover database is used, normally the resolution of the database will differ from the resolution of the satellite image. This makes it compulsory to aggregate local roughnesses (below the pixel resolution) to a roughness length for momentum that is valid for the pixel. This effective roughness length for momentum can be defined as a value that by using boundary layer similarity theory over a given landscape structure and topography yields a surface stress that coincides with the area-representative momentum flux (Wang et al., 1998). The problem of establishing an effective roughness length has already been addressed in the discussion of the Blümel model where an aggregation method according to fractional vegetation coverage has been proposed. Since at a 1 km resolution more vegetation types can occur, aggregation has to be performed on all of these vegetation types. Area-averaging of roughness lengths is highly nonlinear (Hasager et al. 1999). Noilhan and Lacarrere (1995) applied a widely used logarithmic average

$$\ln z_{0M \text{ eff}} = \sum (a_i \ln z_{0M,i}) \quad (4.60)$$

where a_i is the fractional coverage of patch i in the area to be aggregated. Because friction velocity is inversely proportional to roughness length for momentum (eq. 3.23), Wang (1998) proposes an inverse logarithmic relationship

$$(-\ln z_{0M \text{ eff}})^{-1} = \sum (a_i / -\ln z_{0M,i}) \quad (4.61)$$

Wang also considers a inverse quadratic averaging by pointing out that after inserting eq. 3.10 into eq. 3.23 roughness length shows an inversely squared to momentum flux.

$$(-\ln z_{0M\ eff})^{-2} = \sum (a_i / (-\ln z_{0M\ i})^2) \quad (4.62)$$

In section 4.3 it has been stated that in a neutral atmosphere a logarithmic wind profile can be observed. In actual terrain this profile only occurs in the ideal stationary case with a very long homogeneous upwind terrain fetch, say > 10 km (Wieringa, 1993). Upwind terrain characteristics will influence the flow behavior to a considerable extent. Elliot (1958) and Brooks (1961) have shown that if terrain changes occur at upwind fetch distance x (i.e. changes in surface roughness), the wind profile will only be related to the local terrain roughness within an *internal boundary layer (IBL)* of limited height $\delta(x)$, while the wind structure at higher levels is still determined by the roughness at upwind distances larger than x. Thus roughness for momentum will be a property of flow rather than a mere local property of the terrain. Hasager and Jensen (1999) have developed a flux aggregation model based on a linearized set of the atmospheric flow equations solved by fast Fourier transforms. These flow equations (eq. 3.5) have been simplified to represent a stationary neutrally-stratified flow without rotation. Furthermore the pressure perturbation term (the fifth term in eq. 3.5) is neglected. The effective roughness length is modeled as the sum of the logarithmic average ($\ln z_{0M,a}$) and a perturbation term:

$$\ln z_{0M\ eff}(x, y) = \ln z_{0M,a} + m(x, y) \quad (4.63)$$

In fact the logarithmic average can be considered as the roughness within the internal boundary layer whereas the perturbation represents the upwind effects. Converted to Fourier space flow equations together with eq. 4.61 can be solved. Thus an effective roughness length for momentum is obtained with wind speed, wind direction and internal boundary layer height as input parameters.

Now these aggregation models can be used to estimate effective roughness lengths for momentum from land cover databases. In this project the Corine land cover database (CEC, 1993) with a resolution of 100 m has been used for this purpose. The Corine project has no indication of landscape structure or orography. To cover these aspects the land cover database could be combined with a *Digital Elevation Model (DEM)* and an appropriate tool (a *GIS-application*) to perform a spatial analysis in order to establish the landscape structure. In this project however a more limited approach has been chosen. Roughness lengths are assigned to each land cover class by comparing them to the LGN3-landcover classes, which have been provided with a roughness length classification by Wieringa et al. (1993). Furthermore a study into representative roughness parameters for homogenous terrain by Wieringa (1993) has been used to attribute roughness lengths to land cover classes. The accuracy of the database only has been confirmed for the areas under study. The result of this roughness classification is tabulated in appendix 2a. In the last column of appendix 2a an indication has been made if a seasonal correction to the roughness length could be appropriate in winter, spring and autumn. Since most of the ATSR images used in this project are well within the growing season, no seasonal correction has been made.

The procedure to derive the roughness maps is as follows. First the roughness length is attributed to the classes at a resolution of 100 m. For this purpose the IDL program Corinez.pro has been developed (Appendix 1d). Next the aggregation procedure is carried out. The IDL program Logagg.pro (Appendix 1e) performs a logarithmic averaging (eq. 4.60), Logrecagg.pro (Appendix 1f) performs an inverse logarithmic averaging (eq. 4.61), Logrecquadagg.pro (Appendix 1g) performs an

inverse cubic logarithmic averaging (eq. 4.62) and Hasag.pro (Appendix 1h) performs the aggregation according to the microscale model by Hasager and Jensen. All aggregation methods have been looked into and finally logarithmic averaging has been chosen to be used in the estimation of the heat fluxes. Details are to be found in chapter five, section 5.4.6.

4.7 The Parallel Source Model

Vegetated surfaces generally will be cooler than bare soil under the same conditions (figure 2). Within a partly vegetated area bare soil patches and vegetated patches will interact separately with the overlying air and locally will produce different heat fluxes. Thus a *dual source model* should consider the aerodynamic resistances of bare soil to canopy air and of vegetation to canopy air. In fact Blümel's model, in which four different sensible heat fluxes are distinguished is a good example to such an approach. Jia et al. (2001) have proposed a dual source model using three aerodynamic resistances (soil -canopy air, leaf-canopy air and canopy air - overlying air). Both models consider interactions between the heat fluxes which originate from bare soil and the heat fluxes which originate from vegetation (i.e. the fluxes into the canopy air are coupled). In a more simple approach this coupling is not considered and heat fluxes are calculated with only two resistances (canopy air to reference height and bare soil to reference height). The stand geometry which could be associated to this model is the second model variation from the Blümel model (eq. 4.25, Blümel however considers within canopy resistances as well). According to this approach Su (unpublished, personal communication) developed a *Parallel Source Model* by extending the SEBS-scheme. Evaporative fractions are calculated by

$$\Lambda = \frac{\lambda E_c \cdot F + \lambda E_s \cdot (1 - F)}{Q^* - G_0} \quad (4.64)$$

where λE_c is the latent heat flux originating from vegetation, λE_s is the latent heat flux originating from bare soil and F is the fractional vegetation coverage. Net energy Q^* and soil heat flux G_0 are calculated for the entire pixel (the composite surface) according to the original SEBS scheme.

The evaporative fractions for vegetation and bare soil are estimated separately by invoking the SEBS scheme for each component. For the vegetation component the fractional vegetation coverage is set to unity and vegetation height is calculated from eq. 4.16. The vegetation component potential temperature (section 4.1.6) is used in eq. 3.22 as surface potential temperature θ_0 . A net energy term and the soil heat flux is estimated as if the pixel were entirely vegetated. Next the stability functions are determined using the same assumption and finally the evaporative fraction for the vegetation component Λ_c is calculated from energy balance considerations by using eq. 4.55a rather than eq. 4.55. An analogous procedure is developed for the calculation of the bare soil component evaporative fraction Λ_s . Here the bare soil potential temperature is used for the surface potential temperature θ_0 , the fractional vegetation coverage is set to zero and for the vegetation height the roughness height of bare soil is taken (section 4.2.1). Now the evaporative fraction can be calculated by eq. 4.64 using

$$\Lambda_x = \frac{\lambda E_x}{Q_x^* - G_{0,x}} \quad (4.65)$$

with $x \in \{c,s\}$.

In order to be able to compare the results from the parallel source model with the single source model, the IDL code of the parallel source model (Su, unpublished, personal communication), a small modification has been brought about. Although it does not reflect a physical reality, it is possible that the estimation of eq. 3.22 results in a sensible heat flux greater than the net energy minus the soil heat flux (I will call this latter quantity the *available energy per square meter*). In very dry circumstances (no evaporation) the sensible heat flux must equal the available energy. For instance a small overestimation of the temperature difference between air and soil will result in too high a sensible heat flux. If evaporative fraction is calculated (energy balance approach) as the ratio of available energy minus sensible heat flux and available energy this will result in a negative evaporative fraction. In the Penman Monteith approach (eq. 4.55 and figure 3) an overestimation of the temperature difference in very dry circumstances will result in a dry limit temperature difference being smaller than the actual temperature difference. This also causes the evaporative fraction to be negative. For practical purposes these situations easily can be ruled out by putting the sensible heat flux on a par with the sensible heat flux at the dry limit. In the parallel source model two results are calculated: one in which this rule has been implemented (the flagged result) and one comparable to SEBS in which sensible heat fluxes greater than the ones at the dry limit are permitted (the unflagged result). Roughness length for momentum transfer is estimated both from NDVI and the Corine land cover database and roughness length for heat transfer again is calculated both from the Massman and the Blümel model.

4.8 Modifications to the Original Code

Some changes have been introduced to the original IDL code.

- For the time series a version of SEBS has been made in which all values that are related to the satellite image and are stored in arrays (e.g. z_{om} , NDVI etc.) are converted to simple variables of the appropriate type.
- The possibility of using roughness lengths derived from land cover classes already have been mentioned (Appendix 1.i.1).
- Where appropriate (e.g. eq. 4.57, soil heat flux and eq. 4.31, Blümel model) fractional vegetation coverage derived from eq. 4.2 is used instead of an estimation through NDVI (Appendix 1.i.2).
- Moist air density is calculated with a temperature in degrees Kelvin instead of temperature in degrees Celsius. (Appendix 1.i.3).
- The reference height temperature which is used in the calling statement of the BAS subroutine is given as an actual temperature in degrees Celsius. Because the reference height temperature from the SEBS-input is given as potential temperature in degrees Kelvin, a conversion is carried out (Appendix 1.i.4).
- To circumvent the Broyden function in those cases where it cannot be calculated or where it no longer makes sense to calculate it (e.g. where Obukhov Lengths are near zero) neutral values are produced (Appendix 1.i.5).
- Wind speed, humidity, air temperature and air pressure are measured on at reference height. In section 4.3 it has been pointed out that the choice for the use of ASL or BAS stability functions will depend on this measurement height. To the BAS code (the module that calculates either ASL or BAS stability) a reference height (z_{ref}) and the height of the PBL (h_i) are to be passed on. In the original code both are set to the variable used in SEBS for the measurement height (z_{pbl}). This means that measurements from towers almost always will be calculated by BAS functions (eq. 4.36). Therefore if measurements are made at

heights less than 100 m a default PBL-height of 1000 m is passed on (Appendix 1.i.6).

- For the calculation of the net radiation (eq. 3.1) in the BAS module the formula from the SEBS module is used, i.e. without multiplying the downward longwave radiation with emissivity (Appendix 1.i.7).

4.9 Flux measurements

Validation of the calculated fluxes has been carried out by using measurements from the *MEDEFU project (Carbon and Water fluxes of Mediterranean forests)*, from the Alterra project *'Hydrologie en waterhuishouding van bosgebieden in Nederland'* and from the *EWBMS project (Energy and Water Balance Monitoring System)*. In the first two project fluxes are measured with Eddy devices, in the third project scintillometers are used.

4.9.1 Eddy devices

Vertical heat fluxes are determined by the covariance of vertical wind speed perturbation w' and temperature perturbation θ'_v (sensible heat flux) or specific humidity perturbation q' (latent heat flux). In chapter 3 this has been expressed by equations 3.6 and 3.7. Eddy devices are operated by this principle. They are equipped with fast sensors which measure vertical wind speed, temperature and specific humidity at least ten times per second. Subsequently the data are stored and processed by a computer (De Bruin, 1998). Eddy devices are mounted on a measurement tower and as a consequence of this are only representative for a relatively small area. An assessment by Roerink et al. (2001, /2) has shown that most of the flux measured by the instrumented tower in the Alterra project *'Hydrologie en waterhuishouding van bosgebieden in Nederland'* comes from a relatively close source, i.e. 60 m. It also has been estimated that fluxes at more than 1500 m away from the tower still contribute to the measured flux.

4.9.2 Scintillometers

The *Large Aperture Scintillometer (LAS)* consists of a transmitter equipped with a light emitting diode (in the EWBMS project $\lambda = 940$ nm) and a receiver. The beam of light passes through the atmosphere of which the refractive index fluctuates due to fluctuation in temperature, humidity and static pressure. The LAS measures the variance of the logarithmic amplitude fluctuations of the received electromagnetic wave. This signal is proportional to the *structure function parameter of the refractive index*, C_n^2 (the structure function describes a relation of position and separation in space). Hill et al. (1980) have shown that the structure function parameter of the refractive index can be expressed in terms of structure function parameter index of temperature $C_{T_y}^2$ and humidity $C_{q_p}^2$ and pressure $C_{p_p}^2$. For $\lambda = 940$ nm the latter two are negligible. C_T^2 can be expressed in terms of sensible and latent heat flux (Moene et al. 2001) :

$$C_T^2 = C_n^2 \frac{T^2}{A_T^2} \left(1 + \frac{0.03 \cdot \lambda E}{H} \right)^{-2} \quad (4.66)$$

Where A_T is a coefficient depending on air pressure and atmospheric temperature T (K). For C_T^2 a number of similarity relations are developed, expressing C_T^2 as a

function of displacement height, the height of the scintillometer beam above the ground, the Obukhov Length and the specific temperature (eq. 3.16). In an iterative procedure using this similarity relationship and eq. 3.16, eq. 3.17 and eq. 3.23 the sensible heat flux can be estimated by eq. 4.66. Within the EWBMS project four similarity relationships are used to calculate the sensible heat fluxes:

- Sensible heat flux under stable conditions;
- Sensible heat flux under conditions of free convection (buoyant convective processes dominate, no iterative calculation scheme necessary, De Bruin et al., 1995)
- Sensible heat flux under conditions of forced convection (mechanical turbulence production dominates);
- Sensible heat flux calculated under conditions where both buoyant and mechanical turbulence production are important. Similarity relationship is calculated according to a similarity formulation by De Bruin.

The EWBMS data set contains these four calculated sensible heat fluxes. The structure function parameter of the refractive index is not included.

The scintillometer paths are $1070\text{m} \pm 40\text{ m}$ (Tomelloso), $4440\text{m} \pm 200\text{ m}$ (Lleida) and $5250\text{ m} \pm 200\text{ m}$ (Badajoz). Although among others dependent on wind speed and landscape structure the footprint of these scintillometers will be in the order of the pixel(s) of the satellite image and much larger than the ones of the eddy devices.

Appendix 1j shows a program of a semi-automatic procedure to calculate mean values over the scintillometer path of the Badajoz site. It will identify pixels on the scintillometer path and its vicinity (a total of 24 pixels) with a negative value (i.e. pixels that have been flagged). Next these pixels can be omitted in the second part of the routine, after which a mean value is printed onto the screen.

5 Estimation of heat fluxes in Spain and the Netherlands

5.1 Measurement Sites in Spain and the Netherlands

In Spain within the framework of the *EWBMS project* three *Large Aperture Scintillometers (LAS)* have been installed at sites near Lleida (Lérida), Badajoz and Tomelloso (figure 5.1). Each scintillometer site additionally is equipped with a short wave radiometer to measure global radiation.

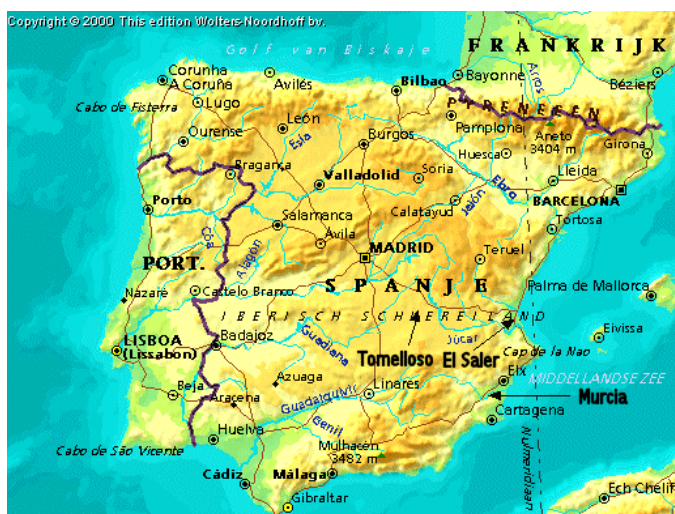


Fig. 5.1 measurement sites in Spain

The *Badajoz* LAS is located in a region with large scale irrigation (sprinkler irrigation) at an altitude of 168 m. Crops being grown are wheat, corn, alfalfa, lettuce, olives, beans, and tomatoes. The distance between transmitter and receiver is $5250 \text{ m} \pm 200 \text{ m}$. The receiver is installed on top of a hill on a house, 68 m above the surrounding terrain at co-ordinates $38^{\circ}55'41.82''\text{N}$, $6^{\circ}36'35.4''\text{W}$. The transmitter is installed on a water tower, 56 m above the surrounding terrain at co-ordinates $38^{\circ}56'17.9''\text{N}$, $6^{\circ}40'8.46''\text{W}$ (Moene, 2001). Meteorological data are obtained from a station some 7 kilometers from the LAS receiver. Ground cover of the station is short grass. Downward long wave radiation is not recorded.

The scintillometer near *Lleida* is installed in a region with small scale irrigation at an altitude of 130 m. Main crops are fruit trees (peaches) and alfalfa. The distance between transmitter and receiver is $4440 \text{ m} \pm 200 \text{ m}$. Both receiver and transmitter are installed on a hill, on a tripod at a height of respectively 45 m and 39 m above the surface at co-ordinates $41^{\circ}34' 57.72''\text{N}$, $0^{\circ}52' 26.64''\text{E}$ and $41^{\circ}32'38.64''\text{N}$, $0^{\circ}51'38.64''\text{E}$ (Moene, 2001). Meteorological data are obtained from the meteo station near Juneda ($41^{\circ}33'\text{N}$ $0^{\circ}49.5'\text{E}$). Downward longwave radiation is not recorded.

The landscape of the *Tomelloso* site comprises a nearly level, alluvial floodplain to the north and a tilted old alluvial plain to the south. The latter has a distinct gradient in elevation from northwest to the southeast, from 665 to 833 m. The vegetation

consists of non-irrigated vineyards, and a few olive orchards. The vines are broadly spaced and trellises are not used. At mid-season canopy coverage is less than 50% (ESA/ESTEC, 1999). The distance between transmitter and receiver is $1070 \text{ m} \pm 40 \text{ m}$. Both receiver and transmitter are installed on a steel mast at a height of respectively 4.15 m and 4.56 m above the surface at co-ordinates $39^{\circ}07' 39.18''\text{N}$, $2^{\circ}55' 57.06''\text{W}$ and $39^{\circ}07'21.42''\text{N}$, $2^{\circ}55'18.84''\text{W}$ (Moene, 2001). Altitude of the scintillometer is 670 m. Meteorological data are obtained from a meteo station near Tomelloso ($39^{\circ}10'29.22''\text{N}$ $3^{\circ}0'2.16''\text{W}$). Ground cover of the station is bare soil and grass. Longwave and short wave radiation data, both incoming and outgoing are available from this meteo station.

The fourth Spanish site is located at El Saler ($39^{\circ}20'10.05''\text{N}$ $0^{\circ}19'42.31''\text{W}$), approximately 10 km south of Valencia. The measurement site is situated in a narrow and elongated forest area (mean width a few hundred meters, total area approx. 195 ha) parallel to the coast with as main forest species *P. halepensis* (Aleppo pine) and *Q. coccifera* (Holly Oak) (Roerink et al., 2001/2). On the west this forest is bounded by salt marshes and rice fields, on the east it is bounded by a small strip of beaches and leisure facilities which lie directly by the Mediterranean Sea. Figure 5.2 depicts the surroundings of the El Saler site (the measurement tower being the conical shape which is located in the elongated forest area represented by the dark color). Flux measurements are carried out using Eddy devices which are operated on a height of 15 m. Downward longwave radiation is not measured.

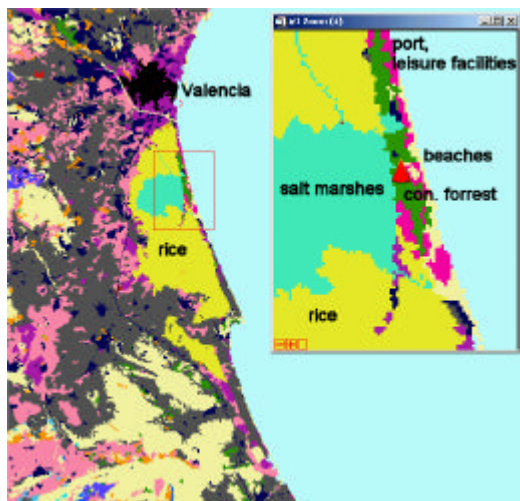


Fig. 5.2 El Saler



Fig. 5.3 Measurement sites in the Netherlands

The two Dutch sites are situated in forested areas (figure 5.3). At both sites longwave and short wave radiation data, both incoming and outgoing are measured. The Loobos site is located two kilometers south-west of Kootwijk at co-ordinates $52^{\circ}10'00''\text{N}$ $5^{\circ}44'38''\text{E}$. Measurements are carried out at a height of 22 m above the surface. In a radius of 500 m 89% of the vegetation consists of pine trees, 3.5% is open vegetation e.g. heather and the remainder is a mixture of coniferous and deciduous trees (Roerink et al., 2001/2).

The Fleditebos site is located at co-ordinates $52^{\circ}19'06''\text{N}$ $5^{\circ}27'12''\text{E}$ which is approximately 5 km west of Zeewolde. The measurement tower is 24 m high. In a radius of 500 m 93.5% of the vegetation consists of deciduous forest. The main forest type is poplar (76%). Other forest species are ash (9.4%), oak (3.8%) and maple (3.0%) (Roerink et al., 2001/2).

Radio soundings are retrieved from a database of the British Atmospheric Data Centre (<http://www.badc.rl.ac.uk>). For this project an account has been granted to access the BADC global radio sonde archive. The data consists of vertical profiles of temperature, dew-point temperature, relative humidity, humidity mixing ratio, wind speed and wind direction, from the surface to pressures of approximately 20mb. For each day in the time series and for each day for which a satellite image is available radio soundings are retrieved. For each measurement specific humidity and potential temperature is determined (where no height is available, height is retrieved from air pressure). Next temperature, wind speed and specific humidity are graphically displayed against height and against the logarithmic value of the height. An example of this approach is given in Appendix 2b. On the face of it the height of the planetary boundary layer then is determined. Since wind speed and specific humidity appeared to show almost never a logarithmic profile, in most cases the temperature profile has been used to determine PBL-height. Between the earth's surface and a height of 3000 m rarely more than 8 points with a complete set of data has been available and in a number of cases only 1 or 2 points in a sounding comprise the data set of the lower atmosphere. Especially wind measurements showed to be prone to malfunction. From Appendix 2b it becomes clear that the interval at which measurements are taken is too great to warrant an exact identification of the PBL-height. This is even more a problem when measurement failures occur. In the Netherlands radio sondes are operated in De Bilt at 12.00 UTC. Satellite overpass is about three quarters of an hour earlier. In this project for the Spanish sites radio sonde data from Murcia, Madrid and Zaragoza are used. Usually the Spanish radio sondes are operated at 11.00 UTC, which is at approximately at the same time as the satellite overpass.

5.1.1 Sensitivity Analysis: Sensitivity towards Input Parameters

Because SEBS contains a number of discontinuities (e.g. equations 4.34a and 4.34b, equations 4.36 and 4.37) an analytical determination of sensitivity towards input parameters should be carried out for each range for which the appropriate equations are valid. Furthermore an analytical determination of sensitivity of sensible heat flux necessarily will be an expression in terms of friction velocity and Obukhov length. Therefore it has been thought to be more convenient to determine sensitivity on the basis of measurements.

Sensible heat fluxes are calculated in an iterative procedure together with the Obukhov Length and the friction velocity using eq. 3.17, eq. 3.22 and eq. 3.23. In the SEBI module the evaporative fraction is calculated either by expressing the normalized actual temperature gradient with reference to the theoretical wet and dry limit temperature gradient or (in the energy balance approach) by expressing the sensible heat flux with reference to the theoretical minimum and maximum sensible heat flux. These formulations are identical and in both cases the theoretical limits are expressed by using the available energy $Q^* - G_0$. The latent heat flux then is calculated from

$$\lambda E_{SEBI} = \Lambda_{SEBI} \cdot (Q^* - G_0) \quad (5.1)$$

At the scintillometer sites no latent heat flux measurements were carried out. Because sensible heat flux from the iteration, the soil heat flux and the latent heat flux (from

eq. 5.1) are independently calculated they not necessarily add up to the net available energy. To represent the results from the SEBI estimation at the scintillometer sites, sensible heat flux also can be calculated as a remainder:

This H_{rest} is the complementary part of the latent heat flux as calculated by SEBI:

The sensitivity of the latent heat flux calculated by SEBI and of the sensible heat flux

$$H_{rest} = Q^* - G_0 - \lambda E_{SEBI} \quad (5.2)$$

$$H_{rest} = (1 - \Lambda_{SEBI}) \cdot (Q^* - G_0) \quad (5.3)$$

calculated as remainder by eq. 5.2 towards an input parameter x is only equal (but of opposite sign) if this input parameter does not influence $Q^* - G_0$:

$$\frac{\partial \lambda E_{SEBI}}{\partial x} = \frac{\partial(\Lambda)}{\partial x} \cdot (Q^* - G_0) + \Lambda \cdot \frac{\partial(Q^* - G_0)}{\partial x} \quad (5.4)$$

$$\frac{\partial H_{rest}}{\partial x} = -\frac{\partial(\Lambda)}{\partial x} \cdot (Q^* - G_0) + (1 - \Lambda) \cdot \frac{\partial(Q^* - G_0)}{\partial x} \quad (5.5)$$

Depending on the sign of the sensitivity of $Q^* - G_0$ towards x and of the magnitude of the evaporative fraction sensitivity of either the latent heat flux from SEBI or H_{rest} will be greater. In order to be able to assess the results at the scintillometer sites in the sensitivity analysis the sensible heat flux H_{rest} from eq. 5.3 also is evaluated.

Sensitivity of evaporative fractions towards input parameters is given as Λ_{SEBI} and Λ_{BAS} :

$$\Lambda_{BAS} = \frac{Q^* - G_0 - H_{BAS}}{Q^* - G_0} \quad (5.6)$$

where H_{BAS} is the sensible heat flux calculated in the iterative procedure. These two evaporative fractions are used to assess the measurements with the Eddy devices.

An alternative way to calculate evaporative fractions would be to take the latent heat flux from SEBI (eq. 5.1) and the sensible heat flux from Bulk Atmospheric Similarity (BAS or ASL functions):

$$\Lambda_{ALT} = \frac{\lambda E_{SEBI}}{\lambda E_{SEBI} + H_{BAS}} \quad (5.7)$$

Inserting eq. 5.6 into of eq. 5.7 gives

$$\Lambda_{ALT} = \frac{\Lambda_{SEBI} \left(\frac{1}{1 - \Lambda_{BAS}} \right)}{\Lambda_{SEBI} \left(\frac{1}{1 - \Lambda_{BAS}} \right) + 1} \quad (5.8)$$

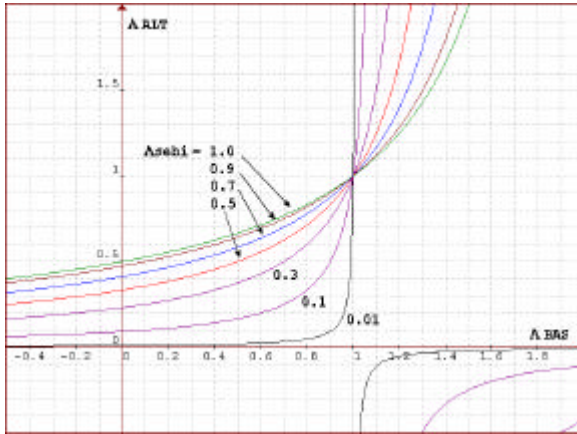


Figure 5.4: L_{BAS} vs. L_{ALT} for various L_{SEBI}

From eq. 5.8 and from figure 5.4 it will be clear that within a range of L_{BAS} from 0 to 1, L_{ALT} will be in the range from 0.5 to 1 at $L_{SEBI} = 1$ and with lower L_{SEBI} gradually will extend to the interval of L_{BAS} . At very low L_{SEBI} there is a tendency for L_{ALT} to stay near to L_{SEBI} until L_{BAS} is near to 1. Within a range of evaporative fractions of 0 to 1, L_{ALT} will lie between L_{SEBI} and L_{BAS} . Therefore L_{ALT} has not been worked out separately.

SEBS is applied to two cases and heat fluxes are calculated for a range of values for each input parameter for which the sensitivity has to be determined. Each case is calculated with a roughness length for heat transfer according to both Blümel model and Massman model. Furthermore each case is calculated with meteo data from the measurement tower (which usually will be calculated with ASL stability functions) as well as with meteo data from a radio sounding (which usually will be calculated by invoking BAS stability functions).

The first case chosen is in the Netherlands at the Loobos site. At May 7, 1997 at 11.00 a.m. the temperature difference between air and soil was small (1 K at 22 m). Wind speed was rather low (about 3 m/s at 22 m and 7 m/s at PBL-height). Short wave and longwave radiation data suggest a heavily overcast sky ($K^{\downarrow} = 309 \text{ Wm}^{-2}$, $L^{\downarrow} = 310 \text{ Wm}^{-2}$). In this case the top of the ASL will be calculated from eq. 4.37.

The second case chosen is in Spain at the Tomelloso site. At June 2, 1999 at 11.00 a.m. at a height of 10 m the potential temperature difference between air and soil was 4 K. Wind speeds were comparable to the first case (about 4 m/s at 10 m and 8 m/s at PBL-height). Short wave and longwave radiation data suggest a clear sky ($K^{\downarrow} = 1165 \text{ Wm}^{-2}$, $L^{\downarrow} = 347 \text{ Wm}^{-2}$). The top of the ASL will be calculated from eq. 4.36.

In appendix 3a the results from this sensitivity analysis are represented. For Spain calculations are carried out with a roughness length for momentum transfer from the Corine database (i.e. 0.5 m). An extra set of calculations is performed using a roughness length estimated by NDVI (eq. 4.59, by taking the mean value of calculated roughness lengths from the ATSR images of June and July 1999). For 'NDVI-roughness' only results from the Massman algorithm are rendered. Heat fluxes and evaporative fractions which are estimated with this roughness are provided with the suffix 0.084 (i.e. the mean value of the 'NDVI-roughness'). In section 5.4 the results with the 'NDVI roughness' will show that an analogous determination with 'NDVI roughness' at the Loobos site is less useful. In appendix 3b sensitivities for an appropriate range are tabulated. This range is bound to be near-linear and the actual value of the input parameter lies within it.

In general the sensitivities at the Spanish site are higher than in the Netherlands. Since in all cases sensitivities calculated with the 'NDVI roughness' appeared to be equivalent to those calculated with the 'land cover database roughness', these values are not tabulated. The Dutch series is just on the edge of stability and instability. The tower measurement leads to a description of an unstable atmosphere whereas the measurements with the radio soundings show a stable environment¹. Thus in the Dutch series we see some discontinuities which can be attributed to the switch from stable to unstable integrated correction functions (e.g. tower measurement, air temperature at 283.5 K, radio soundings, air pressure at 985 kPa and soil temperature at 282 K).

Since the *albedo*, *longwave incoming radiation* and *short wave incoming radiation* are not input parameters in the Bulk Atmospheric Similarity Model (BAS), sensible heat flux from BAS shows no sensitivity towards it. Evaporative fractions and λE_{SEBI} show an appreciable sensitivity towards albedo. For Tomelloso (radio sounding) a rise of albedo with 0.1 would result in a drop of λE_{SEBI} with 85.7 Wm^{-2} (Massman model for heat transfer) or 102.9 Wm^{-2} (Blümel model for heat transfer). For Loobos these values are respectively 37.7 Wm^{-2} and 42.1 Wm^{-2} . This means (with heat fluxes of a few hundred Wm^{-2}) the atmospheric correction for VIS/NIR channels (§ 4.1.4) has to be performed with an accuracy well below an error of 0.1. For the time series albedo has been calculated by taking the ratio of reflected and incoming short wave radiation. For Loobos ($n=45$) an albedo of 0.080 has been calculated with a maximum of 0.090 and a minimum of 0.067 with a standard deviation of $6.4 \cdot 10^{-3}$. For Tomelloso these values are respectively 0.175, 0.194, 0.158 and $1.4 \cdot 10^{-2}$. Thus natural day to day albedo differences will only exert a small influence on calculated fluxes. The H_{res} shows a slightly concave form: it rises at low albedo and drops again at higher albedo. This can be understood by looking at eq. 3.1 and eq. 5.3: although the available energy ($Q^* - G_0$) decreases when albedo increases, at very low albedo, the effect of the increase in $(1 - \Lambda)$ is stronger and causes a small increase in sensible heat flux. In terms of eq. 5.2: at small albedo the decrease of available energy is less than the decrease of λE_{SEBI} .

Sensitivity of the algorithm towards NDVI increases at smaller NDVI. Within the range for which it is valid (NDVI must lie between 0.16 and 0.7: eq. 4.56 and eq. 4.59) the algorithm shows only a moderate sensitivity towards NDVI. Tomelloso, with a lower NDVI due to a lower fractional vegetation coverage, shows the greatest sensitivity. Most sensitive is the Massman model where an increase of NDVI with 0.1 would induce a decrease of latent heat flux of 13.6 Wm^{-2} (tower measurement).

Sensitivity of latent heat flux and evaporative fractions calculated with Massman resistance for heat transfer increase at higher *fractional vegetation coverage* F whereas evaporative fractions from the Blümel model tend to decrease (the Netherlands) or stay even (Spain). A closer look at the estimated kB^{-1} -factors reveals the occurrence of a minimum kB^{-1} -value in the fractional coverage series with the Massman model for the Netherlands and with both models for Spain (see Appendix 3c). In terms of the Massman model: with increasing F at low F the contribution of the last term of eq. 4.8 decreases faster than the contribution of the two other terms increases. In terms of the Blümel model: the ratio of effective roughness for momentum and effective roughness for heat transfer shows a minimum value at $F \approx 0.2$. If the results from the Massman and the Blümel model are compared, it becomes clear that a small

¹ In the BAS-module also comprises the 'stable counterparts' of eq. 4.34 and 4.35. These have not been discussed in chapter four because only satellite images on days with clear skies will be used. Under those conditions at about 11.00 a.m. during the growing season a stable atmosphere is not very likely.

change in the kB^{-1} -factor can induce a considerable difference in calculation of the evaporative fraction. For instance in the Tomelloso tower measurement at $F = 0.3$, the Massman algorithm gives a kB^{-1} -factor of 6.01 with an evaporative fraction of 0.310 whereas the Blümel model estimates a kB^{-1} -factor of 5.86 and an evaporative fraction of 0.531. In this example the ratio of roughness lengths for momentum and heat transfer is respectively 408 and 351.

At the Dutch site Massman and Blümel algorithm show an opposite behavior. With the Massman model the kB^{-1} -factor increases with increasing F , with the Blümel model the kB^{-1} -factor shows a maximum at about $F = 0.1$ after which it decreases. I.e. the weighting functions eq. 4.8 and 4.31 are parameterized in such a way that in this case eq. 4.8 (Massman) causes the evaporative fraction to increase whereas eq. 4.31 causes a decrease of the evaporative fraction at fractional vegetation coverage greater than 0.1. This behavior should be further looked into.

The greatest sensitivity of the SEBS algorithm towards fractional cover occurs using the Blümel model with the estimation of λE_{SEBI} . Here a change of fraction cover of 0.1 causes an increase of the latent heat flux of more than 40 Wm^{-2} (radio sounding, tower measurement, Tomelloso). Since at the Tomelloso site fractional coverage lies at the low end of the range, the actual sensitivity will be lower.

For the Loobos site sensitivity towards *roughness length for momentum* z_{0m} is fairly low and stays well below $1 \text{ Wm}^{-2}\text{cm}^{-1}$ (heat fluxes) and 1 \%cm^{-1} (evaporative fractions). From the graph it is clear that sensitivity increases towards smaller roughness lengths. For the Spanish site sensitivity towards z_{0m} has been determined for two ranges around the 'NDVI roughness' and the 'land cover database roughness'. Here sensitivities are appreciably higher than in the Netherlands. Around the 'NDVI roughness' sensitivities are a factor 2 - 3.5 (tower measurement) or 4 - 5.5 (radio sounding) higher than around the 'land cover database roughness'. The Massman model shows the greatest sensitivity at the estimation of the latent heat flux (and of the remainder term H_{res}): $8.3 \text{ Wm}^{-2}\text{cm}^{-1}$ and of the evaporative fraction by SEBI: -1.6 \%cm^{-1} . In the Netherlands the sensitivities towards roughness length is lower for the radio sounding series than with the tower measurements, in Spain this is only the case with the 'land cover database roughness'. For the 'NDVI roughness' sensitivities from both series are approximately equal.

The algorithm shows a sensitivity towards ambient air pressure of about $20 \text{ Wm}^{-2}\text{kPa}^{-1}$. Apart from the discontinuity from the stable to unstable correction functions at the Loobos site (radio sounding), this sensitivity is rather constant throughout the whole range of 3 kPa. On a spatial scale of a few hundred kilometers and measured at the same height air pressure fluctuations will be far below 1 kPa.

Sensitivity towards *potential air temperature* and *soil temperature* is of opposite sign and lies both for the Loobos and the Tomelloso site as for the tower measurements and radio soundings in a range of 15 to $37 \text{ Wm}^{-2}\text{K}^{-1}$ (absolute values). Because at the Loobos site the heat fluxes are lower than at Tomelloso, sensitivity of evaporative fraction here lies within a range of 9 \%K^{-1} to 18 \%K^{-1} , whereas these values for the Tomelloso site are 3 \%K^{-1} to 8 \%K^{-1} (absolute values). The slight change in sensitivity towards the highest air temperature and towards the lowest soil temperature at the Tomelloso site can, just like the sensitivity changes at Loobos, be attributed to a switch from the correction function for an unstable to correction functions for a stable atmosphere. For the Tomelloso site the Massman model turns out to be more sensitive than the Blümel model. In the Netherlands there appears to be little difference between both models. Because errors in temperature measurements of 1K or more are readily made and because spatial variability of air temperature (which in contrast to the radiometric soil temperature is not measured by the satellite) also

contributes to uncertainty in the determination of the temperature difference (eq. 3.22, eq. 4.55), sensitivity of the algorithm towards temperature will prove to be important.

From appendix 3a and 3b it is clear the algorithm shows very little sensitivity towards *specific humidity*.

Sensitivity towards *wind speed* increases strongly towards lower wind speeds, except at the Loobos site for the sensible heat fluxes calculated by Bulk Atmospheric Similarity. Here a very small temperature difference limits the increase of sensible heat flux. The Loobos case with the measurements by radio sounding describes a stable atmosphere and the sensible heat flux, calculated by Bulk Atmospheric Similarity becomes less negative at lower wind speeds. In this case H_{rest} decreases at lower wind speed, which can be understood by looking at eq. 4.55. In a stable atmosphere soil temperature is lower than the air temperature, which results in a change of sign of all four fractions in the last term of eq. 4.55. Thus it acts in a similar manner as in an unstable atmosphere where soil temperature lies above air temperature. Here Bulk Atmospheric Similarity gives the adequate description of the physical process and SEBI cannot be used.

At very low wind speeds (for Spain below 1 ms^{-1} for tower measurements and below 3 ms^{-1} for the radio soundings) the algorithm starts to show a jittery behavior. The calculated values of heat fluxes below these limits can be changed by decreasing or increasing the tolerance and/or the number of iterations in the Broyden function. I.e. this effect occurs because the iteration of eq. 3.17, eq. 3.22 and eq. 3.23 does not lead to a convergence because if friction velocity gets close to zero, the Obukhov length will get close to zero. Subsequently both stability terms in eq. 3.23 and eq. 3.22 will get very large, which leads to a failing estimation of the sensible heat flux.

Within the chosen wind speed ranges observed sensitivities are considerable. For the tower measurement at Loobos an increase in wind speed of 1 ms^{-1} induces a decrease of latent heat flux of 20 Wm^{-2} and a decrease of evaporative fraction of about 0.1. For the tower measurement in Spain a similar increase in wind speed results in a decrease of latent heat flux and evaporative fraction of respectively about $40 \text{ Wm}^{-1}\text{s}^{-1}$ and 0.08 s^{-1} and an increase of sensible heat flux of about $40 \text{ Wm}^{-1}\text{s}^{-1}$. For the radio sounding these figures are a decrease of about $20 \text{ Wm}^{-1}\text{s}^{-1}$ and 0.04 s^{-1} and an increase of $20 \text{ Wm}^{-1}\text{s}^{-1}$.

Sensitivities toward incoming short wave and longwave radiation cannot be neglected. An increase of incoming radiation with 10 Wm^{-2} will cause an increase in latent heat flux of about 5 to 10 Wm^{-2} . Spatial fluctuations in radiation budget will occur because of clouds, height differences and reflections and (longwave) radiation from surrounding objects.

5.1.2 Sensitivity Analysis: Sensitivity towards Variability of Meteorological Data

In the previous section temperature difference and wind speed were identified as input parameters for which the SEBS algorithm shows appreciable sensitivity. Air temperature and wind speed are measured at meteo stations and radio soundings. Soil temperature is determined by satellite image or by measurement of outgoing longwave radiation at a meteo station (radiometric soil temperature is retrieved by applying Stefan-Boltzmann's law).

First of all data from meteo stations and radio soundings are compared. Because measurements are taken at different heights the potential air temperature from the meteo station is expected to be higher than the potential air temperature from the radio sounding. Wind speed at the tower is expected to be lower than higher up in

the atmosphere. In both cases data should however be well correlated. Wind direction should ideally be equal for tower measurement and radio sounding. If radio sounding sites and meteo station are at the same altitude, air pressure at ground level from the tower should coincide with the ground level air pressure from the radio sounding (i.e. from the measurement taken before the balloon has been set loose). Where radio soundings are taken at a lower altitude than the altitude of the meteo station, air pressure at ground level has been calculated by taking the altitude nearest to the meteo station ground level and retrieving the ground level pressure by applying the barometric height formula. In Appendix 3d the results of this analysis are represented in a graphical way. Furthermore for each combination a correlation coefficient r has been calculated.

Loobos and the site where the radio sondes are operated, i.e. de Bilt, lie 44 km apart. For the Loobos-de Bilt combination correlation overall is quite good. Potential air temperature (at PBL height) however lies above the potential air temperature measured at the tower. A look at the data from the soundings reveals logarithmic temperature profiles with a difference between ground and PBL temperature of mostly more than 5 K. Because a forest generally is cooler than the open space from which the radio sonde is operated, this effect could imply that the air temperature at Loobos is strongly influenced by the forest lying below the tower. Wind speed is rather well correlated ($r = 0.7$) in all cases but one (which occurs at very low wind speed), wind speeds from the sounding lie below the tower measurements. Wind direction is well correlated ($r = 0.8$) except for one outlier which stems from the same low wind speed measurement.

For Spain three combinations are tested: two radio sounding sites near Murcia and Madrid and the meteo station near Tomelloso. Murcia lies at an altitude of 61 m in the south east of Spain some 40 km from the coast and 245 km from Tomelloso. Madrid (altitude 631 m) and Tomelloso are 145 km apart and both are situated on the *Meseta*. For all combinations correlation is poor. In about half of all cases potential air temperature measured at the tower is lower than the radio sounding PBL-temperature. Wind speed measurements are only slightly correlated (for the Tomelloso-Murcia combination $r = 0.2$), wind direction for the Murcia-Madrid combination is negatively correlated ($r = 0.5$). A reason for this poor correlation could, apart from differences due to a larger spatial variability, be the much higher level of turbulence in Spain, compared to the Netherlands. I.e. measurements are taken at a scale on the low side of the spectral gap (§ 3.3) where, due to higher atmospheric forcing, in Spain variability could be higher than in the Netherlands. This however leaves the rather large differences in ground level air pressure unaccounted for (the Tomelloso-Madrid combination air pressure in Madrid is more than 1 kPa higher than in Tomelloso). Since tower measurements and radio soundings are operated independently, calibration differences in measurement equipment could at least for a part play a role.

In order to assess the impact of this variability of meteorological data on the SEBS algorithm, for one month the standard deviation (σ) of wind speed and potential air temperature of radio soundings and meteo stations is calculated. These calculations are carried out for the Loobos site and the Tomelloso site using the Massman algorithm for heat transfer. The standard deviation of soil temperature is calculated by taking the soil temperature of two adjacent measurements 10 minutes before and 10 minutes after 11.00 UTC. The rationale behind this is the expectation that in a rapidly changing environment (e.g. a soil that warms up quickly) differences between meteo station and scintillometer site will be more outspoken than in an environment

where virtually no changes take place. Hence calculated standard deviations for Loobos are 1.4 K (temperature difference) and 0.93 ms^{-1} (wind speed). For Tomelloso standard deviations are respectively 1.52 K and 1.4 ms^{-1} . Now a time series of available data of one month (Loobos, May 1997, Tomelloso, June 1999) is calculated, using a wind speed minus one standard deviation of the wind speed and a temperature difference minus one standard deviation of the temperature difference to establish a low limit for the sensible heat flux. In an analogous manner a high limit for the sensible heat flux has been calculated. In section 5.2.1 it has been discussed that in a stable atmosphere sensible heat flux becomes more negative with increasing wind speed. Thus where a stable atmosphere is measured for the calculation of the low limit of H from Bulk Atmospheric Similarity (depending on reference height either by BAS or ASL functions) the combined effect of variability is calculated by combining a wind speed plus one standard deviation of the wind speed and a temperature difference minus one standard deviation of the temperature difference. Since the algorithm cannot be used below wind speeds of 3 ms^{-1} (radio soundings, measurement at PBL height) or 2 ms^{-1} (tower measurements, see previous section), with a standard deviation of 1.5 ms^{-1} , days at which wind speeds lower than 4.5 ms^{-1} (radio soundings) or 3.5 ms^{-1} (tower measurements) occur must be discarded.

In appendix 3e the results of this analysis are represented. For each measurement the relative contributions from wind speed and temperature difference are indicated. For the Loobos site evaporative fractions are given, both from Bulk Atmospheric Similarity as from SEBI. Evaporative fractions from the Eddy devices higher than 2 or lower than -0.5 are represented as 2 and -0.5 respectively. For the Tomelloso site sensible heat fluxes calculated from Bulk Atmospheric Similarity as well as from SEBI are represented. Sensible heat fluxes from the scintillometer are represented according to the algorithm by which they are calculated (§ 4.9.2). Furthermore also available energy per square meter ($Q^* - G_0$) is depicted.

In general sensitivity towards a difference of one σ appears to be in the same order as the fraction or flux being calculated. For Loobos sensitivity with measurements at PBL-height is higher than with MOS-similarity, for Tomelloso these are approximately equal. Wind speed and temperature difference generally are of the same weight but sometimes (e.g. day 1 at Loobos and Tomelloso) temperature difference plays a greater role. Sensitivity in the series with the roughness length of 0.5 m is appreciably higher than in the series with the lower roughness. Of course an offset of 1 σ is somewhat ambiguous. However with the results of the comparison between tower measurements and radio soundings in mind, uncertainties in temperature differences and wind speed will rather be greater than 1 σ (1.5 K and 1.5 ms^{-1}).

5.2 Time Series

At the Loobos site outgoing longwave radiation and reflected short wave radiation are measured. Hence it is possible to calculate the soil temperature by invoking Stefan-Boltzmann's law, to calculate albedo from the ratio incoming and reflected short wave radiation and to apply SEBS apart from a satellite image. At the Tomelloso site this data is available also, but radiation measurements are carried out at a meteo station of the University Castilla-la Mancha some km apart from the scintillometer. Therefore and because variation of albedo values between days on the same hour of the day is smaller than the difference of albedo between meteo station (a mean value over the days of the time series of 0.1) and scintillometer site, for

Tomelloso a mean albedo value (0.3) from the ATSR images is used. Two time series have been calculated. In May 1997, July 1997 and September 1997 at 45 days data was available for the Loobos site (measured at 11.00 UTC). At the Tomelloso site in 1999 in April, May and June 40 days appeared to have a complete dataset for measurements at 11.00 UTC. Some of this data had to be discarded because wind speeds were below the limits which have been discussed in section 5.2.1 (e.g. in the time series of Tomelloso - data meteo station - 14 measurements have been discarded because of wind speeds lower than 1 ms^{-1}). Both Massman's model and Blümel's model have been elaborated and for the Tomelloso site time series are calculated for a roughness length for momentum transfer of 0.5 m (i.e. the roughness from the land cover database) and 0.084 m (i.e. the roughness from NDVI, eq. 4.59). In appendix 4 the results of the time series are represented. Evaporative fractions measured by eddy devices at the Loobos site (appendix 4a) and sensible heat fluxes measured by the scintillometer at the Tomelloso site (appendix 4b) are joined by a light gray line to improve the readability of the graph. This line does not have a physical meaning, i.e. it does not represent the course of evaporative fractions at interjacent time stamps. This also holds for the line indicating net radiation minus ground heat flux ('*Available Energy*') in appendix 4b. Evaporative fractions from eddy devices higher than 2 or lower than -0.5 are represented as 2 and -0.5 respectively. In the statistical analysis these values have been discarded. For the Loobos site measured and calculated evaporative fraction, measured sensible heat flux and H_{BAS} and measured latent heat flux and $I E_{SEBI}$ are represented in a scatter plot. For the Spanish site measured sensible heat flux, using the free convection formulation, is plotted with H_{BAS} and H_{rest} (eq. 5.3).

As statistical measure for error the root mean squared error (RMSE) or standard error of regression is taken. The RMSE is the standard deviation of the residuals (here: measured value minus calculated value) and represent the average error of prediction expressed in units of evaporative fraction, sensible heat flux or latent heat flux. With the scatter plots the line '*calculated entity*' = '*measured entity*' is represented. Furthermore for each data the result of linear regression is represented in the scatter plots by a dotted line. Coefficients of determination (i.e. the percentage of the variance in the calculated entity accounted for by the measured entity) together with the regression coefficient (r.c.) and intercept with the '*calculated entity axis*' are tabulated in table 5.1 and table 5.2. If errors are normally distributed, we expect the regression line to coincide with the line '*calculated entity*' = '*measured entity*'. In other cases systematic errors could occur. Therefore coefficients of determination should be evaluated together with intercepts and regression coefficients.

5.2.1 Time Series: Loobos

At the Loobos site L_{BAS} (eq. 5.6) always is higher than L_{SEBI} , and in most cases calculated evaporative fractions are higher than measured evaporative fractions. Both for meteo data from tower measurements and meteo data from radio soundings, calculations with the Massman and Blümel algorithm for heat transfer give almost similar results. Generally correlations are rather poor with an exception of H_{BAS} vs. H_{Eddy} with tower data, which has a coefficient of determination greater than 0.8. Results from radio soundings show a larger spread than results from tower measurements, i.e. a lower coefficient of determination. Both with tower measurements and radio soundings measured sensible heat fluxes H_{Eddy} are approximately five times as high as calculated sensible heat fluxes H_{BAS} (regression coefficient ≈ 0.2). Thus rather well correlated H_{BAS} and H_{Eddy} lead to poor

STATISTICS	RMSE	R ²	r.c.	intercept
Loobos - Tower Measurements - Massman				
EF Bas vs. EF eddy	0.469	0.04	-0.05	0.96
EF SEBI vs. EF eddy	0.272	0.01	-0.01	0.6
H BAS vs. H eddy	135.2	0.8	0.16	3.5
LE SEBI vs. LE eddy	93.7	0.45	0.97	53.6
Loobos - Tower Measurements - Blumel				
EF Bas vs. EF eddy	0.458	0.041	-0.06	0.95
EF SEBI vs. EF eddy	0.259	0.001	-0.02	0.57
H BAS vs. H eddy	132.2	0.81	0.18	3.77
LE SEBI vs. LE eddy	85.4	0.45	0.92	49.4
Loobos - Radio Soundings - Massman				
EF Bas vs. EF eddy	0.59	0.057	-0.25	1.128
EF SEBI vs. EF eddy	0.349	0.01	-0.09	0.737
H BAS vs. H eddy	144.59	0.259	0.189	-10.46
LE SEBI vs. LE eddy	123.72	0.332	0.959	75.54
Loobos - Radio Soundings - Blumel				
EF Bas vs. EF eddy	0.563	0.076	-0.22	1.12
EF SEBI vs. EF eddy	0.4139	0.014	-0.11	0.86
H BAS vs. H eddy	149.37	0.275	0.15	-9.82
LE SEBI vs. LE eddy	151.77	0.363	1.11	89.96

Table 5.1 - statistics time series Loobos

correlations of L_{BAS} with L_{Eddy} and L_{SEBI} with L_{Eddy} . Furthermore in consequence of this evaporative fraction L_{BAS} seems to be within a very small range. Measurement of heat fluxes by eddy devices requires sensors to measure vertical wind speed, temperature and specific humidity (see section 4.9.1). Eddy devices are mounted on the same tower at the same height as the equipment to measure ambient air temperature and wind speed. Thus at least for the results from the tower measurements it is not very likely that the difference between H_{BAS} and H_{Eddy} should be explained by a systematic difference from measurements. Instead it seems that Bulk Atmospheric Similarity under-estimates sensible heat flux at the Loobos site. In contrast to the sensible heat flux, measured and calculated latent heat fluxes are in the same order. Regression coefficients for latent heat fluxes are near unity, intercepts are between 50 and 100 Wm^{-2} , suggesting a systematic over-estimation of latent heat flux by SEBS.

RMSE of L_{BAS} is approximately twice the RMSE of L_{SEBI} , due to the small ratio of H_{BAS} and H_{Eddy} . For the same reason RMSE of H_{BAS} is greater than RMSE of L_{SEBI} , even if the coefficient of determination for H_{BAS} is higher than for L_{SEBI} . RMSE of the heat fluxes lies between 85 Wm^{-2} and 151 Wm^{-2} , with measured fluxes from -37 Wm^{-2} to 398 Wm^{-2} (mean measured sensible heat flux 129 Wm^{-2} , mean measured latent heat flux 139 Wm^{-2}).

Results from tower measurements of July and September are better than the results of May. Especially L_{SEBI} for May too high. In May mean temperature difference and mean wind speed are about the same as in July and September. However in May mean air temperature and mean soil temperature are approximately 5 K lower than in July and September.

5.2.2 Time Series: Tomelloso

In contrast to the site in the Netherlands at the Tomelloso site sensible heat fluxes calculated with the roughness length for momentum transfer from the Corine land cover database and Massman resistance to heat transfer are higher than the measured sensible heat fluxes. This applies for sensible heat flux calculated from Bulk Atmospheric Similarity (H_{BAS}) as well as sensible heat flux calculated from SEBI (H_{SEBI}), which is reflected by regression coefficients larger than unity and intercepts with the 'calculated sensible heat flux axis' above the origin. Sensible heat fluxes calculated with NDVI-roughness generally are a bit lower - with the meteo data from the tower and with the meteo data from the radio soundings with Blümel heat transfer - or are in the same order - radio soundings and Massman heat transfer - as compared to measured fluxes. In all cases sensible heat fluxes calculated with Blümel resistance to heat transfer are lower than those calculated with Massman heat transfer. With Massman heat transfer and Corine roughness for momentum on a considerable number of days calculated sensible heat fluxes exceed net radiation minus soil heat flux ('Available Energy'). Since this is physically impossible, calculated fluxes must be too high.

STATISTICS		RMSE	R ²	r.c.	intercept
Tomelloso - Tower Measurements - Massman					
Corine-z0m	H scint.free vs. H BAS	183.6	0.66	1.42	69.9
	H scint.free vs. H SEBI	159.9	0.61	1.01	136.2
NDVI-z0m	H scint.free vs. H BAS	63.3	0.6	0.8	37.2
	H scint.free vs. H SEBI	75.8	0.55	0.71	82.3
Tomelloso - Tower Measurements - Blümel					
Corine-z0m	H scint.free vs. H BAS	79.6	0.58	0.89	46.9
	H scint.free vs. H SEBI	92.5	0.49	0.73	100.3
NDVI-z0m	H scint.free vs. H BAS	70.3	0.62	0.64	30.9
	H scint.free vs. H SEBI	72.5	0.49	0.59	65.4
Tomelloso - Radio Soundings - Massman					
Corine-z0m	H scint.free vs. H BAS	215.4	0.44	1.56	55
	H scint.free vs. H SEBI	191.6	0.45	1.27	103.9
NDVI-z0m	H scint.free vs. H BAS	99.24	0.63	1.01	38.1
	H scint.free vs. H SEBI	104.55	0.6	0.91	69.9
Tomelloso - Radio Soundings - Blümel					
Corine-z0m	H scint.free vs. H BAS	83.2	0.4	0.91	34.8
	H scint.free vs. H SEBI	90.6	0.35	0.85	61.4
NDVI-z0m	H scint.free vs. H BAS	73.2	0.39	0.78	29.1
	H scint.free vs. H SEBI	81.9	0.31	0.72	48

Table 5.2 - statistics time series Tomelloso

Coefficients of determination are rather low and never exceed 0.66. Analogous to the Loobos time series, heat fluxes from tower measurements show a better correlation than heat fluxes from radio soundings. In all but one case with Massman resistance to heat transfer correlation between measured and calculated fluxes seems to be slightly higher as compared to the Blümel heat resistance.

RMSE's again are larger for all but one case with meteo data from radio soundings and lie between 63 Wm^{-2} and 215 Wm^{-2} with measured fluxes between 4.7 Wm^{-2} to 370 Wm^{-2} (mean measured sensible heat flux with free convection formulation = 195 Wm^{-2}). Because linear regression approximately coincides with the line 'calculated flux = measured flux', the coefficients of determination can be used to assess the relative error of calculated and measured fluxes. This error lies in the order of half of the measured quantity and with an exception of the NDVI roughness - Blümel heat transfer combination is larger for the results from tower measurements than for the

radio soundings. With the same exception, errors with 'Corine roughness' are about the same as errors with 'NDVI roughness'. On the face of it differences between results from tower measurement and meteo stations are larger for the Spanish site.

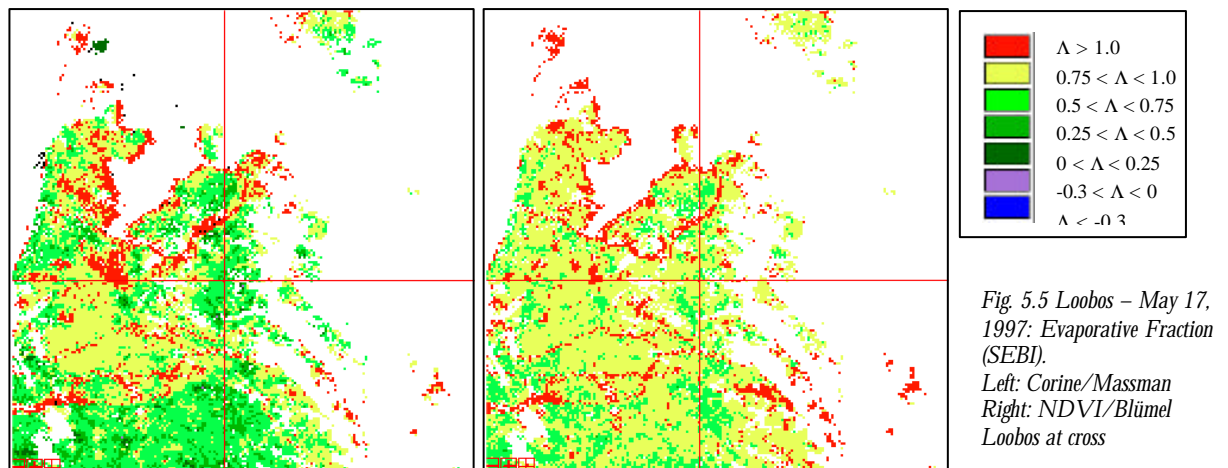
5.3 ATSR Data: Single Source

For Spain 19 ATSR images of 13 days from April 1999 till September 1999 have been processed. For the Netherlands 3 ATSR images - of May 17, August 17 and August 20, 1997 - have been processed. Theoretically this should yield respectively 25 and 6 data points. Due to too low wind speeds, malfunction of measurement equipment and cloud screening this maximum never is achieved. For instance for the Lleida site only from radio soundings complete data sets were available. No pixels have been discarded because of sensor saturation. For the Tomelloso site and the Badajoz site radio soundings from Madrid have been used, for the Lleida site soundings from Zaragoza and for the El Saler site soundings from Murcia have been used (fig. 5.1). For the runs using roughness for momentum from the Corine land cover database, aggregation from 100 m resolution to 1000 m resolution has been carried out by logarithmic averaging.

Similar to the time series ATSR images have been processed using roughness length for momentum transfer from the Corine land cover database as well as from NDVI (eq. 4.59) and resistance to heat transfer by the Massman algorithm as well as by the Blümel algorithm. The results are represented in appendix 5a (the Netherlands) and appendix 5b (Spain). Statistics are tabulated in appendix 6. Since each Dutch site has yielded only two data points, no statistical analysis is carried out for results of the Netherlands. Atmospheric correction is assessed by comparing albedo and soil temperature from satellite images with albedo and soil temperature from radiation measurements.

5.3.1 ATSR Data: Single Source – the Netherlands

Figure 5.5 shows two images of evaporative fraction using the Corine roughness for momentum / Massman resistance to heat transfer combinations. In the east of the area pixels are cloud-screened. Water surfaces which are not properly screened appear in the image with an evaporative fraction of more than unity. Thus the rivers Waal and Maas as well as the Randmeren (i.e. the lakes in between Flevoland and Gelderland) are recognizable. SEBS cannot be applied to water surfaces (for instance the ground heat flux should be parameterized in a different way). The areas to the north and the south east of Amsterdam also show Λ_{SEBI} of more than one. This also could be due to a large 'water surface content' of the pixel. An evaporative fraction above unity occurs if the normalized wet temperature gradient is larger than the normalized actual temperature gradient (eq. 4.55). Over land surfaces this could be associated with advective effects (i.e. the '*Oasis effect*' – warm and dry air moves into an area with colder and moist air, thus causing an evaporation larger than the theoretical limit).



From appendix 5a it becomes clear that analogous to the time series results from tower measurements show a smaller spread than results from radio soundings. On August 20 measured as well as calculated evaporative fraction is a bit higher for Fleditebos than for Loobos. Differences between measured and calculated evaporative fractions lie between 0 and 0.5, and are in the same order as RMSE's in the time series. Because only four ATSR points are available for validation, hence no conclusions can be drawn. Best results are achieved with the Corine roughness / Massman heat resistance combination. For the two sites the roughness length with the Corine database has been aggregated to 1.22 m, which with eq. 4.16 gives a vegetation height of 8.9 m. NDVI (eq. 4.59) gives a vegetation height of 1.54 m (Loobos) and 1.24 m (Fleditebos).

In table 5.3 radiometric soil temperature and albedo from radiation measurements and from ATSR images - i.e. the results of the atmospheric correction - are compared. Correlation coefficient for soil temperature is 0.61 and RMSE is 1.64 K.

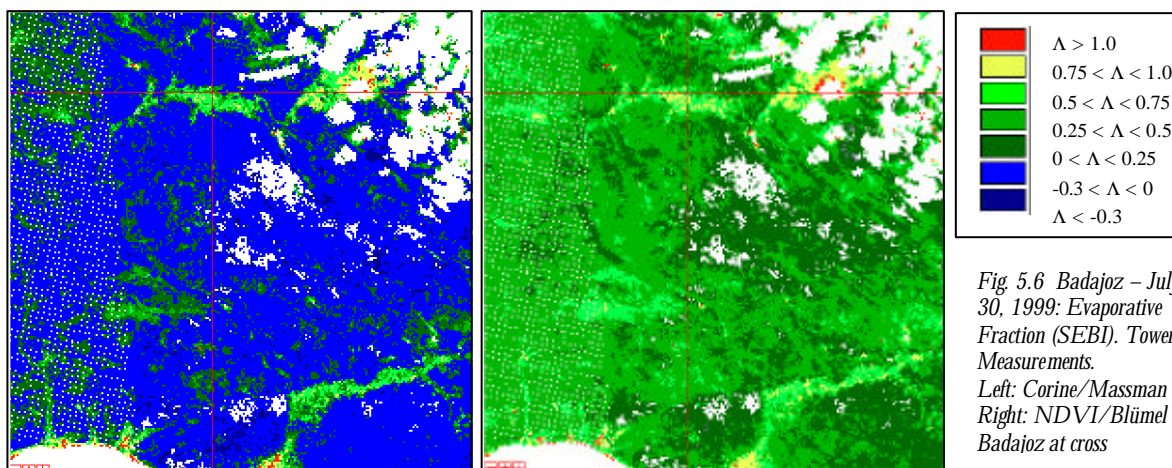
Loobos / Fleditebos	Rad. Soil Temp.		Albedo	
	Rad.M.	ATSR	Rad.M.	ATSR
5-17-97	300.8	301.7	0.08	0.13
8-20-97	299.7	301.3	0.09	0.11
8-17-97	301.2	303.9	0.16	0.16
8-20-97	300.5	300.1	0.17	0.15

Table 5.3 – Comparison between radiometric soil temperature and albedo from Radiation Measurements and from ATSR Images.

Now let us assume that the validity of the sensitivity analysis can be extended to all measurement days. For Fleditebos on August 17, with the Corine roughness / Blümel heat transfer combination a sensible heat flux of 62 Wm^{-2} is calculated. With a sensitivity of $30 \text{ Wm}^{-2}\text{K}^{-1}$ (see appendix 3b) a soil temperature error of 2.7 K can cause an error in the calculated sensible heat flux of more than 130%. For albedo correlation coefficient and RMSE are respectively 0.86 and 0.03. For Loobos on May 17 with the Corine roughness / Blümel heat transfer combination a sensible heat flux of 79 Wm^{-2} is calculated. With a sensitivity of $4 \text{ Wm}^{-2}\%$ an albedo error of 0.05 would cause an error in the calculated sensible heat flux of approximately 25 %. There are however too few points to make any final conclusions about the quality of the atmospheric correction.

5.3.2 ATSR Data: Single Source – Badajoz

Badajoz is situated near the river Guadiana, its riverbed clearly discernable on figure 5.6. Also the riverbed of the Guadalquivir in the southeast and the mouth of the Rio Guadiana to the west of the Guadalquivir can be seen. The white areas in the northeast are clouds. The spots on the left of the picture are an artefact of the geometric correction procedure.

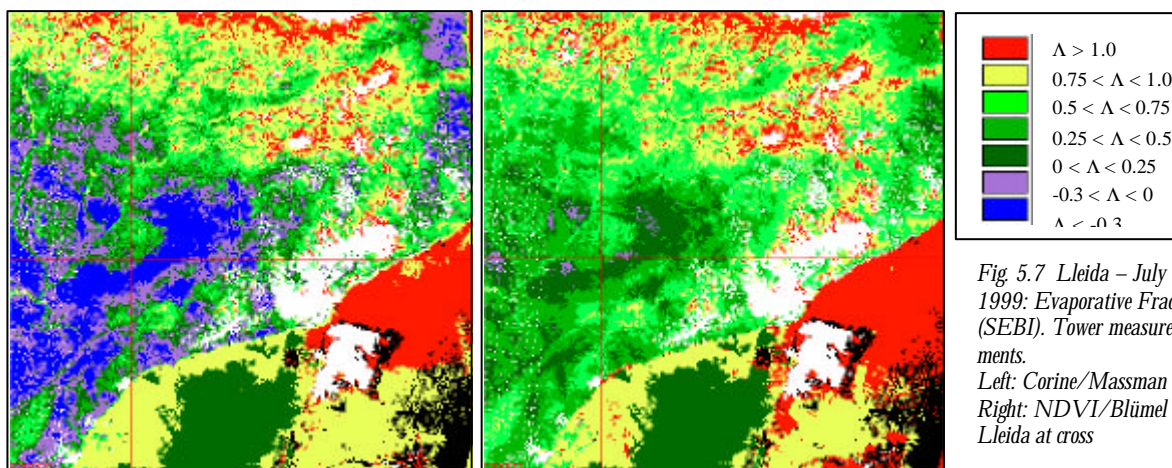


From appendix 5b it becomes clear that for the three data points all calculation methods give sensible heat fluxes lower than net radiation minus soil heat flux. Sensible heat fluxes calculated with Bulk Atmospheric Similarity always are lower than sensible heat fluxes calculate with SEBI. In all but one case – H_{BAS} July 30, radio sounding – calculated sensible heat fluxes with the Corine roughness length / Massman heat transfer combination are higher than measured fluxes. kB^{-1} -factors are approx. 5 for the Massman method and 7.5 for the Blümel algorithm. In fig. 5.6 for the major part of the left image – the Corine/Massman combination – calculated evaporative fractions are less than zero. This does not represent a condensation process but is a result of the calculation of a sensible heat flux larger than net radiation minus soil heat flux. In fact for practical purposes evaporation should be set equal to zero. In almost all cases NDVI roughness gives a lower RMSE than roughness from the Corine land cover database. For the Badajoz pixels NDVI and Corine land cover estimate roughness lengths of respectively 0.086 m and 0.21 m. Hence vegetation heights are 0.66 m and 1.51 m. The decrease of evaporative fraction with 0.25 is consistent with the sensitivity analysis for the Tomelloso site (appendix 3). Though with three data points statistical significance is small, the high coefficients of determination for the tower measurements nevertheless are remarkable.

5.3.3 ATSR Data: Single Source – Lleida

Figure 5.7 shows an image of evaporative fraction of the area around Lleida. The Pyrenees are situated in the north and show, both with the Corine/Massman and NDVI/Blümel combinations high evaporative fractions. Since no orographic correction has been made, it is likely that roughness lengths for momentum in these mountains are too low, causing too low an estimate for sensible heat flux. Water

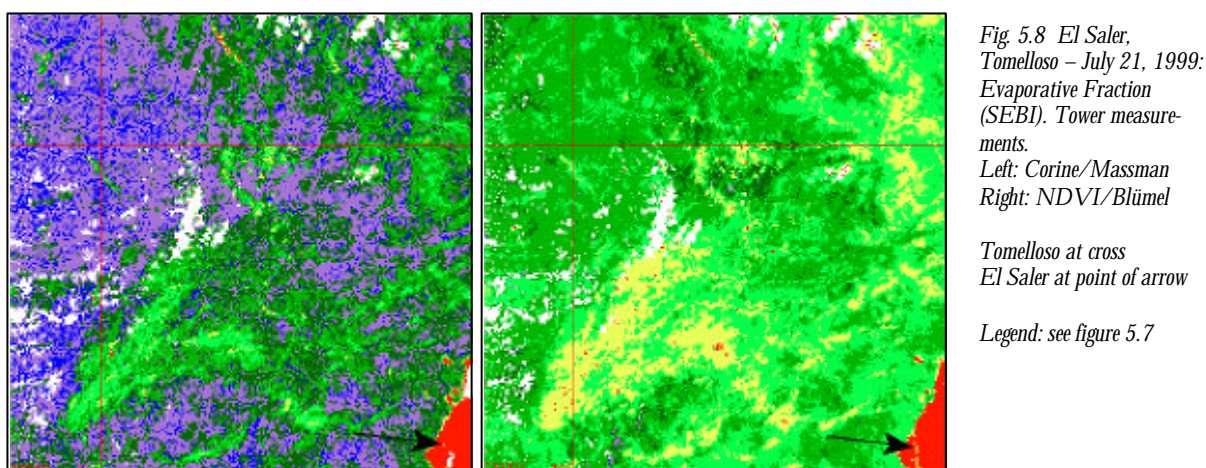
surface screening for this ATSR image hasn't worked properly. Because sea water temperature was higher than soil temperature in the Pyrenees, the threshold in the 12 μm channel (see section 4.1.1.) could not be set to distinguish water and land surface pixels. Also the maximum reflectance in the 0.67 μm channel could not be lowered without losing the pixels around the Lleida area (both sea and land pixels show a reflectance of about 29%).



The results for the Lleida data points show a similar behavior as the Badajoz data points, although calculated heat fluxes are a bit closer to the available energy per square meter. H_{BAS} is smaller than H_{SEBI} . NDVI roughness shows a smaller RMSE as compared to Corine roughness. Mean roughness length across the scintillometer path is 0.084 m with NDVI and 0.27 m with Corine land cover database. Hence vegetation heights are 0.62 m and 2.02 m. The difference between results with the Blümel algorithm and Massman algorithm seems to be more pronounced than the difference between the two roughness length models. RMSE's are smaller for the Blümel algorithm than for the Massman algorithm. kB^{-1} -factors are approx. 5 for the Massman method and 8.5 for the Blümel algorithm.

5.3.4 ATSR Data: Single Source – El Saler

Figure 5.8 represents an image of evaporative fraction of Tomelloso and El Saler. Comparing fig. 5.2 and fig 5.8 shows that both for the Corine/Massman and the NDVI/Blümel combination evaporative fractions of more than unity is calculated. A



few pixels of the elongated forest have evaporative fractions between 0.75 and 1.0. Unfortunately no wind direction data were available from the measurement tower. Therefore it could not be assessed if on days with relative low evaporation wind direction preferably was east (i.e. with sea winds the oasis effect will be absent). For El Saler measured evaporative fractions are much lower than the calculated ones – RMSE's from 0.32 up to 0.63 – and coefficients of determination are low (0.02 up to 0.34). k_B^{-1} -factors are approx. 5 for the Massman method and 5.5 for the Blümel algorithm.

5.3.5 ATSR Data: Single Source – Tomelloso

Since measured sensible heat fluxes and available energy are rather close, for the Tomelloso site evaporation will be low. Except for September 29, sensible heat flux calculated by the Corine roughness / Massman heat transfer combination exceed available energy, sometimes by more than a factor two. Sensible heat flux calculated with the NDVI-roughness length is appreciably lower than sensible heat flux calculated by the Corine roughness. On June 22 a difference between sensible heat flux calculated with Bulk Atmospheric Similarity/Corine roughness/Massman heat transfer and SEBI/NDVI roughness/Blümel heat transfer was calculated of 560 Wm^{-2} (available energy 308 Wm^{-2}). With a roughness length from the Corine database, the RMSE's with the Blümel method are 90 up to 260 Wm^{-2} lower as compared to the Massman algorithm. RMSE's with NDVI-roughness length are approx. $80 - 90 \text{ Wm}^{-2}$. k_B^{-1} -factors are approx. 5 for the Massman method and 8 (Corine roughness) and 6 (NDVI roughness) for the Blümel algorithm. Coefficients of determination are rather low for the results with tower measurements ranging from 0.33 to 0.62 and approximately zero for the results with radio soundings. The roughness length is 0.012 m with NDVI and 0.42 m with Corine land cover database. Hence vegetation heights are calculated as 0.087 m and 2.81 m.

As compared with the time series RMSE's for the ATSR images are higher with an exception of the radio sonde/NDVI/Massman combination, which however has a coefficient of determination for the ATSR images close to zero. With the tower measurements coefficients of determination for ATSR data generally are appreciably lower than for the time series.

Tomelloso	Rad. Soil Temp.		Albedo	
	Rad.M.	ATSR	Rad.M.	ATSR
4-13-99	301.9	306.0	0.19	0.31
6-6-99	308.5	314.8	0.18	0.32
8-28-99	315.4	317.0	0.19	0.33
9-16-99	306.1	307.4	0.16	0.31

Table 5.4 – Comparison between radiometric soil temperature and albedo from Radiation Measurements (Univ. la Mancha) and from ATSR Image (Tomelloso site).

At 4 out of 9 days with ATSR data, radiation equipment has been functioning properly. Therefore a comparison between radiometric soil temperature and albedo from radiation measurements and ATSR data only comprises four data points. Ground cover of the meteo station of the University Castilla la Mancha is grass. Since the ATSR pixel of the meteo station only for a very small part is composed of this ground cover, ground temperature and albedo cannot be validated. Therefore only a comparison is made between the data from the meteo station and the results

from SEBS at the Tomelloso site with the ATSR images. The radiometric soil temperature of the Tomelloso pixel is 1.3 to 6.3 K warmer than the temperature at the meteo station with RMSE of 3.9 K and the albedo at Tomelloso is 0.12 to 0.15 higher with RMSE of 0.14.

5.3.6 ATSR Data: Single Source – Discussion

The SEBS algorithm needs a number of input variables which partly must be measured on the ground and partly can be determined from the satellite image. Furthermore within the algorithm a number of parameterizations are modeled (e.g. the soil heat flux by eq. 4.57, vegetation height by eq. 4.16). From the sensitivity analysis it becomes clear that SEBS shows appreciable sensitivity towards all input variables but specific humidity. Some variables can be measured well and will show little or predictable spatial variability. For instance air pressure on a scale of 100 km generally will change mainly through altitude differences. If large emissions in the atmosphere are absent, short wave clear sky incident radiation will mainly change through latitude. Some variables show a great spatial variability but can be estimated by remote sensing. Albedo, NDVI, fractional vegetation coverage and soil temperature are estimated from the ATSR image. With increasing albedo and fractional coverage sensitivity increases but in most cases these two effects will counteract (i.e. an increasing albedo often coincides with a decreasing fractional coverage). If NDVI (and wind speed) become very small sensitivity increases dramatically. Of all remotely sensed variables soil temperature shows the greatest sensitivity. For the Dutch sites a comparison between ground measurement and ATSR images shows for two of the four points an estimate within 1 K. Nevertheless this can cause a significant error in the estimation of the sensible heat flux. The surface of the Tomelloso site apparently differs from the surface of the meteo station to a high degree. If the results of the time series are compared with the results of the ATSR images with the 'Corine/Massman' combination, sensible heat fluxes calculated with Bulk Atmospheric Similarity for ATSR are 167 Wm^{-2} higher (mean value) and evaporative fraction by SEBI is 0.39 lower (mean value). The figures for the combination of NDVI roughness and Blümel heat transfer are respectively 80 Wm^{-2} higher and 0.39 lower. If the difference of surface properties is considered as the only source of error in establishing soil temperature, then calculated sensible heat fluxes in the time series for Tomelloso are systematically too low.

Although measurement of air temperature and wind speed is rather easy, especially the latter shows an appreciable spatial variability. A comparison between tower measurements and radio soundings shows that in the Netherlands there is a reasonable correlation between the two data sets. In Spain however with wind speed and especially with wind direction data of tower measurements and radio soundings only are weakly correlated. For air temperature the correlation is stronger but errors nevertheless are considerable. Since SEBS is very sensitive to both wind speed and air temperature, errors from wind speed and air temperature measurements will have a major impact on the calculated heat flux. The systematic poorer results with radio soundings, in the time series as well as with the satellite images, will for an important part be due to this error.

Roughness length for momentum transfer z_0 and roughness length for heat transfer z_{0h} cannot be measured directly and show a great spatial variability. Sensitivity of SEBS towards both variables is considerable. In table 5.5 results with roughness length z_0 from NDVI and Corine land cover are tabulated. From the information about the crops being grown in the Badajoz area it is difficult to decide whether

NDVI roughness or Corine roughness is the better. The same applies to the Lleida site. Fruit trees will be higher than 2 m, alfalfa will be lower than 0.62 m. At the Tomelloso site measured NDVI is small. A resulting vegetation height of nearly 9 cm certainly will be too low, even for a non-irrigated vineyard. On the other hand the z_0 from the Corine land cover database seems too high. For the forested strip at El

	NDVI	z0m		vegetation height	
		NDVI	Corine	NDVI	Corine
Badajoz	0.47	0.086	0.21	0.66	1.51
Tomelloso	0.18	0.012	0.42	0.087	3.08
Lleida	0.48	0.084	0.27	0.62	2.02
El Saler	0.43	0.07	0.04	0.48	0.30
Loobos	0.7	0.21	1.22	1.54	8.98
Fleditebos	0.64	0.17	1.22	1.24	8.98

Table 5.5 – Comparison between roughness lengths from NDVI and Corine land cover. Vegetation height from eq. 4.16

Saler both NDVI and Corine land cover produce vegetation heights far too low. With the NDVI method this will be due to the fact that the ATSR resolution is too coarse to produce pixels that are entirely made up of forest. Comparing figure 5.2 and figure 5.8 it can be seen that each pixel of the forested area for a large part is made up of salt marshes, rice fields, beaches or sea. With the Corine land cover method a similar effect takes place: with the aggregation large parts of adjacent land cover classes are incorporated in the El Saler pixel. In the Netherlands vegetation heights determined by NDVI clearly are too low. Vegetation heights of approx. 9 m seem to be of the right order. Since green pastures and forests can have the same NDVI it is obvious that for high vegetation the NDVI method is less suited. On the other hand there are problems associated with the use of land cover information to determine roughness length for momentum as well. Land cover information is very general. Vines in a semi arid area probably will be lower and smaller than vines in a cooler and moister environment. Early in the growing season plants will have less leaves and will be smoother than later up in the year. Plant diseases or drought can cause vegetation to be less dense. Land use can change quicker than updates on the database are performed.

The alternative aggregation methods discussed in section 4.6 all produced equal or higher roughness lengths than logarithmic averaging. For Spain larger roughness lengths would produce larger sensible heat fluxes. Although from literature (e.g. Stull, 1999) too low roughness lengths could be expected, with the underlying results nothing would be added to the understanding of the underlying physical process by applying larger roughness lengths. For this reason only logarithmic averaging has been elaborated. In the Netherlands, Loobos and Fleditebos pixels are aggregated from pixels of one land cover class, i.e. forest. Therefore no other aggregation methods are tested for the Netherlands either.

Roughness lengths for heat transfer z_{0h} always are smaller with the Blümel algorithm as compared with the Massman model. For the Netherlands this is different from the time series where no major differences between results with Blümel and Massman algorithm were found. Since from the time series it is clear that kB^{-1} can show considerable variation for a point on different days, and because for the Dutch sites only four points are available, no final conclusions can be drawn. The effect of a higher kB^{-1} factor in the Blümel model towards calculated heat fluxes seems to be more outspoken at higher available energy levels and is most pronounced at the Tomelloso site, and the least at the Badajoz site. I.e. at these high energy levels the Blümel algorithm seems to prevent the calculated heat fluxes to exceed available energy. Variability from pixel to pixel is much greater with the Blümel than with the

Massman method. This is illustrated in appendix 7 by a South-North profile across Badajoz of kB^{-1} . In table 5.6 mean kB^{-1} factors over the scintillometer path and kB^{-1} factors at the tower where the eddy devices are situated are given. Because roughness lengths for momentum are smaller, the kB^{-1} factors for the NDVI roughness are smaller than for the Corine roughness. kB^{-1} factors for small fractional cover (Spain) only are slightly lower than for large fractional cover (the Netherlands). A small decrease of kB^{-1} nevertheless means a considerable decrease of z_{oh} . Since fractional cover in the Netherlands is below 0.78 (see eq. 4.24) but considerably higher than in Spain, with the Blümel heat transfer a larger difference could be expected. Since so many variables are involved, kB^{-1} factors cannot be measured, and very few points are available it is not possible to decide which algorithm for determination of resistance to heat transfer performs best.

kB^{-1} factors	Massman		Bluemel	
	NDVI	Corine	NDVI	Corine
Badajoz	4.5	5.0	7.0	8.0
Tomelloso	5.0	5.0	6.0	8.0
Lleida	5.0	5.0	8.0	9.0
El Saler	4.5	4.5	6.0	5.5
Loobos	4.5	6.0	7.0	9.0
Fleditebos	4.5	6.0	7.0	9.0

Table 5.6 – Comparison between kB^{-1} factors from Massman and Blümel model with roughness for momentum from NDVI and Corine land cover

A number of parameters (e.g. Leaf Area Index, Leaf width, ratios of soil heat flux to net radiation for full canopy and bare soil) are not assessed in this project. It cannot be ruled out that especially soil heat flux should be parameterized differently for different soil types.

If the results for El Saler can be discarded, we see SEBS to have a tendency to underestimate evaporation in Spain and overestimate evaporation in the Netherlands. This applies to the Bulk Atmospheric Similarity part as well as the SEBI part of SEBS. Since ATSR overpass in the Netherlands is approx. three quarters of an hour before the radio sounding, measured air temperature from radio sonde will in most cases be a bit too high, and partly could explain the underestimation of evaporative fraction in the Netherlands. This however doesn't apply to measurements in Spain nor to tower measurements in the Netherlands. The reason for these systematic errors is difficult to identify, but since modeling of atmospheric instability is used in both Bulk Atmospheric Similarity and SEBI, this could be a first aspect to look into. Footprints of measurements differ between eddy devices and scintillometers. Also scintillometer paths vary in length, so footprints between different scintillometer measurements vary also. It cannot be concluded that the Tomelloso site with a scintillometer path approx. equal to the ATSR resolution shows a better performance than the sites with larger footprints (Badajoz and Lleida) or with smaller footprints (Loobos, Fleditebos and El Saler).

5.4 ATSR Data: Parallel Source

With the separation of soil and foliage temperatures three masks are used to discard clouded pixels in either view angle and to mask pixels in very homogeneous terrain. Therefore compared with the single source model less data points are available. In the Netherlands no separation has been achieved because of homogeneity, i.e. with all land pixels very small temperature differences indicate that per pixel only a very small bare soil part was 'seen' by the satellite. For the El Saler site no data points are

available either. Due to the low pass convolution (see section 4.1.6) the pixels in the forested strip are smoothed with pixels from rice fields and salt marshes to such an extent that temperature difference between forward and nadir view become less than 0.5 K. For the Badajoz, Lleida and Tomelloso sites respectively 31%, 64% and 78% of the pixels at the scintillometer path has a temperature separation. The results of the parallel source model are given in appendix 8, the statistical analysis can be found in appendix 9.

5.4.1 ATSR Data: Parallel Source – Badajoz

Analogous to the single source model the results from the tower measurements are much more in line with the scintillometer measurements than the results with the radio soundings. Flagging of pixels (see section 4.7) only has effect on the results with the roughness length from the Corine land cover database, because here sensible heat flux for bare soil exceeds available energy. With the tower measurements on two of three days with Corine roughness sensible heat flux from parallel source model is larger than sensible heat flux from the single source model (either by BAS or by SEBI). Lowest calculated sensible heat fluxes in most cases are calculated by single source BAS. Generally RMSE's for the parallel source (no flag) results are higher as compared with the single source results with an exception for the sensible heat fluxes calculated from SEBI with NDVI roughness. In the latter cases however regression coefficients are lower and intercepts are further away from unity than in the single source results. Generally coefficients of determination for the parallel source model are lower than for the single source model.

5.4.2 ATSR Data: Parallel Source - Lleida

Sensible heat flux calculated by single source SEBI in all cases is higher than the double source heat fluxes. In 10 out of 16 combinations with single source BAS lowest sensible heat fluxes are calculated. Only on June 19 and July 15 sensible heat flux for bare soil exceeds available energy. RMSE's for sensible heat fluxes calculated by SEBI are considerably lower for the double source model, whereas coefficients of determination are approximately the same or higher. For sensible heat fluxes from Bulk Atmospheric Similarity, coefficients of determination in the parallel source model on all four days are higher, although, except for the Blümel/NDVI combination, RMSE's are higher as well. In general the parallel source seems to perform a little better than the single source model.

5.4.3 ATSR Data: Parallel Source – Tomelloso

In figure 5.9 two images of evaporative fraction from SEBI with the Corine roughness length / Blümel heat transfer combination illustrate the effect of setting sensible heat fluxes higher than available energy equal to available energy. In the left figure, nearly all pixels with a positive evaporative fraction have a bare soil sensible heat flux below available energy and stay unchanged in the right figure. All pixels with a negative available energy however stem from situations where bare soil sensible heat flux exceeds available energy and get a small positive evaporative fraction in the right figure. Furthermore the effect of the 5 by 5 and 3 by 3 convolution filters is clearly noticeable as compared with figure 5.8.

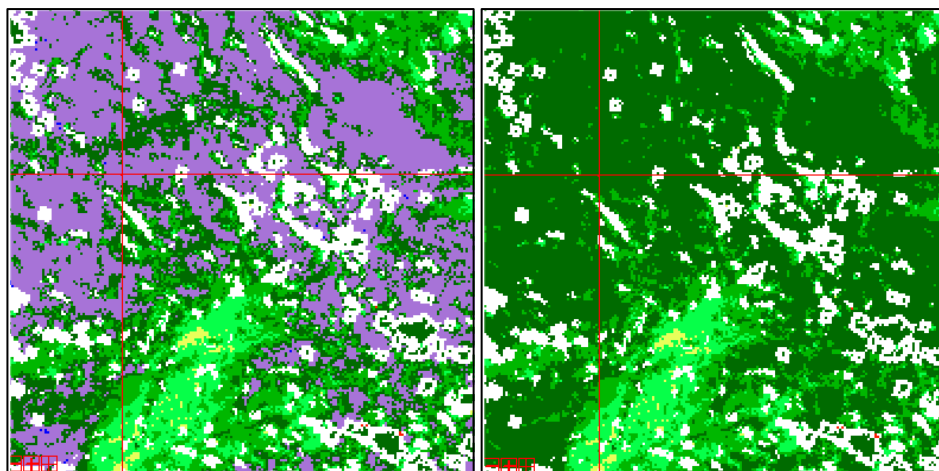
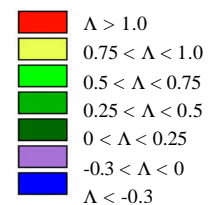


Fig. 5.9 Tomelloso (at cross) – August 28, 1999: Evaporative Fraction (SEBI, Corine/Blümel combination) with parallel source model. Tower measurements. Left: non-flagged Right: flagged



With the Corine/Massman combination parallel source sensible heat flux always is higher than the corresponding single source heat flux. Flagged values however are with the tower data always lower than the single source results and with the radio soundings 32 times out of 48 combinations. RMSE's for all non-flagged parallel source Corine roughness combinations are higher than the corresponding single source values. All other combination (40) show a lower RMSE for the parallel source algorithm. Parallel source coefficients of determination however are lower for all but three cases with the tower data but higher for all cases with the radio soundings. Regression coefficients for non-flagged Corine roughness parallel source combinations are always higher than unity whereas flagged parallel source combinations give regression coefficients lower than unity (i.e. with increasing measured values calculated sensible heat fluxes stay behind). Intercepts with single and parallel source models lie in the same order.

5.4.4 ATSR Data: Parallel Source – Discussion

If single source and parallel source results are compared one should bear in mind that with the parallel source results not all pixels on and near the scintillometer path contribute. If masking occurs from the homogeneity filter, then either parallel source sensible heat fluxes are too low if fully vegetated pixels are masked or too high if fully bare soil pixels are masked. For Spain neither possibility can be ruled out. At the site with the lowest fractional vegetation coverage – Tomelloso –, the parallel source sensible heat flux always is higher than the corresponding single source sensible heat flux. At the two other sites sensible heat flux of the parallel source model often lies in between single source sensible heat flux from Bulk Atmospheric Similarity and SEBI. Since the bare soil part is modeled identical for all three sites and for the two roughness methods, it is remarkable to see the strongest influence of the vegetation part occurs at the site with the lowest fractional vegetation coverage. Apparently with a roughness length from Corine land cover even for the vegetation at Tomelloso a sensible heat flux is calculated larger than the available energy. This could mean that the temperature difference is estimated too high, but more likely is that roughness length for momentum should be taken smaller.

Although it is difficult to draw conclusions on the basis of three, four and six data points respectively, by looking at the statistics it is hard to decide whether the parallel source model is an improvement compared to the single source model. For Badajoz

single source results seem to give a better fit to the scintillometer data, for Lleida the parallel source model generally seems to perform a little better than the single source model. Especially for the results with NDVI roughness and radio sounding data at the Tomelloso site the parallel source model seems to outperform the single source model. However, even in this case correlation between measured and calculated heat fluxes still is rather poor. If only results with roughness lengths from Corine land cover are considered, decrease of RMSE's with the flagging of the results is considerable. If flagged sensible heat fluxes are compared with available energy – which in fact is a better way of comparing both data sets, i.e. by putting sensible heat flux equal to available energy in those cases where a sensible heat flux higher than available energy is estimated – this decrease is less spectacular. Nevertheless in contrast to the single source model, the parallel source model in these cases gives a physically based estimate of evaporation.

6 Conclusion

One of the objectives of this project has been to validate single source and parallel source SEBS with the use of existing data sets. In general validation of results from non stationary satellites is a difficult task. On the ground often measurement sites at low spatial distribution are available which offer data, often at high temporal resolution. The satellite however has a high spatial resolution – this of course is also the power of remote sensing – but non-geostationary satellites like ERS only deliver one image during daylight each day. Furthermore numerous variables and parameters are involved, which make it difficult to isolate a key variable or parameter.

The algorithm appears to show appreciable sensitivity towards all input variables except specific humidity. Sensitivity is not constant throughout the range in which variables are varied, and are dependent on atmospheric conditions, e.g. atmospheric stability. For some variables, e.g. wind speed and NDVI, sensitivity increases dramatically if the variable gets close to zero. At wind speeds below 2.5 ms^{-1} with data from radio soundings and below 1.5 ms^{-1} with data from tower measurements, the algorithm cannot be used. Sensitivities in Spain appear to be larger than in the Netherlands. If an input variable is easy and precisely to measure and shows little spatial variation, a large sensitivity however does not impose a major difficulty. SEBS is sensitive towards air pressure, but in an area without major altitude differences, this sensitivity will not cause a large error. Where altitude differences are important, a DEM could be used. Air temperature and wind speed are identified as the ground based measured input variables, for which SEBS shows greatest sensitivity. If NDVI is not below 0.1, soil temperature appears to be the most important remotely sensed input variable in this respect. If these three input variables are assessed together by running SEBS with data from different meteo stations and radio soundings the importance of a precise measurement of them is confirmed.

Throughout this study, in almost all cases in the Netherlands as well as in Spain the results with data from tower measurements gave a lower RMSE and a higher coefficient of determination as compared to the results with data from radio soundings. If the tower measurements are considered to give an accurate description of temperature and wind speed at the spot, either Bulk Atmospheric Similarity at PBL height works less well as compared to the Monin Obukhov Functions for tower height or the data from radio soundings is less representative for the measurement site. From a comparison between temperature, wind speed and wind direction at tower measurement and radio sounding sites, one can conclude that certainly for Spain at least the latter is the case.

For the Netherlands data from tower measurements and radio soundings show a better correlation but here PBL potential temperature is higher than tower potential air temperature at measurement height. This leads to the conclusion that radio soundings are less suited to for wind speed and air temperature input than data from tower measurements. Since the logarithmic profile only is valid for the column of air above the measurement site this poses the problem how to obtain PBL data for the whole area. One way to solve this would be to use Regional Atmospheric Climate Model (RACMO) data. This data of 50 km resolution is generated from measured input and a predictive model.

With tower measurements at the Loobos site calculation of sensible heat flux is rather well correlated with sensible heat flux measured by eddy device, but shows too

low a response. This could be caused by a systematic underestimation of sensible heat flux by Bulk Atmospheric Similarity (both BAS and MOS functions show a similar tendency). This lowered response of sensible heat flux destroys the correlation in evaporative fraction. Therefore and in spite of the advantage of neutralizing footprint effects, some caution should be taken with the assessment of the algorithm only by a composed entity like evaporative fraction.

Roughness length for momentum for high vegetation cannot be determined by NDVI without any further information of vegetation height. Not surprisingly the runs with a roughness length from the Corine land cover database for the Netherlands resulted in a closer fit with measured fluxes than the results with roughness lengths estimated from NDVI. For the Spanish sites the NDVI determined roughness outperformed the results with the Corine roughness length. For Badajoz and Lleida it proved to be difficult to determine which roughness height was the better. For Tomelloso with a more uniform vegetation, the NDVI roughness seems too low whereas the Corine roughness seems too high. Since differences between sensible heat flux determined by NDVI and Corine roughness often are more than a factor two, this forms a striking illustration of the sensitivity of SEBS towards this attribute of the earth's surface. At the same time, an adequate determination of roughness for momentum is one of the most urgent problems to be tackled. Although an abundant amount of literature is available on the subject, it remains hard to solve. The pros and cons of determining roughness length from a land cover database already have been discussed in section 5.4.6. A land cover scheme however can be improved with information from the satellite image. For instance from fractional vegetation coverage a vegetation density filter could be applied and from NDVI a season correction factor could be constructed.

The effect of an increase of roughness length in the process of aggregation from patch to terrain level (e.g. Hasager et al., 1999) could not properly be looked into because differences from aggregation methods only would add to the already surplus roughness length from logarithmic averaging. Therefore only logarithmic averaging on the Corine land cover database has been applied.

In general the Blümel method for resistance to heat transfer produced lower roughness lengths to heat transfer as compared with the Massman algorithm. Also variability from pixel to pixel with the Blümel method seems higher. In both methods kB^{-1} factors for the Netherlands and Spain are in the same order which means that, as expected, roughness length to heat transfer is lower in Spain than in the Netherlands. Furthermore kB^{-1} factors are for both countries considerable higher than the often used value of 2.3 (i.e. a ratio of both roughness lengths of 10). Therefore the conclusion can be drawn that for the Netherlands in a number of cases a lower kB^{-1} factor would have resulted in a better fit with measured values, but for Spain the higher kB^{-1} factor means an improvement. Due to the uncertainty in the determination of the roughness length for momentum transfer, it is impossible to draw conclusion about which algorithm performs better. The decrease of the kB^{-1} factor with the Blümel algorithm at the Loobos site should be further looked into.

Besides input variables there are a number of parameters in SEBS which are not looked into in this study but could exert effects on the estimation of evaporative fraction. Emissivity, partition factors to estimate ground heat flux and the factor to make a conversion from roughness length to vegetation height are a few. In general the conclusion can be drawn that SEBS is very sensitive to a number of input variables. This sensitivity could however reflect a physical reality. Both Bulk Atmospheric Similarity and SEBI however are not bound by available energy. It appeared that in conditions with large temperature differences between surface and

ambient air, negative evaporative fractions and sensible heat fluxes higher than the available energy per square meter are calculated. Here clearly the response of the algorithm on temperature difference is too high. From this study it can not be decided whether this overestimation of sensible heat flux stems from too high roughness lengths or that Bulk Atmospheric Similarity should be parameterized differently. The tendency of underestimation of sensible heat in the Netherlands and the overestimation of sensible heat in Spain certainly focuses attention on the parameterization of the stability functions.

Unfortunately only for a few points an assessment of atmospheric corrections has been possible. For the Netherlands a tendency can be seen towards the ATSR retrieved temperatures to be higher than the temperatures from radiation measurements at the tower. In Spain this is also the case but here the difference is much larger. Both albedo and temperature suggest a much less vegetated surface with the ATSR data. Since scintillometer site and radiation measurements are carried out at different sites this could well be the case. At the same time it means that the time series for Tomelloso are calculated with systematically too low a surface temperature. Thus calculated sensible heat fluxes in the time series are too low, which could explain higher RMSE's with the ATSR results but does not explain the lower coefficients of determination. Although it is dangerous to draw conclusions on the basis of so little data points, statistics suggest errors from atmospheric correction other than due only from temperature retrieval.

A drawback in this project has been the need to retrieve information from different datasets. At El Saler and in the Netherlands eddy devices are used, at the other sites scintillometers are installed. In some cases all measurements are carried out at the measurement site itself, in other cases measurements from stations nearby are used. A wide variety of measurement equipment is deployed. Since sensitivity is so large, extreme attention should be paid to the calibration of measurement equipment. At some instances (e.g. the air pressure measurements in Spain) there is serious doubt about this calibration.

The hypothesis that, because of their path lengths comparable to the ATSR resolution, scintillometers are better equipped for validation purposes with the ATSR satellite, could not be tested properly because the Spanish site equipped with the eddy devices (El Saler) has been situated on a – at least for this research project – unfortunate location. Calculated evaporative fraction on all occasions were higher than measured ones, which can be attributed to the 'dilution' of an ATSR pixel with water surface and to the occurrence of advective effects. Installation of eddy devices on the scintillometer path could provide data to test the hypothesis mentioned above but also could give a useful insight into the footprint of scintillometer and eddy device.

In general a better correlation between measured and calculated fluxes was hoped for but, although it is a difficult task, SEBS can be improved through a better parameterization. Because SEBS is physically based, at the same time this will lead to a better understanding of the underlying physical processes.

The parallel source model makes it possible to estimate evaporation even in semi arid and scarcely vegetated areas. This is an important asset as compared with the single source model. Furthermore it will enable modeling processes in which vegetation is the driving force, e.g. CO₂ fluxes and transpiration. In chapter 2 an example of such a model was mentioned. In the parallel source model a pixel is considered to be for a part fully vegetated and for its complement be fully bare. The model could be improved by coupling aerodynamic resistances for vegetated areas and aerodynamic

resistance for bare soil. A further improvement would be the ability to distinguish shaded and sun lit soil. This could be realized if a remote sensing platform becomes available with more viewing angles than the ATSR satellite.

References

- Baret F. and Guyot G. (1991), Potentials and limits of vegetation indices for LAI and APAR assessment. *Remote Sens. Environm.* 35: 161-174.
- Bastiaanssen, W.G.M. (1995). *Regionalization of surface flux densities and moisture indicators in composite terrain*. Ph.D. Thesis, Wageningen Agricultural University, Wageningen, the Netherlands: 273 pp.
- Bastiaanssen, W.G.M., Menenti, M., Feddes, R.A., Holtslag, A.A.M. (1998), A remote sensing surface energy balance algorithm for land (SEBAL), 1. Formulation. *J. of Hydrology*, 212-213: 198-212.
- Beck, a., Anderson, G.P., Acharya, P.K. et al., (1999), *MODTRAN4 User's Manual*, Air Force Research Laboratory, Hanscom AFB, Ma.
- Becker, F. and Li, Z.L., (1995), Surface temperature and emissivity at various scales: definition, measurements and related problems, *Remote Sens. Rev.* 12: 225-253.
- Blümel, K., 1999, A simple formula for estimation of the roughness length for heat transfer over partly vegetated surfaces, *J. of Applied Meteorology*, 28: 814-829.
- Blyth, E.M., Dolman, A.J. (1995), The roughness length for heat of sparse vegetation. *J. Appl. Meteor.*, 34, 583-585.
- Bohr, T. Jensen, M.H., Paladin, G. Vulpiani, A. (1998), *Dynamical Systems Approach to Turbulence*, Cambridge University Press, Cambridge U.K.
- Brooks. F.A. (1961), Need for Measuring Horizontal Gradients in Determining Vertical Eddy Transfers of Heat and Moisture, *j. Meteorol.* 18: 589-596.
- Brutsaert, W. (1999), Aspects of bulk atmospheric boundary layer similarity under free-convective conditions. *Rev. Geophys.*, 37, 439-451.
- Brutsaert, W., Sugita, M. (1992), Regional surface fluxes from satellite-derived surface temperatures (AVHRR) and radiosonde profiles, *Boundary Layer Meteorol.*, 58, pp 355-366.
- Casado, A. (2001), Worldwide Soaring Turn point Exchange - Unofficial Coordinates for the Spanish Control Points, <http://acro.harvard.edu/soaring/jl/tp>.
- CEC (1993), *CORINE Land Cover technical guide*. European Union, Directorate-General Environment, Nuclear Safety and Civil Protection. Luxembourg. ISBN 92-826-2578-8.

- Choudhury, B.J., Monteith, J.L. (1988), A four layer model for the heat budget of homogeneous land surfaces. *Q.J.R. Meteorol. Soc.*, 114: 373-398.
- De Bruin, H.A.R., Van den Hurk, B.J.J.M., Kohsiek, W. (1995), The scintillation method tested over a dry vineyard area. *Boundary Layer Meteorol.* 76:25-40;
- De Bruin, H.A.R. (1998), *Micrometeorologie*, Wageningen Universiteit, Vakgr. Meteorologie, 156 pp.
- Elliott, W.P. (1958), The Growth of the Atmospheric Internal Boundary Layer, *Trans. Am. Geophys. Union* 39: 1048-1054.
- ESA/ESTEC (1999), *Technical Assistance for the Deployment of Ground-Based Instruments in DAISEX 1999, Field Experiment Report*, University of Valencia, ESTEC 13390/NL/GD.
- Francois, C. and Otle, C., (1996), Atmospheric corrections in the thermal infrared: global and water vapor dependent split-window algorithm. Application to ATSR and AVHRR data. *IEEE Trans. Geosci. Remote Sens.*, 34(2): 457-471.
- Gates, D.M. (1980), *Biophysical Ecology*, Springer Verlag, 610 pp.
- Hasager, C.B., Jensen, N.O. (1999), Surface-flux aggregation in heterogeneous terrain, *Q.J.R. Meteorol. Soc.* 125: 2075-2102.
- Hill, R.J., Clifford, S.F., Lawrence, R.S. (1980), Refractive-index and absorption fluctuations in the infrared caused by temperature, humidity and pressure fluctuations, *J.Opt. Soc. Am.* 70: 1192-1205.
- Högström, U. (1988), Non-dimensional wind and temperature profiles in the atmospheric surface layer: A re-evaluation. *Boundary Layer Meteorol.*, 42, 55-78.
- Jia, L., Menenti, M., Su, Z., Li, Z.L., Wang, J., Jacobs, C. (2001), Development of algorithms for estimation of surface heat fluxes. In: Su, Z., Jacobs, C. (eds.) (2001), *Advanced Earth Observation - land surface climate*. BCRS USP-2 report 01-02, 67-78.
- Kader, B.A., Yaglom, A.M. (1990), Mean fields and fluctuation moments in unstably stratified turbulent boundary layers, *J. Fluid Mech.*, 212, 637-662.
- Kimes, D.S. (1983), Remote sensing of row crop structure and component temperatures using directional radiometric temperatures and inversion techniques, *Remote Sens. Environ.*, 13: 33-55.
- Leinders, J.J.M. et al.(1992), *Remote Sensing*, OUN Heerlen, the Netherlands, ISBN 9035806549.

Lettau, H. (1969), Note on aerodynamic roughness-parameter estimation on the basis of roughness element description. *J. of Applied Meteorology* 8: 828-832.

Li, Z.L., Jia, L., Su, Z. (2001) /1, *ENVISAT - Land Surface processes: Estimation of Vegetation and Soil Component Temperatures from ATSR-2 Data*. BCRS USP-2 report 01-07: 43-54.

Li, Z.L., Jia, L., Su, Z. (2001) /2, *ENVISAT - Land Surface processes: Determination of Atmospheric Water Vapor Content from ATSR Split-window Channel Data*. BCRS USP-2 report 01-07: 23-30.

Li, Z.L., Jia, L., Su, Z. (2001) /3, *ENVISAT - Land Surface processes: Retrieval of Aerosol Optical Depth from ATSR-2 Data for Atmospheric Correction*. BCRS USP-2 report 01-07: 17-22.

Li, Z.L., Stoll, M.P., Zhang, R.H., Jia, L. and Su, Z. (2000), On the separate retrieval of soil and vegetation temperatures from ATSR2 data, *Science in China* (in press).

Li, X. (2001), *Estimation of evaporation with remote sensing in the Urumqi river Basin*, Master of science thesis in Hydrological Engineering, Delft.

Massman, W.J. (1997), An analytical one-dimensional model of momentum transfer by vegetation of arbitrary structure. *Boundary Layer Meteorol.* 83: 407-421.

Massman, W.J. (1999), A model study of four vegetated surfaces using 'localized near-field' Lagrangian theory, *J. Hydrol.*, 223, 27-43.

Massman, W.J. (1999 /2), Molecular diffusivities of Hg vapor in air, O₂, and N₂ near STP and the kinematic viscosity and the thermal diffusivity of air near STP. *Atmos. Environ.*, 33, 453-457.

Massman, W.J., Weil, J.C. (1999), An analytical one-dimensional second order closure of turbulence statistics and the Lagrangian time scale within and above plant canopies of arbitrary structure, *Boundary Layer Meteorol.*, 91: 81-107.

Menenti, M., Choudhury, B.J. (1993), Parameterization of land surface evaporation by means of location dependent potential evaporation and surface temperature range. In: H.J. Bolle et al. (eds.), *Exchange Processes at the Land Surface for a Range of Space and Time Scales*. IAHS Publ. 212, 561-568.

Menenti, M., Jia, L., Li, Z.L., Djepa, V., Wang, J., Stoll, M.P., Su, Z.B., Rast, M., (2000), Estimation of soil and vegetation temperatures from directional thermal infrared observations: The HEIHE, SGP'97, IMGRASS experiments, *Journal of Geophysical Research* (in press).

- Moene A.F., De Bruin, H.A.R. (2001), Sensible heat flux data derived from the scintillometers. In: Su, Z., Jacobs, C. (eds.) (2001), *Advanced Earth Observation - land surface climate*. BCRS USP-2 report 01-02, 85-90.
- Moene A.F. (2001), Description of field experiments. In: Su, Z., Jacobs, C. (eds.) (2001), *Advanced Earth Observation - land surface climate*. BCRS USP-2 report 01-02, 5-7.
- Monteith, J.L. (1973), *Principles of environmental physics*. Edward Arnold Press, 241 pp.
- Mutlow, C, Murray, J., Bailey, P, Birks, A. and Smith, D., 1999, *ATSR-1/2 User Guide Issue 1.0*.
- Myers, V.I., Allen, W.A. (1968), Electro-optical Remote Sensing Methods as Non-destructive Testing and Measuring Techniques in Agriculture, *Applied Opt.* V.7, N.9, 1819-1838.
- Noilhan, J., Lacarrere, P. (1995), GCM grid-scale evaporation from mesoscale modeling. *J. Climate*, 8: 206-223.
- North, P.R.J., Briggs, S.A., Plummer, S.E. and Settle, J.J. (1999), Retrieval of land surface bi-directional reflectance and aerosol opacity from ATSR-2 multiangle imagery, *IEEE transactions on Geoscience and Remote Sensing*, 37(1): 526-537.
- Raupach, M.R. (1989), A practical lagrangian method for relating scalar concentrations to source distribution in vegetation canopies. *Q.J. R. Meteorol. Soc.*, 115: 609-632.
- Roerink, G.J., Menenti, M., Su, Z. (2001). Estimation of evaporation using SEBS-Tuscany. In: Su, Z., Jacobs, C. (eds.) (2001), *ENVISAT - Actual Evaporation*. BCRS USP-2 report 01-05, 21-33.
- Roerink, G.J., De Wit, A.J.W., Pelgrum, H., Mùcher, C.A. (2001 /2), *Remote sensing mapping of carbon and energy fluxes over forests*, Alterra rapport 179, CGI report CGI 7, Wageningen University-Alterra, ISSN 1568-1874, 78pp.
- Sauer, T.J., Norman, J.M. (1995), Simulated canopy microclimate using estimated below-canopy soil surface transfer coefficients. *Airc. For. Meteorol.*, 64: 63-79.
- Saunders, R.W. and Kriebel, K.T., (1988), An improved method for detecting clear sky and cloudy radiances from AVHRR data. *Int. J. Remote Sens.* 9: 123-150.
- Sobrino, J., Li, Z.L., Stoll, M.P. and Becker, F. (1994), Improvements in the split-window technique for land surface temperature determination, *IEEE transactions on Geoscience and Remote Sensing*, 32(2): 243-253.
- Shuttleworth, W.J. (1989), Macrohydrology the new challenges for process hydrology. *J. of Hydr.* 100, pp 31-56.

- Stull, R.B. (1999), *An Introduction to Boundary Layer Meteorology*, Kluwer Academic Publishers, Dordrecht, the Netherlands, ISBN 90-277-2768-6, 669 pp.
- Su, Z. (1996), *Remote sensing applied to hydrology: the Sauer River Basin study*, Ph.D. Dissertation, Heft 15, Schriftenreihe Hydologie/Wasserwirtschaft, Faculty of Civil Engineering, Ruhr University Bochum, Germany.
- Su, Z., Troch, P.A., de Troch, F.P. (1997), Remote sensing of bare surface soil moisture using EMAC/ESAR data. *Int. J. Remote Sens.*, 18:2105-2124.
- Su, Z., Schmugge, T. , Kustas, W.P., Massman, W.J. (2001), *Advanced algorithms for estimation of surface heat fluxes*, BCRS USP-2 report 01-07: 55-80.
- Su, Z. (2001), Brief Description of the Surface Energy Balance System (SEBS) for estimation of turbulent fluxes. In: Su, Z., Jacobs, C. (eds.) (2001), *ENVISAT - Actual Evaporation*. BCRS USP-2 report 01-05, 3-11.
- Taconet, O., Bernard, R., Vidal-Madjar, D. (1986), Evapotranspiration over an agricultural region using a surface flux/temperature model based on NOAA-AVHRR data. *J.Climate Appl. Meteor.*, 25: 284-307.
- Termaat, K (2001), Map marking information for Terlet, Netherlands, <http://acro.harvard.edu/JL/TP/Terlet/terlet00>
- US National Research Council (1994), *Natural Climate Variability on Decade-to-Century Time Scales*, Washington, ISBN 0309054494
- Van de Griend, A.A., Owe, M. (1993), On the relationship between thermal emissivity and the normalized difference vegetation index for natural surfaces. *Int. J. Remote Sens.* 14(6): 1119-1131.
- Van der Hoven, I. (1957), Power spectrum of horizontal wind speed in the frequency range from 0.0007 to 900 cycles per hour. *Bull. Am. Meteor. Soc.*, 65: 450-456
- Verhoef, W., M., de Bruin, H.A.R., van den Hurk, B.J.J.M., (1997), Some practical notes on the parameter for sparse vegetation. *J.Appl. Meteorol.*, 36, 560-572.
- Vermote, E.F., Tanre, D., Deuze, J.L., Herman, M. and Morcrette, J.J., (1997), Second simulation of the satellite signal in the solar spectrum, 6S: An overview, *IEEE transactions on Geoscience and Remote Sensing*, 35: 675-686.
- Wang, J., Bastiaanssen, W.G.M., Ma, Y., Pelgrum, H. (1998), Aggregation of land surface parameters in the oasis-desert systems of Northwest China, In: Roerink, G.J., Menenti, M., (eds.) (1998), *Climate and hydrology at mesoscale: the contribution of future sensor systems*, BCRS report 98-01, 108-122.

Wieringa, J. (1993), Representative roughness parameters for homogeneous terrain. *Boundary Layer Meteorology*, 63: 323-363.

Wieringa, J, Wartema L. (1993), *Agrometeorologie*, Wageningen University, Wageningen, the Netherlands.

Zhang, R, Sun, X., Zhu, Z., Su, H., Chen, G. (2001), Remote sensing model of CO₂ flux for wheat, In: Su, Z., Roerink G.J. (eds.) (2001), *Envisat – Land*

Appendix 1 Program code

Appendix 1 a ALB.PRO code

```
; Language: IDL
; This function calculates the mean of the surface reflectance from aerom1.
; It prevents artefacts occurring if 1, 2 or 3 of the used channels are masked by
cloud screening
; Han Rauwerda, 06/12/2001.
;-----
function alb, b1,b2,b3,b4
n1=float(b1)
n2=float(b2)
n3=float(b3)
n4=float(b4)

ptr1 = where(n1 EQ 9999., count1)
ptr2 = where(n2 EQ 9999., count2)
ptr3 = where(n3 EQ 9999., count3)
ptr4 = where(n4 EQ 9999., count4)
if (count1 NE 0 or count2 NE 0 or count3 NE 0 or count4 NE 0) then begin
    n1(ptr1)=0.
    n2(ptr2)=0.
    n3(ptr3)=0.
    n4(ptr4)=0.
endif
result=byte((n1+n2+n3+n4)/400.)
return, result
end
```

Appendix 1 b FC_NDVI.F code

```
c language: FORTRAN
c program fc_ndvi
c do-loop 430 is extended to avoid dividing by zero
do 430 J=1,nc
    if(IRN(2,J).gt.9998 .or. IRF(2,J) .gt.9998
        .or. IRN(2,J).eq.0 .or. IRF(2,J).eq.0) then

c language: FORTRAN
c program fc_ndvi
c Modification Han Rauwerda: in ENVI no signed bytes possible
c first modification after calculation nadir NDVI
c second modification after calculation forward NDVI
    if(ndvi(1,J).lt.0 then
        ndvi(1,J)=120
    endif

    if(ndvi(2,J).lt.0 then
        ndvi(2,J)=120
    endif
```

Appendix 1 c TOBY.PRO code

```
; Language: IDL
; Function (TOBY) changes the integer file to byte format without testing the size
of the
; integer - intended for using in conjunction with INV_TS_TV with fc_ndvi files
only!!
; together with the low pass convolution filters this function replaces Focal
Enhancement
; from ERDAS IMAGINE - Han Rauwerda, 07/05/2001.
; -----
function toby, b1
n1=UINT(b1)
result=byte(n1)
    return, result
end
```

Appendix 1 d CORINEZ.PRO code

```
; Language: IDL
; Program Corinez attributes roughness lengths to land cover classes
; ; Han Rauwerda, 2001, April 11
; -----
PRO corinez, path, corinefile, ncols, nrows, z0_file

CLOSE, /ALL

; open corinefile
OPENR, 1, path+corinefile
w = ASSOC(1,bytarr(ncols,nrows))
corclass = w(0)
close,1

; make an array of nrows x ncols and store values of class and z0
; z0 values as integer (i.e. z0*1000)
clc = INTARR(1,ncols,nrows)
FOR j=0,nrows-1 DO BEGIN
    print, 'row:', j
    FOR i=0,ncols-1 DO BEGIN
        ;clc(0,i,j)=corclass(i,j)
        CASE 1 OF
            ;1 stands for TRUE
            (corclass(i,j) EQ 0): clc(0,i,j)=0
            (corclass(i,j) EQ 1): clc(0,i,j)=11052
            (corclass(i,j) EQ 2): clc(0,i,j)=9000
            (corclass(i,j) EQ 3): clc(0,i,j)=7000
            (corclass(i,j) EQ 4): clc(0,i,j)=35
            (corclass(i,j) EQ 5): clc(0,i,j)=2000
            (corclass(i,j) EQ 6): clc(0,i,j)=700
            (corclass(i,j) EQ 7): clc(0,i,j)=1000
            (corclass(i,j) EQ 8): clc(0,i,j)=500
            (corclass(i,j) EQ 9): clc(0,i,j)=2000
            (corclass(i,j) EQ 10): clc(0,i,j)=6000
            (corclass(i,j) EQ 11): clc(0,i,j)=5000
            (corclass(i,j) EQ 12): clc(0,i,j)=2000
```



```

(corclass(i,j) EQ 13): clc(0,i,j)=2000
(corclass(i,j) EQ 14): clc(0,i,j)=2000
(corclass(i,j) EQ 15): clc(0,i,j)=5000
(corclass(i,j) EQ 16): clc(0,i,j)=6000
(corclass(i,j) EQ 17): clc(0,i,j)=6000
(corclass(i,j) EQ 18): clc(0,i,j)=334
(corclass(i,j) EQ 19): clc(0,i,j)=6000
(corclass(i,j) EQ 20): clc(0,i,j)=4000
(corclass(i,j) EQ 21): clc(0,i,j)=8000
(corclass(i,j) EQ 22): clc(0,i,j)=6000
(corclass(i,j) EQ 23): clc(0,i,j)=12214
(corclass(i,j) EQ 24): clc(0,i,j)=12214
(corclass(i,j) EQ 25): clc(0,i,j)=12214
(corclass(i,j) EQ 26): clc(0,i,j)=408
(corclass(i,j) EQ 27): clc(0,i,j)=1000
(corclass(i,j) EQ 28): clc(0,i,j)=2000
(corclass(i,j) EQ 29): clc(0,i,j)=4000
(corclass(i,j) EQ 30): clc(0,i,j)=12
(corclass(i,j) EQ 31): clc(0,i,j)=100
(corclass(i,j) EQ 32): clc(0,i,j)=1000
(corclass(i,j) EQ 33): clc(0,i,j)=2000
(corclass(i,j) EQ 34): clc(0,i,j)=6
(corclass(i,j) EQ 35): clc(0,i,j)=100
(corclass(i,j) EQ 36): clc(0,i,j)=408
(corclass(i,j) EQ 37): clc(0,i,j)=100
(corclass(i,j) EQ 38): clc(0,i,j)=6
(corclass(i,j) EQ 39): clc(0,i,j)=6
(corclass(i,j) EQ 40): clc(0,i,j)=2
(corclass(i,j) EQ 41): clc(0,i,j)=2
(corclass(i,j) EQ 42): clc(0,i,j)=2
(corclass(i,j) EQ 43): clc(0,i,j)=2
(corclass(i,j) EQ 44): clc(0,i,j)=2
else: print, 'something wrong: unexpected class values!'
ENDCASE
ENDFOR
ENDFOR

OPENW, 1, path+z0_file
WRITEU, 1, clc
CLOSE, 1

STOP
END

```

Appendix 1 e LOGAGG.PRO code

```
;Language: IDL
;Program to aggregate z0 values by logarithmic averaging (eq. 4.60)
;Han Rauwerda, 2001, June 13
; -----

PRO logagg, path, z0file, ncols, nrows, z0_agg_file

CLOSE, /ALL
pcol=ncols/10
prow=nrows/10

;make an array of pcol x prow to store aggregated z0 values
newcol=0 & newrow= 0
z0m_agg=fltarr(1,pcol, prow)

;make an array to determine the maximum z0 in a sub array
z0_sub=fltarr(1,pcol, prow)
z0max=0.

;open z0 file
OPENR, 1, path+z0file
a=ASSOC(1,INTARR(ncols,nrows))
z0 = a(0)
CLOSE,1

;make a 'convolution filter'-array
cdpix=FLTARR(1,10,10)

FOR j=0, nrows-10 DO BEGIN
  Print, 'Rij: ', j
  FOR i=0, ncols-10 DO BEGIN
    ;x and y will be the upper left pixel in the filter
    if ((i/10.- i/10) eq 0. and (j/10.- j/10) eq 0) then begin
      ;print, 'row', j, 'col', i
      y=j & tel_r=-1 & x=i & tel_c=-1
      newrow=y/10 & newcol=x/10
      FOR b=y, y+9 DO BEGIN
        tel_r=tel_r+1
        FOR a=x,x+9 DO BEGIN
          tel_c=tel_c+1
          ;make a 10x10 array with log-values
          if z0(a,b) eq 0 then cdpix(0,tel_c,tel_r)=ALOG(0.0002)
          ;divide by 10000. to retrieve the floating point value of z0
          if z0(a,b) ne 0 then cdpix(0,tel_c,tel_r)=ALOG((z0(a,b)/10000.))
        ENDFOR
        tel_c=-1
      ENDFOR
      tel_r=-1
      cd_100=total(cdpix,0)/100
      z0m_agg(0,newcol,newrow)=exp(cd_100)
    endif
  ENDFOR
ENDFOR

OPENW,2,path+z0_agg_file
WRITEU,2,z0m_agg
CLOSE,2

STOP
END
```

Appendix 1 f LOGRECAGG.PRO code

```
;Language IDL - Program to aggregate z0 values reciprocal logarithmic averaging (eq. 4.61)
;Han Rauwerda, 2001, June 13
; -----
PRO logrecagg, path, z0file, ncols, nrows, z0_agg_file

CLOSE, /ALL & pcol=ncols/10 & prow=nrows/10

;make an array of pcol x prow to store aggregated z0 values
newcol=0 & newrow= 0 & z0m_agg=fltarr(1,pcol, prow)

;make an array to determine the maximum z0 in a subarray
z0_sub=fltarr(1,pcol, prow) & z0max=0.

;open z0 file
OPENR, 1, path+z0file & a=ASSOC(1,FLTARR(ncols,nrows)) & z0 = a(0)
CLOSE,1

;make a 'convolution filter'-array
cdpix=FLTARR(1,10,10)

FOR j=0, nrows-10 DO BEGIN
  FOR i=0, ncols-10 DO BEGIN
    ;x and y will be the upper left pixel in the filter
    if ((i/10.- i/10) eq 0. and (j/10.- j/10) eq 0) then begin
      ;print, 'row', j, 'col', i
      y=j & tel_r=-1 & x=i & tel_c=-1
      newrow=y/10 & newcol=x/10
      FOR b=y, y+9 DO BEGIN
        tel_r=tel_r+1
        FOR a=x, x+9 DO BEGIN
          tel_c=tel_c+1
          ;make a 10x10 array with log-values
          IF z0(a,b) eq 0. then begin
            cdpix(0,tel_c,tel_r)=(1/(-1*ALOG(0.0002)))
          ENDIF
          IF z0(a,b) NE 0. then begin
            cdpix(0,tel_c,tel_r)=(1/(-1*ALOG(z0(a,b))))
          ENDIF
        ENDFOR
        tel_c=-1
      ENDFOR
      tel_r=-1
      cd_100=total(cdpix,0)/100
      z0m_agg(0,newcol,newrow)=0.
      ;to avoid z0 values greater than 10.
      if (cd_100 gt -0.4343 and cd_100 lt 0.) then begin
        z0m_agg(0,newcol,newrow)=10.
      endif
      ;to avoid z0 values smaller than 0.0002
      if (cd_100 gt 0.117 or cd_100 lt -.4343) then begin
        z0m_agg(0,newcol,newrow)=exp(-1/cd_100)
      endif
    endif
  ENDFOR
ENDFOR

OPENW,2,path+z0_agg_file
WRITEU,2,z0m_agg & CLOSE,2
STOP
END
```

Appendix 1 g LOGRECQUADAGG.PRO code

```
;Program to aggregate z0 values reciprocal quadratic logarithmic averaging (eq. 4.62)
; Language IDL - Han Rauwerda, 2001, June 13
; -----
PRO logrecquadagg, path, z0file, ncols, nrows, z0_agg_file

CLOSE, /ALL & pcol=ncols/10 & prow=nrows/10

;make an array of pcol x prow to store aggregated z0 values
newcol=0 & newrow= 0 & z0m_agg=fltarr(1,pcol, prow)

;make an array to determine the maximum z0 in a subarray
z0_sub=fltarr(1,pcol, prow) & z0max=0.

;open z0 file
OPENR, 1, path+z0file & a=ASSOC(1,FLTARR(ncols,nrows)) & z0 = a(0) & CLOSE,1

;make a 'convolution filter'-array
cdpix=FLTARR(1,10,10)

;to avoid border problems make an offset of 10 rows/columns
FOR j=0, nrows-10 DO BEGIN
  FOR i=0, ncols-10 DO BEGIN
    ;x and y will be the upper left pixel in the filter
    if ((i/10.- i/10) eq 0. and (j/10.- j/10) eq 0) then begin
      ;print, 'row', j, 'col', i
      y=j & tel_r=-1 & x=i & tel_c=-1
      newrow=y/10 & newcol=x/10
      FOR b=y, y+9 DO BEGIN
        tel_r=tel_r+1
        FOR a=x, x+9 DO BEGIN
          tel_c=tel_c+1
          ;make a 10x10 array with log-values
          IF z0(a,b) eq 0. then begin
            cdpix(0,tel_c,tel_r)=(1/(ALOG(0.0002))^2)
          ENDIF
          IF z0(a,b) NE 0. then begin
            cdpix(0,tel_c,tel_r)=(1/(-1*ALOG(z0(a,b)))^2)
          ENDIF
        ENDFOR
        tel_c=-1
      ENDFOR
      tel_r=-1
      cd_100=total(cdpix,0)/100
      z0m_agg(0,newcol,newrow)=0.
      ;to avoid z0 values greater than 10.
      if (cd_100 gt -0.4343 and cd_100 lt 0.) then begin
        z0m_agg(0,newcol,newrow)=10.
      endif
      ;to avoid z0 values smaller than 0.0002
      if (cd_100 gt 0.117 or cd_100 lt -.4343) then begin
        z0m_agg(0,newcol,newrow)=exp(-1/cd_100)
      endif
    endif
  ENDFOR
ENDFOR

OPENW,2,path+z0_agg_file
WRITEU,2,z0m_agg & CLOSE,2
STOP
END
```

Appendix 1 h HASAG.PRO code

```
;Program to aggregate z0 values by according to the microscale model by Hasager and Jensen
; ; Language IDL - Han Rauwerda, 2001, June 25
; -----

; zib: height of internal boundary layer
; ws : wind speed
; wdir: wind direction (0=north, 90=east)

PRO hasag, path, z0file, ncols, nrows,zib,ws,wdir, z0_agg_file

; von Karman constant
kappa = .4

; Notes
; Number of columns and number of rows must be a multiplicity of 10, the program
; aggregates by a factor 10 (i.e. a 10 100 m pixels become 1 km pixel)
; This program needs a geometrically corrected file
; for projections other than latlong, assume a North-South orientation of the image
; for Spain in UTM the error is 1 degree/900 km so for an ATSR image about .5 degree.
; this is far below the uncertainty in the wind direction measurement.

; estimate the wind speed in the x- and y-direction (0=north, 90=east)
; express the wind speed in pixels per second (to avoid difficult normalization)
; N and W winds positive (because in the 10X10 grid the upper left pixel will be taken)
; rotate the wind coordinates so they coincide with grid(k and l positive to the right and
down)
wdir=wdir+90
uw=(-ws*sin((wdir/360) *2!*pi))
vw=(ws*cos((wdir/360) *2!*pi))
;print, 'uw - ', 'vw', uw, vw

;open z0file
CLOSE, /ALL
OPENR, 1, path+z0file
a=ASSOC(1,INTARR(ncols,nrows))
z0 = a(0)
CLOSE,1

pcol=ncols/10 & prow=nrows/10

;meters per pixel before aggregation
met=100.

;make an array of pcol x prow to store aggregated z0 values
newcol=0 & newrow= 0
z0m_agg=fltarr(1,pcol, prow)

;make an array to store the z0 values of the grid
z0grid=FLTARR(1,10,10)
z0lngrid=FLTARR(1,10,10)

;make an array to store the ustar values of the grid
ustar=FLTARR(1,10,10)

;make an array to store the z0-perturbation map
m=FLTARR(1,10,10)

;make an array to store the Fourier transform of the z0-perturbation map
MF=COMPLEXARR(1,10,10)

;make an array to store the Fourier transform of the wind perturbation
```

```

UF=COMPLEXARR(1,10,10)

;make an array to store the inverse Fourier transform of the wind perturbation
UACC=FLTARR(1,10,10)

FOR j=0, nrows-1 DO BEGIN
  ;Print, 'Rij: ', j
  FOR i=0, ncols-1 DO BEGIN
    ;x and y will be the upper left pixel in the filter
    IF ((i/10.- i/10) eq 0. and (j/10.- j/10) eq 0) THEN BEGIN
      y=j & cr=-1 & x=i & cc=-1
      ;in the first loop determine the value of z0a (i.e. the logarithmic averaged z0
value)
      newrow=y/10 & newcol=x/10
      FOR b=y, y+9 DO BEGIN
        cr=cr+1
        ;print,'rijen binnen eerste loop', b
        FOR a=x,x+9 DO BEGIN
          cc=cc+1
          ;determine the z0a value
          ;divide by 10000. to retrieve the floating point value of z0
          z0grid(0,cc,cr)=z0(a,b)/10000.
          if z0(a,b) eq 0 then z0lngrid(0,cc,cr)=ALOG(0.0002)
          if z0(a,b) ne 0 THEN BEGIN
            z0lngrid(0,cc,cr)=ALOG((z0(a,b)/10000.))
          endif
        ENDFOR
        cc=-1
      ENDFOR
      cr=-1

      ;determine the logarithmic averaged roughness length for this grid
      z0_100=total(z0lngrid,0)/100.
      z0a=exp(z0_100)

      ;ustar_null under neutrally stratified condition is (here the logarithmic
      ;averaging of roughness values applies)
      ustarn=(kappa*ws)/ALOG(zib/z0a)

      ;in a second loop determine the perturbation map
      cr=-1 & cc=-1
      FOR b=y, y+9 DO BEGIN
        cr=cr+1
        FOR a=x, x+9 DO BEGIN
          cc=cc+1
          zpix = z0(a,b)
          if z0(a,b) eq 0 then zpix = 0.0002
          m(0,cc,cr)=ALOG((zpix/10000.)/z0a)
        ENDFOR
        cc=-1
      ENDFOR
      rr=-1

      ;determine the forward Fourier Transform of the perturbation map
      mf=FFT(m,-1)

      ;Compute the ustar for each pixel in the frequency domain according (Hasager/Jensen
model)

      ;make i, i.e. a complex value with a real part of 0 and an imaginary part of 1
      imin = complex(0,1)

      ;Set the turbulent exchange coefficients in the vertical (kzet) and $

```

```

;horizontal (kex) direction
;page 2098 Hasager
kzet = kappa*ustarn*zib
; kex/kzet = 20, Panofsky and Dutton 1984, Hasager page 2081
kex = 20.*kzet

;Start a third loop for each grid of 10x10 pixels to calculate the velocity
perturbation
;in the frequency domain
l=-1 & k=-1
FOR b=y, y+9 DO BEGIN
  k=k+1
  FOR a=x, x+9 DO BEGIN
    l=l+1
    ; wave with k = 0 and l = 0 represents the mean of the velocity perturbation
    (eq 0)
    IF (k eq 0 and l eq 0) then UF(0,k,l)=0
    ;Hasager, p 2098, eq. A.15:
    ;compute in the direction of the flow
    ;the angle of {k,l} with the horizontal (k and l only positive)
    ;if k ne 0 then akl=ATAN(l*1./k*1.)
    ;if k eq 0 then akl=.5*!pi
    ;the vector kh*U in the direction of the flow is
    ;vect=ws*((k*1.)^2+(l*1.)^2)^.5*COS((wdir/360)*2*!pi-akl) ; (the same as
    l*uw+k*vw)
    vect=l*uw+k*vw
    IF (k ne 0 or l ne 0) then BEGIN
      UF(0,k,l)=-(ustarn/kappa)*mf(0,k,l)/(((imin*(vect*ws)/10 $
        +kex*(k/10)^2*(l/10)^2))^0.5 * .5*zib*ALOG(zib/z0a))
    ENDIF
  ENDFOR
  l=-1
ENDFOR
k=-1

;Execute the inverse Fourier Transform
;Express the velocity perturbation from pixels per seconds to meters per second
UACC=(FFT(uf,1))
;print, float(uacc)
;Determine the ustar for each pixel within the grid (eq. 18, pp2079)
ustar =kappa*(ws + float(uacc))/(ALOG (zib/z0grid))
ustar_sq=ustar^2
ave_ustar=((total(ustar_sq))/100.)^0.5
z0m_eff = zib/exp(ws*kappa/ave_ustar)
z0m_agg(0,i/10,j/10)=z0m_eff
;print,newrow,newcol,z0m_agg(0,newrow,newcol)
endif

ENDFOR
ENDFOR

;Write the map of the aggregated z0 values
OPENW,2,path+z0_agg_file
WRITEU,2,z0m_agg
CLOSE,2

STOP
END

```

Appendix 1 i Modifications to the original SEBS code

1.

```
;using a roughness file
; -----
; open z0 file
OPENR,1,path+z0file
d = ASSOC(1,fltarr(ncols,nrows))
z0 = float(d(0))
;remove null values (avoid dividing by 0, null roughness values don't occur in nature)
z0_null = WHERE(z0 le 0. , countnullz0)
if (countnullz0 NE 0) then fc(fc_null) = 0.0002
ptr_z0m = z0 ;
close,1
```

2.

```
;using a fractional cover file
; -----
OPENR,1,path+fcfile
c = ASSOC(1,bytarr(ncols,nrows))
fc = float(c(0))/100.
close,1
```

3.

```
; -----
rhoam = (Ps / (Rd*Tsk)) * (1 - 0.378*eaact/Ps) ; moist air density (kg
m-3)
```

4.

```
; -----
cTref =t_pbl*(p_pbl/P0)^.286)-273.15 ;convert potential temperature at PBL to
temperature
```

5.

```
; modification to rule out extreme values for u*, H en L so Broyden will not raise errors
; -----
```

```
X = FLTARR(3)
X[0] = Uref*k/ALOG((Zref - d0)/z0m)
if X[0] lt 0.001 then X[0] = 0.001
ra = ALOG((Zref-d0)/z0h)
```

```
X[1] = (Theta_s - Theta_a)*k*X[0]*rhoa*Cp/ra
if x[1] lt -10000. then x[1] = -9999.
```

```
X[2] = - X[0]^3.*T_v/(k*g*X[1]/(rhoam*Cp))
if x[2] gt 10000 then x[2] = 9999.
if x[2] lt -10000 then x[2] = -9999.
if (x[2] lt 0.0001 and x[2] ge 0.) then x[2] = 0.0001
if (x[2] gt -0.0001 and x[2] lt 0.) then x[2] = -0.0001
```

```
If ((Theta_s - Theta_a) EQ 0. or (Ts LE 0.) or x[0] eq 0.001 or x[1] eq -9999.$
or x[2] EQ 0.0001 or x[2] EQ -0.0001 or x[2] EQ 9999. or x[2] EQ -9999.) then begin
result = X
endif
```

```
If ((Theta_s - Theta_a) NE 0. and (Ts GT 0.) and x[0] ne 0.001 and x[1] ne -9999. $
and x[2] NE 0.0001 and x[2] NE -0.0001 and x[2] NE 9999. and x[2] NE -9999.) then begin
CASE 1 OF
(X[0] LT 0.01): result = X ; This is for very weak wind situation
(Zref LT hst): result = BROYDEN(X,/double, 'ASLfunc', ITMAX= 400, TOLX=0.01) ; ASL,
(Zref GE hst): result = BROYDEN(X,/double, 'BASfunc', ITMAX= 400, TOLX=0.01) ; BAS,
ENDCASE
Endif
```


6.

```
; for measurement towers a default PBL depth of 1000 m is used
; Initial values to call KB_1 and BAS
; -----
cZref = z_pbl
if z_pbl LT 100. then chi = 1000.
If z_pbl GE 100. then chi = z_pbl
```

7.

```
; -----
; Calculation of net radiation in BAS
Rn = (1. -r0)*swgclr + lwg - eps*sigma*T^4
```

Appendix 1 j REKEN.PRO code

```
; semi-automatic procedure to identify flagged pixels
; and to calculate the mean value over the scintillometer path - sample program for Badajoz
; Han Rauwerda, August 2, 2001
; -----
pro reken, path,voor,srt,toev,ncols, nrows

CLOSE,/ALL

OPENR,1,path+voor+srt+toev
a = ASSOC(1,fltarr(ncols,nrows))
dat = float(a(0))
close,1

if (dat(107,43) lt 0) then print , 'dat(107,43) lt 0'
if (dat(107,44) lt 0) then print , 'dat(107,44) lt 0'
if (dat(107,45) lt 0) then print , 'dat(107,45) lt 0'
if (dat(108,43) lt 0) then print , 'dat(108,43) lt 0'
if (dat(108,44) lt 0) then print , 'dat(108,44) lt 0'
if (dat(108,45) lt 0) then print , 'dat(108,45) lt 0'
if (dat(109,43) lt 0) then print , 'dat(109,43) lt 0'
if (dat(109,44) lt 0) then print , 'dat(109,44) lt 0'
if (dat(109,45) lt 0) then print , 'dat(109,45) lt 0'
if (dat(110,43) lt 0) then print , 'dat(110,43) lt 0'
if (dat(110,44) lt 0) then print , 'dat(110,44) lt 0'
if (dat(110,45) lt 0) then print , 'dat(110,45) lt 0'
if (dat(111,43) lt 0) then print , 'dat(111,43) lt 0'
if (dat(111,44) lt 0) then print , 'dat(111,44) lt 0'
if (dat(111,45) lt 0) then print , 'dat(111,45) lt 0'
if (dat(112,44) lt 0) then print , 'dat(112,44) lt 0'
if (dat(112,45) lt 0) then print , 'dat(112,45) lt 0'
if (dat(112,46) lt 0) then print , 'dat(112,46) lt 0'
if (dat(113,44) lt 0) then print , 'dat(113,44) lt 0'
if (dat(113,45) lt 0) then print , 'dat(113,45) lt 0'
if (dat(113,46) lt 0) then print , 'dat(113,46) lt 0'
if (dat(114,44) lt 0) then print , 'dat(114,44) lt 0'
if (dat(114,45) lt 0) then print , 'dat(114,45) lt 0'
if (dat(114,46) lt 0) then print , 'dat(114,46) lt 0'

datgemp=(dat(107,43)+dat(107,44)+dat(107,45)+dat(108,43)+dat(108,44)+dat(108,45)+dat(109,43)
)+dat(109,44)+dat(109,45)+dat(110,43)+dat(110,44)+dat(110,45)+dat(111,43)+dat(111,44)+dat(111,45)+dat(112,44)+dat(112,45)+dat(112,46)+dat(113,44)+dat(113,45)+dat(113,46)+dat(114,44)+
dat(114,45)+dat(114,46)/24.)

print, datgemp

STOP
END
```


Appendix 2a

Corine Land cover database - roughness length for momentum transfer

1	Continuous urban fabric	LGN-3 class L18	1.1052	
2	Discontinuous urban fabric	a bit smoother than C1, rougher than L19	0.9	
3	Industrial and commercial units	less rough than C2, rougher than L19	0.7	
4	Road and rail networks and assoc	LGN3 class L25	0.0035	
5	Port areas	much smoother than C3 (2/3 water surface (L19))	0.2	
6	Airports	in between C3 (1/10) and C4(9/10)	0.07	
7	Mineral extraction sites	rougher than L14, smoother than C3	0.1	
8	Dump sites	a bit rougher than L14	0.05	
9	Construction sites	much rougher than C7	0.2	
10	Green urban areas	about as rough as L9	0.6	x
11	Port and leisure facilities	a bit less rough compared to C10	0.5	
12	Non-irrigated arable land	combination of L2 to L6 and L10	0.2	x
13	Permanently irrigated land	C12	0.2	x
14	Rice fields	C12	0.2	x
15	Vineyards	in between L9 (orchards) and L2 (Maize)	0.5	x
16	Fruit trees and berry plantation	L9	0.6	x
17	Olive groves	about L9	0.6	x
18	Pastures	L1	0.0334	
19	Annual crops associated with perm	about L9	0.6	x
20	Complex cultivation patterns	mix of C12 to C18	0.4	
21	Land principally occupied by agr	mix of C12 to C18 and C22 to C29	0.8	x
22	Agro-forestry areas	smoother than C23/C24 but rougher than C18	0.6	x
23	Broad-leaved forest	L11	1.2214	x
24	Coniferous forest	L12	1.2214	
25	Mixed forest	L11/L12	1.2214	x
26	Natural grasslands	about as rough as L13	0.0408	
27	Moors and heath lands	a bit rougher than L13	0.1	x
28	Sclerophyllous vegetation	a bit rougher than C27	0.2	
29	Transitional woodland-scrub	in between C22 and C28	0.4	
30	Beaches, sand, dunes	about as rough as L15	0.0012	
31	Bare rocks	a bit smoother than L15	0.001	
32	Sparsely vegetated areas	about as rough as C27	0.1	
33	Burnt areas	about as rough as C28	0.2	
34	Glaciers and perpetual snow	rougher than L16 but smoother than L15	0.0006	x
35	Inland marshes	rougher than L16 but smoother than C27	0.01	x
36	Peat bogs	about as rough as L13	0.0408	
37	Salt marshes	about as rough as C35	0.01	
38	Salines	rougher than L16 but smoother than L15	0.0006	
39	Intertidal flats	C38	0.0006	
40	Water courses	about as rough as C41	0.0002	
41	Water bodies	L16	0.0002	
42	Coastal lagoons	about as rough as C17	0.0002	
43	Estuaries	about as rough as C17	0.0002	
44	Sea and Ocean	L17	0.0002	

L = LGN-3 class

C = Corine class

S.C. = Seasonal Correction appropriate

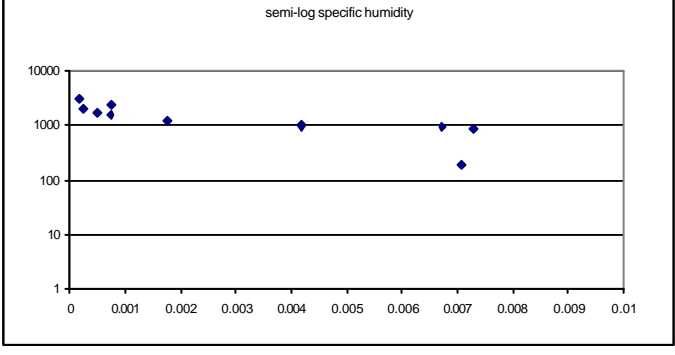
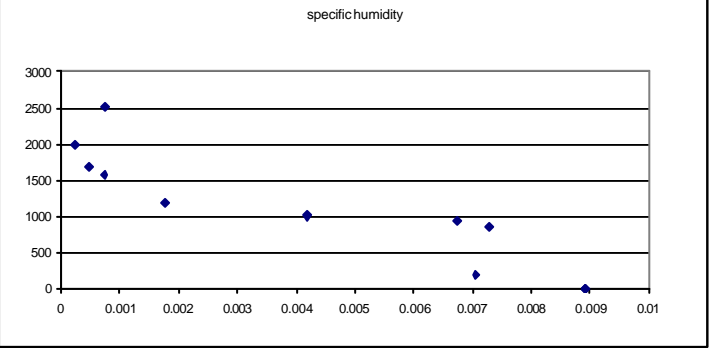
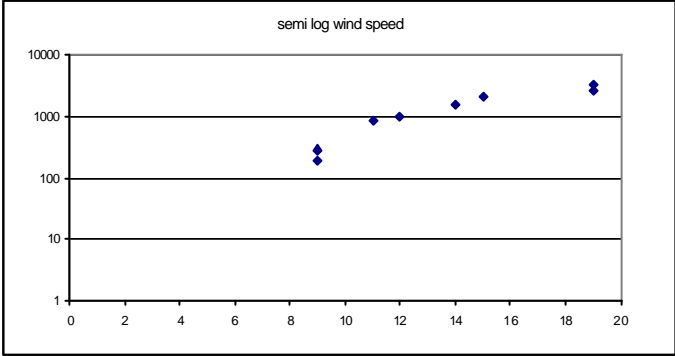
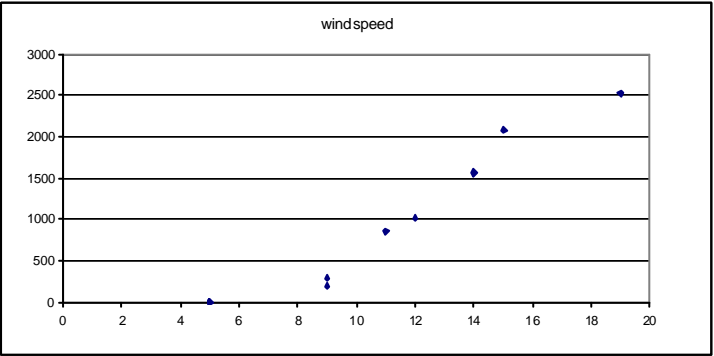
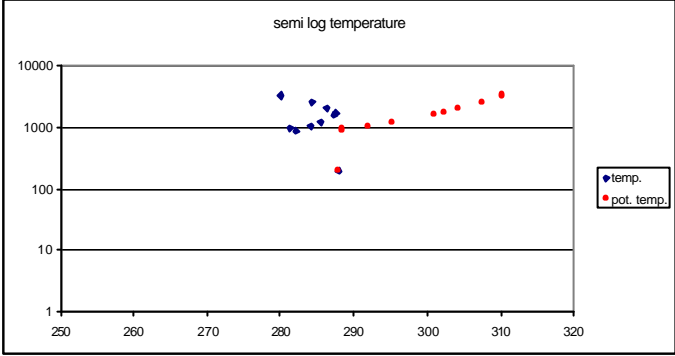
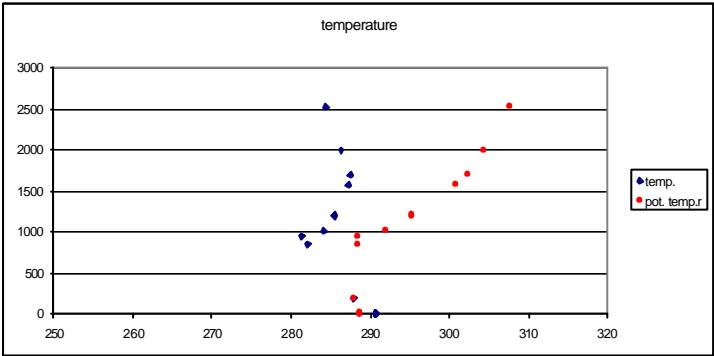
Appendix 2b

Radio Sonde Data - de Bilt, September 8, 1997

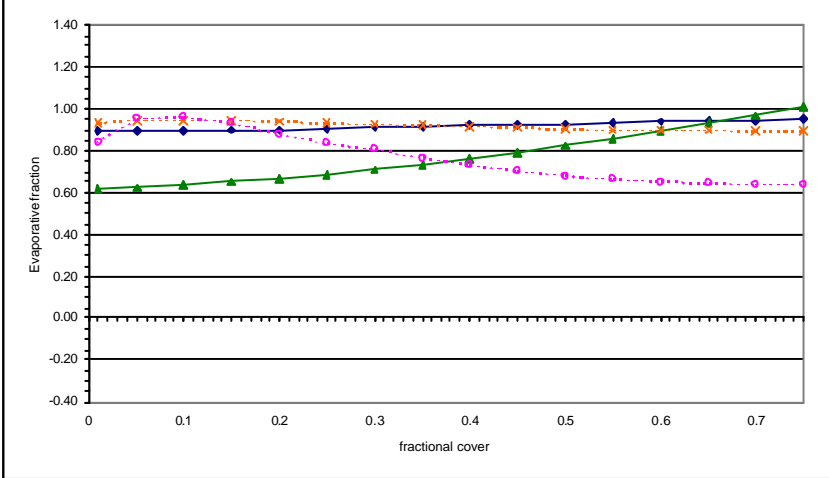
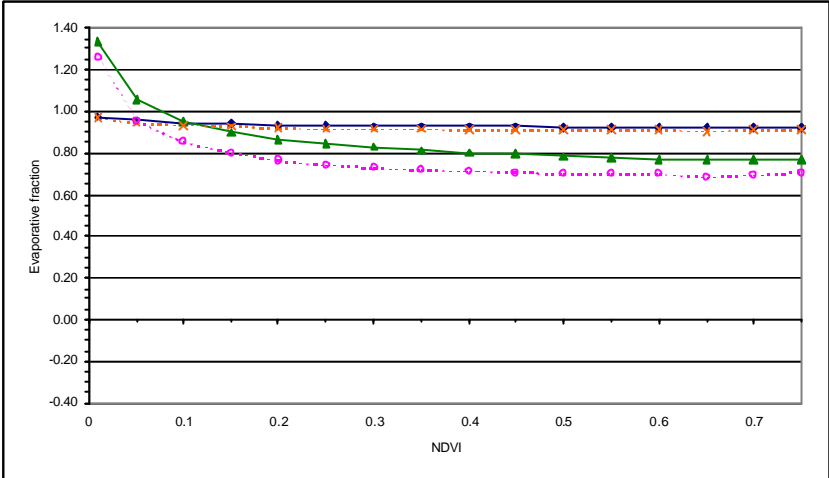
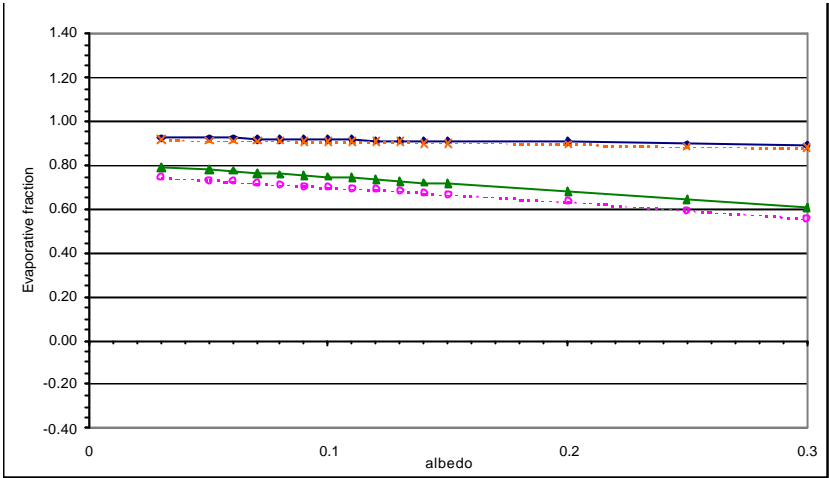
explanation: see § 5. 1

De Bilt, 52.1N 5.18E, 0m
BADC database, global radiosonde

12 h													
PP (P)	HT (m)	TT	TD	DD	FF		h from p	theta	e	esat	RH	w	q
102300 -		290.7	285.7 -				0	288.8156	14.60103044	20.23100464	0.72171554	0.009005764	0.008925384
102300 -		-		280	5		0						
102300	0	290.7	285.7	280	5		0	288.8156	14.60103044	20.23100464	0.72171554	0.009005764	0.008925384
100000	200	287.9	281.9	265	9		192.3613	287.9	11.3078876	16.87751608	0.669997146	0.007113607	0.007063361
98900 -		-		265	9		285.9297						
92500	850	282.1	281.2	275	11		851.8652	288.4606	10.77969616	11.46299888	0.94039058	0.007333733	0.007280341
91500 -		281.3	279.9 -				943.8155	288.5382	9.857090882	10.85377219	0.908171897	0.006773311	0.006727742
90800 -		-		275	12		1008.781						
90800 -		284.1	273.1 -				1008.781	292.051	6.087855371	13.12223278	0.463934414	0.004198262	0.00418071
88800 -		285.5	261.5 -				1197.193	295.3657	2.525393044	14.40837363	0.175272596	0.001773872	0.001770731
85000	1560	287.3	250.3	285	14		1567.166	300.969	0.999452252	16.22716804	0.061591292	0.00073219	0.000731654
83800 -		287.5	245.5 -				1687.443	302.4058	0.654619797	16.4414171	0.03981529	0.000486244	0.000486007
80800 -		286.3	237.3 -				1995.837	304.2998	0.305383012	15.19290365	0.020100372	0.000235162	0.000235107
80000 -		-		290	15		2080.01						
75900 -		-		290	19		2525.056						
75900 -		284.3	249.3 -				2525.056	307.6293	0.916346254	13.29943695	0.068901131	0.000751817	0.000751252
70000	3180	280.1	233.1	290	19		3209.599	310.1809	0.202400598	9.994253354	0.020251698	0.000179891	0.000179858



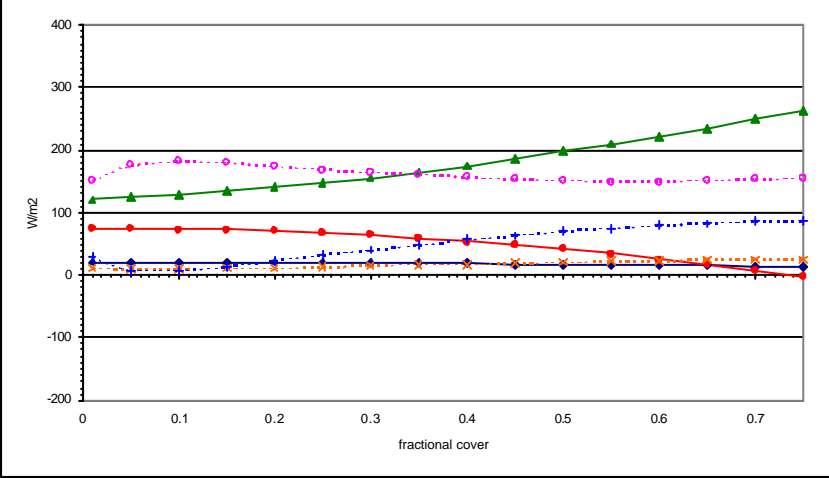
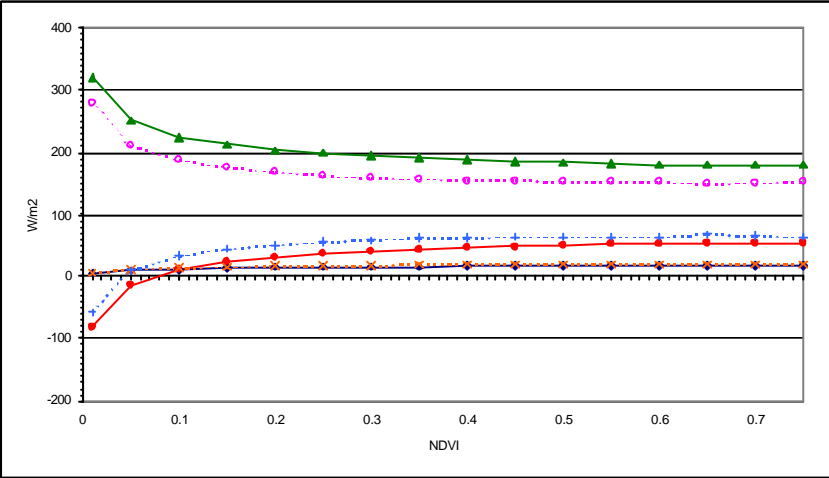
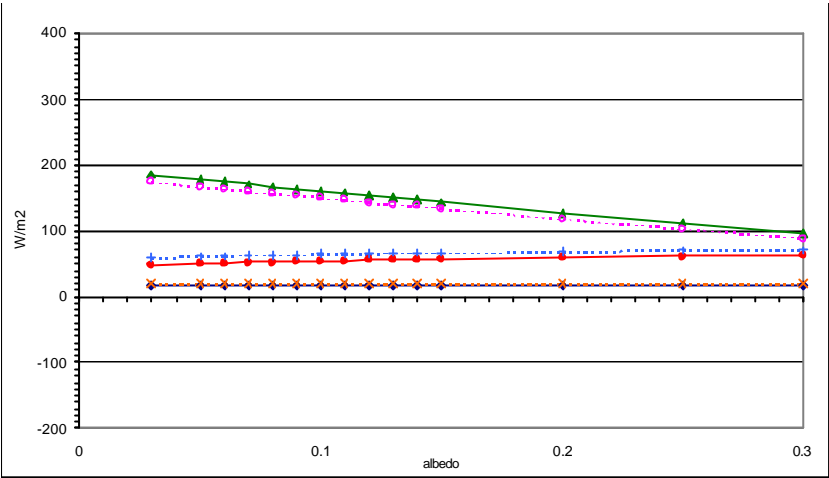
explanation: see § 5.1



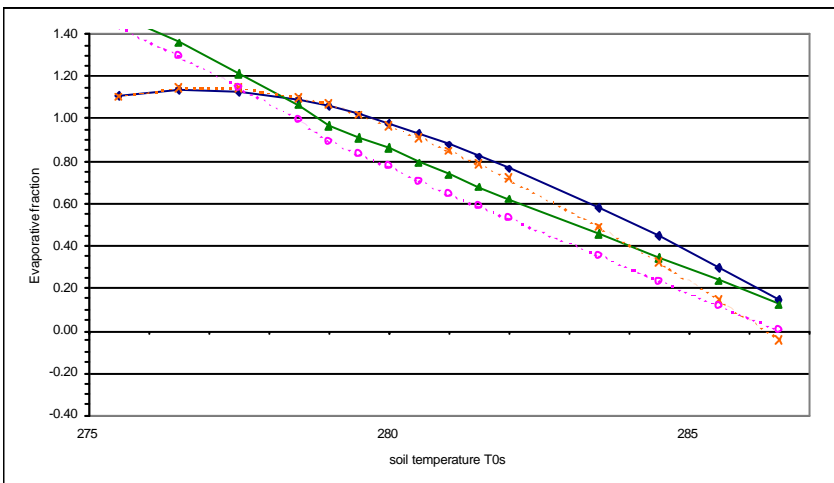
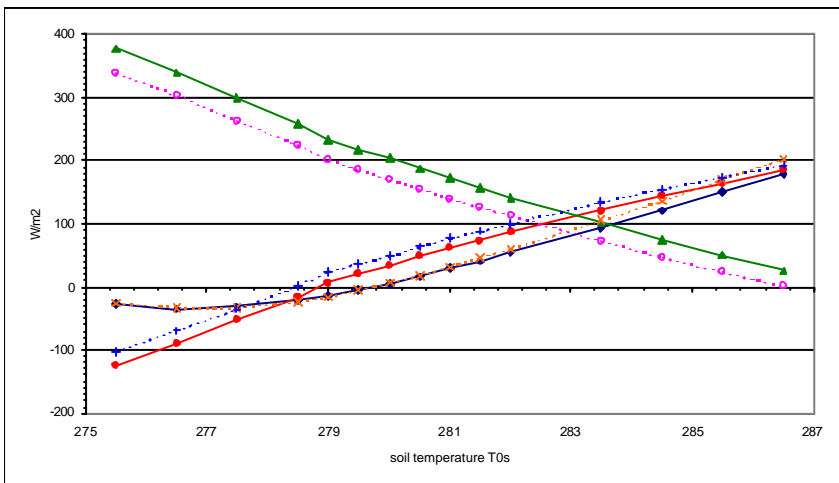
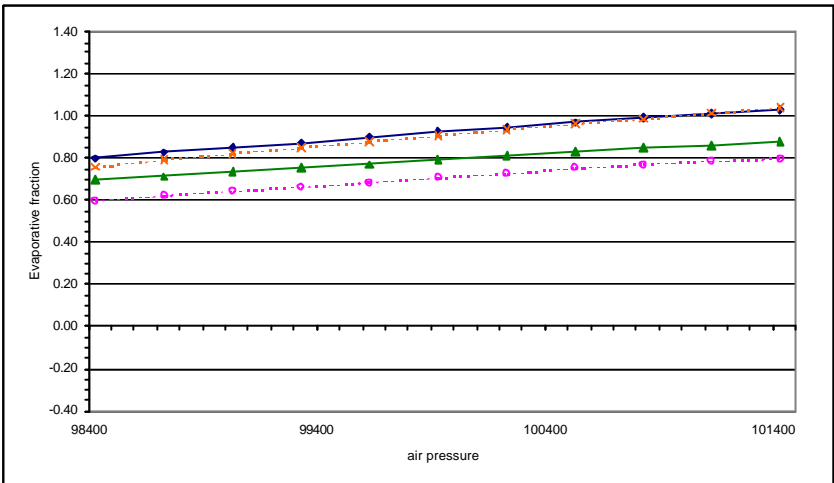
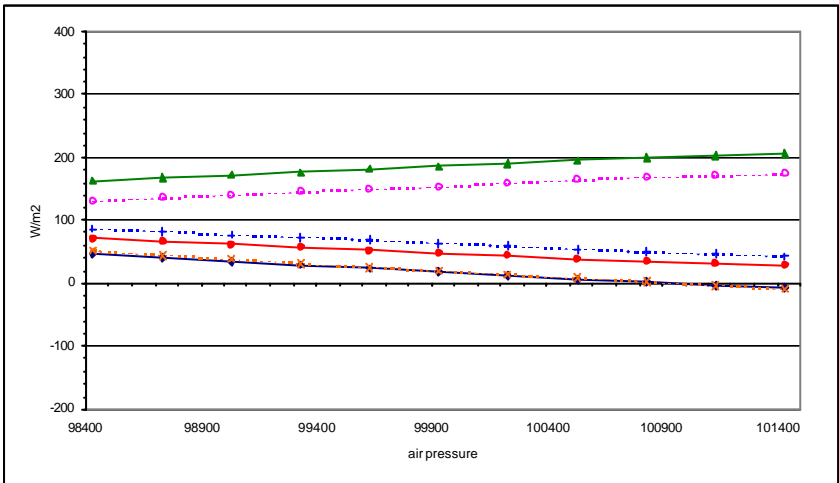
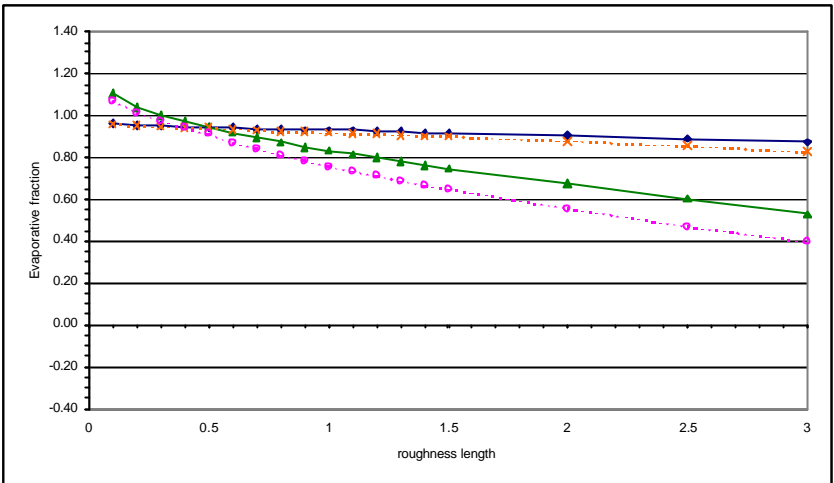
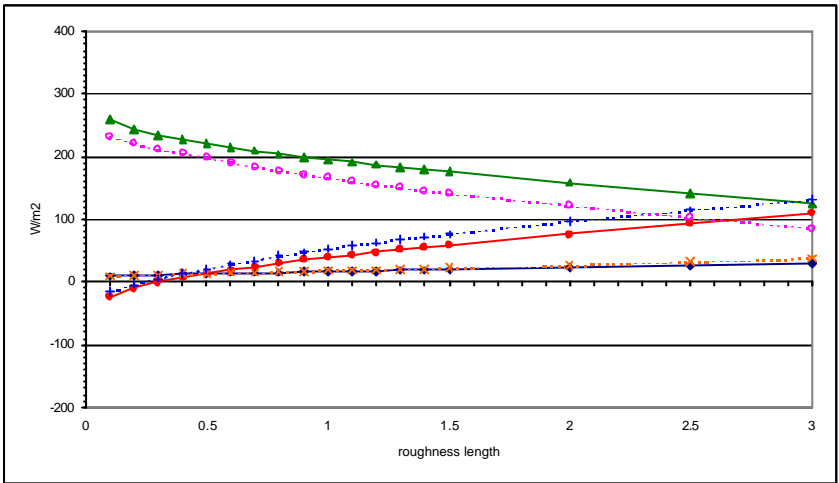
Heat Fluxes:



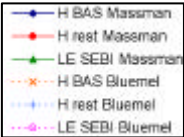
Evaporative Fraction:



explanation: see § 5.1



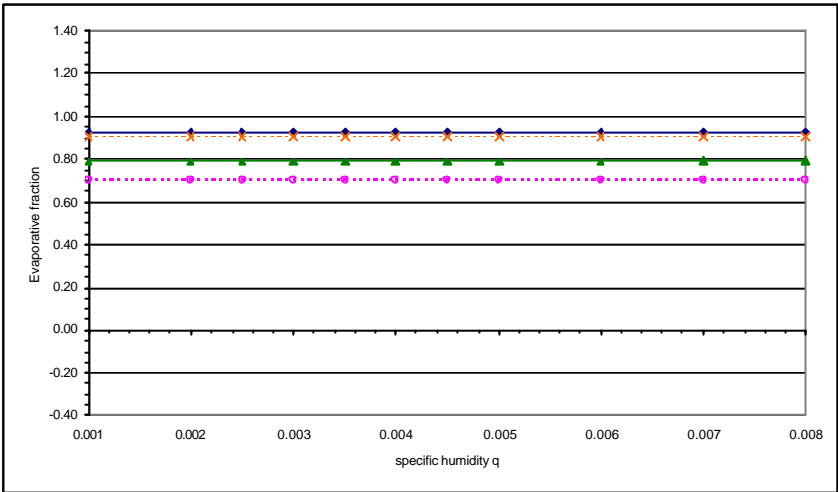
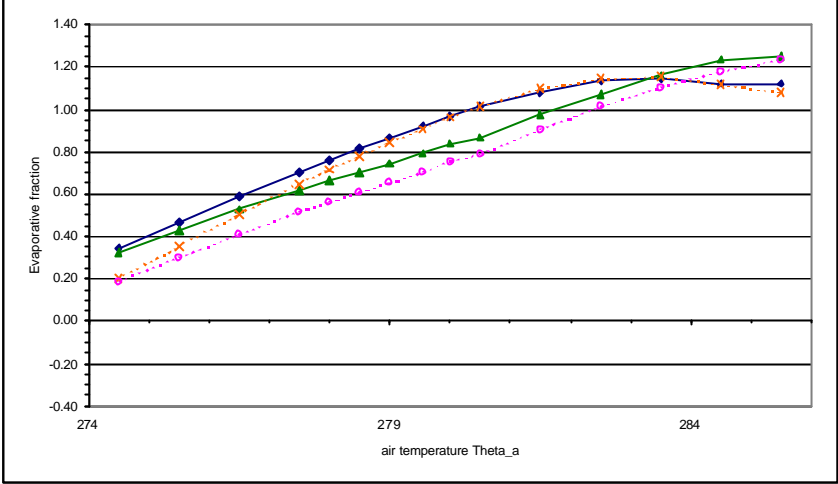
Heat Fluxes:



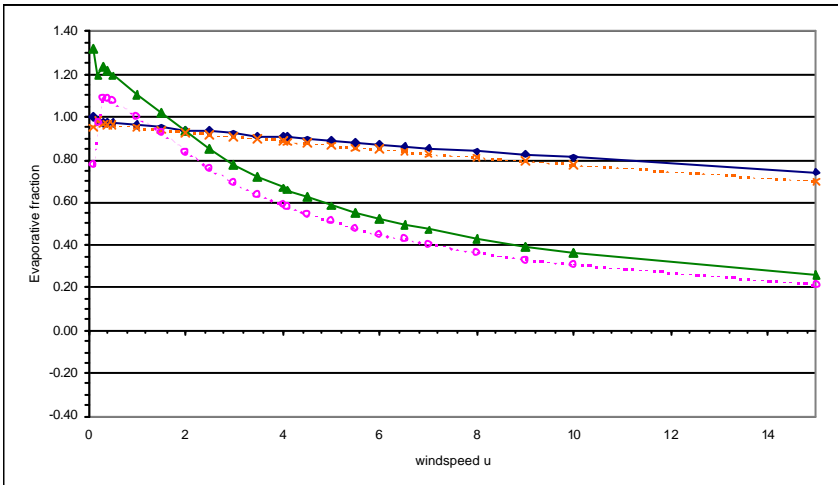
Evaporative Fraction:



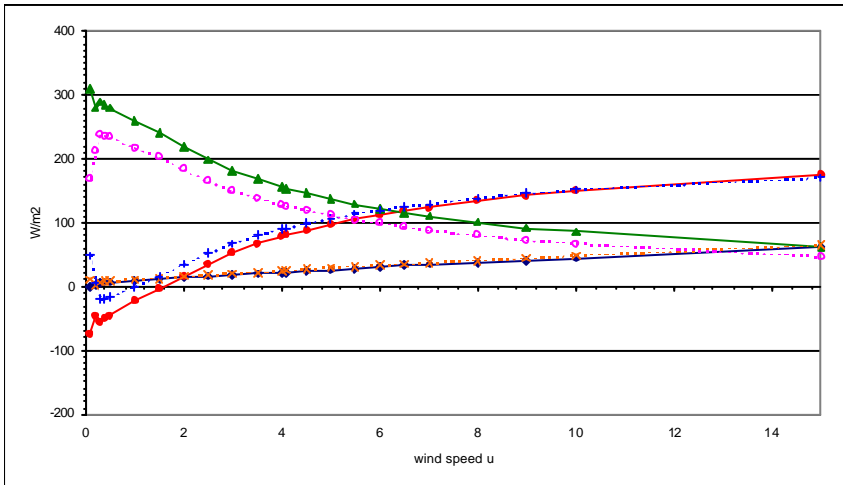
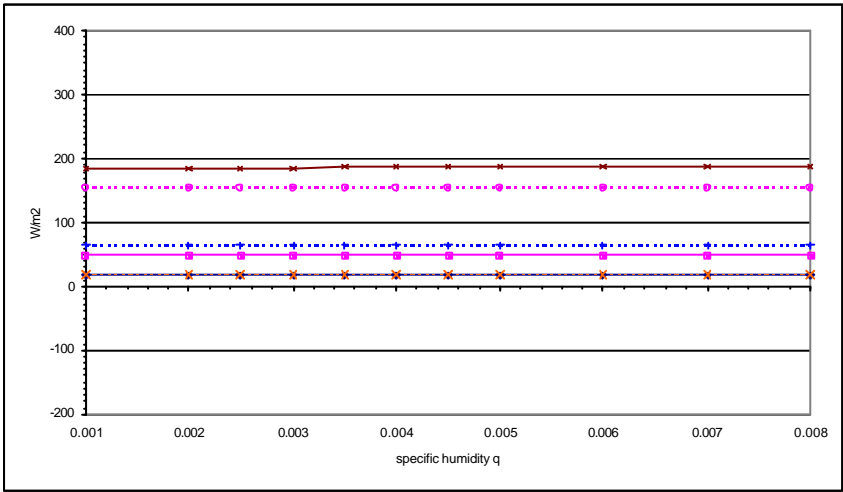
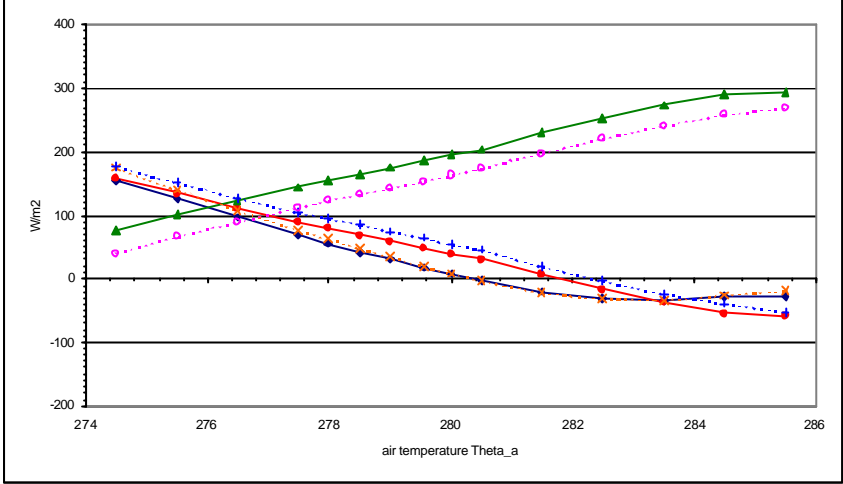
explanation: see § 5.1



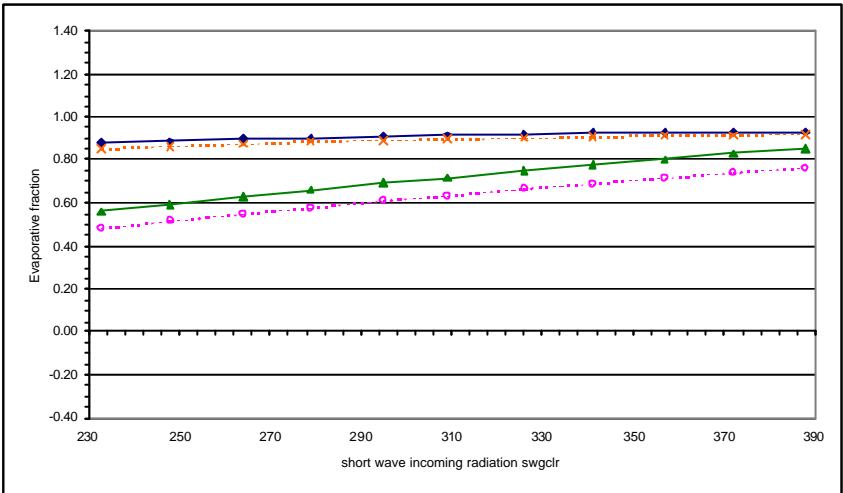
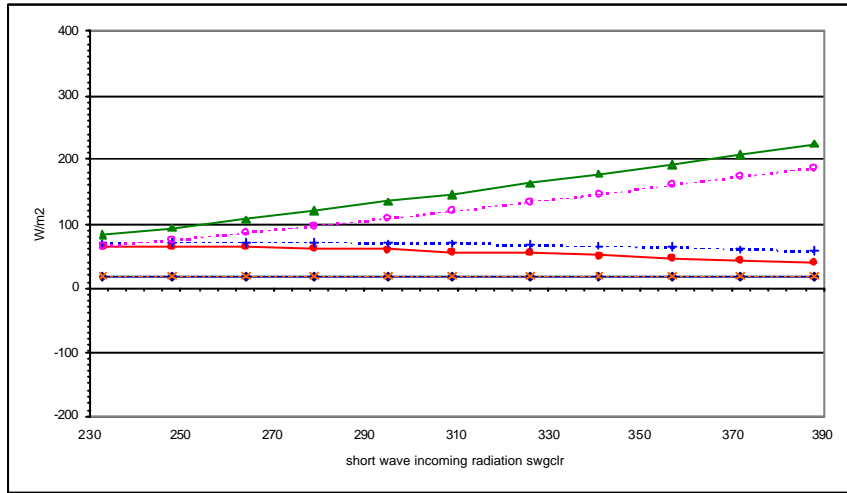
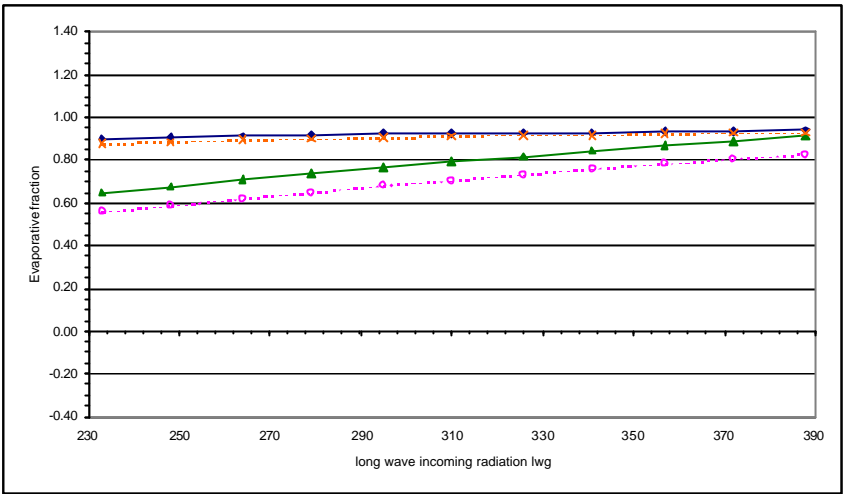
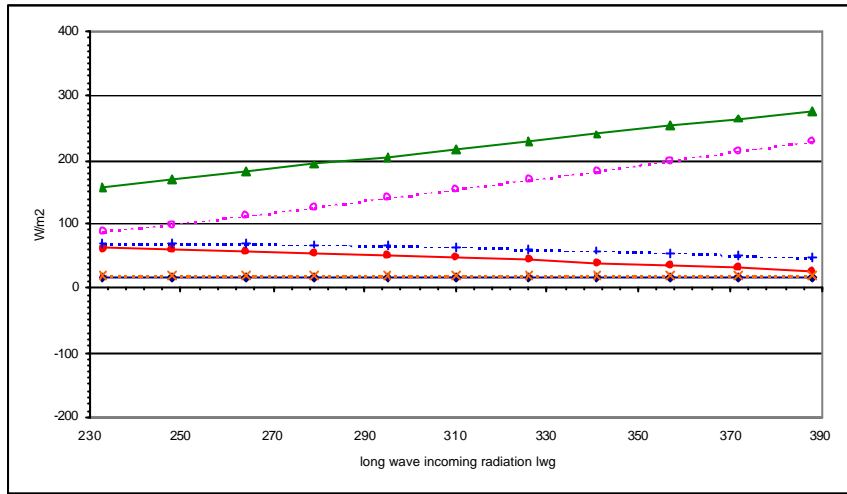
Heat Fluxes:



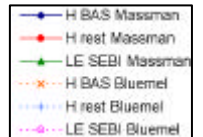
Evaporative Fraction:



explanation: see § 5.1



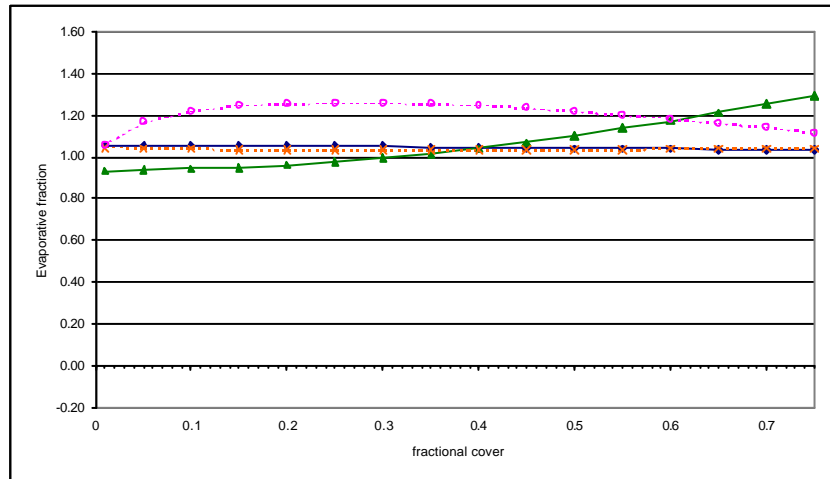
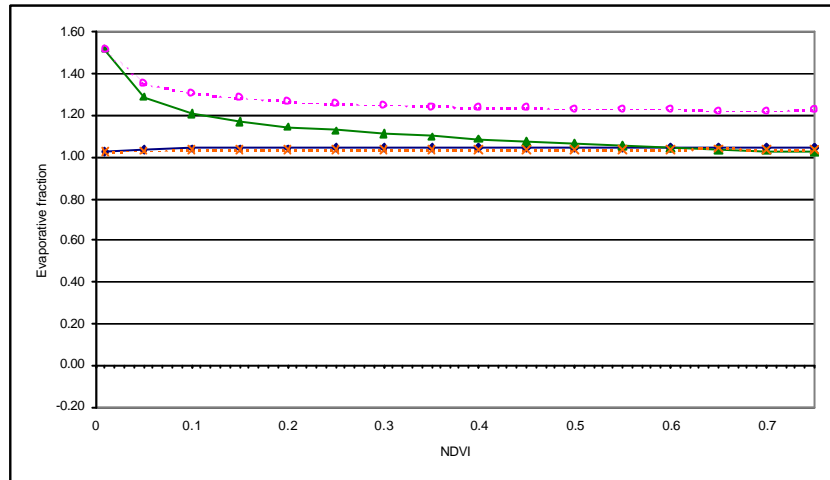
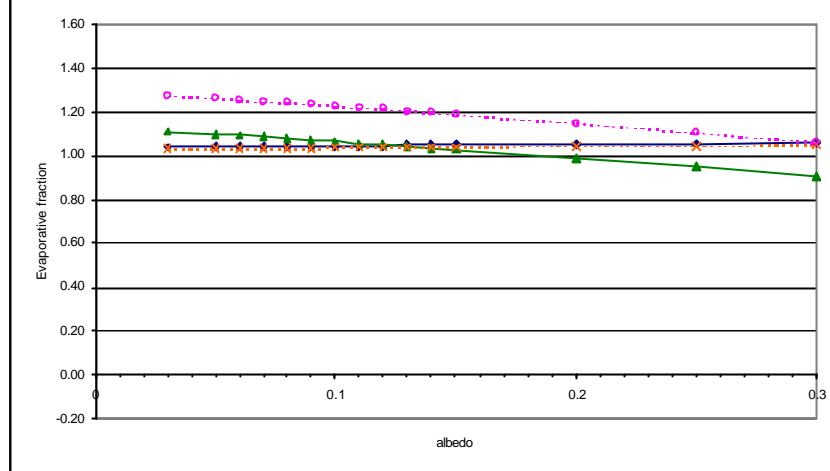
Heat Fluxes:



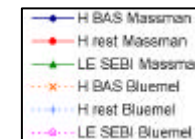
Evaporative Fraction:



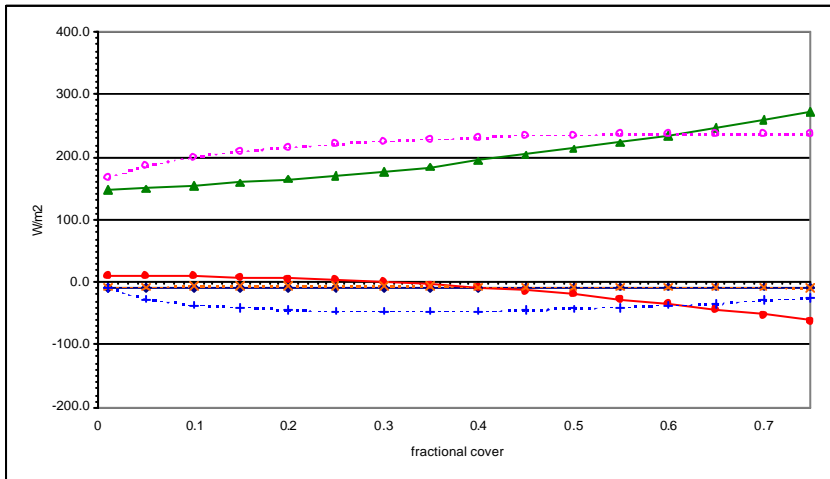
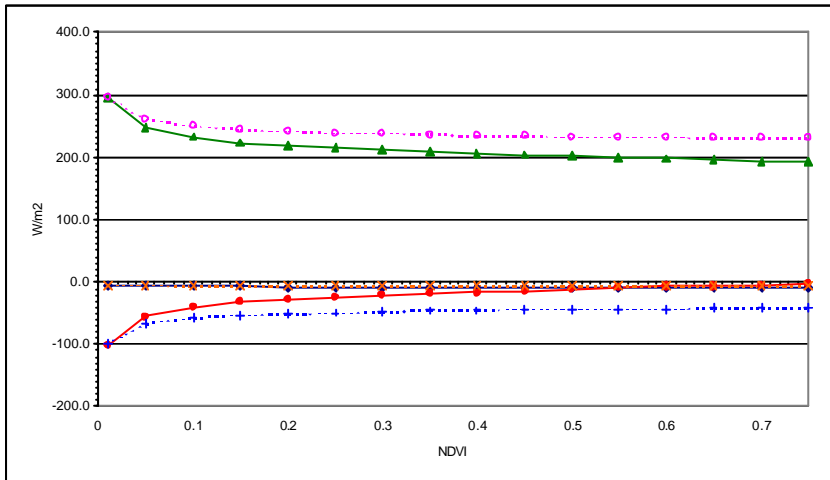
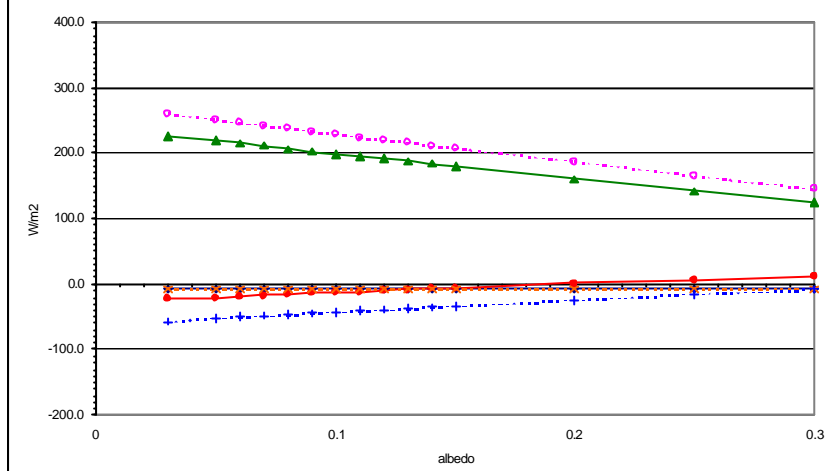
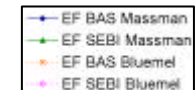
explanation: see § 5.1



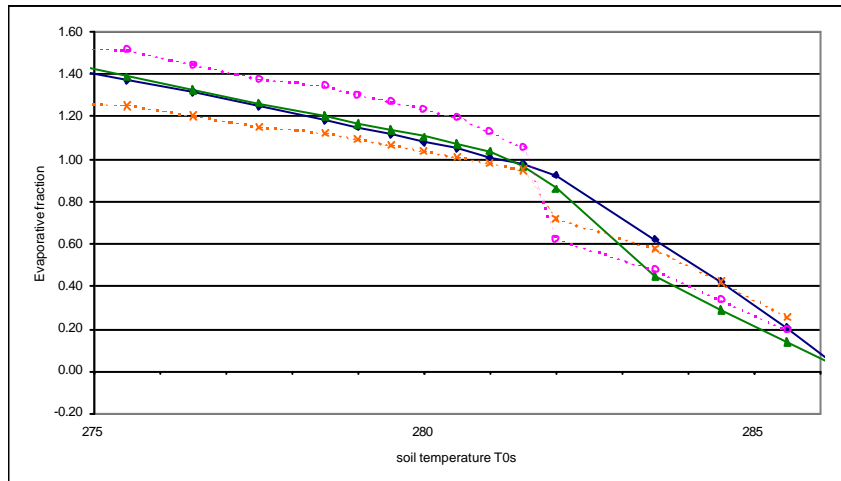
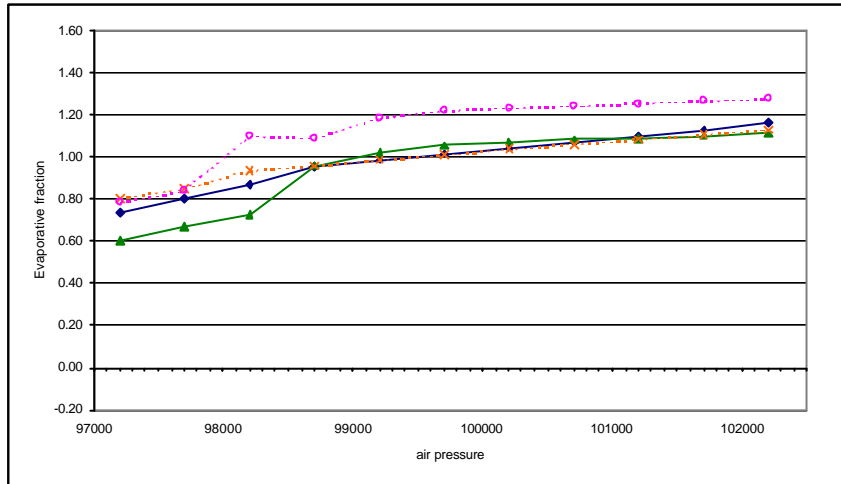
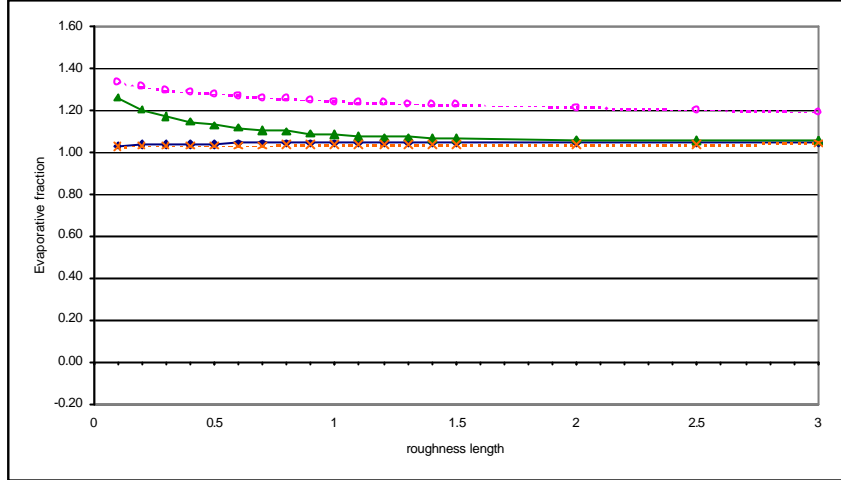
Heat Fluxes:



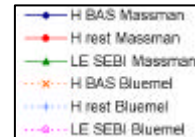
Evaporative Fraction:



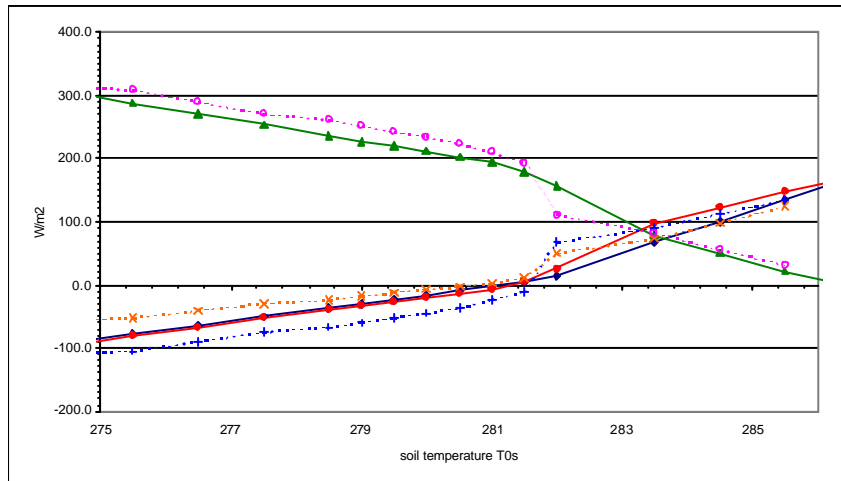
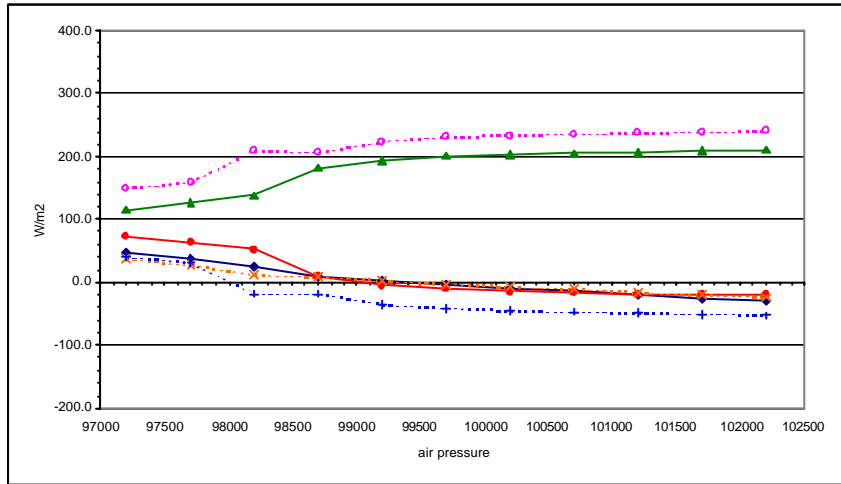
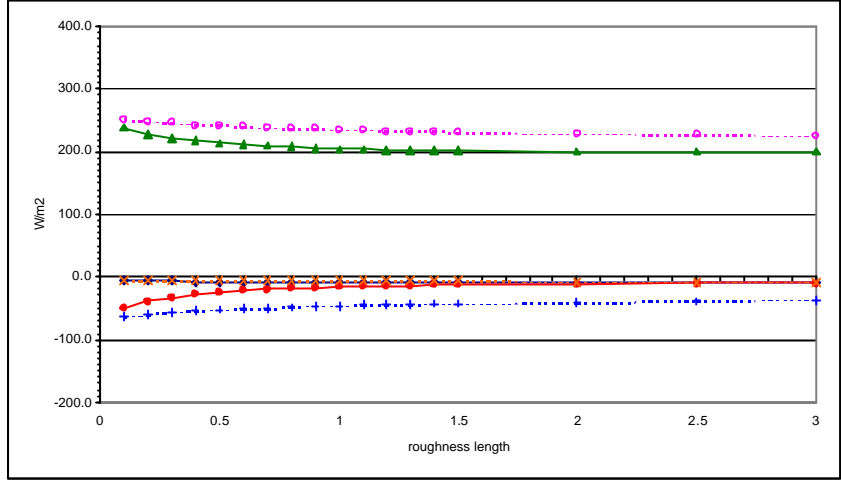
explanation: see § 5.1



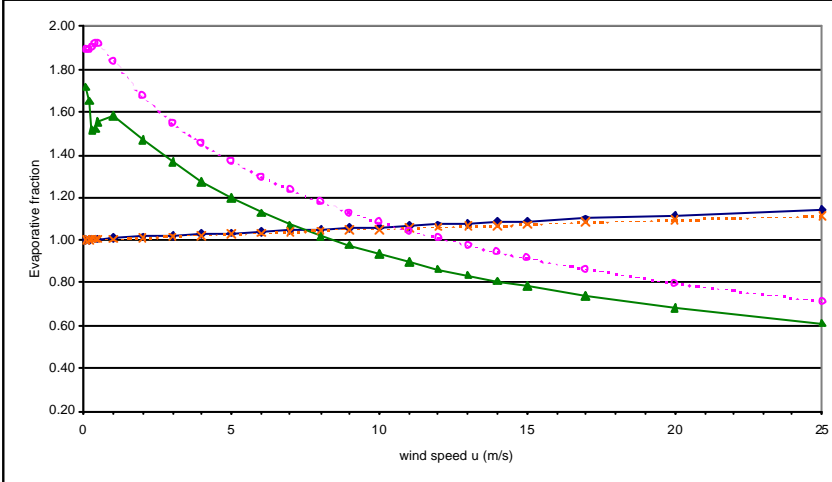
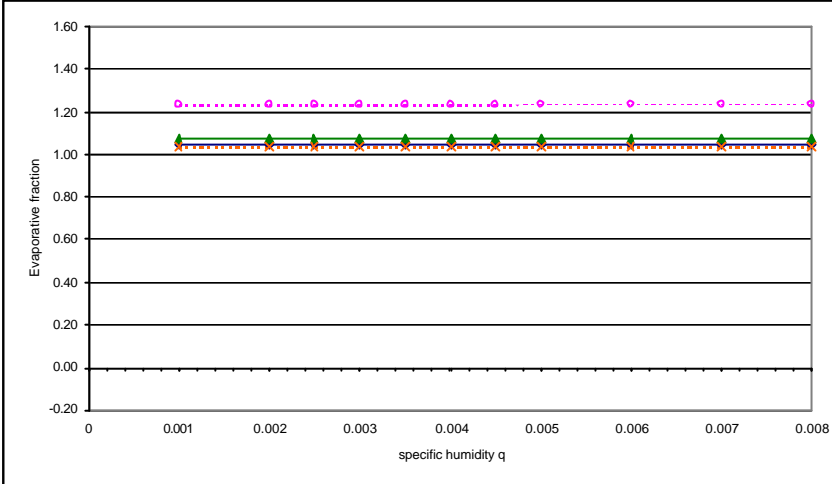
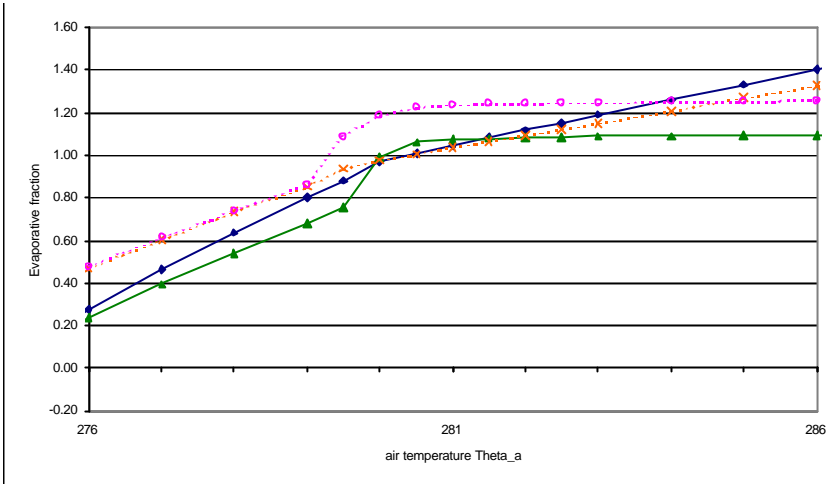
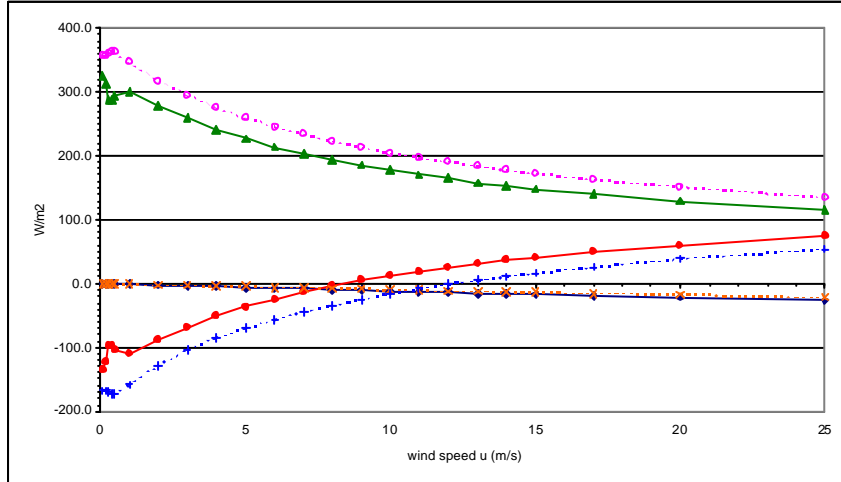
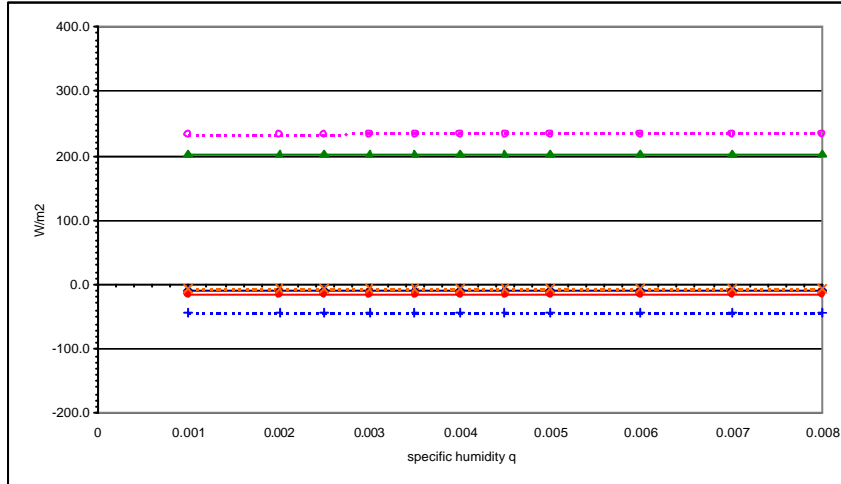
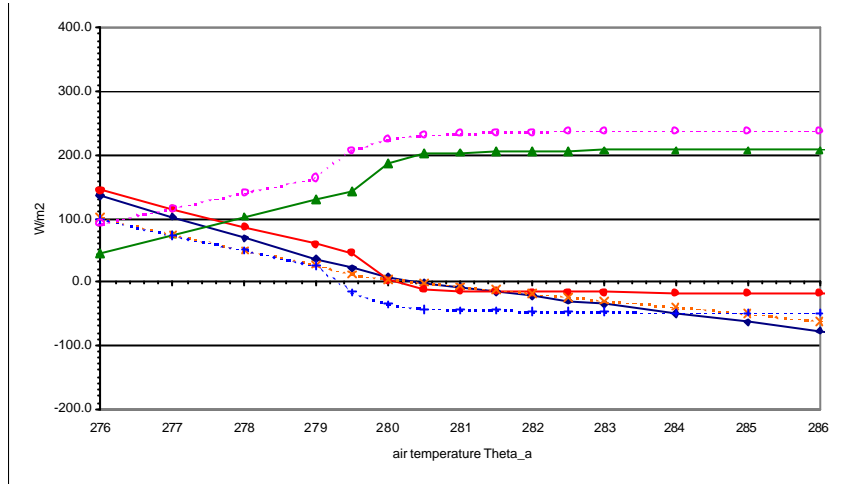
Heat Fluxes:



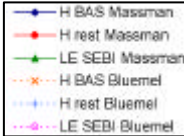
Evaporative Fraction:



explanation: see § 5.1



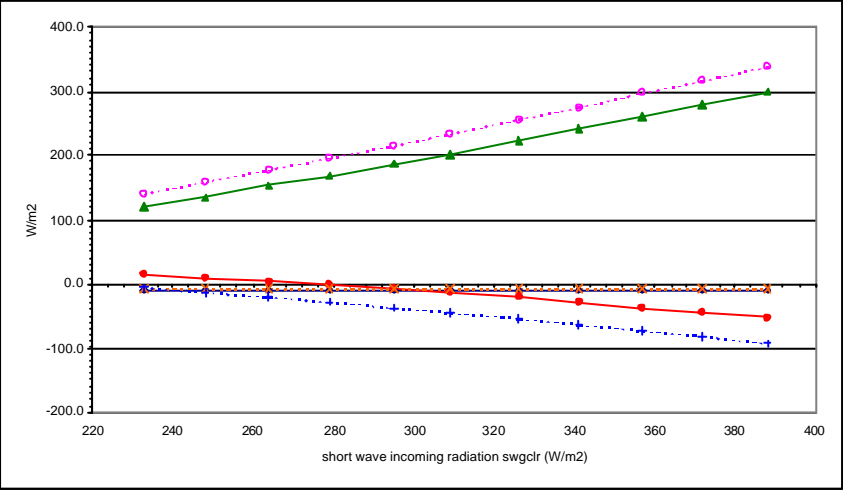
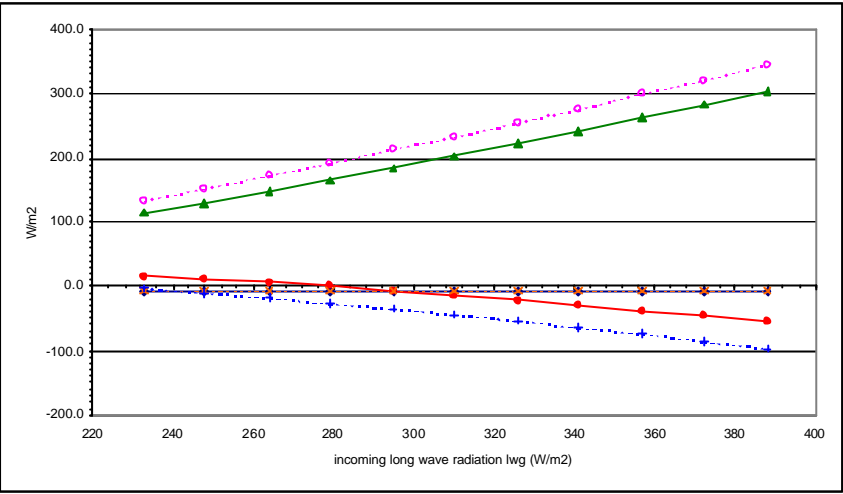
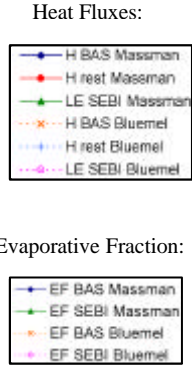
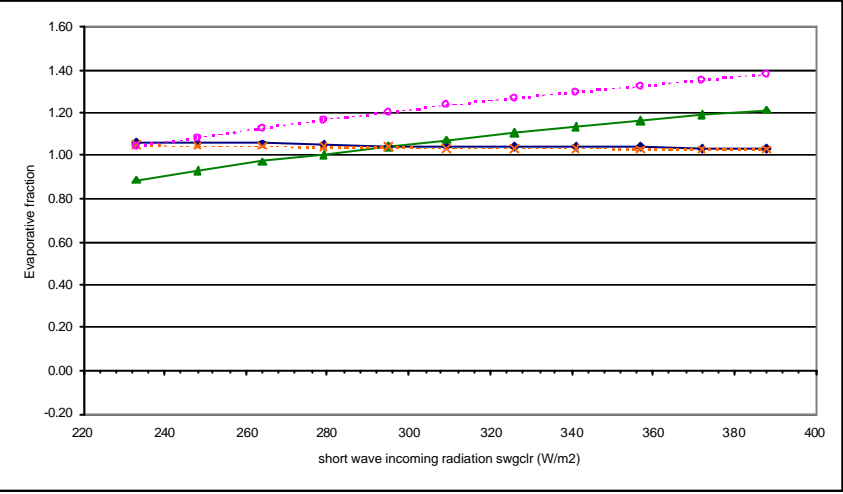
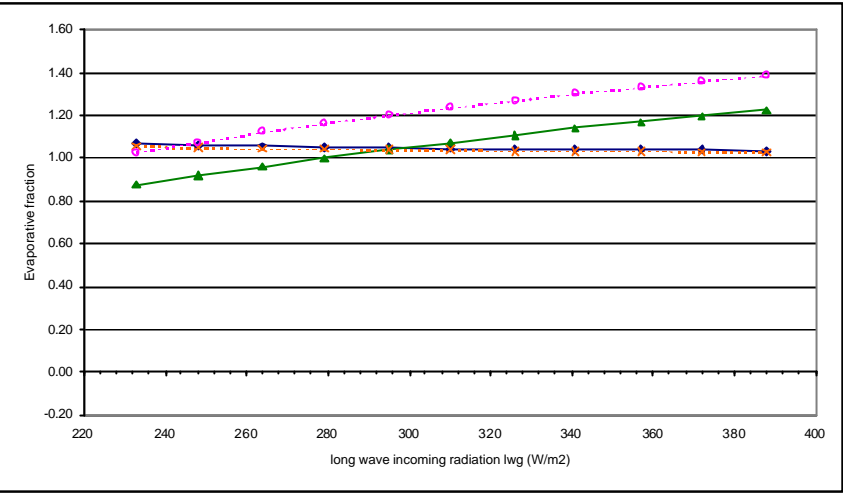
Heat Fluxes:



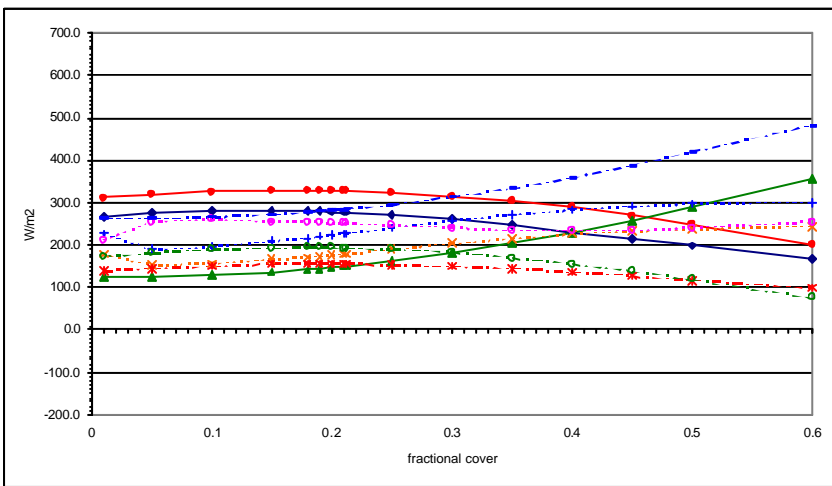
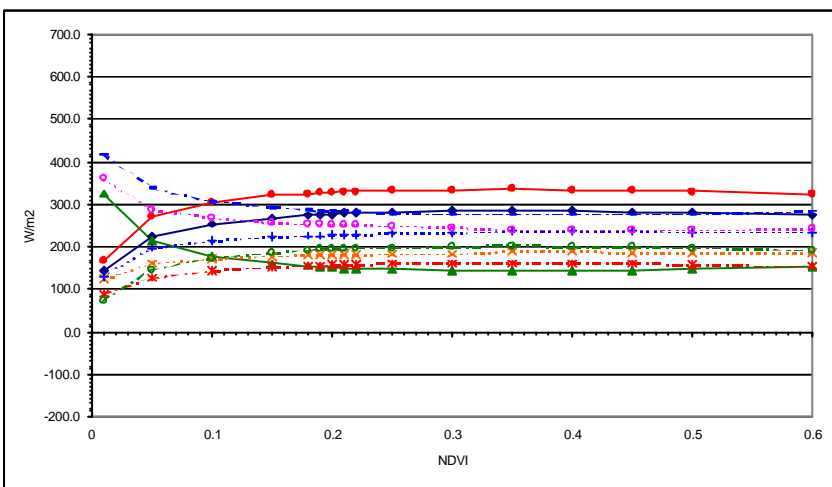
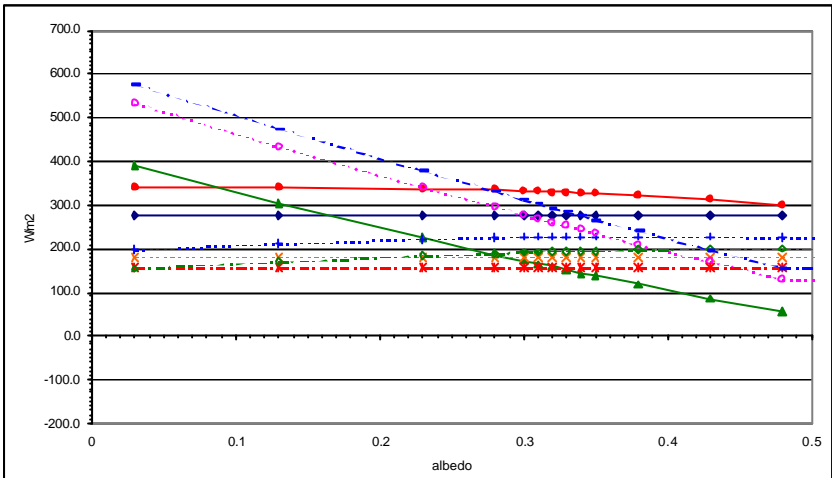
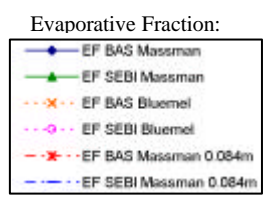
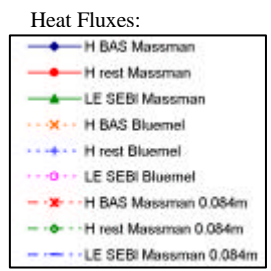
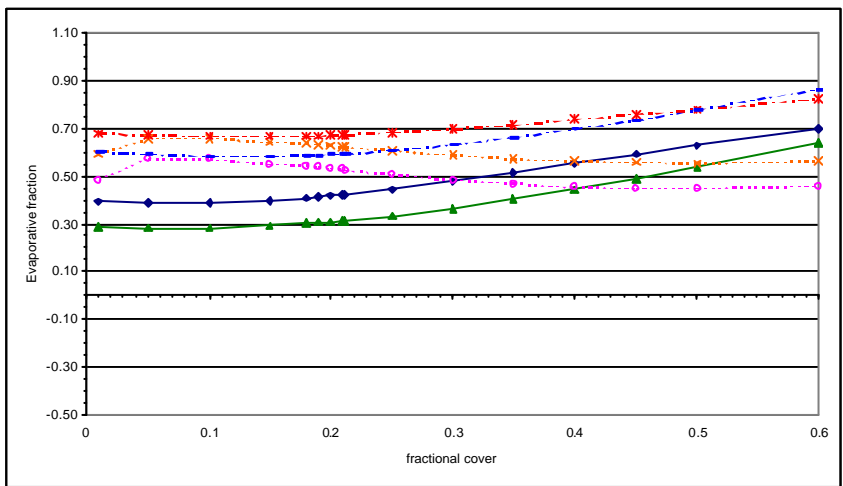
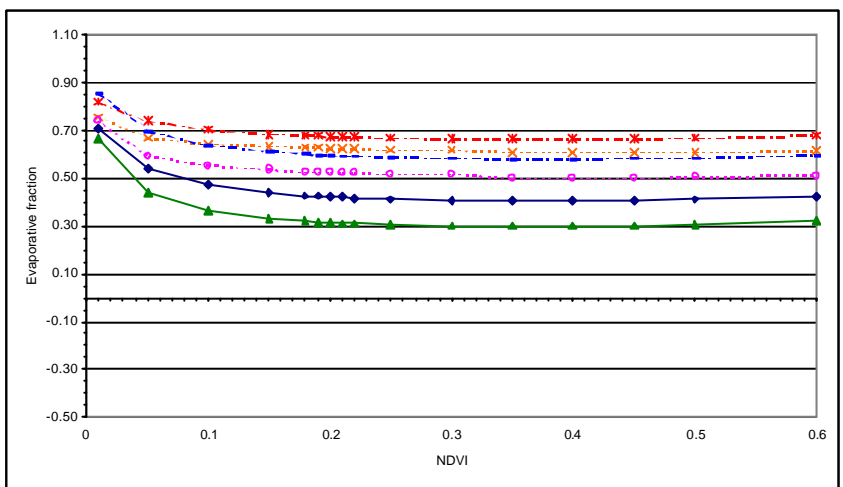
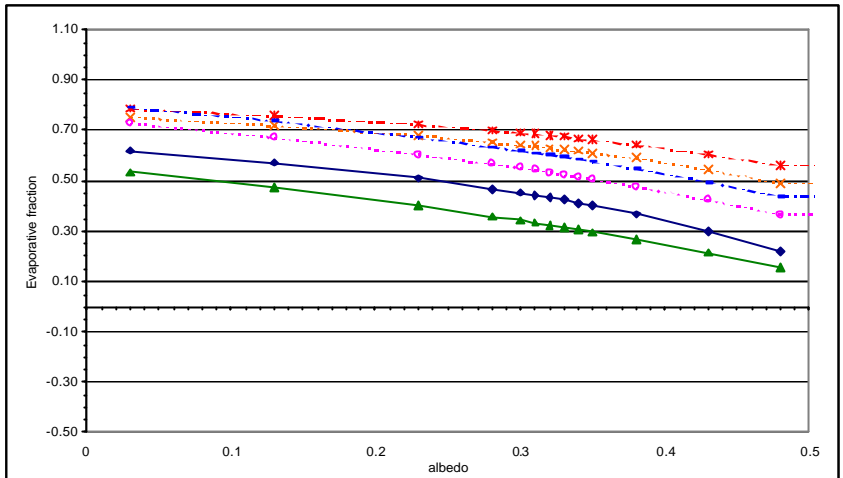
Evaporative Fraction:



explanation: see § 5.1



explanation: see § 5.1

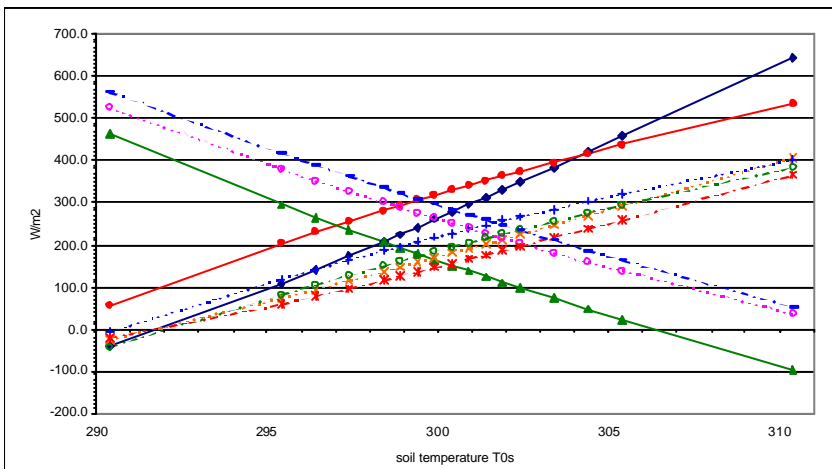
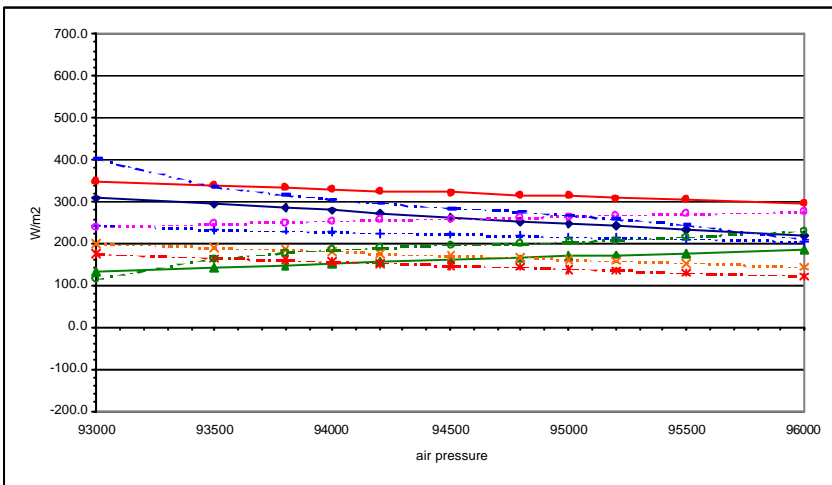
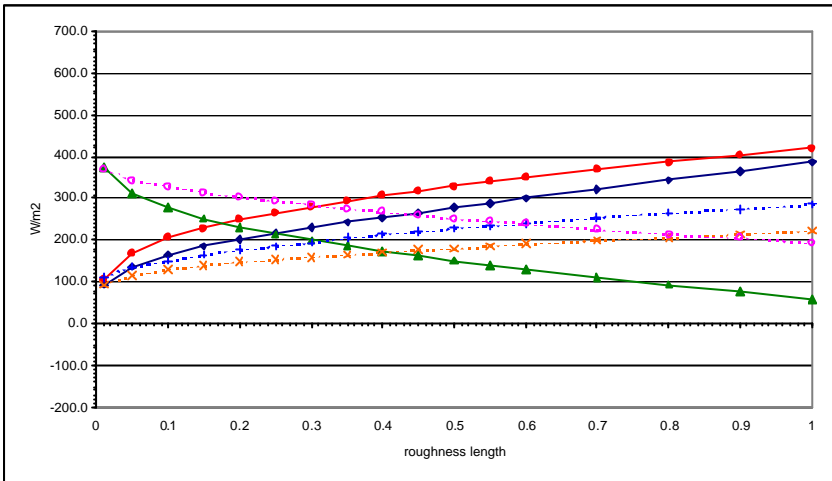
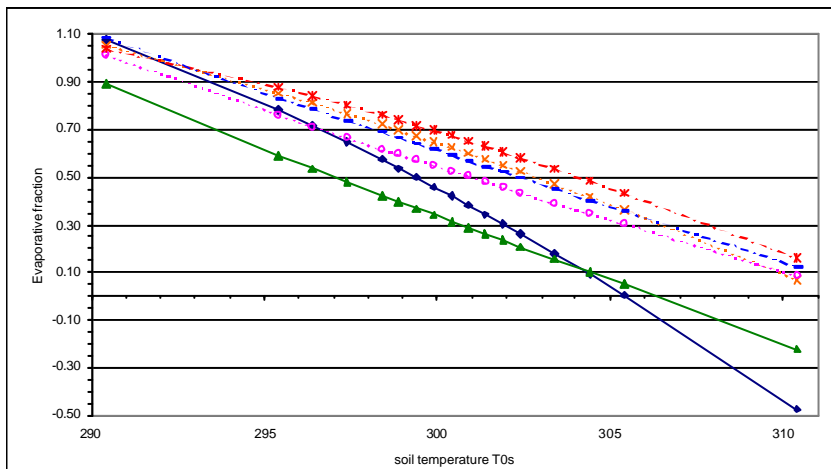
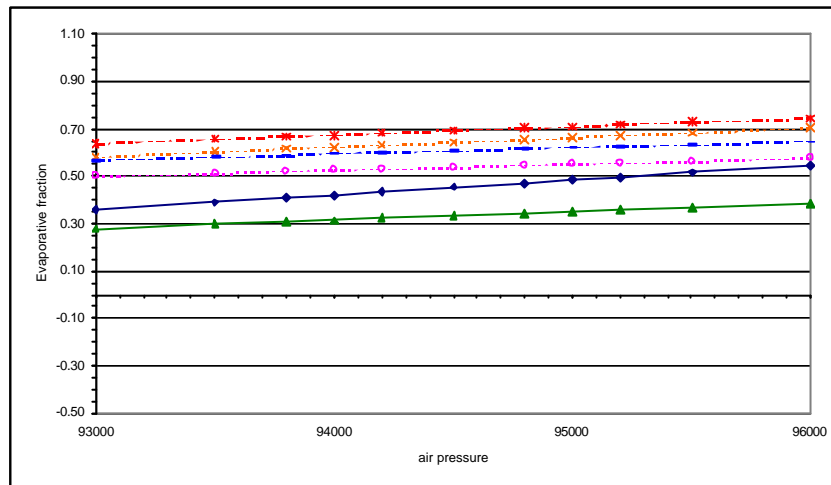
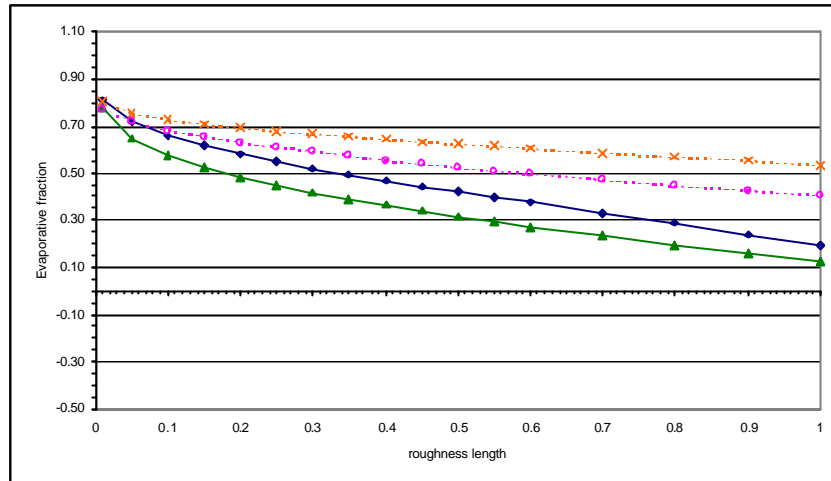


Appendix 3

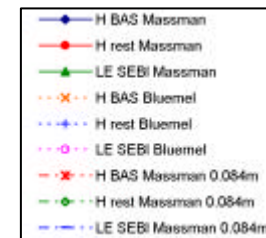
Sensitivity Analysis - Tomelloso - June 2, 1999

Tower Measurements

explanation: see § 5.1



Heat Fluxes:



Evaporative Fraction:

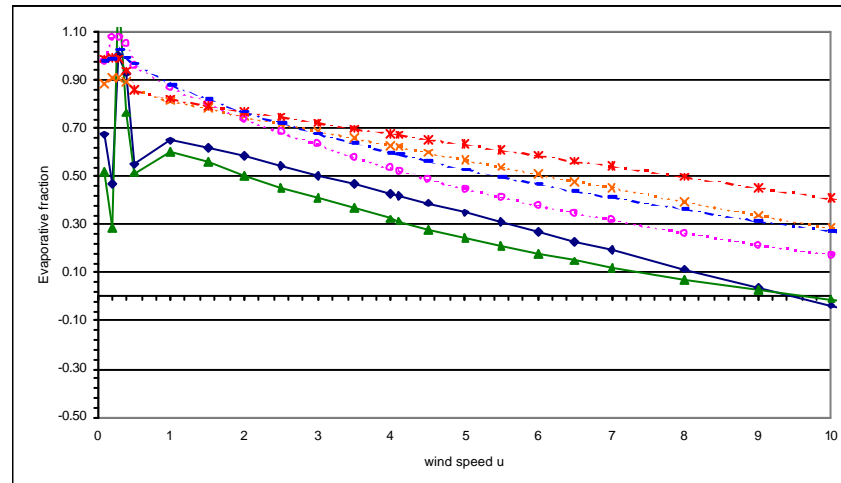
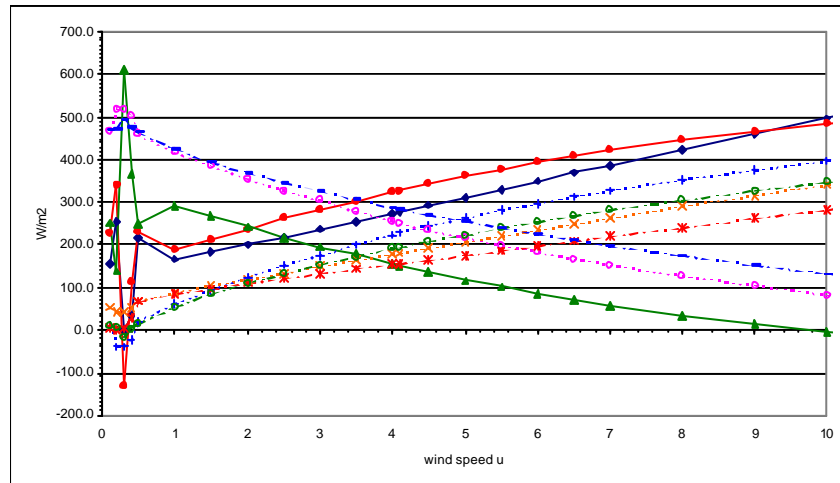
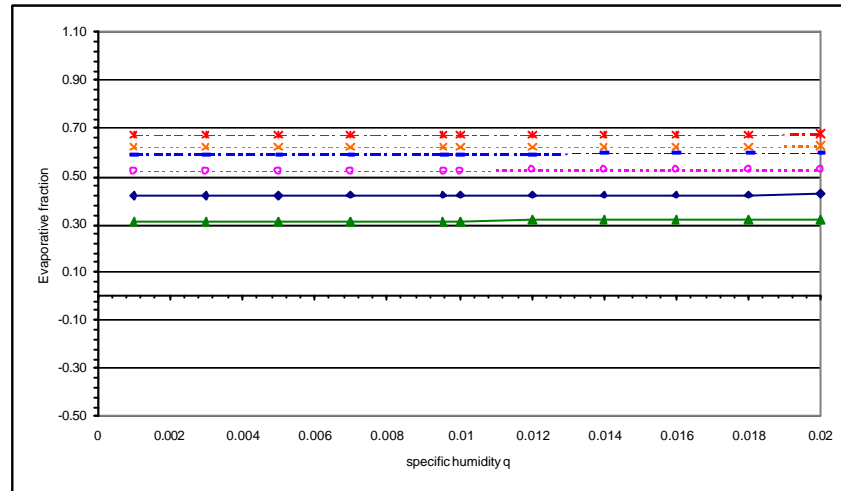
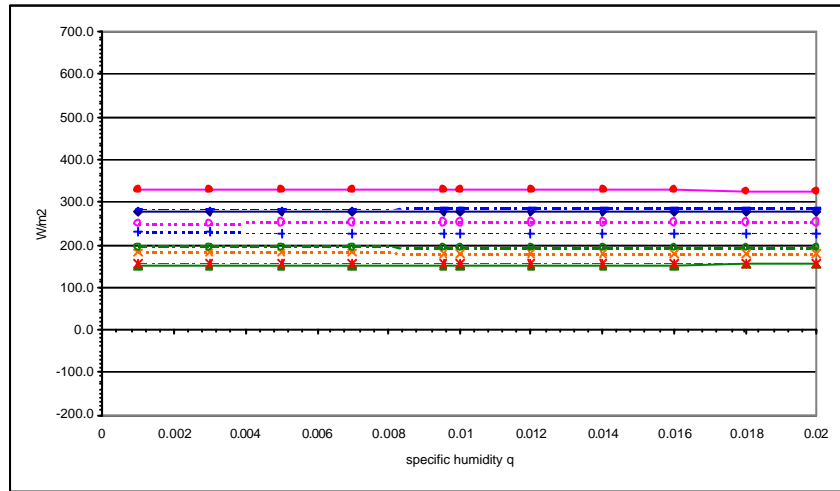
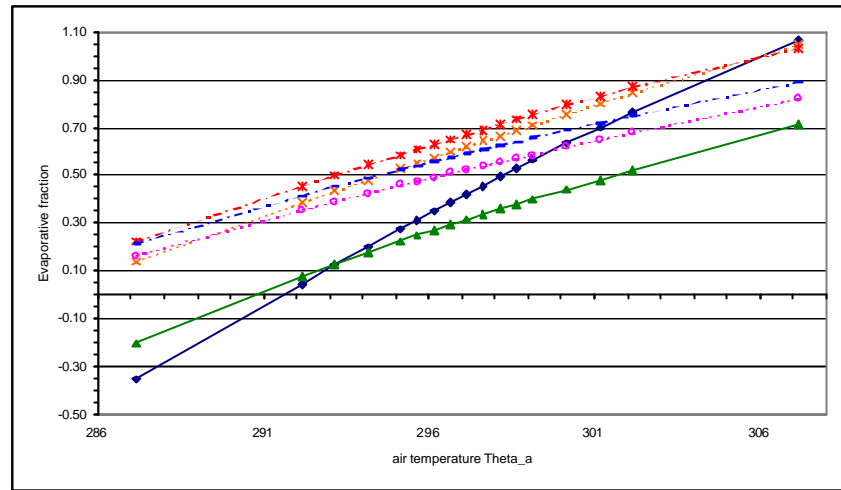
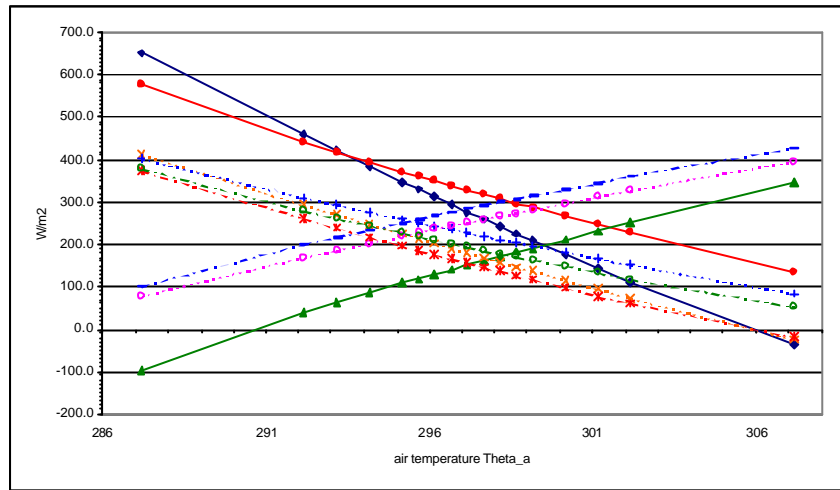


Appendix 3

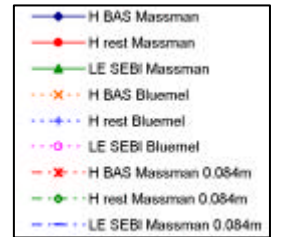
Sensitivity Analysis - Tomelloso - June 2, 1999

Tower Measurements

explanation: see § 5.1



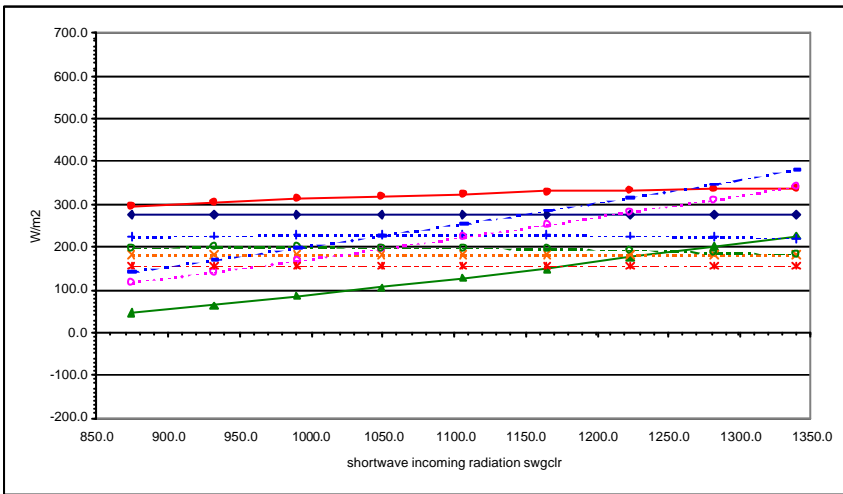
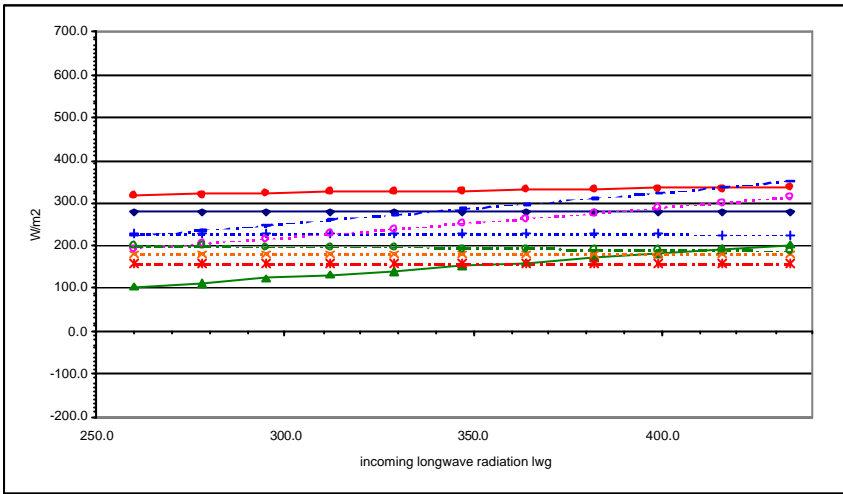
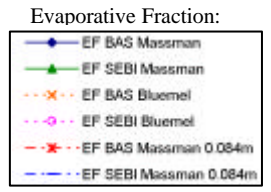
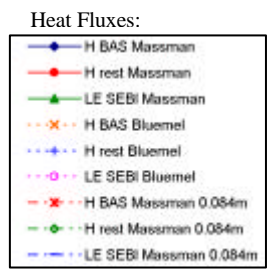
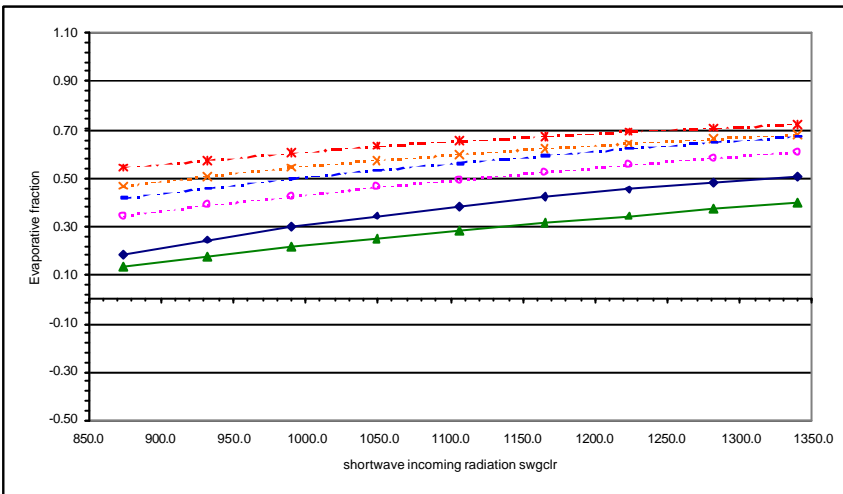
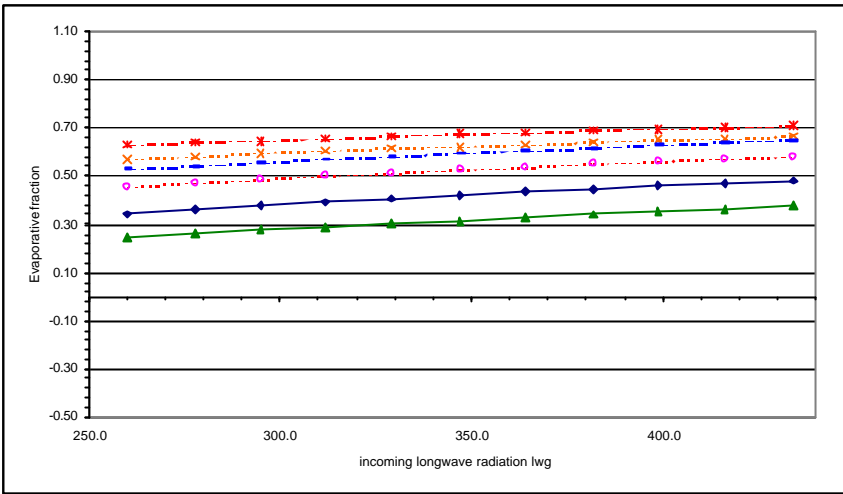
Heat Fluxes:

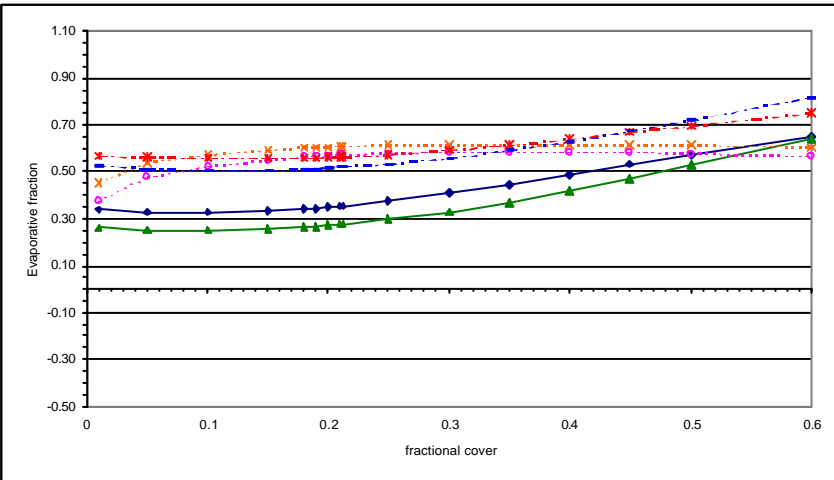
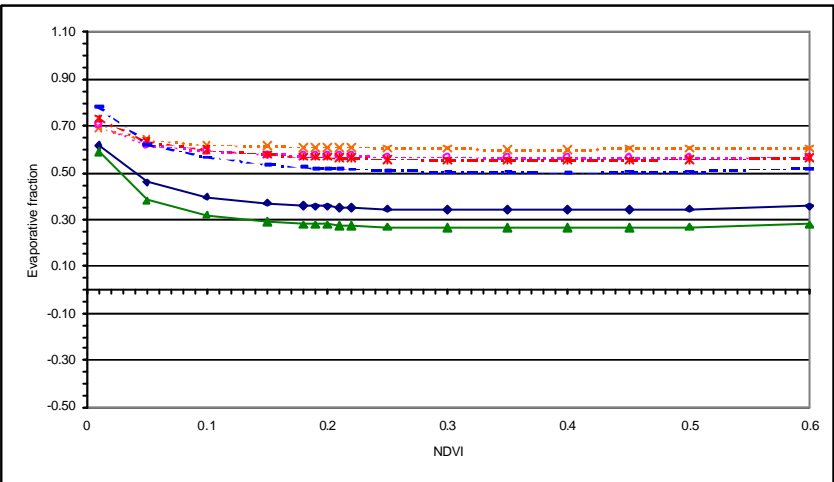
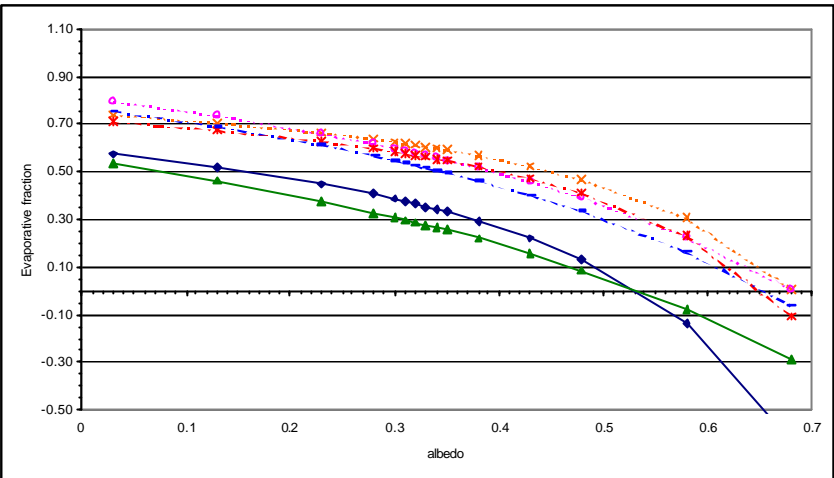


Evaporative Fraction:

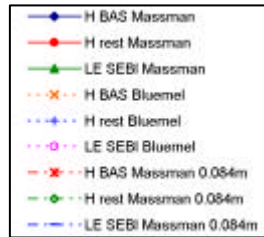


explanation: see § 5.1

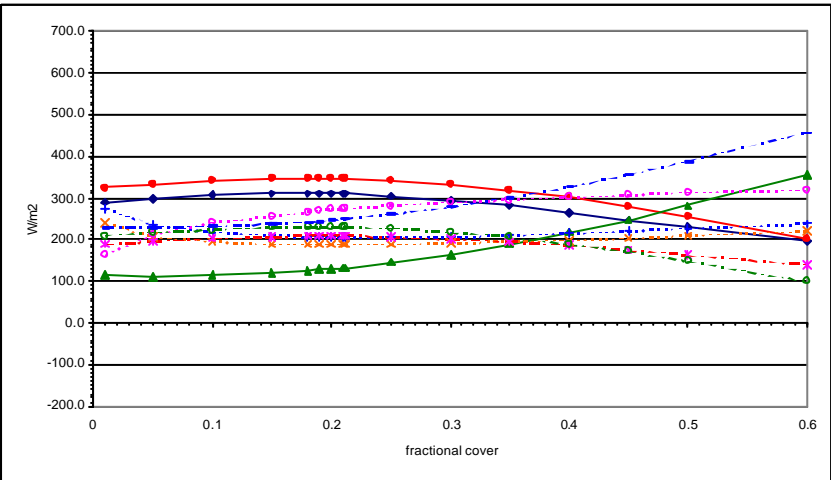
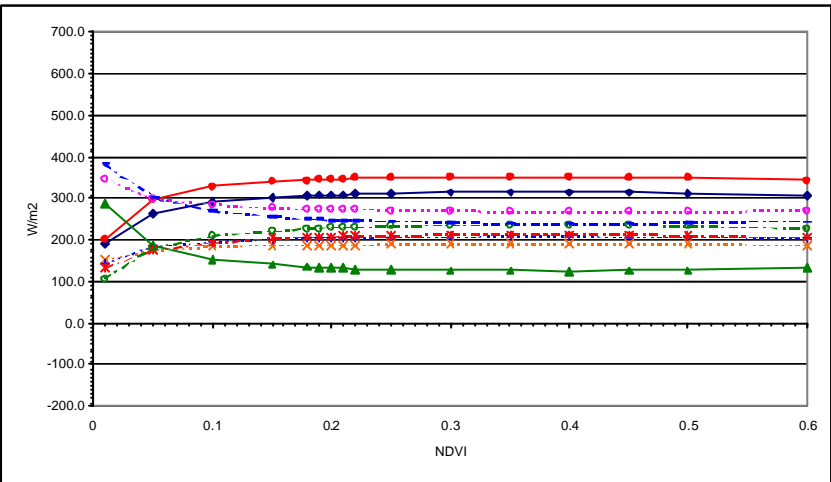
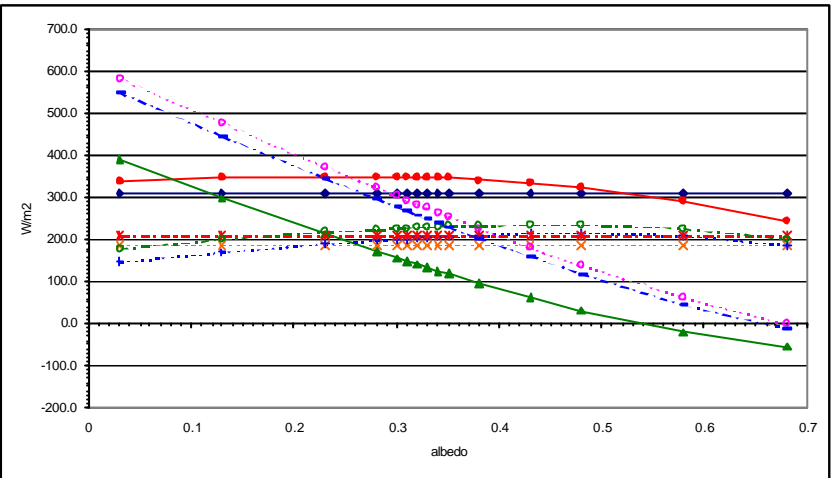
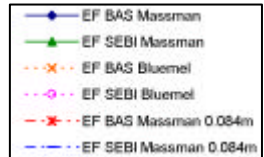




Heat Fluxes:



Evaporative Fraction:

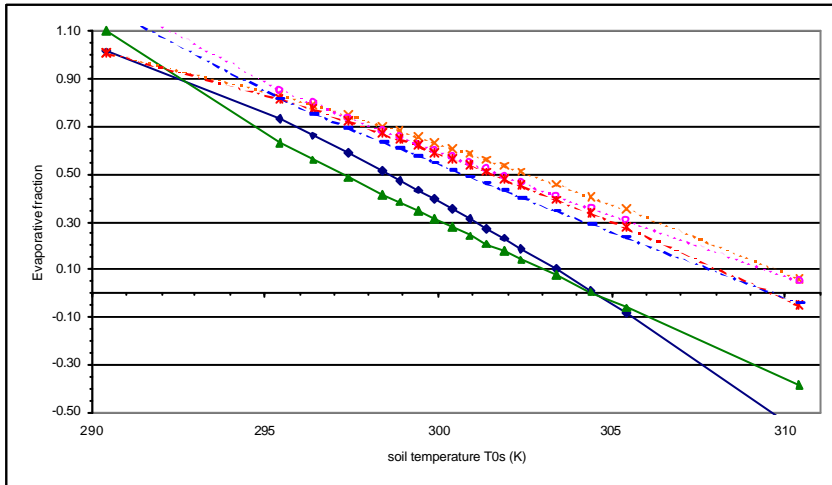
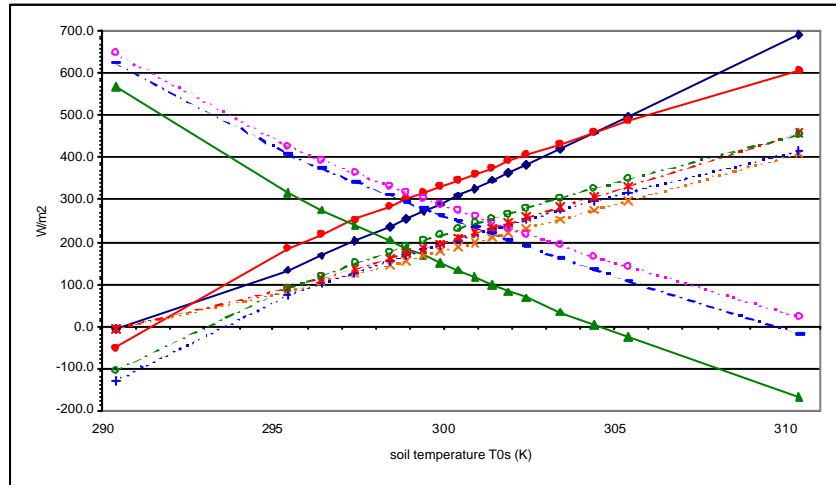
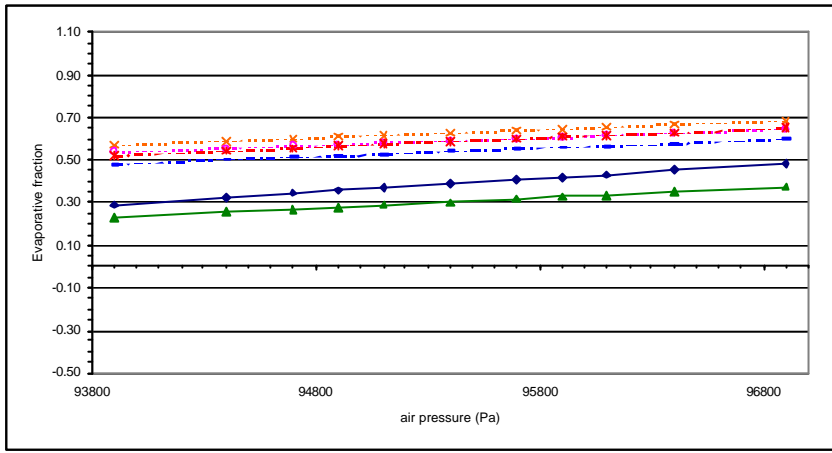
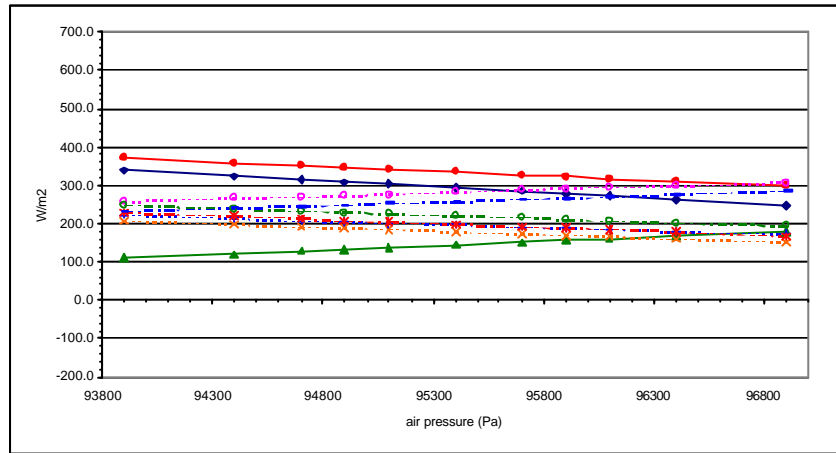
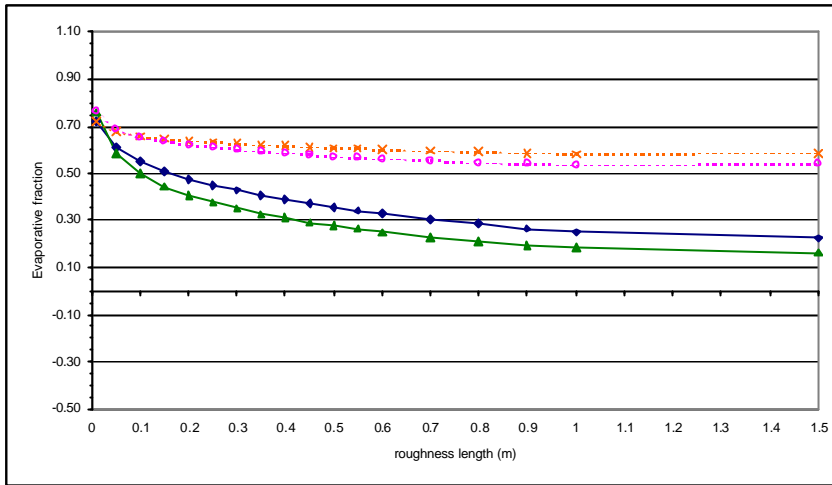
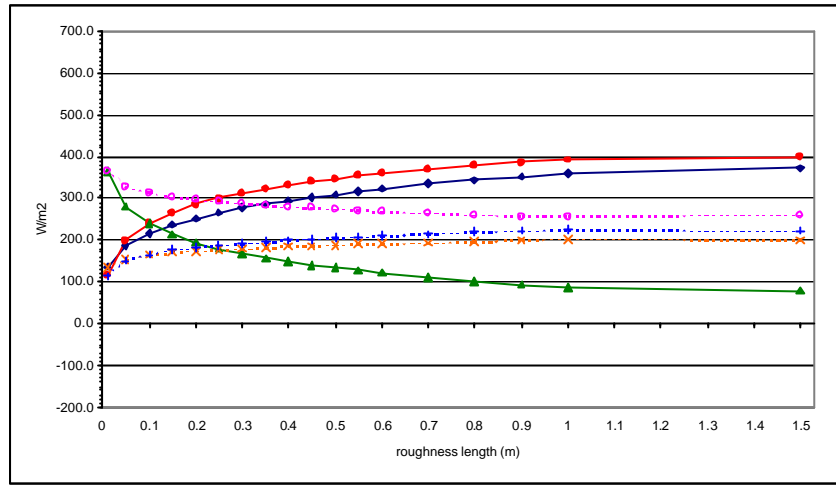


Appendix 3

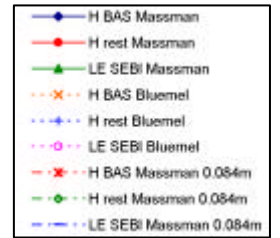
Sensitivity Analysis - Tomelloso - June 2, 1999

Radio Sounding Madrid

explanation: see § 5.1



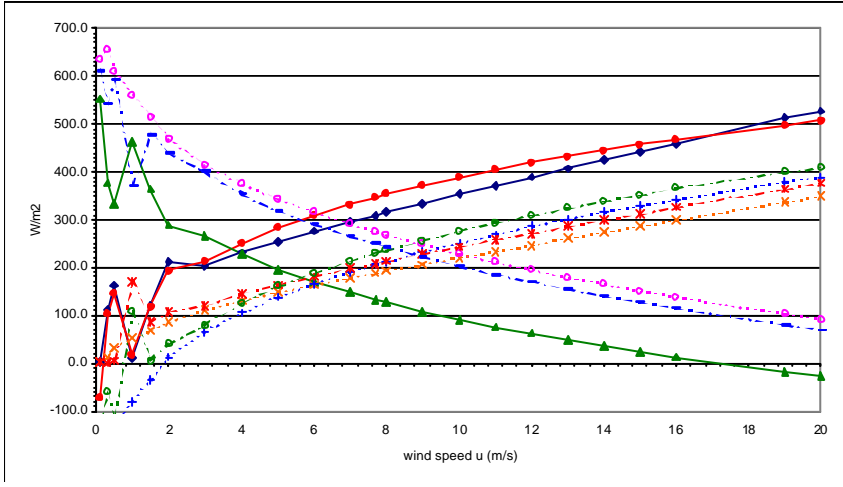
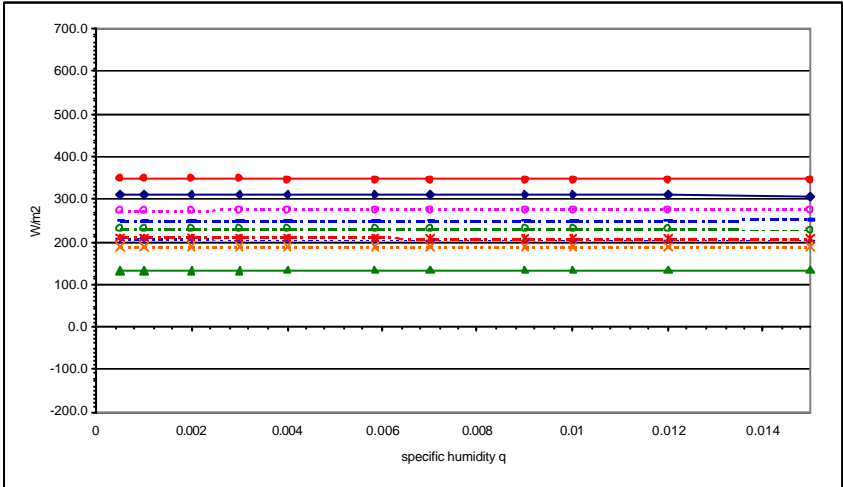
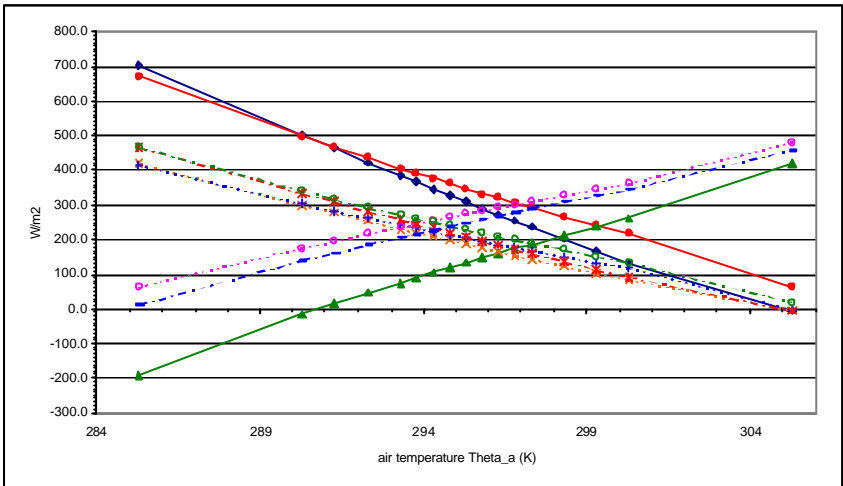
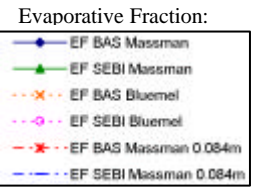
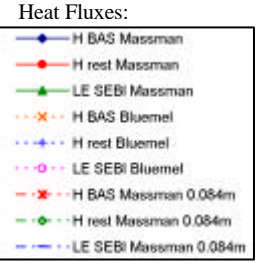
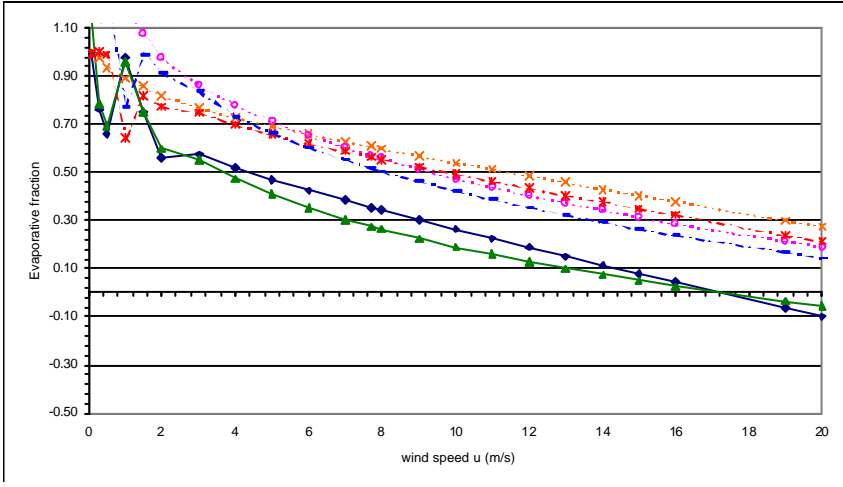
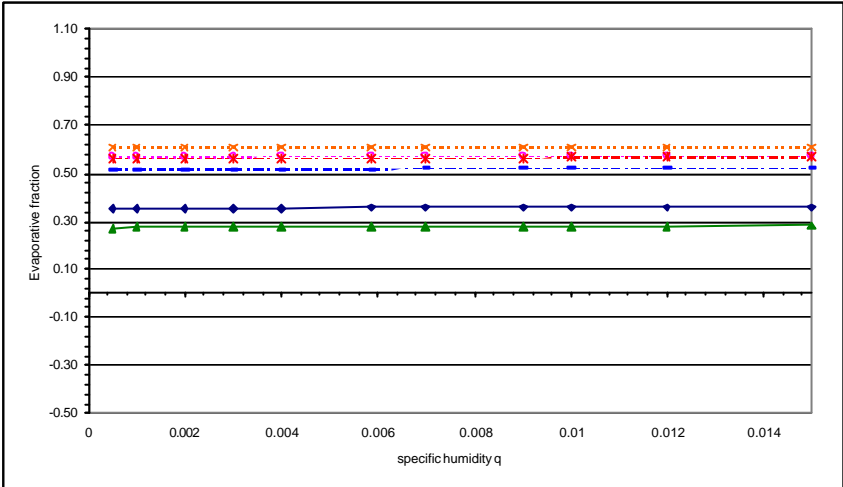
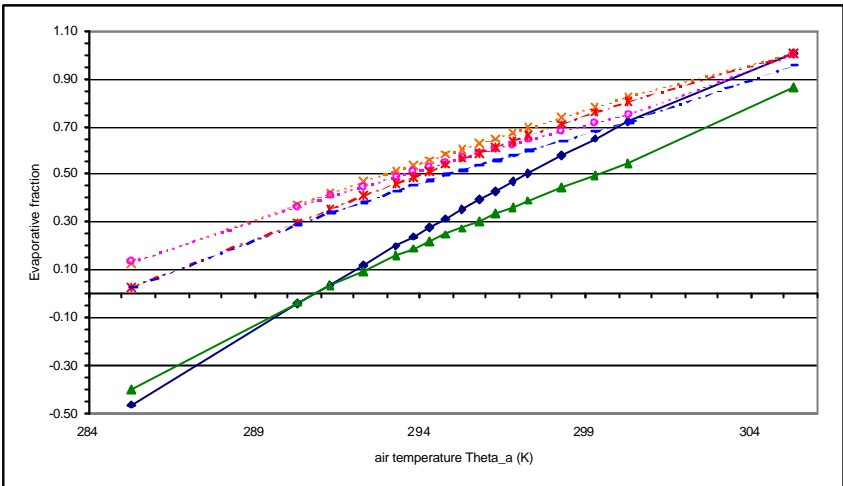
Heat Fluxes:



Evaporative Fraction:



explanation: see § 5.1

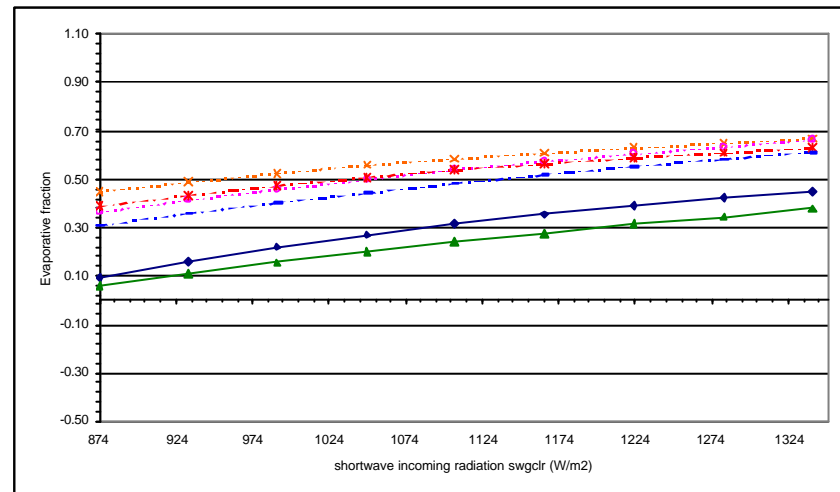
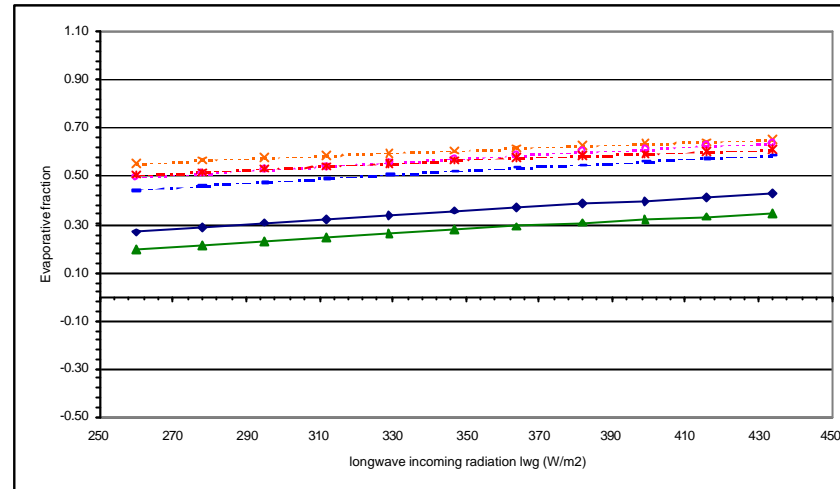


Appendix 3

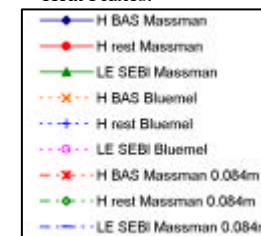
Sensitivity Analysis - Tomelloso - June 2, 1999

Radio Sounding Madrid

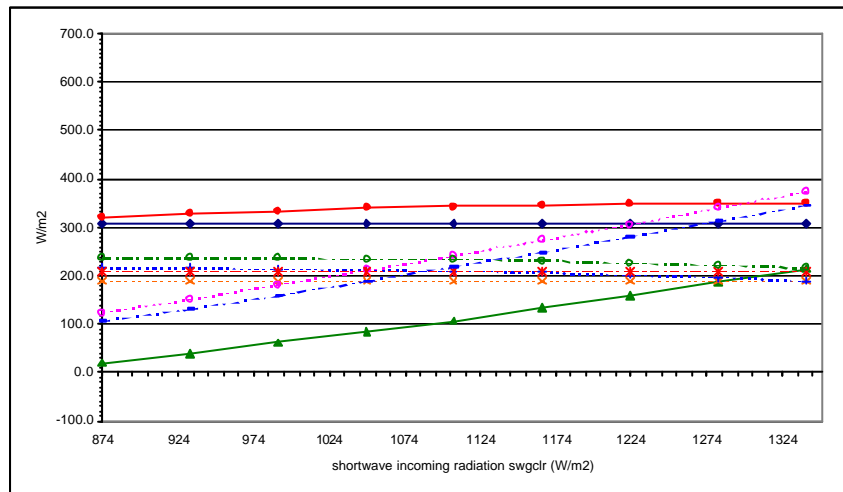
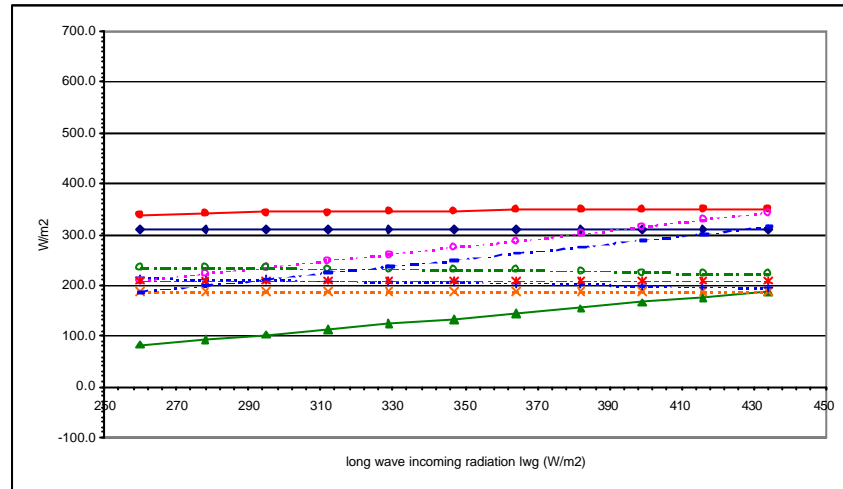
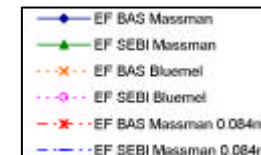
explanation: see § 5.1



Heat Fluxes:



Evaporative Fraction:



Appendix 3b

Sensitivity Analysis - Loobos, May 7, 1997

explanation: see § 5. 2.1

Input-Parameter x	Range	y ¹	Loobos - May 7, 1997 - Tower Measurement									
			$\delta H_{BAS}/\delta x$		$\delta H_{rest}/\delta x$		$\delta \lambda_{E_{SEBI}}/\delta x$		$\delta \Lambda_{rest}/\delta x$		$\delta \Lambda_{SEBI}/\delta x$	
			Ma	Bl	Ma	Bl	Ma	Bl	Ma	Bl	Ma	Bl
albedo	0.03 - 0.3	%	0	0	0.548	0.381	-3.29	-3.13	-0.111	-0.111	-0.704	-0.667
NDVI	0.3 - 0.5	% ²	0.074	0.05	0.495	0.28	-0.535	-0.35	-0.05	-0.05	-0.25	-0.15
frac. cover	0.4 - 0.6	%	-0.161	0.26	-1.44	1.155	2.34	-0.32	0.10	-0.08	0.70	-0.40
z _{0m}	0.5 - 2.0	cm	0.057	0.087	0.423	0.517	-0.423	-0.517	-0.02	-0.04	-0.181	-0.237
air pressure	98.7 - 101.7	kPa	-18.2	-20.2	-14.2	-14.5	14.2	14.5	7.6	9.3	6.0	6.7
T _{0s}	279 - 283.5	K	24.0	26.8	25.3	24.4	-29.1	-28.2	-10.7	-12.9	-11.3	-12.0
θ _{pbl}	276.5 - 280	K	-25.4	-28.6	-20.8	-21.3	20.8	21.3	10.9	13.1	8.9	9.7
sp.hum. q	1 - 8	gkg ⁻¹	-0.01	-0.01	-0.07	-0.07	0.07	0.07	0	0	0	0.02
wind sp. u	3.0 - 5.0	ms ⁻¹	4.2	4.5	22.6	19.7	-22.6	-19.7	-1.5	-2.0	-9.9	-9.0
lwg	233 - 388	Wm ⁻²	0	0	-0.23	-0.15	0.99	0.91	0.03	0.034	0.17	0.18
swgclr	233 - 388	Wm ⁻²	0	0	-0.16	-0.08	0.93	0.79	0.03	0.042	0.18	0.18

input-parameter x	range	y ¹	Loobos - May 7, 1997 - Radio Sounding									
			$\delta H_{BAS}/\delta x$		$\delta H_{rest}/\delta x$		$\delta \lambda_{E_{SEBI}}/\delta x$		$\delta \Lambda_{rest}/\delta x$		$\delta \Lambda_{SEBI}/\delta x$	
			Ma	Bl	Ma	Bl	Ma	Bl	Ma	Bl	Ma	Bl
albedo	0.03 - 0.3	%	0	0	1.34	1.77	-3.77	-4.21	0.074	0.074	-0.741	-0.815
NDVI	0.3 - 0.5	%	-0.02	-0.005	0.47	0.165	-0.51	-0.205	0.05	0	-0.25	-0.10
frac. cover	0.4 - 0.6	%	0.05	-0.055	-1.34	0.435	0.021	0.285	0.05	0	0.65	-0.30
z _{0m}	0.5 - 2.0	cm	-0.008	-0.007	0.09	0.082	-0.09	-0.082	0.067	0.067	-0.047	-0.047
air pressure	98.7 - 101.7	kPa	-26.7	-20.5	-31.7	-31.0	31.7	31.0	14	11	17	16
T _{0s}	279 - 283.5	K	21.5	16.4	29.1	29.7	-32.9	-33.5	-11.8	-8.9	-16.0	-16.0
θ _{pbl}	276 - 279	K	-33.5	-24.3	-28.5	-24.1	28.4	15.0	17.7	12.7	15.3	12.7
sp.hum. q	1 - 8	gkg ⁻¹	0.01	0.01	-0.07	-0.07	0.07	0.07	0	0	0	0.01
wind sp. u	5.0 - 10.0	ms ⁻¹	-1.1	-0.9	9.9	10.8	-9.9	-10.8	0.6	0.4	-5.2	-5.6
lwg	233 - 310	Wm ⁻²	0	0	-0.39	-0.53	1.15	1.29	-0.03	-0.01	0.25	0.27
swgclr	233 - 309	Wm ⁻²	0	0	-0.37	-0.50	1.08	1.21	-0.03	-0.01	0.23	0.24

¹ $\delta H/\delta x$, $\delta \lambda/\delta x$ expressed as W/m²/y, $\delta \Lambda/\delta x$ expressed as %/y.

² If reflectance of bare soil in the VNIR channel and in the red channel are equal and reflectance in the VNIR channel are always greater than the reflectance in the red channel (i.e. if the properties of the surface meet the principles for which the NDVI has been designed, Leinders et al., 1989), the NDVI can be expressed as a percentage.

input-parameter x	range	y ¹	Tomelloso - June 2, 1999 - Tower Measurement									
			$\delta H_{BAS}/\delta x$		$\delta H_{rest}/\delta x$		$\delta \lambda_{E_{SEBI}}/\delta x$		$\delta \Lambda_{rest}/\delta x$		$\delta \Lambda_{SEBI}/\delta x$	
			Ma	Bl	Ma	Bl	Ma	Bl	Ma	Bl	Ma	Bl
albedo	0.03 - 0.33	%	0	0	-0.347	1.02	-7.97	-9.33	0.667	0.433	0.733	0.667
NDVI	0.15 - 0.25	% ²	1.22	0.49	1.16	0.73	-1.36	-0.93	-0.30	0.10	-0.20	-0.17
frac. cover	0.2 - 0.4	%	-2.38	2.47	-2.08	2.96	4.10	-0.94	0.65	-0.35	0.65	-0.39
z _{0m}	0.05 - 0.1	cm	5.64	2.60	7.02	3.18	-7.04	-3.20	-1.20	-0.40	-1.40	-0.66
z _{0m}	0.4 - 0.5	cm	2.22	0.94	2.23	1.43	-2.23	-1.43	-0.45	-0.20	-0.45	-0.30
air pressure	93.0 - 96.0	kPa	-30	-19	-17.2	-12.3	17.2	12.3	6.3	-0.3	3.7	2.6
T _{0s}	298.4 - 303.4	K	35.2	22.2	22.6	19.7	-26.7	-23.8	-7.8	-5.0	-5.2	-4.6
θ _{pbl}	295.2 - 300.2	K	-34.7	-22.0	-20.7	-15.5	20.7	15.5	7.2	4.6	4.2	3.2
sp.hum. q	1 - 10	gkg ⁻¹	-0.19	-0.12	-0.17	-0.16	0.17	0.16	0	0	0.11	0.03
wind sp. u	3.0 - 6.0	ms ⁻¹	37.7	28.6	37.0	40.5	-37.0	-40.5	-8.0	-6.0	-7.7	-8.4
lwg	260 - 434	Wm ⁻²	0	0	0.10	0.03	0.56	0.69	0.08	0.05	0.07	0.07
swgclr	874 - 1340	Wm ⁻²	0	0	0.09	0.03	0.39	0.48	0.07	0.05	0.06	0.06

input-parameter x	range	y ¹	Tomelloso - June 2, 1997 - Radio Sounding									
			$\delta H_{BAS}/\delta x$		$\delta H_{rest}/\delta x$		$\delta \lambda_{E_{SEBI}}/\delta x$		$\delta \Lambda_{rest}/\delta x$		$\delta \Lambda_{SEBI}/\delta x$	
			Ma	Bl	Ma	Bl	Ma	Bl	Ma	Bl	Ma	Bl
albedo	0.03 - 0.33	%	0	0	0.263	1.977	-8.57	-10.29	-0.733	-0.433	-0.867	-0.759
NDVI	0.15 - 0.25	% ²	0.96	0.27	0.93	0.43	-1.13	-0.63	-0.20	-0.01	-0.20	-0.109
frac. cover	0.2 - 0.4	%	-2.28	0.53	-2.33	0.455	4.35	1.565	0.70	0.05	0.75	0.08
z _{0m}	0.05 - 0.1	cm	5.90	1.84	8.28	3.20	-8.26	-3.20	-1.20	0.40	-1.60	0.66
z _{0m}	0.4 - 0.5	cm	1.50	0.37	1.52	0.58	-1.52	-0.58	-0.30	0.10	-0.30	0.123
air pressure	93.9 - 96.9	kPa	-31	-18	-24	-17	24	17	6.3	3.7	5.0	3.5
T _{0s}	298.4 - 303.4	K	36.9	21.7	29.7	24.1	-33.8	-28.3	-8.2	-4.8	-7.0	-5.4
θ _{pbl}	293.8 - 296.8	K	-36.9	-21.8	-27.9	-18.5	27.9	18.5	7.7	4.7	5.7	3.9
sp.hum. q	1 - 10	gkg ⁻¹	-0.22	-0.13	-0.21	-0.19	0.21	0.19	0.1	0	0.1	0
wind sp. u	5.0 - 10.0	ms ⁻¹	19.4	14.3	19.7	21.6	-19.7	-21.6	-4.0	-3.0	-4.0	-4.5
lwg	260 - 434	Wm ⁻²	0	0	0.062	-0.1	0.60	0.77	0.086	0.057	0.086	0.081
swgclr	874 - 1340	Wm ⁻²	0	0	0.065	-0.06	0.41	0.53	0.077	0.047	0.069	0.064

³ $\delta H/\delta x$, $\delta \lambda/\delta x$ expressed as W/m²/y, $\delta \Lambda/\delta x$ expressed as %/y.

³ If reflectance of bare soil in the VNIR channel and in the red channel are equal and reflectance in the VNIR channel are always greater than the reflectance in the red channel (i.e. if the properties of the surface meet the principles for which the NDVI has been designed, Leinders et al., 1989), the NDVI can be expressed as a percentage.

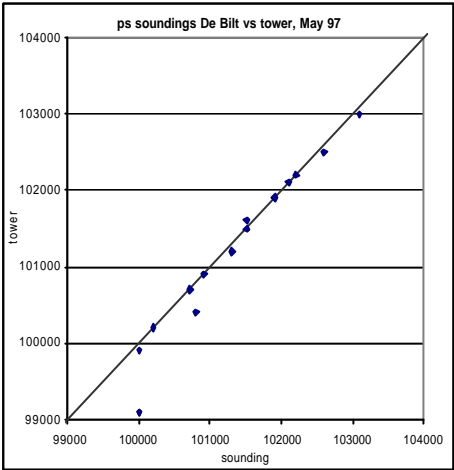
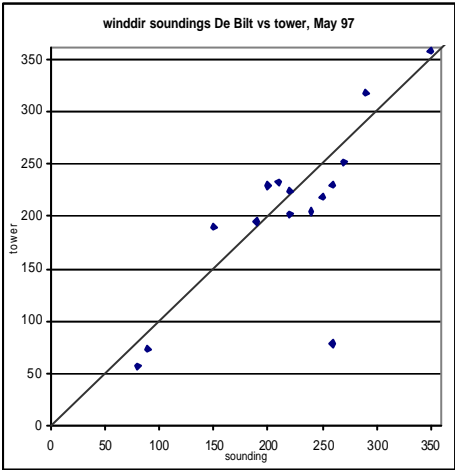
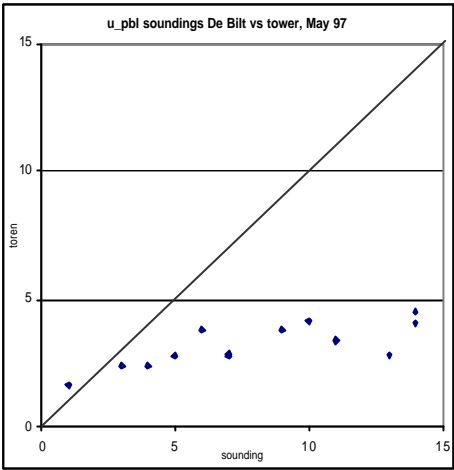
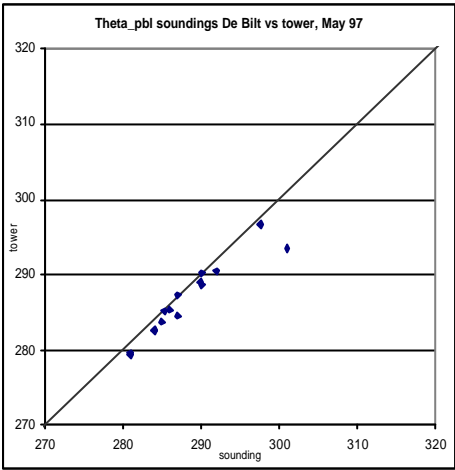
Appendix 3c

Sensitivity Analysis - Fractional Cover and kB^1 factor

explanation: see § 5.2.1

fractional coverage F	Loobos Tower Massman		Loobos Tower Bluemel		Loobos Radio S. Massman		Loobos Radio S. Bluemel	
	kB-1	EF-SEBI	kB-1	EF-SEBI	kB-1	EF-SEBI	kB-1	EF-SEBI
0.01	5.87	0.621	11.311	0.840	6.53	0.935	8.99	1.060
0.05	5.82	0.626	14.161	0.958	6.39	0.937	11.29	1.168
0.1	5.82	0.637	13.930	0.962	6.27	0.942	12.35	1.221
0.15	5.86	0.650	12.748	0.932	6.22	0.950	12.70	1.246
0.2	5.96	0.666	11.332	0.884	6.23	0.962	12.68	1.258
0.25	6.12	0.686	9.930	0.839	6.31	0.978	12.43	1.260
0.3	6.33	0.708	8.932	0.805	6.45	0.997	12.17	1.262
0.35	6.60	0.734	7.931	0.767	6.65	1.019	11.73	1.256
0.4	6.93	0.762	7.096	0.734	6.92	1.044	11.22	1.247
0.45	7.31	0.792	6.415	0.706	7.25	1.073	10.66	1.235
0.5	7.74	0.825	5.870	0.684	7.65	1.105	10.07	1.221
0.55	8.23	0.859	5.443	0.666	8.11	1.139	9.47	1.204
0.6	8.78	0.895	5.112	0.654	8.63	1.175	8.85	1.186
0.65	9.38	0.932	4.862	0.646	9.22	1.213	8.24	1.165
0.7	10.03	0.970	4.674	0.642	9.87	1.252	7.62	1.143
0.75	10.75	1.009	4.536	0.640	10.59	1.293	7.02	1.120

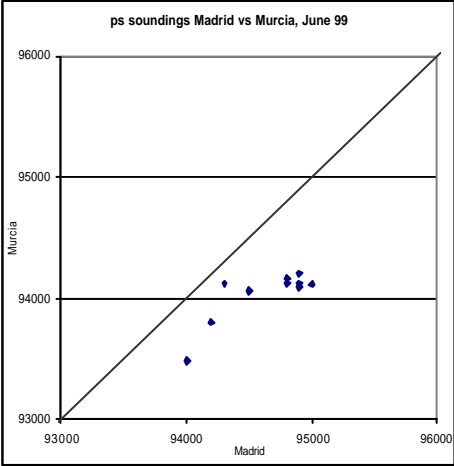
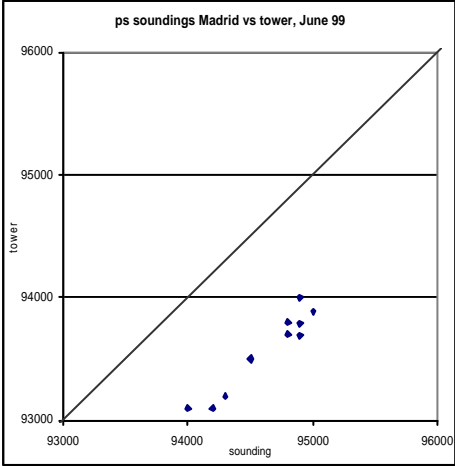
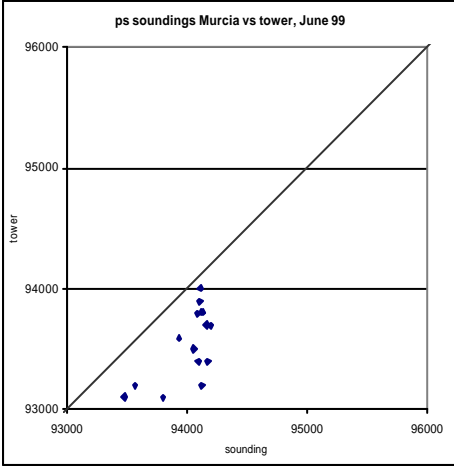
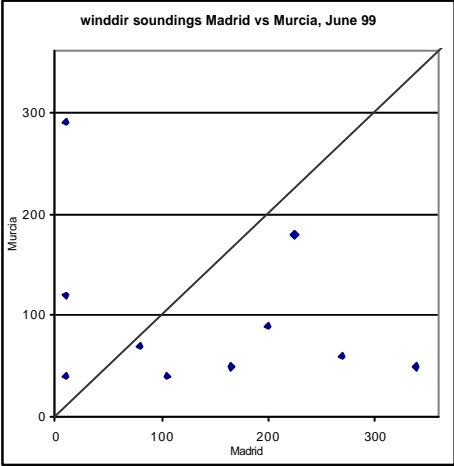
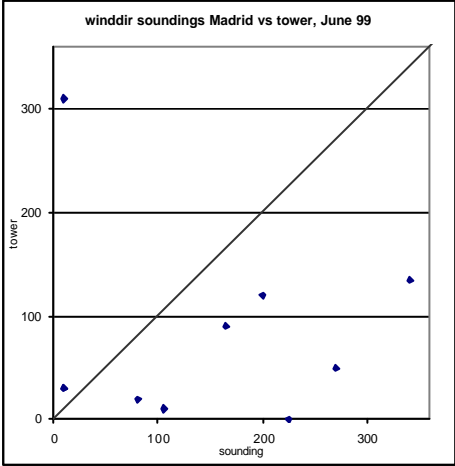
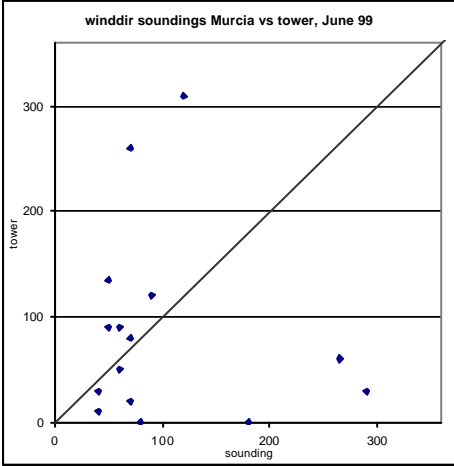
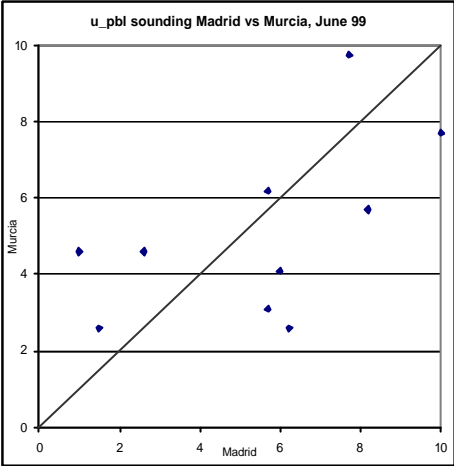
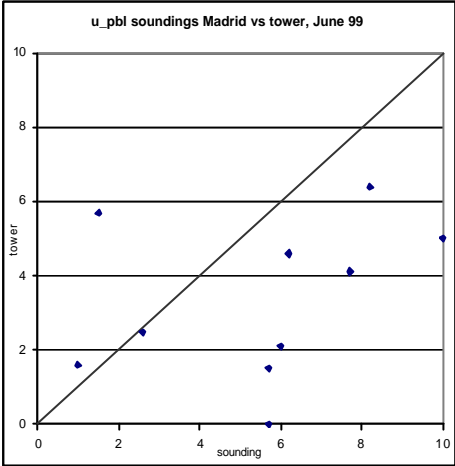
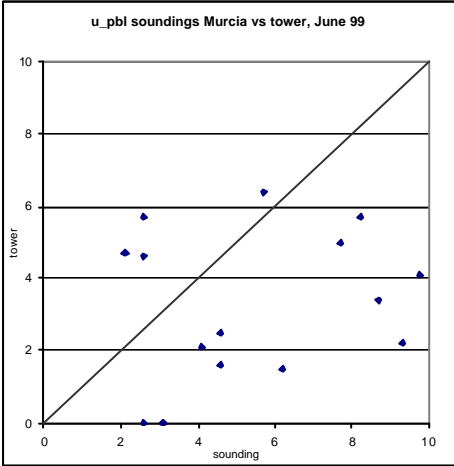
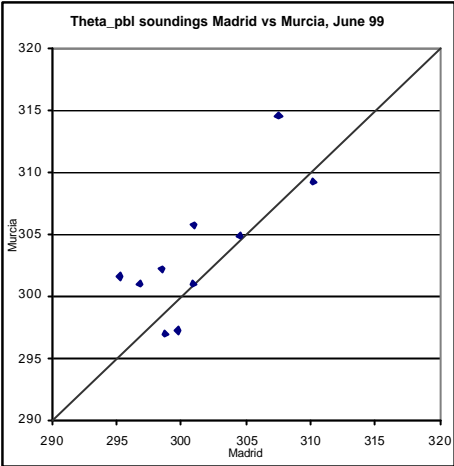
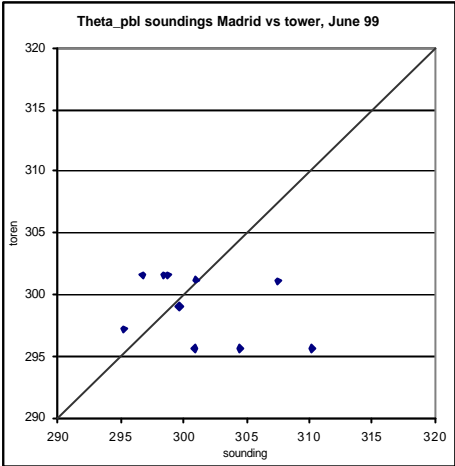
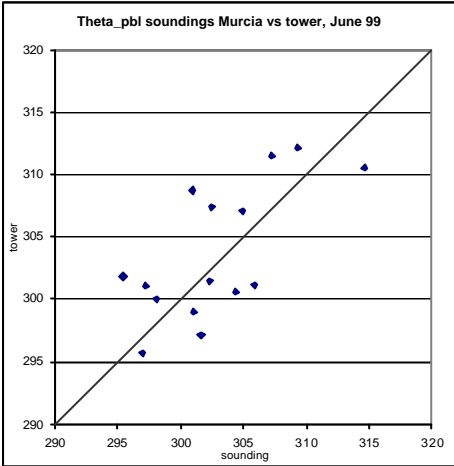
fractional coverage F	Tomelloso Tower Massman		Tomelloso Tower Bluemel		Tomelloso Radio S. Massman		Tomelloso Radio S. Bluemel	
	kB-1	EF-SEBI	kB-1	EF-SEBI	kB-1	EF-SEBI	kB-1	EF-SEBI
0.01	6.34	0.287	6.19	0.484	6.46	0.259	6.31	0.375
0.05	6.13	0.283	5.98	0.571	6.19	0.252	6.04	0.475
0.1	5.96	0.284	5.81	0.574	5.97	0.249	5.82	0.525
0.15	5.92	0.293	5.77	0.550	5.88	0.256	5.73	0.550
0.2	5.96	0.302	5.81	0.542	5.88	0.264	5.73	0.564
0.25	5.98	0.306	5.83	0.537	5.89	0.268	5.74	0.567
0.3	6.01	0.310	5.86	0.531	5.91	0.272	5.76	0.569
0.35	6.04	0.314	5.89	0.526	5.93	0.276	5.78	0.572
0.4	6.04	0.315	5.89	0.525	5.93	0.277	5.78	0.572
0.45	6.21	0.334	6.06	0.506	6.07	0.297	5.92	0.579
0.5	6.53	0.365	6.38	0.484	6.36	0.331	6.21	0.584
0.55	6.98	0.402	6.83	0.466	6.77	0.372	6.62	0.586
0.6	7.54	0.444	7.39	0.454	7.31	0.419	7.16	0.585
0.65	8.23	0.489	8.08	0.448	7.98	0.470	7.83	0.583
0.7	9.04	0.538	8.89	0.447	8.78	0.525	8.63	0.580
0.75	11.01	0.638	10.86	0.460	10.76	0.639	10.61	0.571

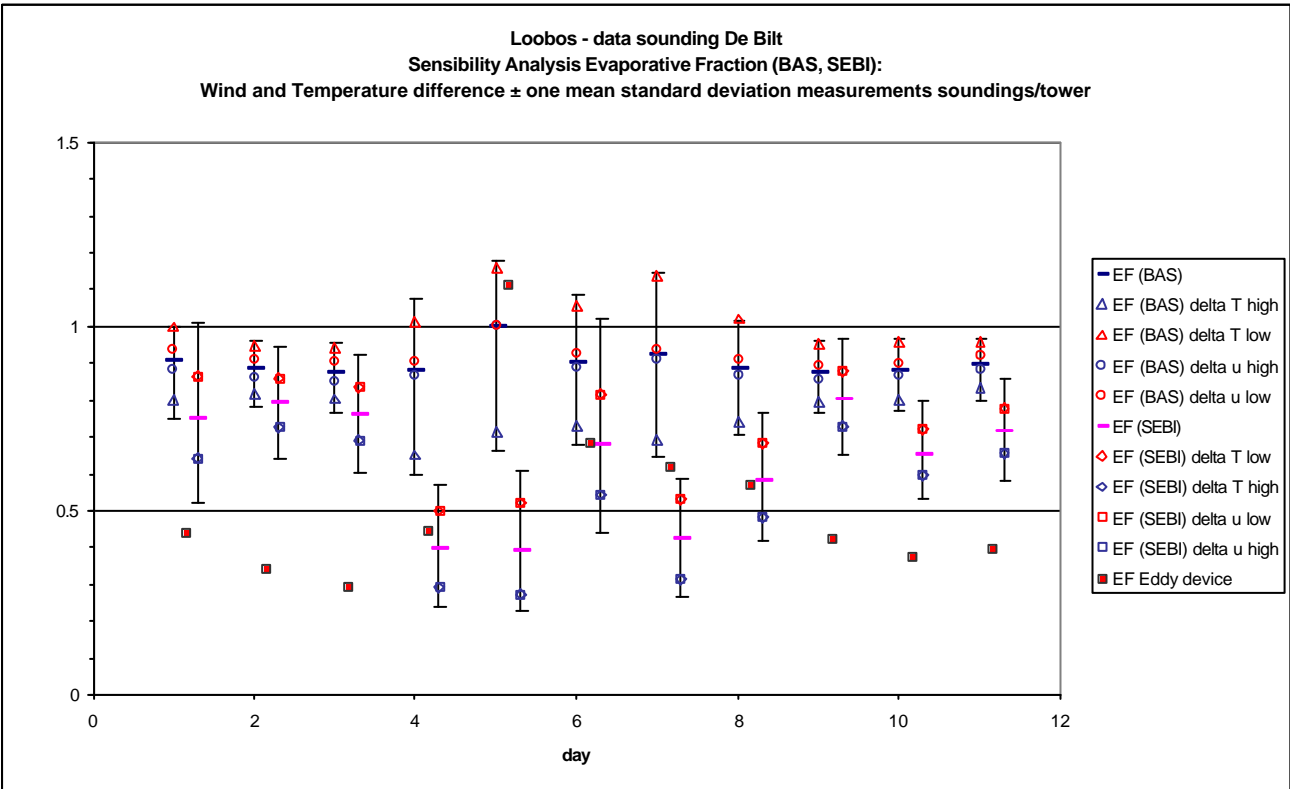
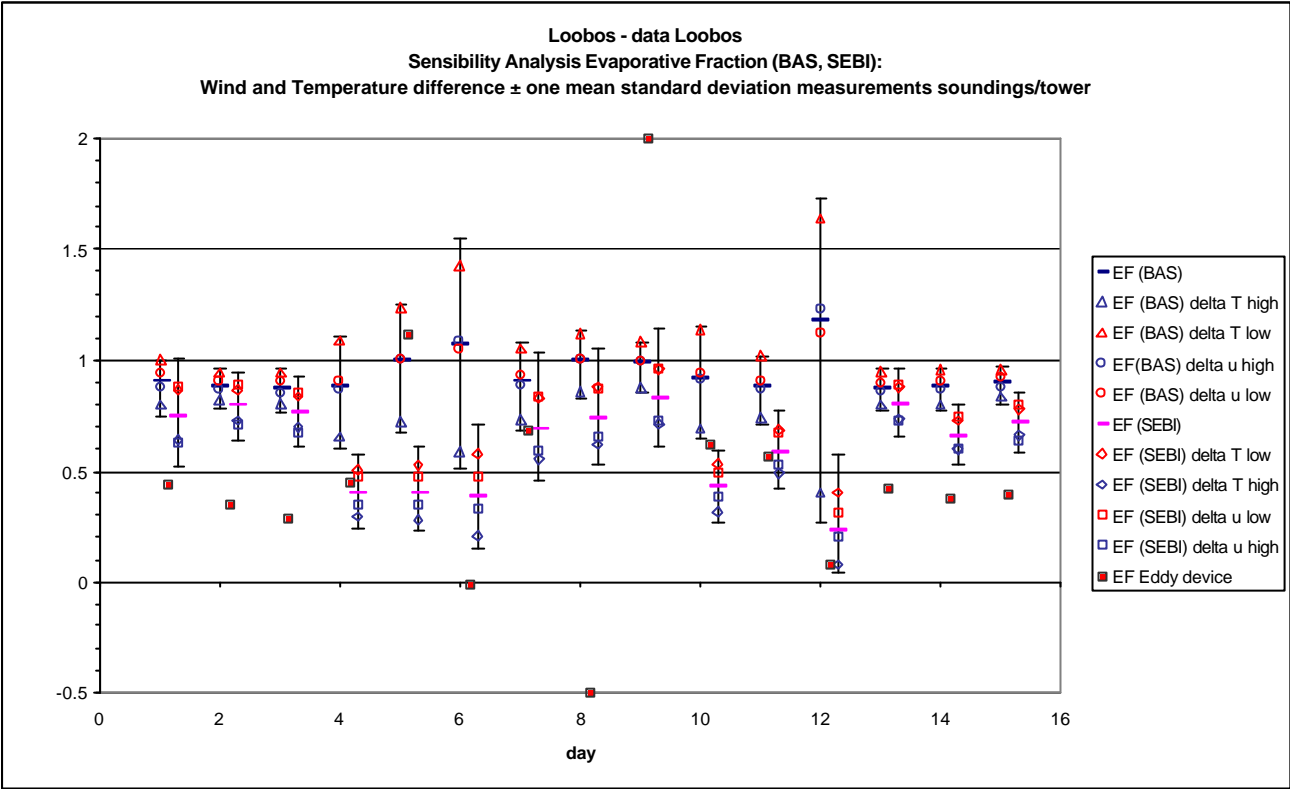


statistics the Netherlands		r
sounding De Bilt vs. tower		
Theta_pbl		0.950
u_pbl		0.697
q_pbl		0.572
ps		0.973
winddir		0.782

statistics Spain (see next page		r
sounding Murcia vs tower		
Theta_pbl		0.732
u_pbl		0.179
q_pbl		0.087
ps		0.620
winddir		0.088
sounding Madrid vs tower		
Theta_pbl		0.887
u_pbl		0.314
q_pbl		0.542
ps		0.959
winddir		0.004
sounding Madrid vs Murcia		
Theta_pbl		0.772
u_pbl		0.570
q_pbl		0.221
ps		0.792
winddir		-0.458

Appendix 3d Sensitivity Analysis - Tower measurements and radio soundings - Tomelloso, June 1999

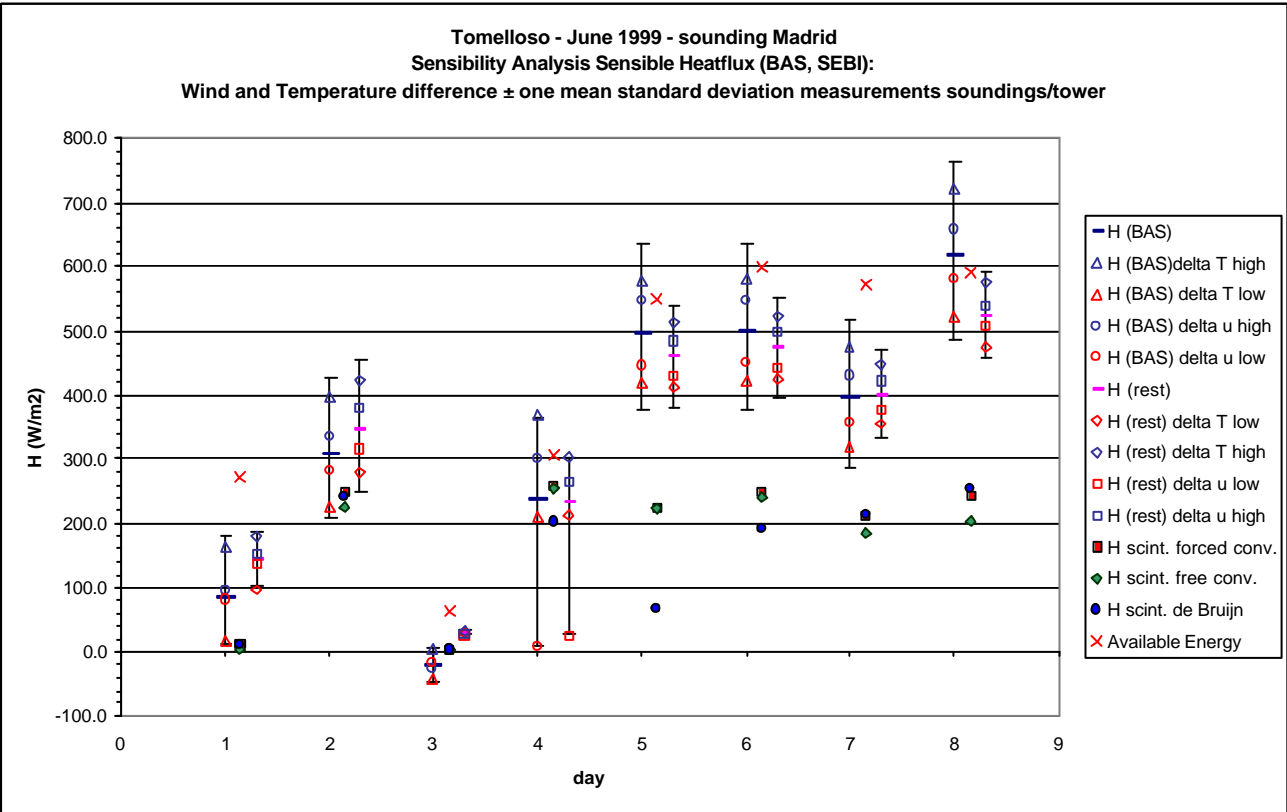
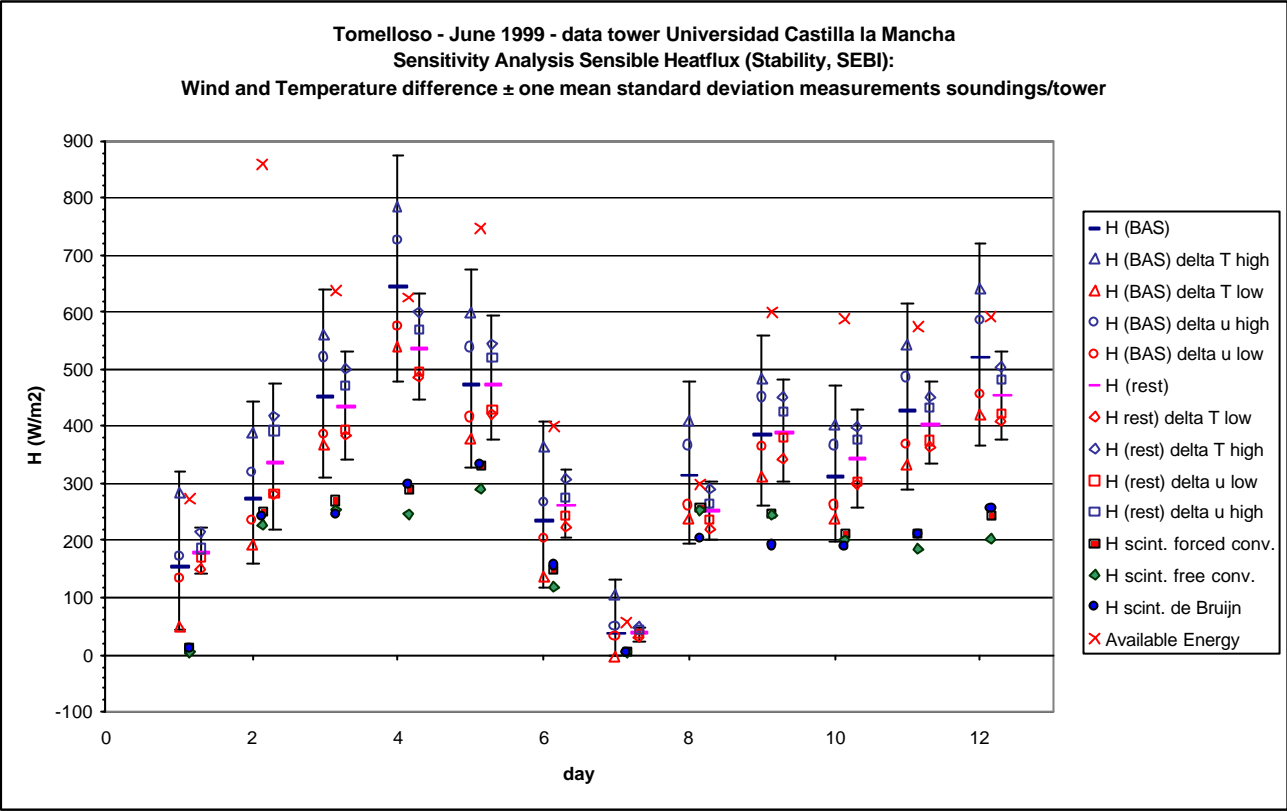




Sensitivity Analysis - sensitivity towards meteorological variables

Tomelloso June 1999 - roughness for momentum transfer = 0.5 m

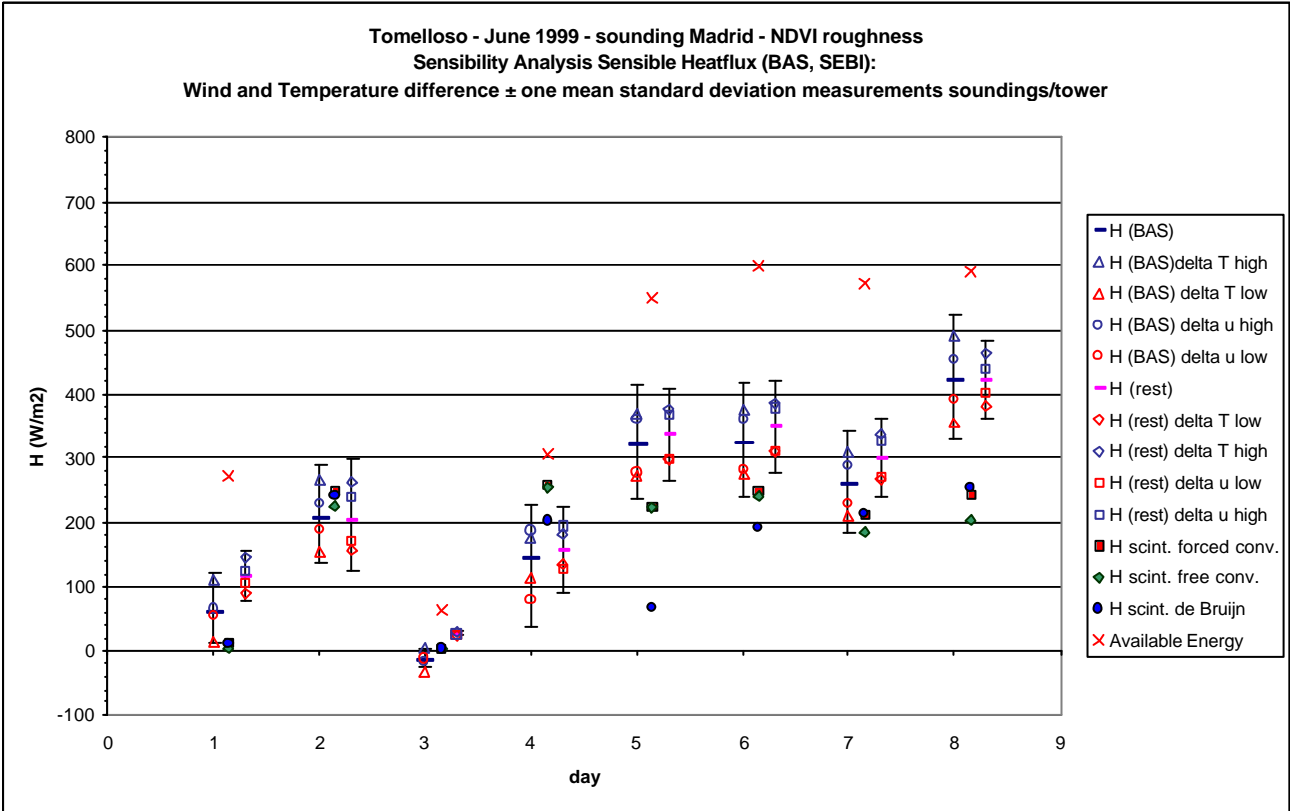
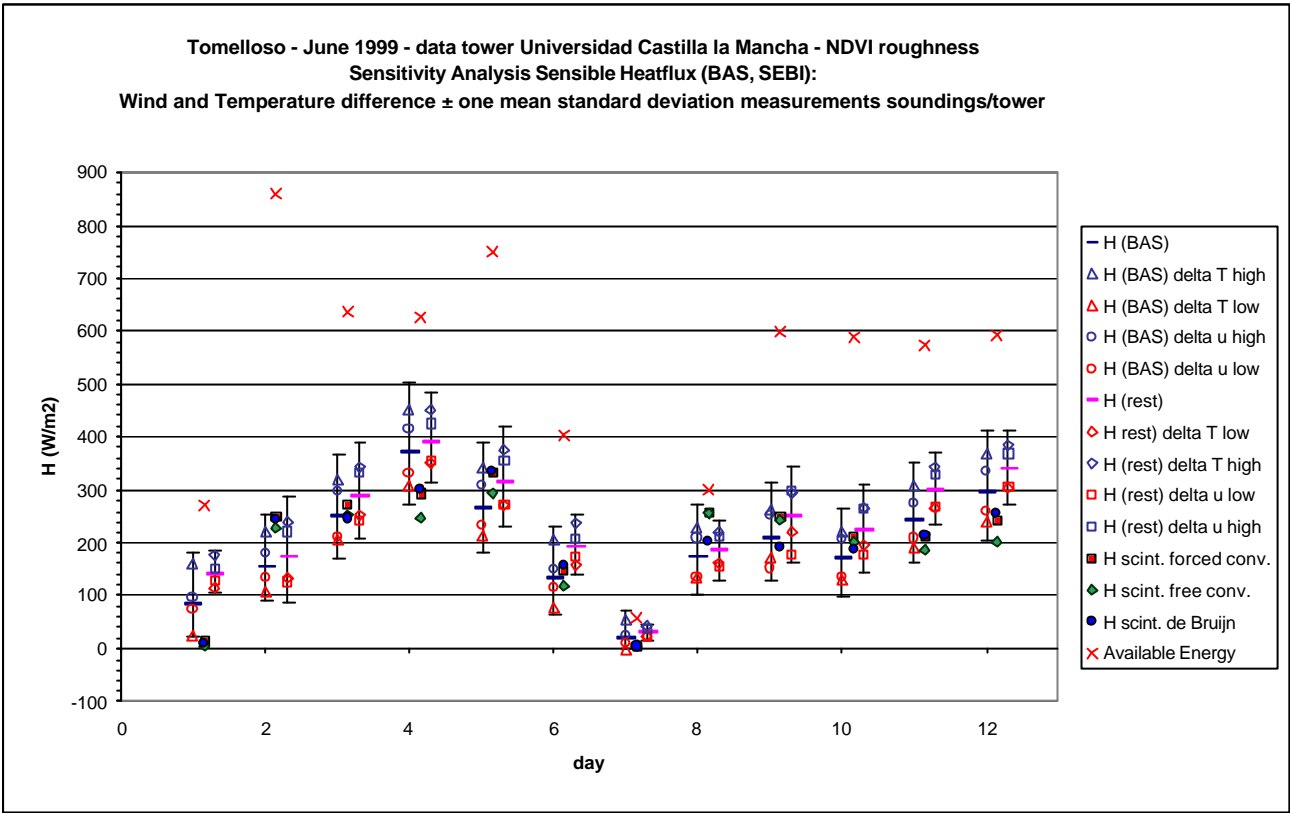
explanation: see § 5.2.2



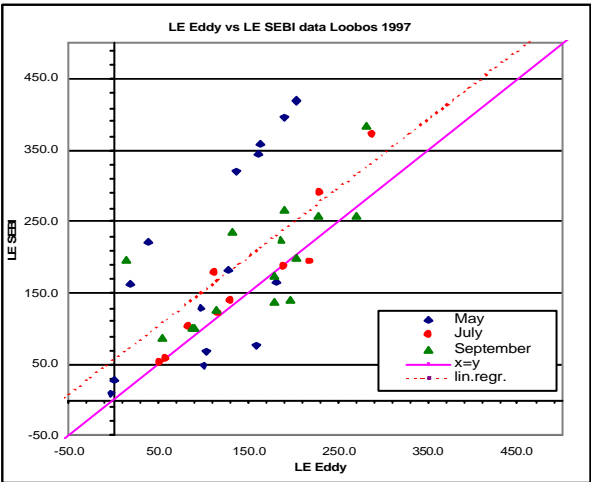
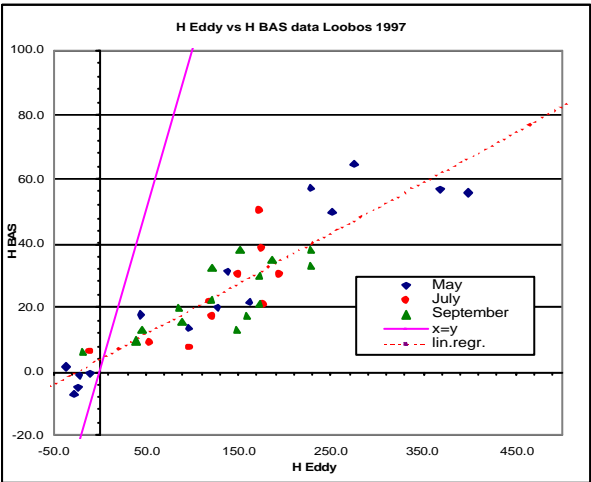
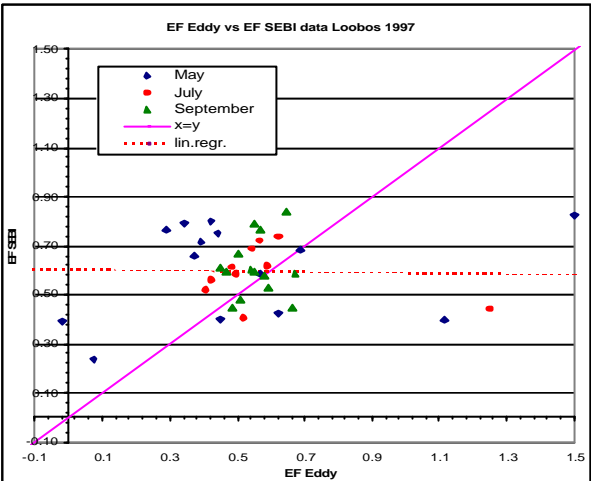
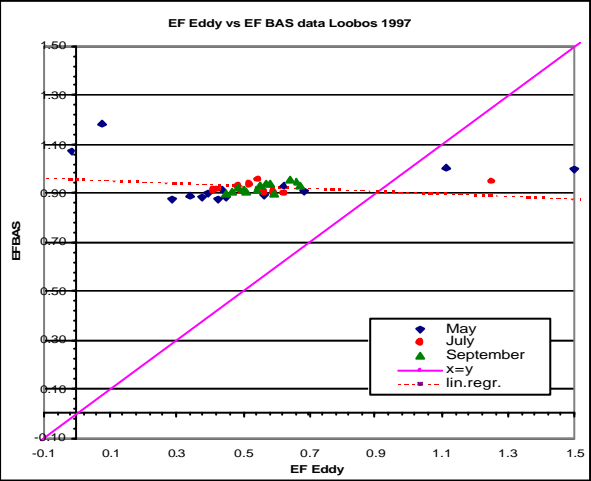
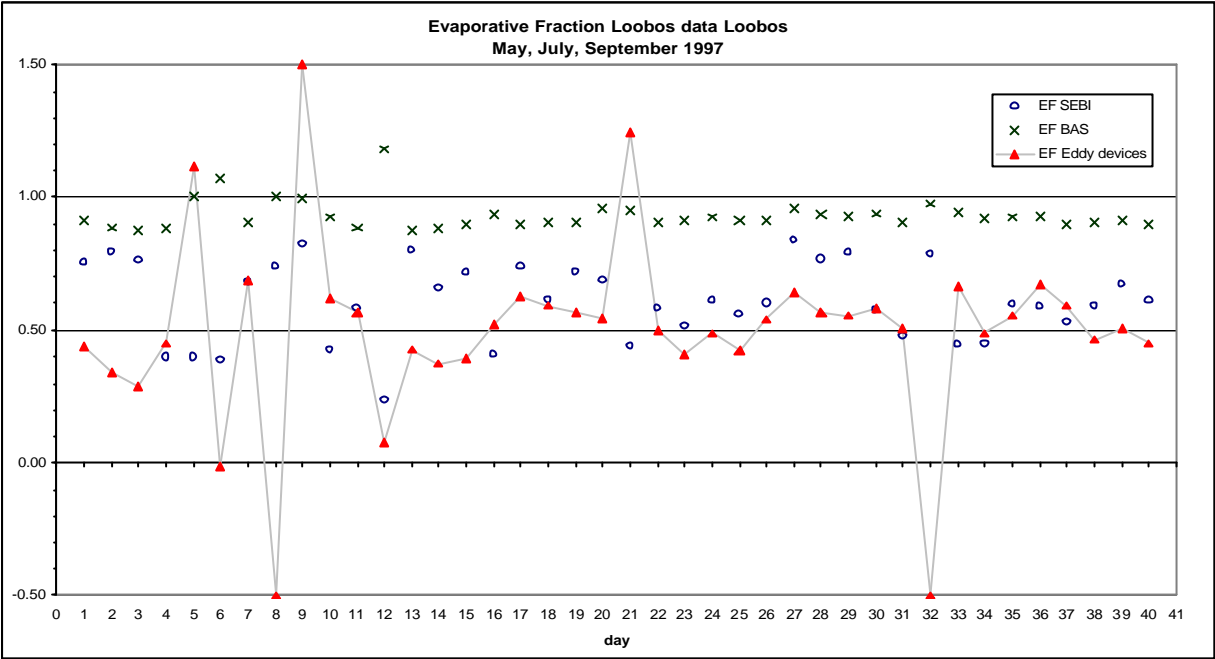
Sensitivity Analysis - sensitivity towards meteorological variables

Tomelloso June 1999 - roughness for momentum transfer = 0.084 m

explanation: see § 5.2.2

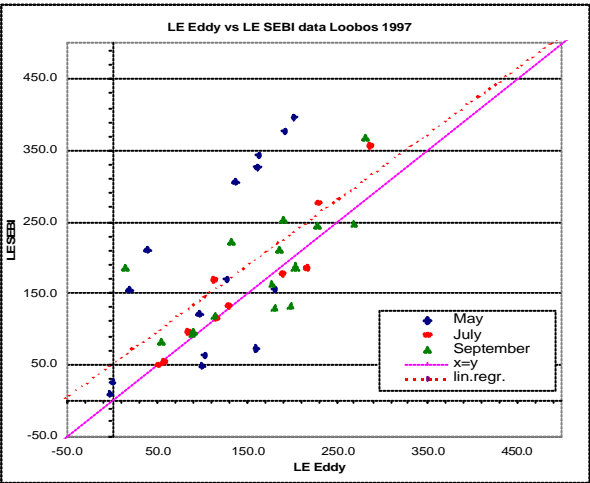
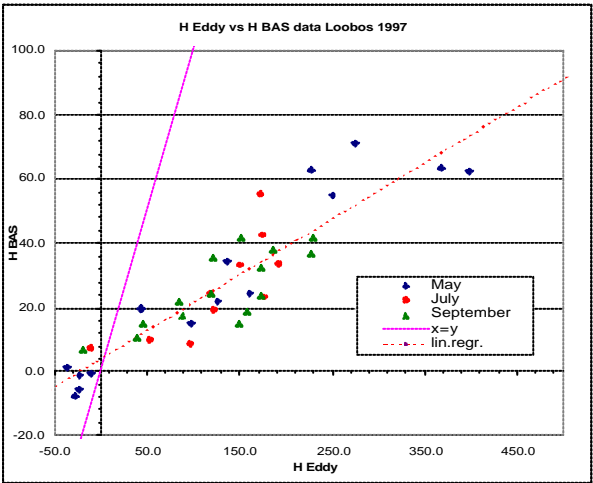
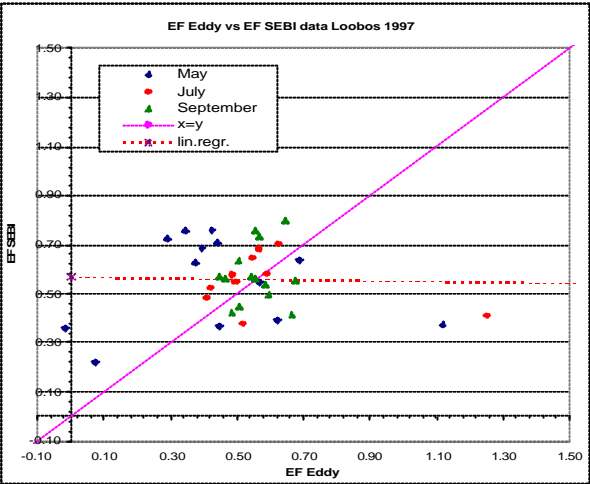
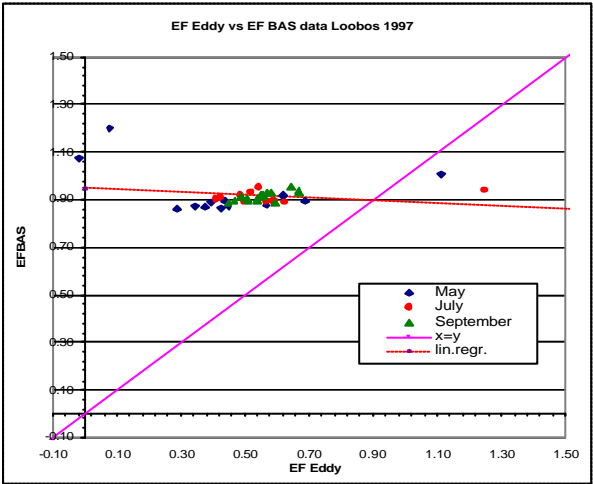
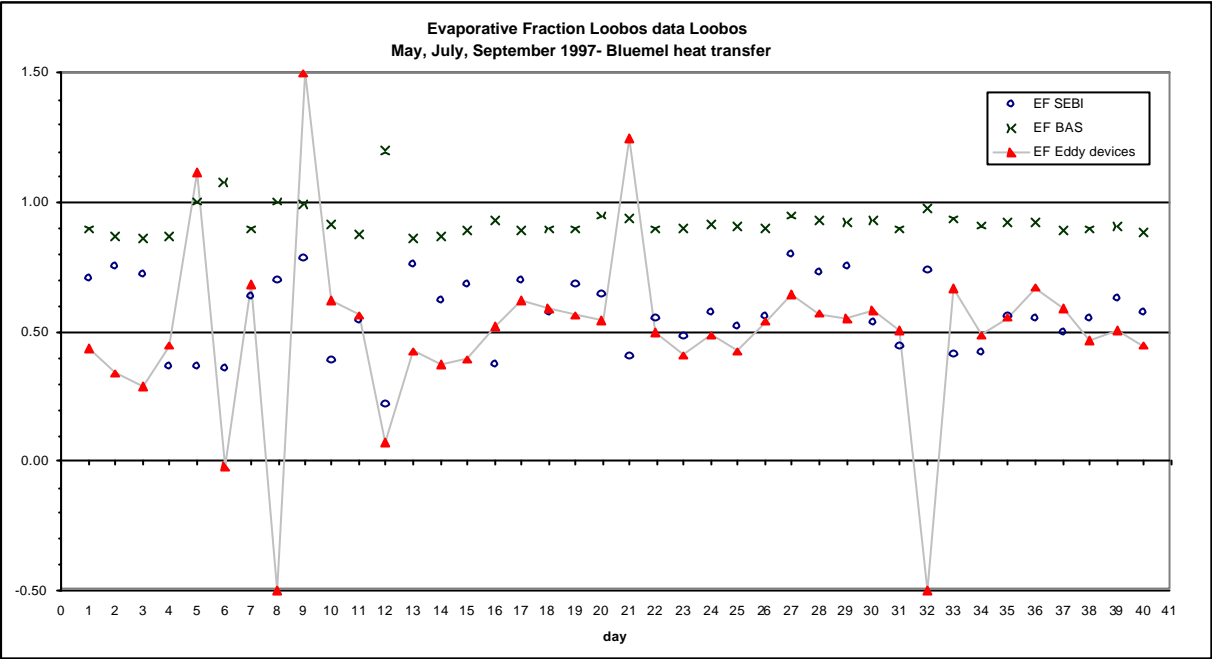


Appendix 4a - Time series - Loobos, May, July, September 1997 - Tower measurements - Massman heat transfer

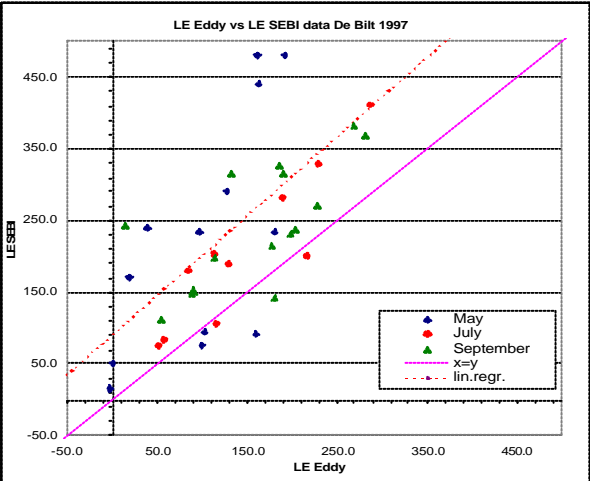
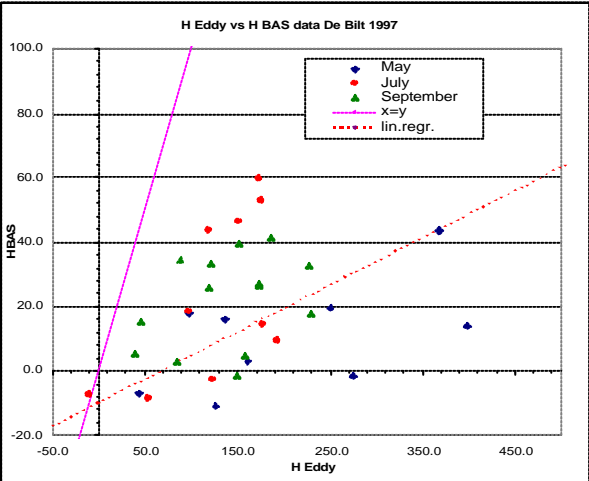
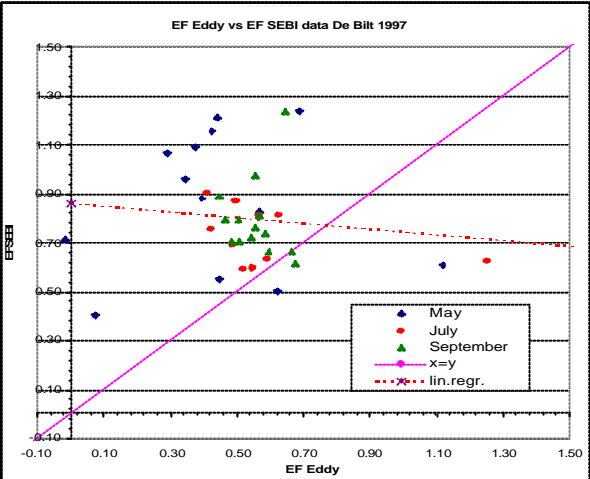
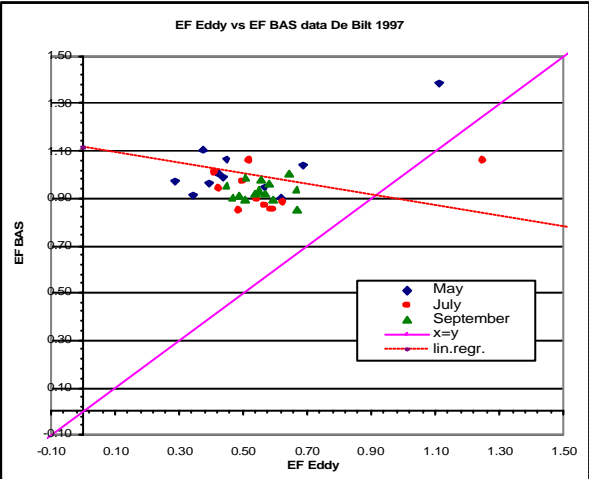
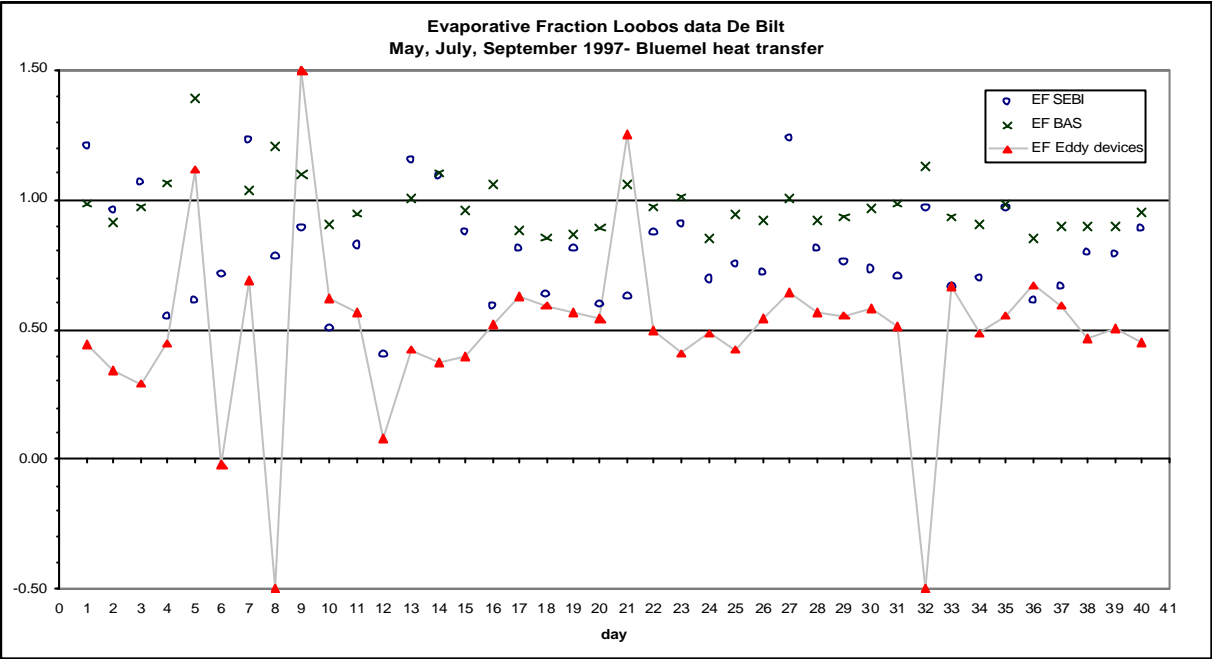


stats	RMSE	R^2	r.c.	intercept
NL Massman				
EF Bas vs. EF eddy	0.469	0.04	-0.05	0.96
EF SEBI vs. EF eddy	0.272	0.01	-0.01	0.6
H BAS vs. H eddy	135.2	0.8	0.16	3.5
LE SEBI vs. LE eddy	93.7	0.45	0.97	53.6

Appendix 4a - Time series - Loobos, May, July, September 1997 - Tower measurements - Blümel heat transfer

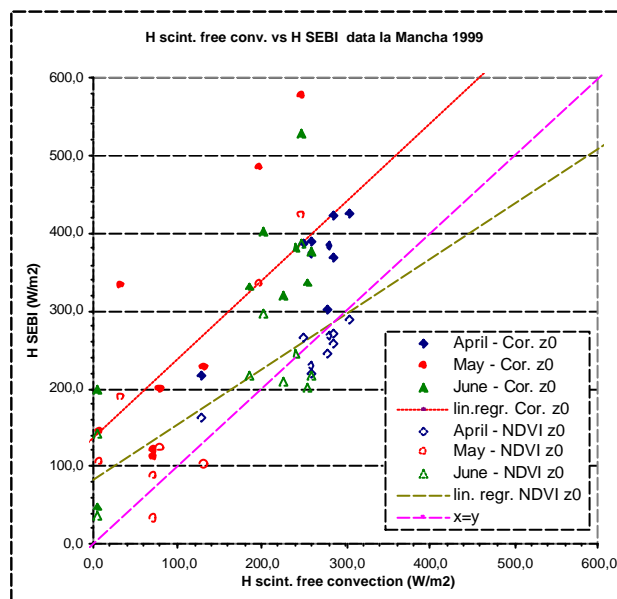
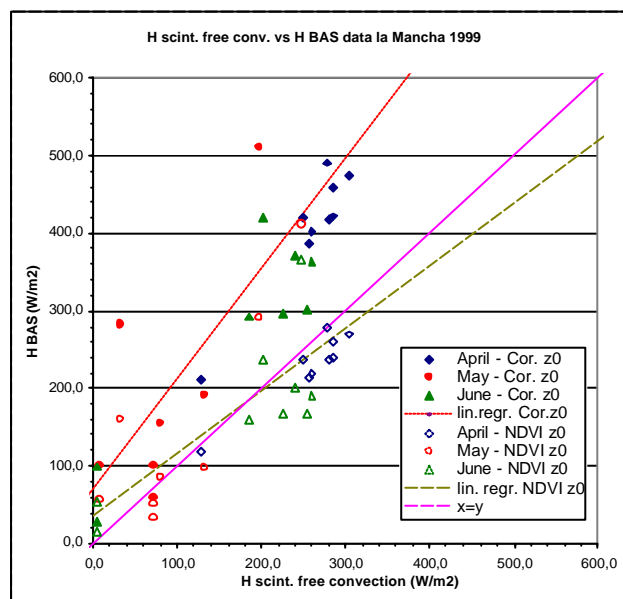
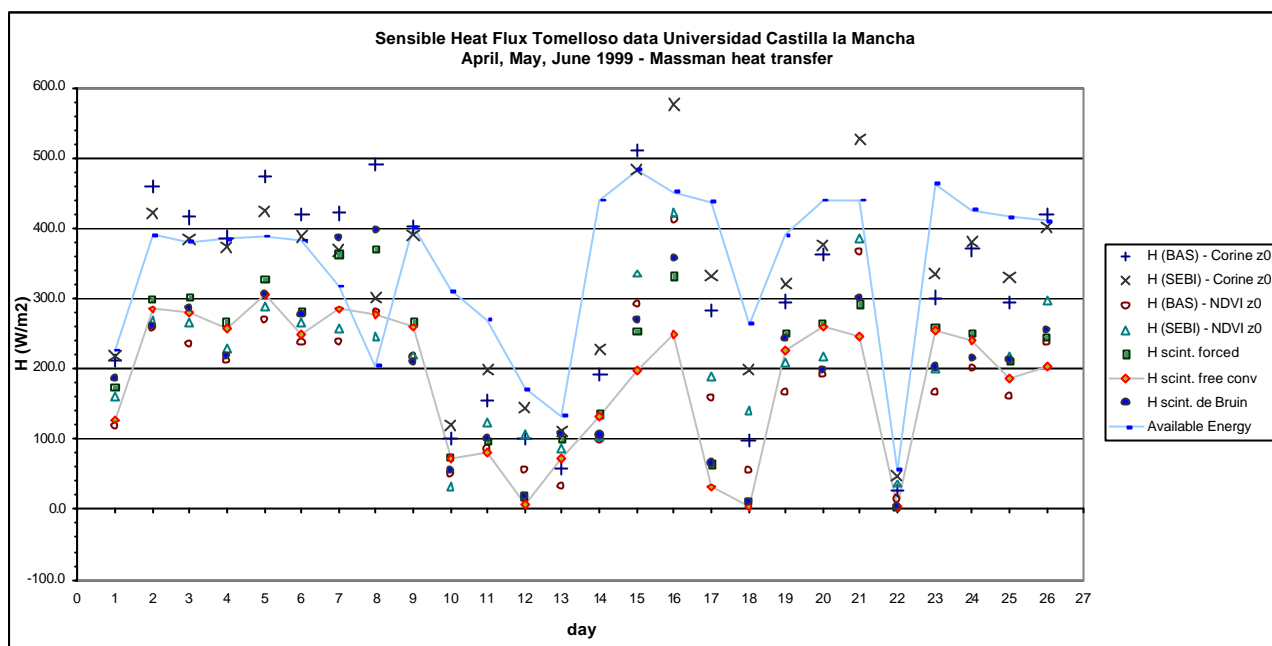


stats	RMSE	R^2	r.c.	intercept
NL Blümel				
EF Bas vs. EF eddy	0.458	0.041	-0.06	0.95
EF SEBI vs. EF eddy	0.259	0.001	-0.02	0.57
H BAS vs.H eddy	132.2	0.81	0.18	3.77
LE SEBI vs.LE eddy	85.4	0.45	0.92	49.4

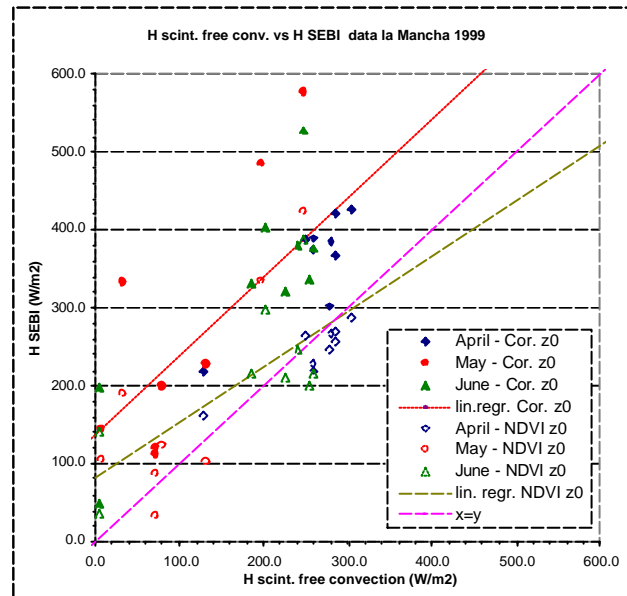
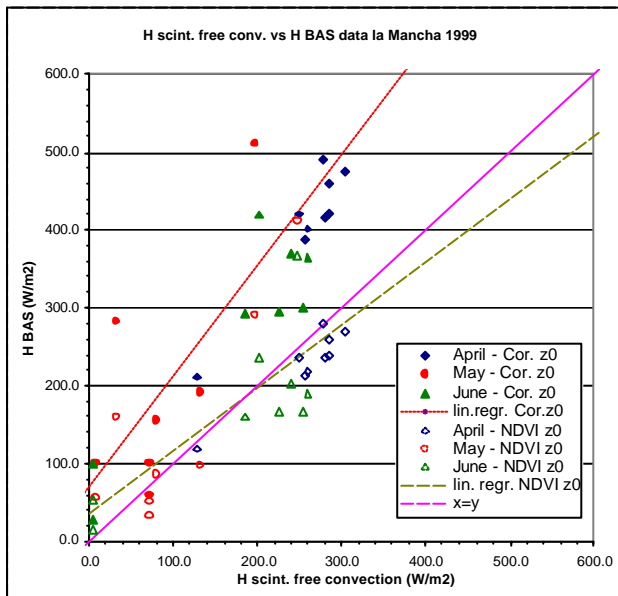
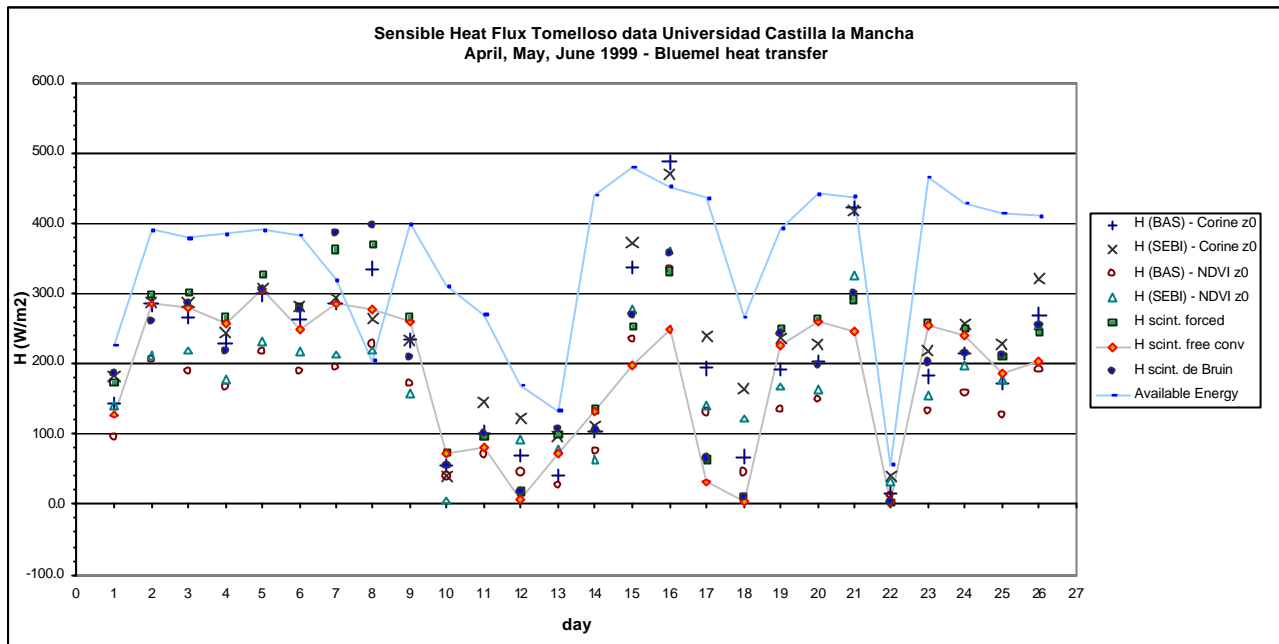


stats radio sounding	RMSE	R^2	r.c.	intercept
NL Blümel				
EF Bas vs. EF eddy	0.569	0.036	-0.28	1.1128
EF SEBI vs. EF eddy	0.439	0.004	-0.09	0.786
H BAS vs. H eddy	149.57	0.239	0.189	-19.88
LE SEBI vs. LE eddy	123.72	0.362	0.159	89.96

Appendix 4b - Time series - Tomelloso, April, May, June 1999 - Tower Measurements - Massman heat transfer

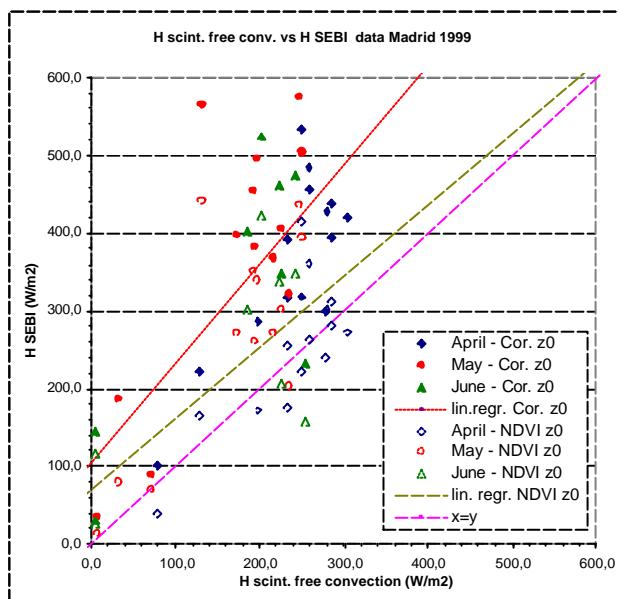
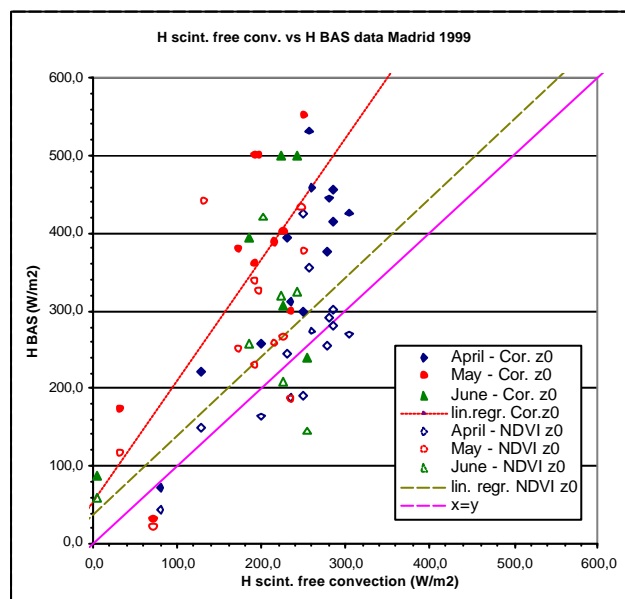
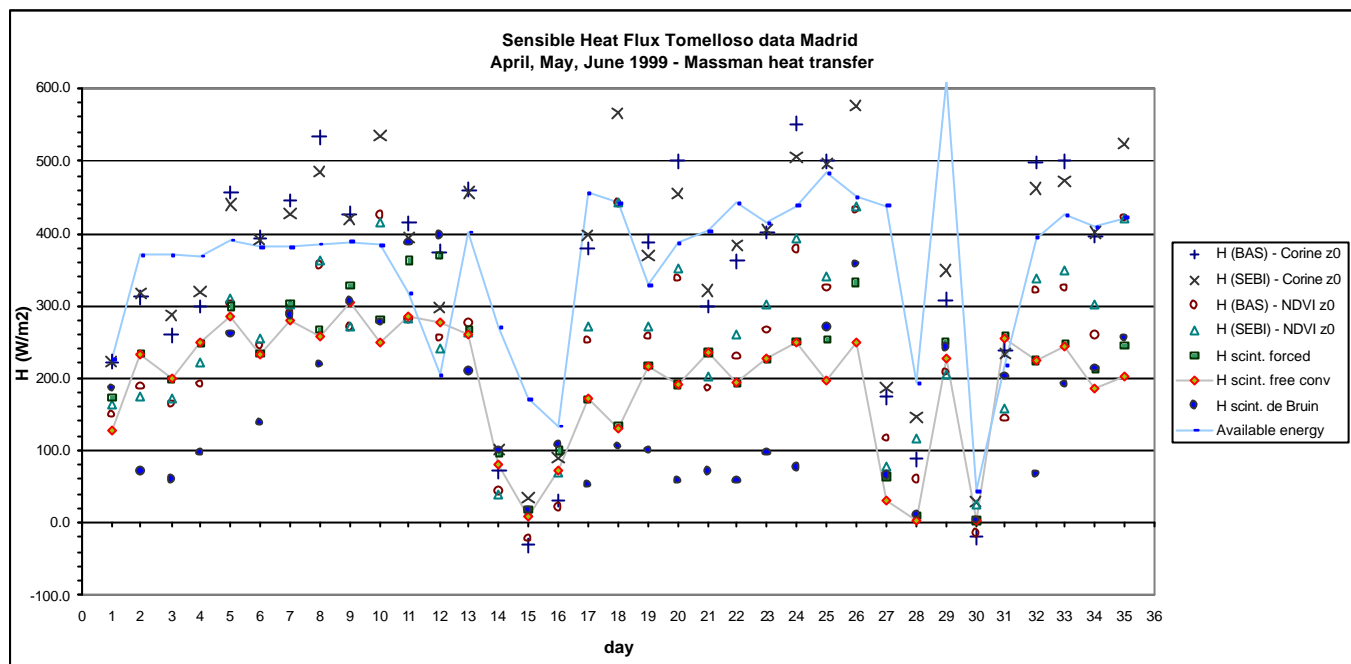


stats tower measurement		RMSE	R ²	r.c.	intercept
Tomelloso Massman					
Corine-z0m	H scint.free vs. H BAS	183.6	0.66	1.42	69.9
	H scint.free vs. H SEBI	159.9	0.61	1.01	136.2
NDVI-z0m	H scint.free vs. H BAS	63.3	0.6	0.8	37.2
	H scint.free vs. H SEBI	75.8	0.55	0.71	82.3

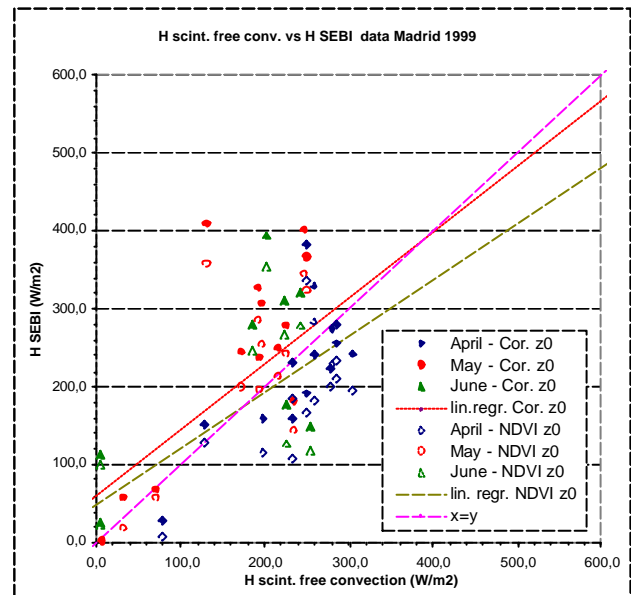
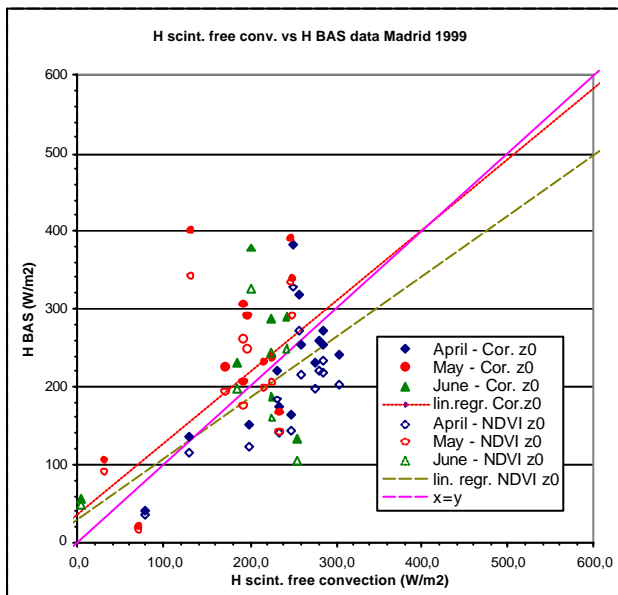
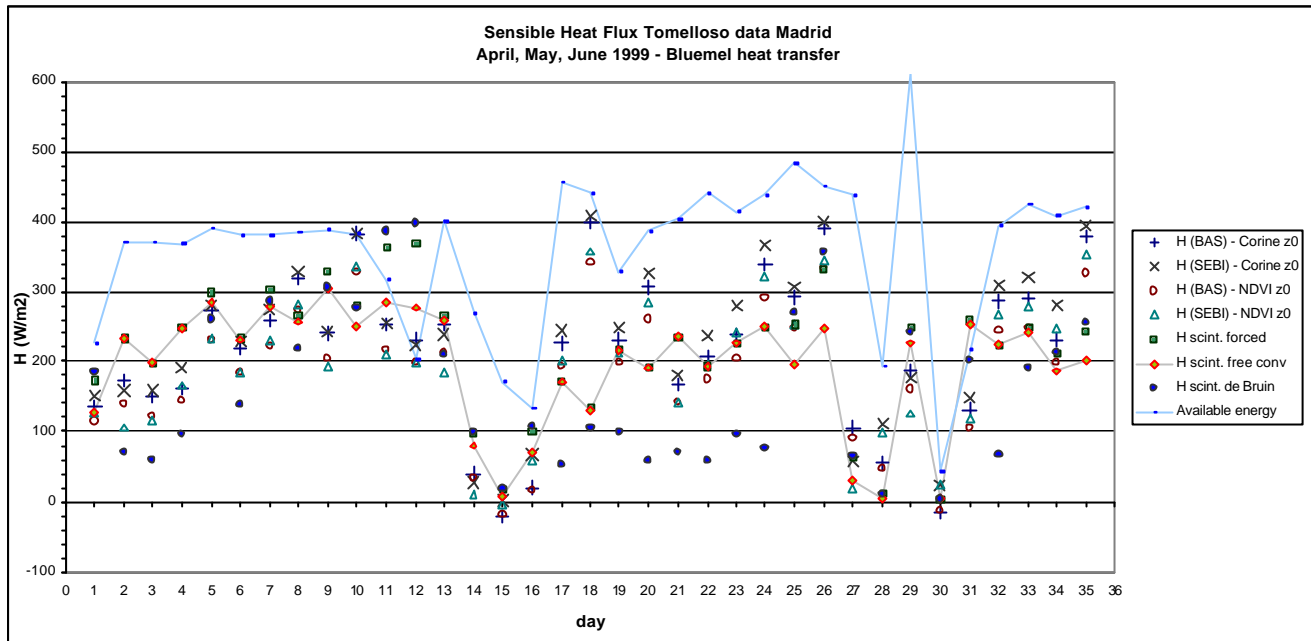


stats tower measurement		RMSE	R ²	r.c.	intercept
Tomelloso Bluemel					
Corine-z0m	H scint.free vs. H BAS	79.6	0.58	0.89	46.9
	H scint.free vs. H SEBI	92.5	0.49	0.73	100.3
NDVI-z0m	H scint.free vs. H BAS	70.3	0.62	0.64	30.9
	H scint.free vs. H SEBI	72.5	0.49	0.59	65.4

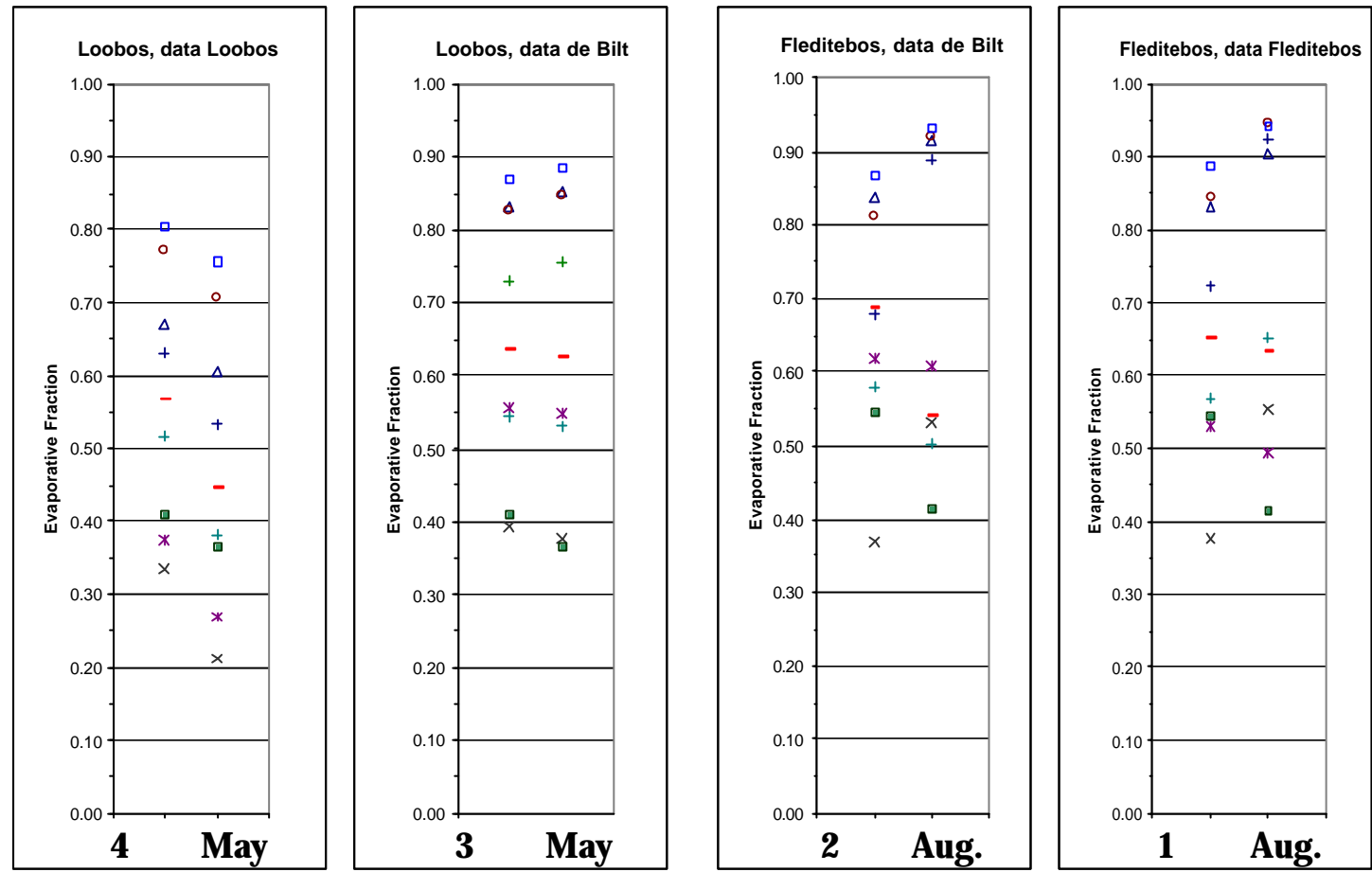
Appendix 4b - Time series - Tomelloso, April, May, June 1999 - Radio Soundings - Massman heat transfer

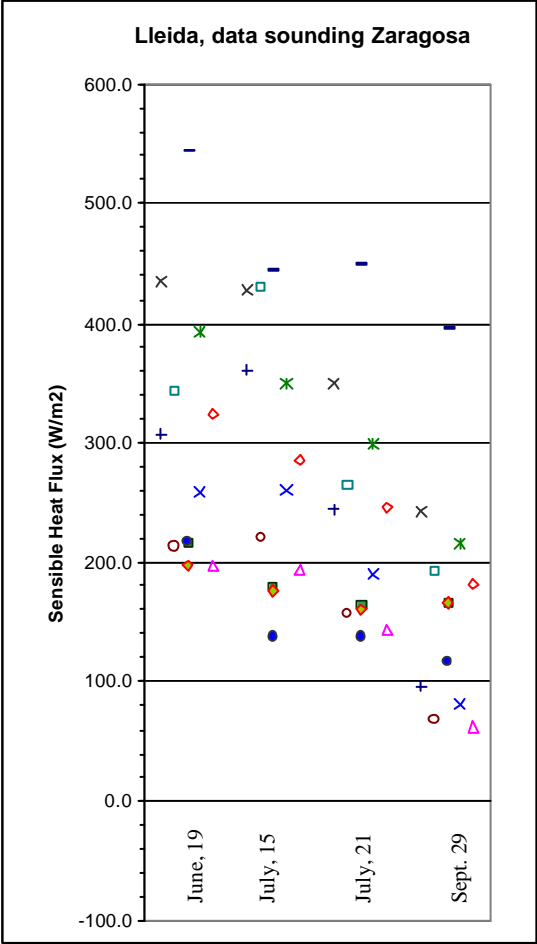
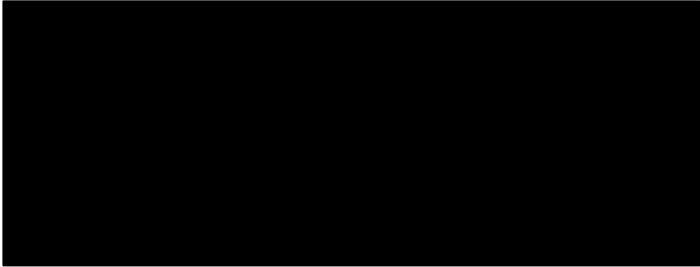
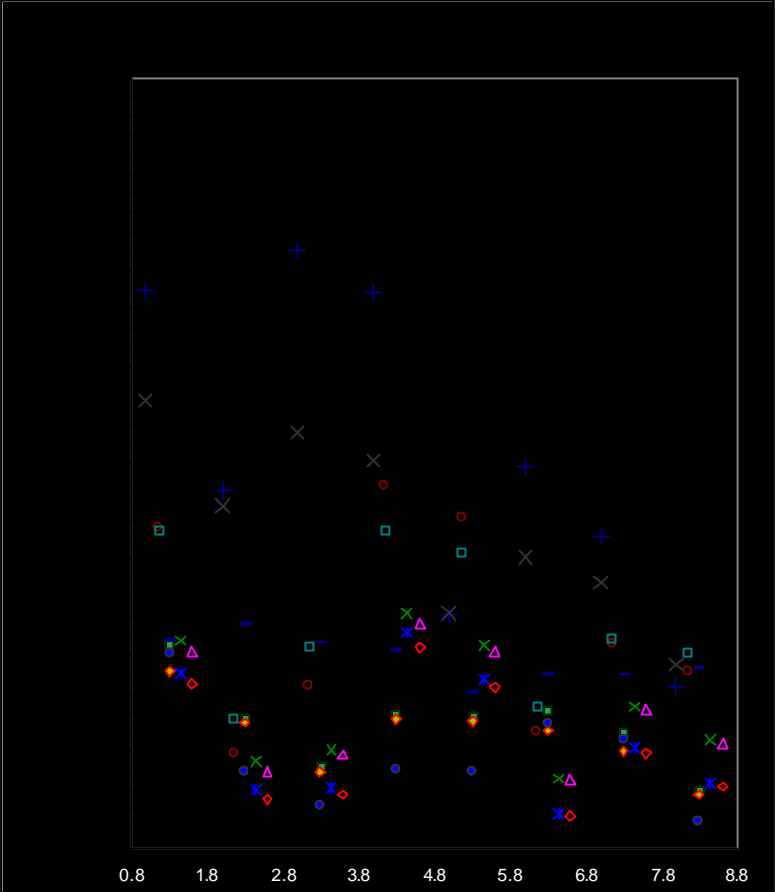
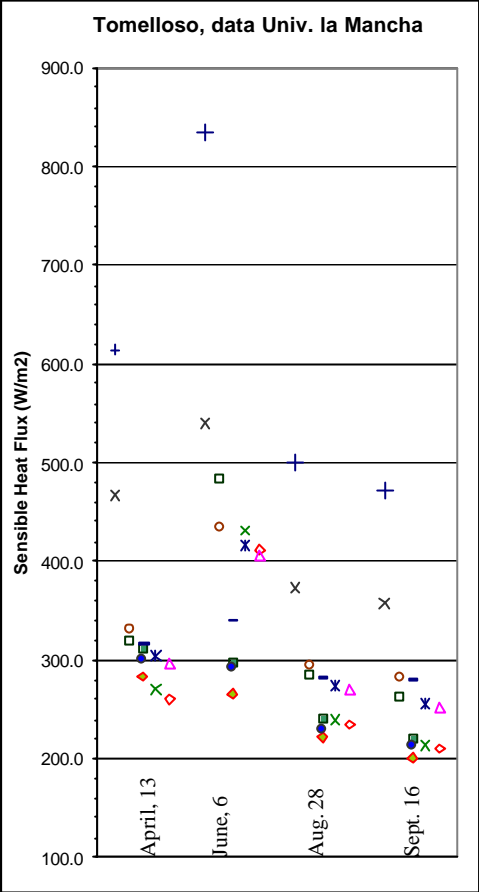


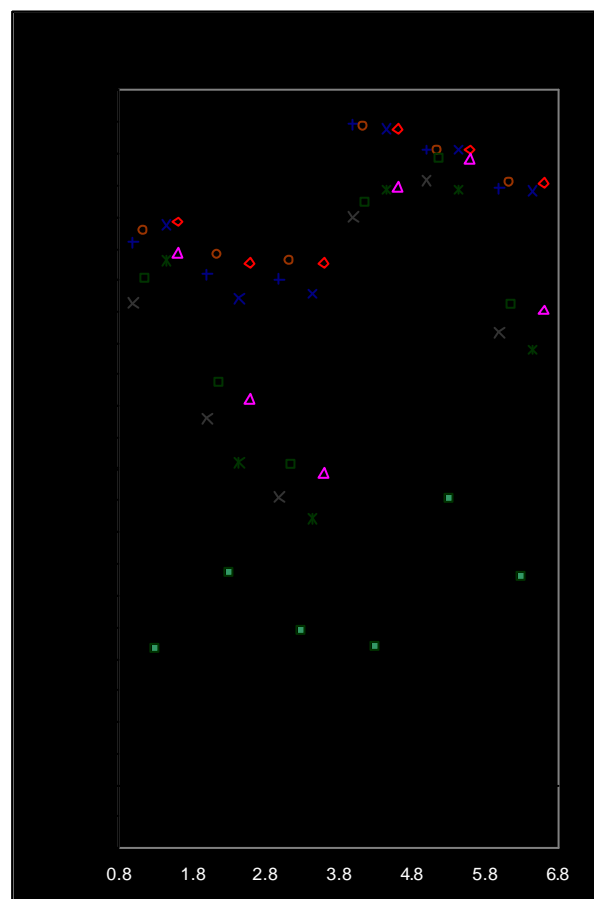
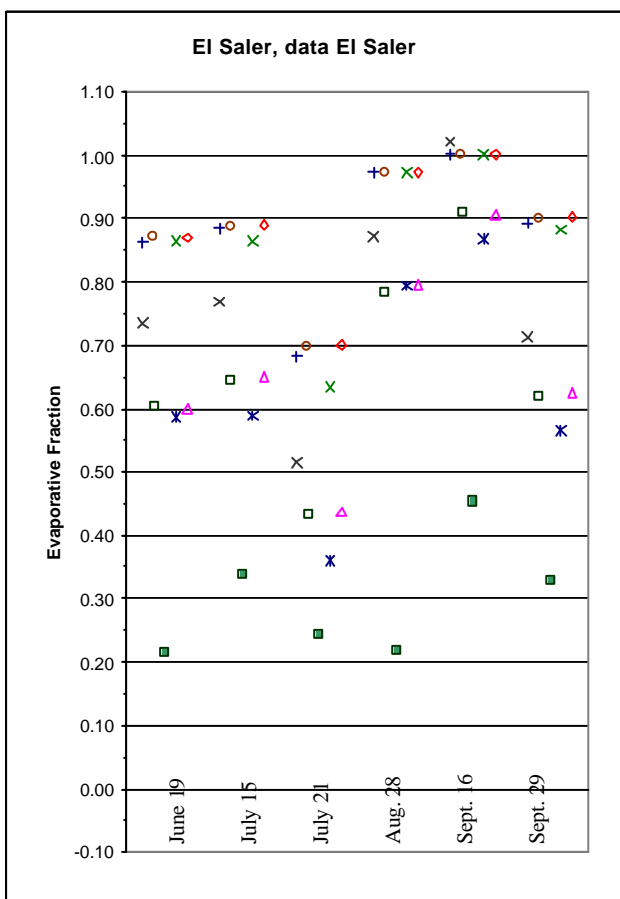
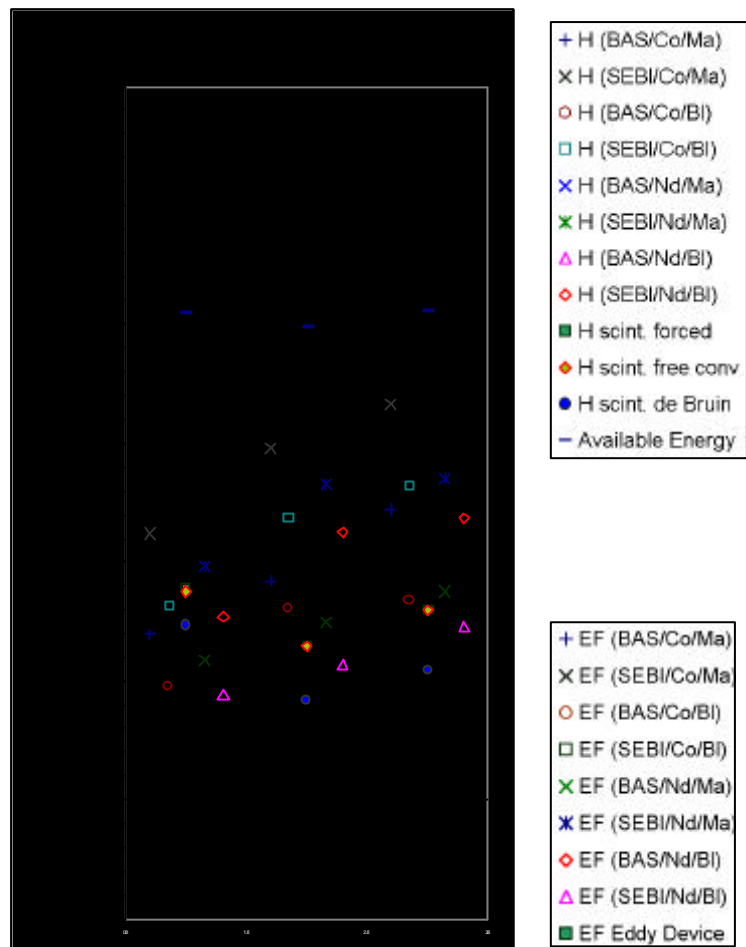
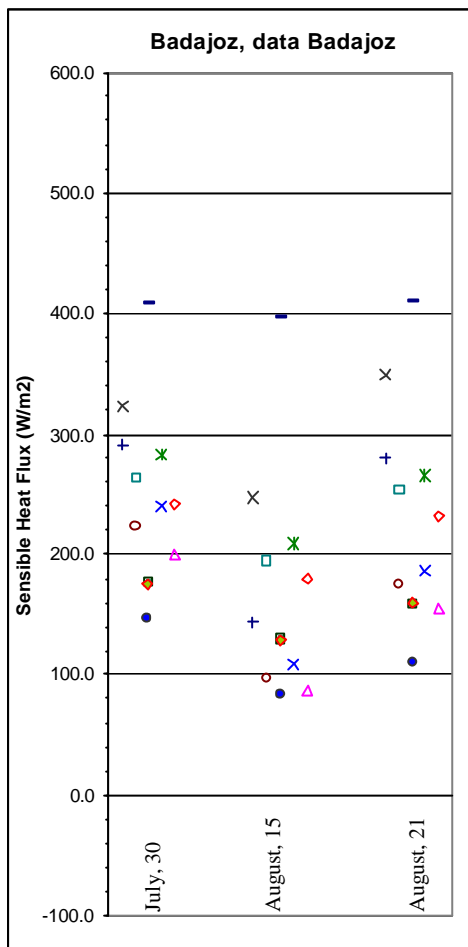
stats radio sounding		RMSE	R ²	r.c.	intercept
Tomelloso Massman					
Corine- z0m	H scint.free vs. H BAS	215.4	0.44	1.56	55
	H scint.free vs. H SEBI	191.6	0.45	1.27	103.9
NDVI- z0m	H scint.free vs. H BAS	99.24	0.63	1.01	38.1
	H scint.free vs. H SEBI	104.55	0.6	0.91	69.9



stats radio sounding		RMSE	R ²	r.c.	intercept
Tomelloso Bluemel					
Corine-z0m	<i>H scint.free vs. H BAS</i>	83.2	0.4	0.91	34.8
	<i>H scint.free vs. H SEBI</i>	90.6	0.35	0.85	61.4
NDVI-z0m	<i>H scint.free vs. H BAS</i>	73.2	0.39	0.78	29.1
	<i>H scint.free vs. H SEBI</i>	81.9	0.31	0.72	48

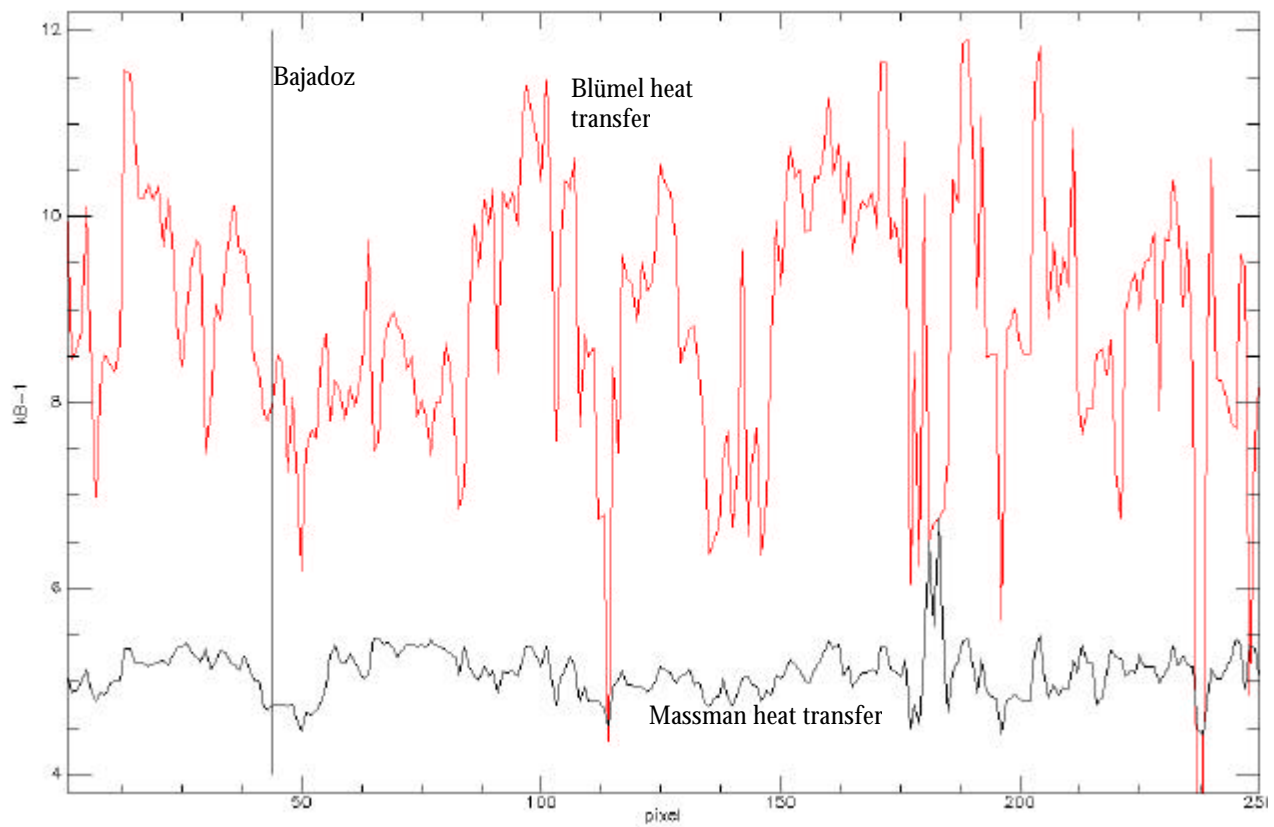


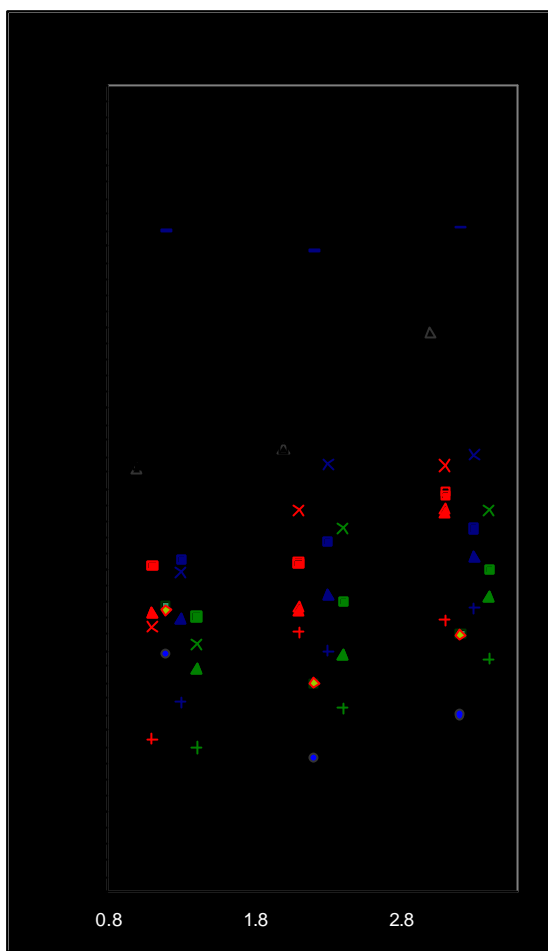
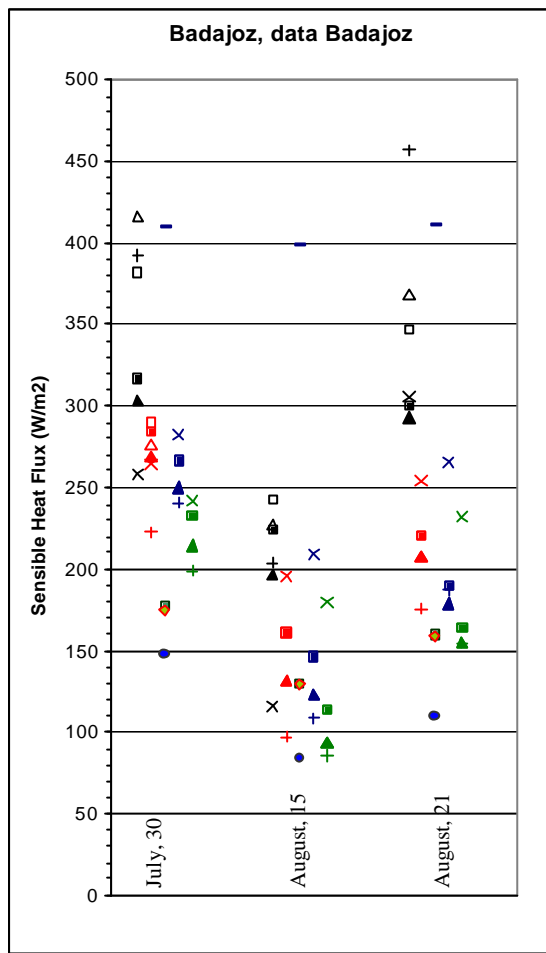




Appendix 6 – ATSR Data – Single Source - Statistics Spain 1999

STATISTICS - ATSR single source						STATISTICS - ATSR single source					
Badajoz - Tower Measurements - Massman - n=3						Tomelloso - Tower Measurements - Massman- n=4					
Corine- z0m	H scint.free vs. H BAS	97.1	0.92	3.39	-285.2	H scint.free vs. H BAS	383.1	0.45	2.39	33.1	
	H scint.free vs. H SEBI	154.5	0.69	1.87	17.0	H scint.free vs. H SEBI	198.1	0.62	1.45	86.5	
NDVI- z0m	H scint.free vs. H BAS	42.5	1.00	2.84	-259.7	H scint.free vs. H BAS	85.5	0.33	1.23	-5.7	
	H scint.free vs. H SEBI	98.6	0.98	1.64	-1.3	H scint.free vs. H SEBI	88.2	0.37	0.95	84.4	
Badajoz - Tower Measurements - Bluemel - n=3						Tomelloso - Tower Measurements - Bluemel - n=4					
Corine- z0m	H scint.free vs. H BAS	34.7	1.00	2.74	-257.5	H scint.free vs. H BAS	122.3	0.33	1.26	37.0	
	H scint.free vs. H SEBI	84.5	0.96	1.57	-5.1	H scint.free vs. H SEBI	107.2	0.39	0.94	110.1	
NDVI- z0m	H scint.free vs. H BAS	28.6	1.00	2.45	-231.9	H scint.free vs. H BAS	75.7	0.33	1.13	9.5	
	H scint.free vs. H SEBI	64.2	0.96	1.42	-1.2	H scint.free vs. H SEBI	86.7	0.36	0.89	94.0	
Badajoz - Radio Soundings - Massman - n=3						Tomelloso - Radio Soundings - Massman - n=8					
Corine- z0m	H scint.free vs. H BAS	61.9	0.07	-0.58	0.3	H scint.free vs. H BAS	326.6	0.17	1.78	124.0	
	H scint.free vs. H SEBI	142.4	0.26	-1.21	472.5	H scint.free vs. H SEBI	229.2	0.30	1.36	137.5	
NDVI- z0m	H scint.free vs. H BAS	36.3	0.16	-0.50	0.4	H scint.free vs. H BAS	78.7	0.02	-0.31	286.0	
	H scint.free vs. H SEBI	102.2	0.53	-1.27	440.9	H scint.free vs. H SEBI	74.9	0.02	-0.30	319.1	
Badajoz - Radio Soundings - Bluemel - n=3						Tomelloso - Radio Soundings - Bluemel - n=8					
Corine- z0m	H scint.free vs. H BAS	49.9	0.50	-1.23	0.1	H scint.free vs. H BAS	148.8	0.04	-0.66	481.3	
	H scint.free vs. H SEBI	87.2	0.33	-1.28	419.5	H scint.free vs. H SEBI	133.2	0.01	-0.29	401.4	
NDVI- z0m	H scint.free vs. H BAS	51.0	0.08	-0.34	0.6	H scint.free vs. H BAS	78.2	0.03	-0.32	278.9	
	H scint.free vs. H SEBI	72.4	0.46	-1.32	408.8	H scint.free vs. H SEBI	72.8	0.03	-0.35	321.4	
El Saler - Tower Measurements - Massman - n=6						El Saler - Tower Measurements - Bluemel - n=6					
Corine- z0m	EF Eddy Dev. vs. EF BAS	0.59	0.22	0.56	0.71	EF Eddy Dev. vs. EF BAS	0.60	0.22	0.53	0.73	
	EF Eddy Dev. vs. EF SEBI	0.49	0.34	1.07	0.45	EF Eddy Dev. vs. EF SEBI	0.32	0.33	1.02	0.36	
NDVI- z0m	EF Eddy Dev. vs. EF BAS	0.58	0.18	0.60	0.69	EF Eddy Dev. vs. EF BAS	0.60	0.22	0.53	0.73	
	EF Eddy Dev. vs. EF SEBI	0.30	0.21	0.90	0.36	EF Eddy Dev. vs. EF SEBI	0.32	0.32	1.00	0.37	
El Saler - Radio Soundings - Massman -n=6						Lleida - Radio Soundings - Massman - n=4					
Corine- z0m	EF Eddy Dev. vs. EF BAS	0.62	0.06	0.27	0.83	H scint.free vs. H BAS	114.7	0.28	3.81	-415.5	
	EF Eddy Dev. vs. EF SEBI	0.46	0.10	0.64	0.53	H scint.free vs. H SEBI	200.8	0.47	-1.75	-314.6	
NDVI- z0m	EF Eddy Dev. vs. EF BAS	0.61	0.03	0.22	0.84	H scint.free vs. H BAS	68.6	0.41	3.43	-403.7	
	EF Eddy Dev. vs. EF SEBI	0.47	0.02	0.34	0.62	H scint.free vs. H SEBI	149.6	0.62	-1.84	-346.4	
El Saler - Radio Soundings - Bluemel - n=6						Lleida - Radio Soundings - Bluemel - n=4					
Corine- z0m	EF Eddy Dev. vs. EF BAS	0.63	0.05	0.22	0.86	H scint.free vs. H BAS	54.1	0.40	2.80	-326.0	
	EF Eddy Dev. vs. EF SEBI	0.50	0.12	0.67	0.57	H scint.free vs. H SEBI	156.5	0.28	-0.95	-297.2	
NDVI- z0m	EF Eddy Dev. vs. EF BAS	0.63	0.04	0.20	0.86	H scint.free vs. H BAS	53.0	0.44	2.62	-310.7	
	EF Eddy Dev. vs. EF SEBI	0.50	0.06	0.52	0.62	H scint.free vs. H SEBI	94.2	0.65	-1.54	-287.4	

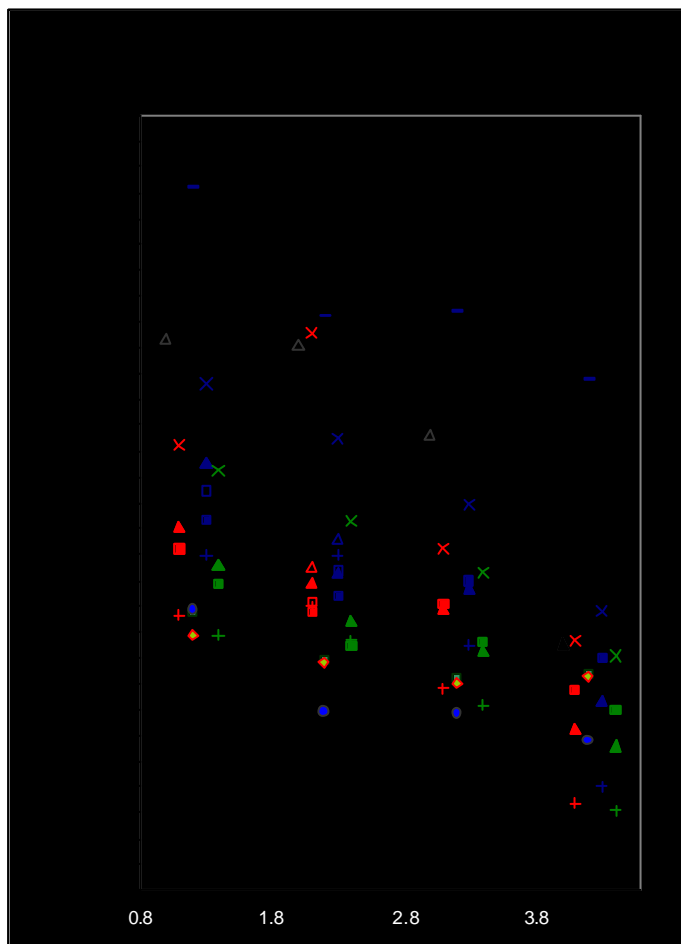


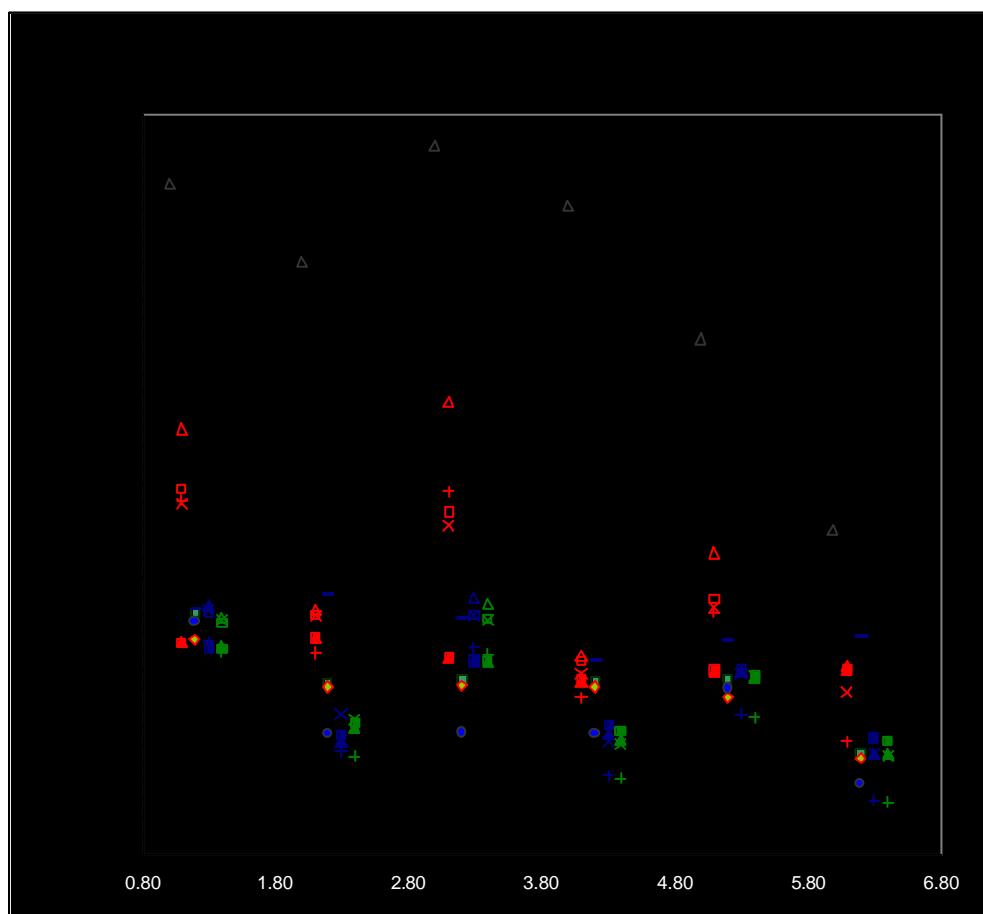
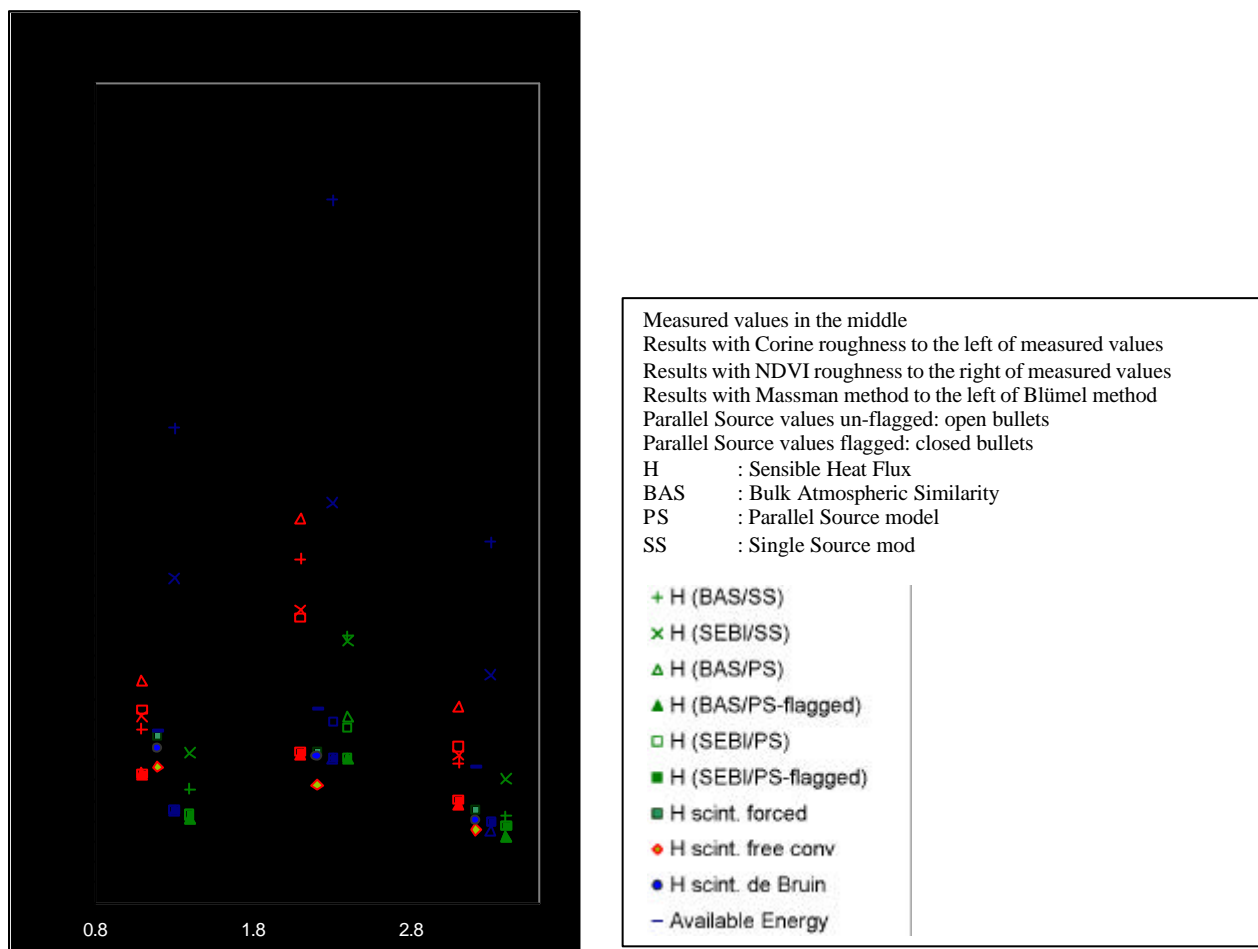


Measured values in the middle
 Results with Corine roughness to the left of measured values
 Results with NDVI roughness to the right of measured values
 Results with Massman method to the left of Blümel method
 Parallel Source values un-flagged: open bullets
 Parallel Source values flagged: closed bullets

H : Sensible Heat Flux
 BAS : Bulk Atmospheric Similarity
 PS : Parallel Source model
 SS : Single Source model

+ H (BAS/SS)
 x H (SEBI/SS)
 Δ H (BAS/PS)
 ▲ H (BAS/PS-flagged)
 □ H (SEBI/PS)
 ■ H (SEBI/PS-flagged)
 ■ H scint. forced
 ◆ H scint. free conv
 ● H scint. de Bruin
 - Available Energy





STATISTICS - ATSR parallel source		RMSE		R^2		r.c.		intercept	
		no flag	flagged	no flag	flagged	no flag	flagged	no flag	flagged
Badajoz - Tower Measurements - Massman - n=3									
Corine-z0m	H scint.free vs. H BAS	193.1	114.0	0.99	0.94	4.23	2.47	-315.7	-116.4
	H scint.free vs. H SEBI	174.4	127.8	0.99	0.97	3.11	2.13	-155.7	-47.9
NDVI-z0m	H scint.free vs. H BAS	44.8	44.8	0.94	0.94	2.67	2.67	-228.0	-228.0
	H scint.free vs. H SEBI	56.8	56.8	0.89	0.89	2.48	2.48	-182.3	-182.3
Badajoz - Tower Measurements - Bluemel - n=3									
Corine-z0m	H scint.free vs. H BAS	64.9	61.0	0.98	0.99	3.10	2.95	-273.0	-253.4
	H scint.free vs. H SEBI	77.6	75.1	0.96	0.96	2.72	2.63	-196.6	-183.4
NDVI-z0m	H scint.free vs. H BAS	30.3	30.3	0.97	0.97	2.54	2.54	-238.5	-238.5
	H scint.free vs. H SEBI	35.0	35.0	0.93	0.93	2.51	2.51	-216.8	-216.8
Badajoz - Radio Soundings - Massman - n=3									
Corine-z0m	H scint.free vs. H BAS	145.8	96.4	0.00	0.17	0.05	0.62	287.0	150.9
	H scint.free vs. H SEBI	141.4	86.6	0.43	0.24	2.74	1.11	-165.5	62.8
NDVI-z0m	H scint.free vs. H BAS	42.4	42.4	0.05	0.05	-0.18	-0.18	214.9	214.9
	H scint.free vs. H SEBI	65.7	65.7	0.17	0.17	-0.16	-0.16	241.1	241.1
Badajoz - Radio Soundings - Bluemel - n=3									
Corine-z0m	H scint.free vs. H BAS	53.5	50.7	0.01	0.02	0.17	0.22	169.9	160.1
	H scint.free vs. H SEBI	69.1	67.4	0.02	0.03	0.14	0.17	196.1	190.3
NDVI-z0m	H scint.free vs. H BAS	27.5	27.5	0.00	0.00	-0.02	-0.02	159.6	159.6
	H scint.free vs. H SEBI	38.1	38.1	0.03	0.03	-0.11	-0.11	200.8	200.8
		RMSE		R^2		r.c.		intercept	
Tomelloso - Tower Measurements - Massman - n=3									
Corine-z0m	H scint.free vs. H BAS	497.1	26.8	0.18	0.57	2.06	0.63	210.5	114.3
	H scint.free vs. H SEBI	232.3	29.6	0.54	0.57	1.80	0.59	22.6	128.8
NDVI-z0m	H scint.free vs. H BAS	50.3	29.4	0.14	0.24	0.77	0.56	69.0	105.6
	H scint.free vs. H SEBI	43.3	28.7	0.12	0.17	0.58	0.44	116.2	142.4
Tomelloso - Tower Measurements - Bluemel - n=3									
Corine-z0m	H scint.free vs. H BAS	172.2	22.9	0.13	0.59	1.12	0.59	122.7	121.3
	H scint.free vs. H SEBI	110.3	25.6	0.25	0.53	1.03	0.54	93.7	135.4
NDVI-z0m	H scint.free vs. H BAS	48.3	33.0	0.14	0.20	0.73	0.56	71.7	101.7
	H scint.free vs. H SEBI	42.4	31.3	0.11	0.14	0.54	0.42	121.2	143.0
Tomelloso - Radio Soundings - Massman - n=6									
Corine-z0m	H scint.free vs. H BAS	460.1	48.4	0.75	0.30	3.22	0.26	-54.9	203.5
	H scint.free vs. H SEBI	304.4	49.9	0.58	0.31	2.20	0.26	22.2	206.9
NDVI-z0m	H scint.free vs. H BAS	52.7	37.9	0.43	0.56	1.20	1.14	37.9	-33.2
	H scint.free vs. H SEBI	44.7	31.7	0.43	0.45	1.01	0.71	7.7	61.1
Tomelloso - Radio Soundings - Bluemel - n=6									
Corine-z0m	H scint.free vs. H BAS	176.3	47.2	0.43	0.23	1.97	0.22	-68.7	209.8
	H scint.free vs. H SEBI	121.3	47.7	0.54	0.26	1.46	0.22	5.5	210.7
NDVI-z0m	H scint.free vs. H BAS	48.2	32.2	0.45	0.54	1.15	0.88	-28.1	17.1
	H scint.free vs. H SEBI	40.9	29.8	0.45	0.50	0.97	0.73	14.5	55.2
		RMSE		R^2		r.c.		intercept	
Lleida - Radio Soundings - Massman - n=4									
Corine-z0m	H scint.free vs. H BAS	194.1	85.4	0.38	0.25	4.28	1.47	-400.9	-5.6
	H scint.free vs. H SEBI	147.8	86.6	0.43	0.24	2.74	1.11	-165.5	62.8
NDVI-z0m	H scint.free vs. H BAS	91.1	84.9	0.66	0.67	3.95	3.89	-444.6	-441.6
	H scint.free vs. H SEBI	77.2	65.5	0.69	0.57	2.73	2.08	-234.4	-130.3
Lleida - Radio Soundings - Bluemel - n=4									
Corine-z0m	H scint.free vs. H BAS	66.1	63.1	0.51	0.53	3.03	3.01	-312.0	-310.7
	H scint.free vs. H SEBI	51.5	49.8	0.51	0.51	2.01	2.00	-136.0	-135.1
NDVI-z0m	H scint.free vs. H BAS	43.4	43.4	0.60	0.60	2.85	2.85	-309.2	-309.2
	H scint.free vs. H SEBI	29.4	29.4	0.59	0.59	1.92	1.92	-146.5	-146.5

